Advanced Control of Active Bearings - Modelling, Design and Experiments

Theisen, Lukas Roy Svane

Publication date:
2016

Document Version
Publisher's PDF, also known as Version of record

Technical University of Denmark

Lukas Roy Svane Theisen

Advanced Control of Active Bearings - Modelling, Design and Experiments

PhD Thesis, May 2016

DTU Electrical Engineering
Department of Electrical Engineering

Advanced Control of Active Bearings - Modelling, Design and Experiments

Lukas Roy Svane Theisen

Technical University of Denmark
Kgs. Lyngby, Denmark, 2016

Technical University of Denmark
Department of Electrical Engineering
Automation and Control (AUT)
Elektrovej Building 326
DK-2800, Kgs. Lyngby
Denmark
Phone: (+45) 45 25 35 76
Email: info@elektro.dtu.dk
www.elektro.dtu.dk

ISBN:

Summary

In all rotating machines relative movements between the stationary parts and the rotating parts imply energy loss and, in many critical cases, vibration problems. This energy loss leads to higher overall energy consumption of the system. Research activities towards the reduction of friction, the enhancement of damping, the extension of operating range and the minimisation of critical vibrations in machine elements are of fundamental importance. The main component to tackle the energy-loss-related problems is the bearing. The area of design of active bearings, while very promising, is still in its early development mainly because of its high complexity and its multi-physics nature. The state-of-the-art models derived from first principles and axioms of mechanics are complex and often subject to significant parameter uncertainties. They are challenging to develop and not easily used for feedback control design. One example is the controllable radial gas bearing, where the lubricant air is injected through controllable injectors to levitate the rotor on an air film. Feedback control of the injection can improve upon the poor damping to reduce the disturbance sensitivity and vibrations near the critical speeds. The feedback control law is preferably designed from a simple model, which captures the dominant dynamics of the machine in the frequency range of interest.

This thesis offers two main original contributions in the field of active bearings. First, an experimental technique is proposed for "in situ" identification of low complexity models of the entire rotor-bearing-actuator-sensor system. The approach employs grey-box identification techniques and is easily applied to industrial rotating machinery with controllable bearings. The approach is applied for identification of a linear parameter-varying model of a rotor supported by an active gas bearing.

Second, is the application of model-based control techniques for controllable gas bearings. The parameter-varying model is shown to suit the design of classical and modern control including observer and state-feedback, $\mathcal{H}_\infty$, LPV and gain-scheduled $\mathcal{H}_2$ control designs to improve upon the dynamic properties of the gas bearing test

rig. Experimental results using the control designs show that the controllers can increase the damping significantly. The damping enhancing controllers are shown to extend the range of safe operation by a 70% increase in shaft angular velocity, thereby allowing safe operation in and above the regions of the first and second critical speeds.

Resumé

I alle roterende maskiner giver relativ bevægelse mellem de stationære og de roterende dele anledning til tab af energi og, i mange kritiske tilfælde, vibrationsproblemer. Dette energitab fører til højere energiforbrug af det samlede system. Forskningsaktiviteter mod reduktion af friktionen, forøgelse af dæmpningen, udvidelse af driftsområdet og minimering af de kritiske vibrationer i maskinelementer er af fundamental betydning. Hovedkomponenten for at håndtere de energitabsrelaterede problemer er lejet. Forskningsfeltet indenfor design af aktive lejer er meget lovende, men det er stadig kun i begyndelsesfasen. Primært på grund af feltets høje kompleksitet og multifysiske natur. State-of-the-art-modellerne udledt fra grundprincipperne og de mekaniske aksiomer er ofte komplekse og lider ofte under signifikante parameterusikkerheder. De er vanskelige at udlede og svære at bruge til design af feedback-regulering. Et eksempel er det regulerbare tvær-luftleje, hvor smøringsluften indsprøjtes gennem regulerbare injektorer for at få rotoren til at svæve på et luftfilm. Feedbackregulering af indsprøjtningen kan forbedre de ellers dårlige dæmpningsegenskaber for at reducere forstyrrelsessensitiviteten og vibrationerne nær de kritiske hastigheder. Feedbackreguleringen designes helst fra en simpel model, der beskriver maskinens dominerende dynamik i det relevante frekvensområde.

Denne afhandling byder på to originale bidrag inden for forskningen i aktive lejer. For det første foreslås en teknik til "in situ"-identifikation af lav-kompleksitetsmodeller af hele rotor-leje-aktuator-sensor-systemet. Metoden anvender grey-box identifikationsteknikker og er let anvendelig på industrielle roterende maskiner med regulerbare lejer. Metoden er anvendt til at idenficere lineært parameter-varierende modeller af en rotor understøttet af et aktivt luftleje.

For det andet anvendes modelbaseret reguleringsstrategier på regulerbare luftlejer. Det påvises at de parameter-varierende modeller er vel-egnede til design af klassisk og moderne regulering, herunder: observer og tilstandstilbagekobling, $\mathcal{H}_\infty$, LPV og gain-skeduleret $\mathcal{H}_2$ regulatordesign til at forbedre de dynamiske egenskaber af

luftlejeopstillingen. Eksperimentelle resultater med de foreslåede regulatordesigns beviser at reguleringen kan øge dæmpningen markant. De dæmpnings-forbedrende regulatorer demonstrerer at det er muligt at øge det sikre driftsområde med 70% i omdrejningshastighed. Det tillader dermed sikker drift i- og over de to første kritiske hastigheder.

Preface

This thesis is submitted as partial fulfilment of the requirements for obtaining the Danish PhD degree. The thesis consists of a summary and a collection of two journal papers and five conference papers written during the PhD project from May 2013 to April 2016. The work has primarily been carried out at the Section of Automation and Control (AUT), Department of Electrical Engineering, Technical University of Denmark (DTU). The Danish Ministry of Science, Innovation and Higher Education provided funding to the project through the FTP research project 12-127502.

The project was supervised by associate professor Hans Henrik Niemann, professor Ilmar Ferreira Santos and associate professor Roberto Galeazzi. Each of them provided a unique guidance for which I am thankful. I would also like to thank Professor Juan Francisco Camino from the University of Campinas (Unicamp), State of São Paulo for letting me join his research group for three months during the fall 2015.

I would like express my gratitude to my closest PhD colleagues and friends at DTU. Especially Søren Enemark and Andreas Søndergaard Pedersen. I have enjoyed our technical discussions during lunch times. I would also like to thank Fabián G. Pierart, Dan Hermann, Bo Bjerregaard Nielsen, André Krabdrup Sekunda, Jonas Skjødt Lauridsen and the other students from the AUT group and from Ilmar's team.

From my stay at Unicamp I would like to thank Ricardo Bonna, Luis Antonio Rodrigues, Guilherme Raya da Costa and Marcos Heringer for their warm welcome and the many technical discussions, which have inspired and encouraged me.

Most of all I would like to thank my wife Ingeborg H. Hansen and my family for their support. They have always been there for me and encouraged me to go further.

Though it is customary at this point to include a quote, I would like to include a famous story:

A biologist, a physicist and a mathematician sit at a bench in a park. They see a man walk into a shed. 10 minutes later, two people walk out. The biologist says “It was reproduction”, the physicist says “It must be bad data”, but the mathematician doesn’t say anything.

A few minutes later, someone else walks in the shed.

The mathematician goes “Ok, now nobody is in the shed”

To the story, I would like to add, that there was a young system identification engineer who said “No, don’t you see it? it all makes 100 % sense; the transfer function of the shed is $H(s) = 2e^{-\tau s},\ \tau = 10$min, and in ten minutes, two people more should come out.”

List of Publications

This thesis is composed of 5 conference papers and 2 journal papers. The papers are listed in the order in which they were written. Journal papers are marked by (*Journal*).

A L. R. S. Theisen, F. G. Pierart Vásquez, H. H. Niemann, I. F. Santos, and M. Blanke. "Experimental Grey Box Model Identification of an Active Gas Bearing". In: *Vibration Engineering and Technology of Machinery*. Ed. by J. Sinha. Springer, 2014, pp. 963–976

B L. R. S. Theisen and H. H. Niemann. "Modelling of Rotor-gas bearings for Feedback Controller Design". In: *Journal of Physics: Conference Series (Online)* 570 (2014)

C (*Journal*) L. R. S. Theisen, H. H. Niemann, I. F. Santos, R. Galeazzi, and M. Blanke. "Modelling and identification for control of gas bearings". In: *Mechanical Systems and Signal Processing* 70–71 (2016), pp. 1150–1170

D L. R. S. Theisen, H. H. Niemann, I. F. Santos, and R. Galeazzi. "Experimental Investigations of Decentralised Control Design for The Stabilisation of Rotor-Gas Bearings". In: *Proceedings of the XVII International Symposium on Dynamic Problems of Mechanics*. 2015

E (*Journal*)L. R. S. Theisen, H. H. Niemann, R. Galeazzi, and I. F. Santos. "Enhancing damping of gas bearings using linear parameter-varying control". In: *Submitted to Journal of Sound and Vibration* (2016)

F L. R. S. Theisen, H. H. Niemann, R. Galeazzi, and I. F. Santos. "Gas Bearing Control for Safe Operation in Critical Speed Regions - Experimental Verification". In: *Journal of Physics: Conference Series (Online)* 659.1 (2015)

G L. R. S. Theisen, H. H. Niemann, and J. F. Camino. “An Application of Gain-Scheduled Control Using State-Space Interpolation to Hydroactive Gas Bearings”. In: *Submitted for IEEE Multi-Conference on Systems and Control 2016* (2016)

Contents

Glossary

critical speed A natural frequency coinciding with the angular velocity of the rotor. The mass imbalance can grow to critical levels in these regions. 1, 8, 55, 56, 58, 63

fluid film The fluid film in journal bearings is the thin layer of lubricant (oil, air or others) that separate the rotor from the bearing housing. 6, 207

journal Part of the rotor in the housing of a journal bearing. 6, 207

journal bearing A bearing where a fluid lubrication results in a full-film or a boundary condition lubrication mode. The journal bearing reduces friction by eliminating surface-to-surface contact between the journal and bearing. Journal bearings can be hydrostatically or hydrodynamically or hydroactively lubricated. In the hydrodynamically lubricated bearings, the pressure in the fluid film is maintained by the rotation of the journal. In the hydrostatically lubricated bearings, a pressurised fluid is injected to lubricate. In the hydroactively lubricated bearings, the injection of fluid is actively controlled. 5, 6, 10, 20, 207

mass imbalance Vibrations induced in a rotating system from the rotor centre of mass differing from its geometrical center. 1, 6, 8, 17, 20, 28, 45, 55, 56

rotor Combination of shaft, discs and impellers. 6, 9, 207

touchdown Impact between rotor and stator when the load exceeds the carrying capacity. 2

Acronyms

AMB active magnetic bearing. 6, 8, 12, 13, 15, 17, 18, 19, 207

CFD computational fluid dynamics. 5, 11, 12

DOF degree of freedom. 9, 36

FE model finite element model. 5, 6, 9, 10, 11, 18

LFT linear fractional transformation. 50

LMI linear matrix inequality. 15, 51, 52

LPV linear parameter-varying. 14, 15, 21, 22, 23, 25, 29, 30, 32, 39, 53, 57, 63, 67, 68

LQR linear quadratic regulator. 11, 17, 18

LTI linear time-invariant. 6, 14, 18, 19, 25, 28, 32, 38, 39, 49

PEM prediction error method. 25

PRBS pseudo-random binary signal. 27, 29

RMS root mean square. 40, 51

Chapter 1

Introduction

This chapter summarises previous work from the field of active bearing design to provide a background and motivate this thesis. The experimental facilities are briefly revisited along with the state-of-the-art in modelling and control of controllable bearings.

In all rotating machines relative movements between the stationary parts and the rotating parts imply energy loss and, in many critical cases, vibration problems. The energy loss reduces the efficiency of the rotating machine. From the viewpoint of sustainable technology, research activities towards the reduction of friction, the minimisation of vibrations, the extension the operating range and the enhancement of load capability in machine elements are of fundamental importance.

The research is in general focussed towards three main goals:

G1 reducing the rotor-bearing friction

G2 obtaining high damping levels

G3 increasing the load carrying capacity

Reduction of the friction (G1) diminishes energy losses and thereby the operational cost; however such a reduction usually entails the overall worsening of the damping properties. Damping (G2) aids to suppress whirl instability [8, 9] and reduces the sensitivity of the rotating machine towards disturbances [10], which in turn reduces the risk of rotor-stator rubbing to avoid wear & tear. The disturbances stem from many sources. The main source is vibrations from *mass imbalance*, but vibrations may also be induced from other rotating machines and from external sources, for instance, mechanical shocks. The mass imbalance provides a force on the rotor, which

is synchronous to its angular velocity. The induced vibrations may become critical when the angular frequency is near the resonance frequencies of the rotor-bearing system. Systems with low damping are especially sensitive to these *critical speeds*.

Various mechanical and mechatronic solutions have been proposed to attain the goals G1-3. In order to tackle the energy loss related problems in one of the most fundamental machine elements, namely the bearing, two main approaches can be used: one based on traditional passive solutions and one based on active synergistic solutions. Passive solutions might include approaches such as optimisation of the geometries, the lubrication fluids, the lubrication mechanisms, the material compliance and the surface roughness. Active solutions normally involve the synergistic integration of three different domains, namely the mechanical, the electrical and the control engineering, giving rise to the so-called mechatronic systems. The mechatronics integrated design solutions can involve mechanical, magnetic, pneumatic, hydraulic and piezoelectric operational principles.

The active solutions may address many of the technical challenges related to new requirements for safety, quality, low vibrations and noise levels, where conventional passive solutions are reaching their limits [11, 12]. The area of active synergistic design in bearings, while very promising, is still in its early development mainly because of its high complexity and its multi-physics nature; hence it needs further research efforts.

Among the passive means are foil bearings [13, 14, 15] that exploit friction between their bumps and foils (see Figure 1.1). Foil bearings are already common in air cycle machines on commercial and military jets [16]. They are fairly cheap, though the design of friction is a significant challenge [17] and *touchdown* occurs during start-up and shut-down which wears the bearing surface.

The design of active bearings is still in its infancy. Solutions have been proposed using different forms of actuation. A few examples are the piezo-electric pushers [18, 19], piezo-actuated tilting pad air bearings [20, 21] (see Figure 1.2 and Figure 1.4), piezo-actuated aerodynamic bearings [22, 23] (see Figure 1.3), giant magnetostrictive materials [24], hydraulic actuators [25], shape memory alloys [26, 27] and active inherent restrictors [28, 29].

The solution considered in this thesis is the controllable gas bearing [31], where piezo-actuators control the lubricant air-injection as described further in Section 1.1. The methods developed in the thesis are general, and they are demonstrated on a laboratory test rig that resembles a typical industrial rotating machine employing controllable gas bearings. Concerning the goals G1-3, gas bearings have very low

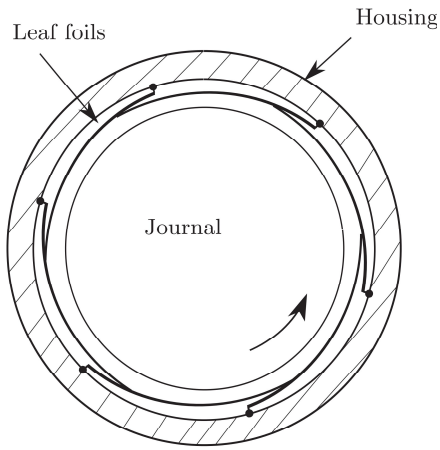

Figure 1.1: Passive leaf foil bearing. For sufficiently high angular velocities, an air film is formed between the journal and the leaf foils to avoid direct rotor-stator contact. (Source: [30]).

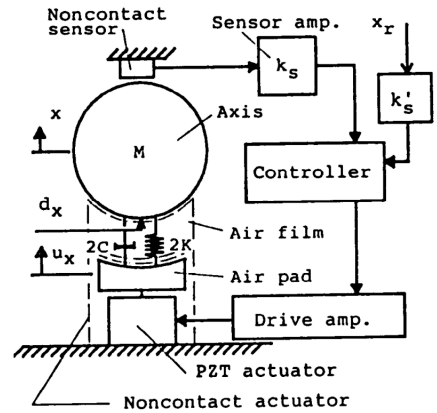

Figure 1.2: Aerodynamic piezo-actuated air bearing. The piezo-actuators control the position of the pad (Source: [20]).

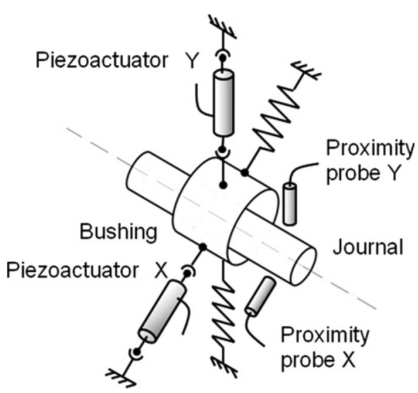

Figure 1.3: Moveable hydrodynamic bushing bearing. Piezo-actuators apply forces to a moveable bushing. The bushing is lubricated with oil (Source: [23]).

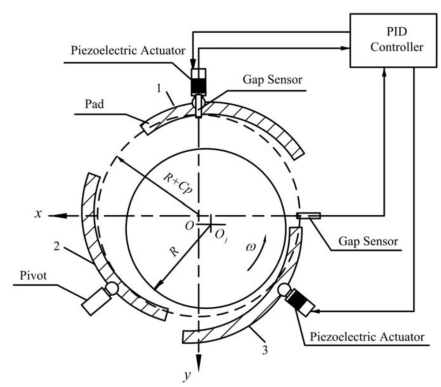

Figure 1.4: Aerodynamic tilting pad air bearing. Piezo-actuators change the angle of the pads to allow vibration control (Source: [21]).

rotor-bearing friction which makes them attractive with respect to G1. In their passive (aerodynamic) form, gas bearings have a low load carrying capacity. The load carrying capacity is increased by the injection of the pressurised lubricant, which makes them attractive as well with respect to G3. This pressure increase typically comes at the cost of reduced damping. It is therefore important to increase the damping, which may be achieved by actively controlling the lubrication.

Concerning modelling, air-injection actuators have only received sparse attention. In contrast, electromagnetic actuators have been well covered (see e.g. [32, 33] and references therein). Gas bearings can be designed to be open loop stable and they are capable of high speed operation at very wide temperature spans [16]. The friction losses are extremely low, and clean and abundant air can act as lubricant, but the damping properties are poor [34, 35, 36]. Though the active air bearings are not yet employed in commercial applications, the air lubrication is advantageous for a number of applications. Two promising applications are for compressors and turbine rotors, which have better aerodynamic efficiency at higher speeds [16, 30]. Another promising application is for turbo-chargers in diesel engines, where traditional oil lubrication contaminates the product.

The development of active air bearings is still a field in early development as shown from the following short historical overview.

1989-90 Horikawa et al. [37, 20] were among the first to design controllable air bearings, where the stiffness could be controlled by adjusting the position of a pad. Experimental results demonstrate the opportunity of controlling the rotor position.

1994 Santos [38] proposed a controllable radial journal bearing design where oil was injected through controllable servo-valves to allow control of the journal. In the same work, the modified Reynolds equation was derived to include the effects of the controllable lubrication into the Reynolds equation.

1996 Mizumoto et al. [28] proposed the active inherent restrictors, where pressurised air is injected through orifices with controllable diameter. The inherent restrictors are controlled by PI-algorithms and experimental results demonstrate the feasibility of controlling the air injection to reduce vibrations for a constant low angular velocity.

1998 The work of [38] was extended in Santos and Russo [39] where control of the servo-valves modified the injection pressures to influence the hydrodynamic

forces.

2003 Santos and Scalabrin [40] proposed a solution scheme to the modified Reynolds equation where a decentralised controller was included in the modified Reynolds equation to tune the controller. Experimental results demonstrate that the controller halves the mass imbalance for the considered operating condition.

2011 Morosi and Santos [41] propose a modified Reynolds equation to model the controllable gas bearing considered in this thesis where the radial injection of pressurised air through piezo-actuated injectors allows control of the journal.

2016 Pierart and Santos [42] further developed the model from [41]. The solutions obtained from the modified Reynolds equation were compared to those obtained by computational fluid dynamics (CFD) simulations, to show that a loss factor is required to account for modelling errors of the complex airflow in the controllable injectors. Using the proposed model, a proportional controller is designed and shown to provide a significant damping enhancement for the considered operating condition.

A challenge for controllable *journal bearings* is the design of control systems.

The present state-of-the-art models [31, 43, 42, 41] rely on the modified Reynolds equation [38] coupled with a finite element model (FE model) of the rotor. The non-linear partial differential Reynolds equation can currently only be solved with computationally heavy iterative schemes. These models are not easily developed, and they often have forms which are not directly suited for the design of feedback control due to unknown input-output relationships, very high model orders (> 100 non-linear states) and considerable parameter uncertainties [43, 31, 44]. The controllers for such systems could then be tuned experimentally with the uncertainty, lack of quality assurance and limitations this method implies. Alternatively, they could be stringently designed with documentable performance properties based on dynamic models of a suitable complexity.

This motivates the need for models, which in a simple manner describe the relation from actuator input to measured output, representing the dynamics of the rotor-bearing system in the frequency range where control authority is needed [3]. Those models could well be obtained using system identification [45, 46], where collected input-output data sets allow estimation of the dynamics of interest. The models should preferably capture the parameter-varying dynamics of the rotating

machinery, but the identification of parameter-varying models is still a research topic with many open challenges.

Our literature survey shows that system identification for modelling of controllable gas bearings is a novel application. However, identification has been widely applied to active magnetic bearings (AMBs) [47, 48, 49, 50, 51], mainly for non-rotating shafts that are to operate at low angular velocities, where linear time-invariant (LTI) models suffice. The identified models have been shown effective for the design of modern and advanced control systems to reject the undesirable vibrations from mass imbalance [52, 53, 54].

The aim of the thesis is to increase the damping of controllable radial gas bearings using feedback control. The increase of damping reduces the vibrations near the natural frequencies which in turn allows an increase of the angular velocity. The design of modern control systems requires control relevant models, which are different from those considered the state-of-the-art. The thesis aims at developing such models to avoid the need for complex models relying on solution schemes to the Reynolds equation and FE models.

1.1 Experimental Facilities

The experimental setup considered throughout the project consists of a *rotor* supported in one end by a ball bearing, and in the other end by an active gas journal bearing as shown in Figure 1.5.

The main machine components are the rotor with a flexible shaft (a) and rigid disc (b). The rotor is supported in one end by a ball bearing (c) and in the other end by the active gas bearing (d). The shaft rotation is generated by the injection of pressurised air in the air turbine (e). The flexible coupling (f) transfers the rotational energy from the turbine to the rotor.

In the controllable gas bearing, four piezo-actuated injectors are mounted as shown in Figure 1.6 to push plastic pins. These pins control the injection flow of pressurised air into the bearing housing. If the injection pressure is sufficiently high, it levitates the rotor on a *fluid film*. The clearance (nominal distance between bearing and journal) is only 25μm. When a voltage is applied to a piezo-actuator, it expands and pushes the plastic pin to reduce the flow and thereby the pushing force on the rotor.

The disc position (horizontal and vertical) is measured with eddy current sensors (g). A pressure transducer measures the pressure of the air injected in the gas

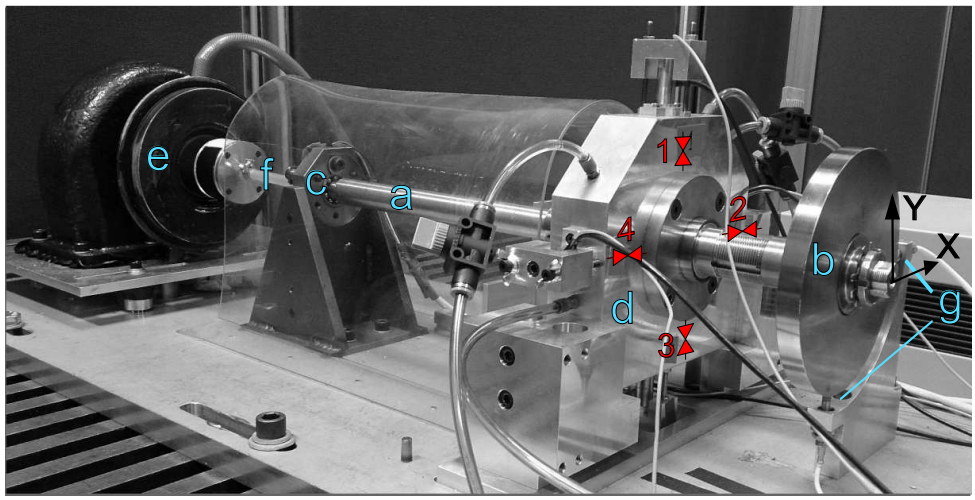

Figure 1.5: The experimental controllable gas bearing setup.

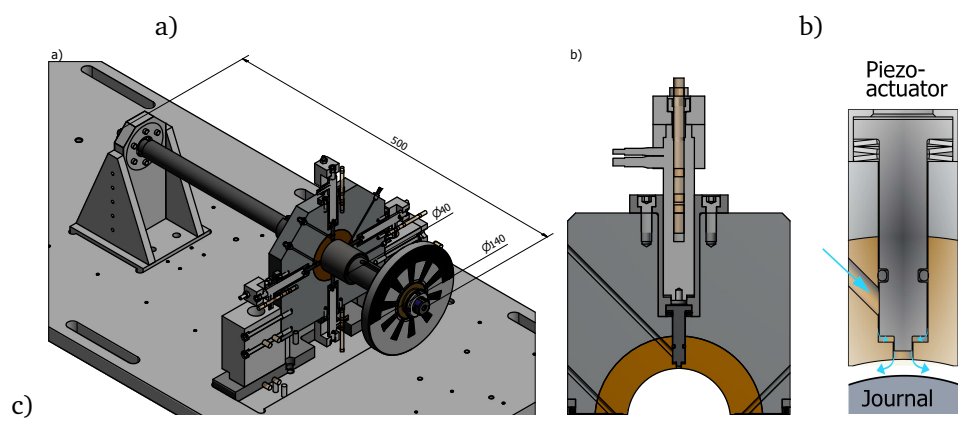

Figure 1.6: CAD drawing of the test rig: a) the test rig with the controllable gas bearing cut in half. Major dimensions are included in millimetres $[mm]$. b) zoom of a piezoactuator. The piezo-electric stack pushes a pin, which controls the injector opening. c) zoom of the injector pin and journal. Pressurised air is supplied at the location of the upper left arrow. It then flows past the pin and into the journal to generate a force on the rotor. The air can flow out by the sides of the journal (in and out of the paper). The piezo-actuator can be elongated by increasing the supply voltage to reduce the flow and thereby the force on the rotor.

bearing. In an industrial application, the injection pressure could be time-varying. For the test rig considered, the pressure can be changed with a manual valve. The pressure is measured before the air flow is split to the four individual pipes that supply the air to the gas bearing. The dynamics of the gas bearing is a function of this injection pressure. The angular velocity is approximated in real time as the time derivative of the angular rotor position, which is measured with a three channel optical incremental encoder mounted behind the ball bearing (c). The interested reader is referred to Appendix H for further description of the test rig.

1.1.1 Mass imbalance

Due to imperfections in the production process, the rotor's centre of mass will not coincide with its geometrical centre. This causes mass imbalance, which is distributed over the length of the shaft and the disc, and can be modelled as elements of mass imbalance. Each elements has imbalance mass m_u positioned at a distance e_u from the centre of mass. For an angular velocity Ω, the mass imbalance force acting on the rotor is then [9]:

$$\mathbf{f}_u(t) = \Omega^2 m_u e_u \begin{bmatrix} \cos(\Omega t) \\ \sin(\Omega t) \end{bmatrix} \tag{1.1}$$

The mass imbalance therefore causes vibrations with a frequency equal to the angular velocity denoted as synchronous vibrations.

This simple model (1.1) assumes a perfect alignment of the shaft and the bearing. In practice, this is not the case and the shaft is always translated and rotated relative to the bearing. The effects of misalignment become more pronounced in applications including air bearings where the tolerances are low. The misalignment causes vibrations with higher harmonics of the angular velocity ($2\Omega,\ 3\Omega,\ 4\Omega,\ ...$) [9, 55, 56, 57]. The forces related to the higher harmonic components are usually much lower than the first harmonic. These higher order harmonic oscillations are observable in the previous work [31] for the test rig at hand and in [51, Fig. 3.1b] for a test rig supported by two AMBs. Experimental mass imbalance responses during run-up for the controllable gas bearing are included in Papers F and E

The mass imbalance becomes critical as the angular velocity approaches the lowly-damped natural frequencies of the rotor-bearing system where the vibrations are strongly amplified. The coinciding angular velocities and natural frequencies are denoted as the critical speeds. The large amplitude vibrations near the critical speeds cause risk of rubbing where the rotor impacts the bearing housing and wears the

bearing surfaces. To prevent rubbing, it is a standard guideline to avoid stationary operation within $\pm 15\%$ of the critical speeds. The vibration build-up can be avoided by accelerating or decelerating the angular velocity sufficiently fast. The deceleration of the controllable gas bearing is very slow due to the low viscosity of the air[1]. It is therefore limited to operation below the first critical speed, which is a limiting factor during operation.

1.2 State-of-the-Art in Modelling of Rotating Machinery

This section first covers modelling of rotordynamic systems based on first principles. It then proceeds to survey the usage of system identification for control design and finally it surveys the use of active control of bearings.

1.2.1 First Principles Modelling

State-of-the-art models of rotating machinery commonly consist of interconnections of rotor and bearing models [31, 42, 11, 58, 32]. FE models are commonly derived for the rotor [9, 32] whereas the modelling of the bearings may be more challenging.

These models are originally derived to be useful tools to optimise the bearing design without the need for constructing multiple bearings to optimise a given design. The field of designing and modelling active journal bearings is very young. In recent years, research has been focussed towards developing the models to also be useful for control design. The state-of-the-art modelling approaches for the controllable gas bearing are summarised in the following.

Finite Element Modelling of Flexible Shaft The flexible shaft is modelled using a finite element (FE) method, where the shaft is divided into a number of sections connected in nodes. Each node has four degree of freedoms (DOFs) to model the bend and rotation relative to its neighbours. The stiffness and mass of each section is calculated from the geometry of the shaft and its material properties. The equations of motion for each node is expressed as a four second order coupled differential equations to describe the linear and angular positions, velocities and acceleration for the horizontal and the vertical axis $\mathbf{z}_F = [z_1,\ z_2, \ldots, z_{4n}]^{\mathrm{T}}$, where n is the number of

[1] Experiments in [31] showed that the controllable gas bearing was able to accelerate across the two first critical speeds before the vibrations became critically large. However, the slow deceleration caused rubbing during the coast-down.

nodes. The model is formulated using the mass matrix $\mathbf{M}_F$, the stiffness matrix $\mathbf{K}_F$, the gyroscopic matrix $\mathbf{G}_F$ and the damping matrix $\mathbf{D}_F$:

$$\mathbf{M}_F\ddot{\mathbf{z}}_F(t)+(\mathbf{D}_F-\Omega\mathbf{G}_F)\dot{\mathbf{z}}_F(t)+\mathbf{K}_F\mathbf{z}_F(t)=\mathbf{f}_F(t),\quad \mathbf{z}_F=[z_1,z_2,\ldots,z_{4n_n}]^{\mathrm{T}}, \tag{1.2}$$

where Ω is the angular rotor velocity. $\mathbf{f}_F(t)$ is the external forces acting on each node of the FE model from the fluid film, external disturbances and other forces to be included. The above equation (1.2) can be represented in state-space as:

$$\begin{bmatrix}\dot{\mathbf{z}}_F(t)\\ \ddot{\mathbf{z}}_F(t)\end{bmatrix}=\begin{bmatrix}\mathbf{0} & \mathbf{I}\\ \tilde{\mathbf{K}}_F & \tilde{\mathbf{D}}_F\end{bmatrix}\begin{bmatrix}\mathbf{z}_F(t)\\ \dot{\mathbf{z}}_F(t)\end{bmatrix}+\begin{bmatrix}\mathbf{0}\\ \tilde{\mathbf{B}}\end{bmatrix}\mathbf{f}_F(t), \tag{1.3}$$

where in the above the "stiffness equivalent" is defined $\tilde{\mathbf{K}}_F=-\mathbf{M}_F^{-1}\mathbf{K}_F$, and similarly the "damping equivalent" is $\tilde{\mathbf{D}}_F=-\mathbf{M}_F^{-1}(\mathbf{D}_F-\Omega\mathbf{G}_F)$ and $\tilde{\mathbf{B}}=\mathbf{M}_F^{-1}$.

FE models of the shaft for the flexible gas bearing have approximately 15-20 nodes resulting in state-space models with order 120-160.

Derivations of the FE model can be found in [59, 9, 31, 43].

Bearing Modelling The active gas bearing and the ball bearing supports the rotor. The latter is modelled as being linear with a very high stiffness, whereas the journal bearing is commonly modelled using the Reynolds equation. For controllable gas bearings, Morosi and Santos [31] derived an extended Reynolds equation to include the effects of the controllable air lubrication. The equation is derived from the Navier-Stokes equations from a set of assumptions[2] [60, 43, 31] and it is a non-linear partial differential equation. It models the pressure in the fluid film $\mathsf{p}(\mathsf{x},\mathsf{y},\mathsf{z},\mathsf{h})$ as a function of the fluid film thickness $\mathsf{h}(\mathsf{x},\mathsf{y},\mathsf{z},t)$. The fluid film thickness is a function of the radial journal position in the bearing housing:

$$\frac{\partial}{\partial\mathsf{y}}\left(\mathsf{ph}^3\frac{\partial\mathsf{p}}{\partial\mathsf{y}}\right)+\frac{\partial}{\partial\mathsf{z}}\left(\mathsf{ph}^3\frac{\partial\mathsf{p}}{\partial\mathsf{z}}\right)=6\mu U\frac{\partial(\mathsf{ph})}{\partial\mathsf{y}}+12\mu\frac{\partial(\mathsf{ph})}{\partial t}+12\mathsf{p}V_I \tag{1.4}$$

The fluid film coordinate frame $(\mathsf{x},\mathsf{y},\mathsf{z})$ is: the shaft radial coordinate x oriented towards the centre of the rotor, the circumferential coordinate y and the axial coordinate z. The viscosity of the gas is denoted by μ, the linear relative velocity of

[2] Required assumptions of the Reynolds equation: laminar Newtonian airflow. The air is an ideal, isothermal gas, whose inertia is neglected, there is no slip between boundary surfaces, the rotor is perfectly aligned, does not move axially and has linear behaviour, the rotor is decoupled from the turbine. The injection pressure at the entry of the piezo-actuated injectors is the same and equal to the measured injection pressure. The surfaces are perfectly smooth and the gas bearing is perfectly cylindrical. Elastic deformations of solid parts due to pressure changes are neglected.

the rotating shaft is U and the velocity profile of the injected gas is V_I. This velocity profile is not easily modelled due to the compressibility of the injected air, and the short length of the injector. In [31], it was assumed to have parabolic shape with a linear pressure drop along the length of the injectors assuming Hagen–Poiseuille flow.

The modified Reynolds equation has no analytical solution for bearings of finite dimensions. It must therefore be spatially discretised and solved iteratively for the particular configuration of the rotor using a qualified starting guess. The resulting equations from the spatial gridding can thereby be reduced to a finite order. The time derivative terms $\left(\frac{\partial \mathsf{p}}{\partial t}$ and $\frac{\partial \mathsf{h}}{\partial t}\right)$ which emerge from expansion of (1.4) are included by backwards finite difference approximation. The discretised Reynolds equation can then be solved to obtain the pressure profile. The integral of the pressure profile over the area of the bearing provides the horizontal and vertical forces from the fluid film acting on the shaft $\mathbf{f}_{be}(t) = [f_{X,be}(t),\ f_{Y,be}(t)]^{\mathrm{T}}$. The forces can then be used in two ways: their non-linear form or their linearised form. For small harmonic perturbations, the forces may be approximated as linear [61], in which case the bearing dynamics is approximated by an equivalent stiffness and damping matrix. In the general non-linear case, the Reynolds equation must be solved for every time step, and the pressure profile must be integrated to calculate the forces at the given time instant. The forces are then included in time simulations of the FE model to act on the rotor. The differences between the non-linear and linear model predictions may be significant as demonstrated for an active tilting pad journal bearing lubricated with oil[62]. The linearised models should therefore be used alongside with the time simulations. For control design, it is a challenge that the input-output relations are essentially unknown. It is difficult even to bound the forces at a given time instant. The model is therefore not easily used for control design. Two preliminary PD controllers were tuned [31] for the test rig, one from computationally highly demanding time simulations [41], but this controller was not validated experimentally. The other was tuned experimentally [11] and to demonstrate the possibility of enhancing the damping to reduce the vibrations.

Parametric studies [31, 41] found that the stiffness and damping coefficients of the gas bearing are function of the operating condition defined by the combination of the angular velocity of the rotor and the injection pressure of the lubricant air. Thereby the rotor-bearing dynamics is also a function of the operating condition. The same study concluded that the temperature-dependency is nearly insignificant due to the low friction losses in the bearing.

Recent works [43, 44] showed that the air injection mass flows predicted by the modified Reynolds equation from [31] are approximately a factor 10^5 higher than those predicted by CFD models. A loss factor was therefore proposed to account for the compressibility of the air. The input-output relations could be obtained by including the piezo-actuator position in the loss factor. This is shown to improve the model predictions. The updated model including the linearised Reynolds equation has been used successfully in [42] for design of a linear quadratic regulator (LQR) with a state observer.

The adopted injection model requires a relatively high spatial grid resolution in the regions near the injectors. The time required to solve the Reynolds equation is therefore high. The backwards finite difference approximation of the time derivative terms is known to require a high temporal resolution (small time step size) to avoid numerical instability and to reduce the numerical errors [30].

Summary of the first principles models The models derived from first principles are not easily derived, and they are often in forms which are not directly suited for the design of feedback control due to unknown input-output relationships, very high orders (> 100 states) and parameter uncertainties. The pressure profile must be solved for every configuration, which leaves the non-linear model unable to describe the relation from actuator input voltage to shaft displacement on a form suitable for modern model based controller design. It may be possible to obtain input-output relationships on a form suitable for control design [42], but the model predictions from the Reynolds equation may differ significantly from predictions using CFD models and from experimental observations.

1.2.2 System Identification for Control

Models suitable for controller design can be developed using system identification. Such models can have low complexity and can yet provide a convenient basis for synthesising controllers [46]. Identification-based modelling offers the flexibility of defining model structures of the desired complexity to capture the phenomena relevant for control design.

From thorough literature surveys, it appears that the application of system identification techniques to derive models suitable for control system design applied to gas bearings is novel. The literature is rich on identification for control of AMBs and the identified models have shown fruitful results for the design of controllers. The

identification of AMBs has some overlap with the identification of controllable bearings, but certainly also a number of differences. For instance, AMBs have inherently unstable dynamics [63, 64, 65] and therefore require stabilising controllers. The identification must therefore be performed from closed loop experiments, whereas gas bearings can be designed to be open loop stable. For the non-rotating case, the horizontal and vertical AMB dynamics are in general uncoupled, therefore a separate model is developed for each of the two directions.

The authors of [64, 50] use sub-space based identification approaches to develop black-box models of rotors supported by AMBs. This allows development of high order continuous time models for a rotor supported by AMBs. In [49], a frequency based method is proposed for identification of the transfer function matrix model of a non-rotating shaft supported by AMBs. The method consisted of steps identifying the submodels separately and finally combining them together. In [63], a similar approach is proposed where the controllers are chosen to improve the identification of the poles on the real axis.

In [48], a predictor-based subspace identification algorithm is proposed to identify the dynamics of a non-rotating AMB system to allow a subsequent robust control design. In [47], an iterative frequency based joint identification/controller design scheme for a non-rotating shaft supported by AMBs is applied using an linear quadratic criterion. It is also possible to identify the models online using a simple black-box model [66], but convergence of the model parameters is not easily ensured.

The above mentioned methods have only been used for identification of non-rotating shafts. This eliminates the need during identification for methods to address the harmonic vibrations from mass imbalance, which may be a significant challenge. One result has been found where system identification has been applied for modelling of a rotating rigid shaft supported by AMBs [67], but the model did not include the effects of the parameter variation. The applications are then limited to systems with negligible parameter dependencies.

Controllable gas bearings differ from AMBs in the sense that gas bearings can be designed to be open loop stable. This allows the usage of open loop identification schemes and can eliminate the need for the backup bearings required for AMBs. However, the lateral dynamics is coupled due to aero-static effects even in the non-rotating case. Due to the gyroscopic forces, the dynamics of rotors supported by AMBs is a function of angular velocity. The dynamics of rotors supported by bearings with controllable lubrication is further a function of the injection pressure.

1.2.3 Identification of Linear Parameter-Varying Models

The identification strategies mentioned in the previous section are developed for identification of systems, where the parameter dependency is negligible, which restricts their usage. All rotordynamic systems are parameter dependent due to the gyroscopic forces. Some rotordynamic systems are furthermore parameter-varying in injection pressures [68, 43, 31] and in temperatures [27, 26].

The identification of parameter-varying systems is a topic of broad interest to obtain linear parameter-varying (LPV) models or to determine parameters in first principles models.

The present LPV identification methods can be divided in two classes: local and global [69]. The global approaches directly identify the parameter-varying model from experiments where the scheduling parameter and the controllable inputs are excited simultaneously. In the local approaches, local LTI models are obtained of the system for a number of constant scheduling parameters. These local models can either be obtained from linearisation of a non-linear model or from LTI system identification. When the local models are in "suitable" representations, the LPV model is obtained from interpolation of the parameters of the local models as function of the scheduling parameters.

Both approaches have their advantages and disadvantages. The global method is useful for systems with fast parameter variations since it can capture the effects rate of change of the scheduling parameter, but the identification of non-linear systems is not as well-established as the identification of LTI models. The local approach is unable to capture the possible effects from the rate of change in the scheduling parameter [69]. For systems with sufficiently fast changes in the scheduling parameters, these effects may cause instability [70] even for systems which are stable when the scheduling parameters are fixed.

The number of data points required for the global approach may quickly grow to intractable amounts of data for systems with several scheduling parameters. In the local approach, this problem is avoided since the local models may identified separately, though the number of local models required increases with the number of scheduling parameters too.

The challenge in the local approaches is to find the suitable representation to allow the interpolation. The state-space parameters must develop continuously with the scheduling parameters. This suitable form can either be one where the poles and zeros [71] or the state-space parameters [72, 69] can be approximated as functions

of the scheduling parameters. Some works propose to identify the models without requiring a specific state-space realisation, and then subsequently transform the models to the suitable state-space representation [72, 71, 69]. This state-space representation could emerge from a partitioning of the system into a number of first and second order systems [71, 69]. These systems require a certain level of manual sorting to allow interpolation of the poles and zeros. Another strategy which is more suitable for MIMO systems, is to transform the local models to internally balanced state-space realisations [72]. The state-space parameters will then usually develop continuously, except for a number of sign changes that require manual interaction. This approach can require significant manual labour for high order systems with a high number of local models since many sign changes may occur. Another approach proposed for LPV identification is to transform the local models using their extended observability or controllability matrices to a coherent state-space basis [73] to obtain a numerically well-balanced LPV model. This method requires numerically well-conditioned models to avoid singular transformation matrices.

1.3 Active Control of Rotating Machinery

The design of feedback laws for controllable journal bearings is challenging due to the multi-physics nature of rotating machinery. This is reflected in literature where many papers rely on experimentally tuned PID control designs typically to one simple specific goal. The classical decentralised controllers are not easily tuned to fulfil multiple control objectives or to work robustly in presence of parameter variations. Results with model based control have mainly been limited to numerical studies though with a few exceptions for systems actuated by electromagnetic actuators. A probable cause is the challenges mentioned with the first principles models (model deviations, high complexity, model structures unsuitable for control design).

The control designs for AMBs are more matured, probably because the modelling of the electromagnetic forces is by now well covered in literature.

Rotordynamic systems are parameter-varying. The controllers for parameter-varying systems can either be adaptive, robust or gain-scheduled. Robust control designs must often sacrifice performance to guarantee stability. Adaptive control may be attractive if the plant dynamics is varying, but it may be difficult to guarantee performance and stability without an accurate model. Furthermore, it is challenging to include multi-objective control requirements into the adaptive control approaches. The control objectives can be included in gain-scheduled control synthe-

sis. Gain-scheduled controllers are either designed from conventional gain-scheduling approaches [74] which are often somewhat ad-hoc. Alternatively, they may be designed systematically using LPV design techniques. The former is attractive for its simplicity and is commonly employed in industry. The stability and performance investigations often rely on exhaustive simulations with the risk that un-investigated critical values or trajectories of the scheduling parameter can cause system failures. The LPV gain-scheduling techniques [75] offer systematic design approaches for guaranteeing stability and performance over the whole operating range, but they still suffer from issues with numerical conditioning and conservatism [74]. The conservatism can be reduced if the rate of variation of the scheduling-parameters can be bounded. For non-affine parameter dependency, the linear matrix inequalities (LMIs) for controller synthesis become infinite dimensional. The LMIs may then be evaluated over a grid of scheduling parameters [76], but the bound for the $\mathcal{L}_2$ gain is no longer guaranteed.

The following literature survey is divided into experimental results with experimentally tuned controllers, numerical studies without experimental validation and model based control designs, which have been validated experimentally.

1.3.1 Experimentally Tuned Control

The early results using piezo-actuated systems from Horikawa and Shimokohbe consider control of a piezo-actuated aerodynamic air pad bearing [20]. Two control designs are proposed, a PD and a squared derivative PDD controller along with a repetitive controller to reduce repeatable rotation errors. The controllers are shown to reduce the vibration amplitude. Later Qiu et al. [77] propose a system with tilting-pad air bearings. The air is not injected through controllable injectors. Instead, piezo-actuators are mounted to adjust the angle of the pads to allow active aerodynamic lubrication. Experimentally tuned PID controllers reduced sub-synchronous vibrations but the synchronous vibrations could not be reduced. The paper highlights the need for control relevant models to understand the control object when multiple control objectives should be addressed. In [23], a test rig is developed where piezoactuators apply forces to a movable bushing. From experimental tests, a proportional controller is shown to extend the onset of instability and thereby extend the operation range of the machine. In [29], an active aerodynamic spindle design is proposed, where the adjustment of piezo-actuated wedges provides aerodynamic damping. A repetitive control design is proposed along with an experimentally tuned classical controller.

Early PD control designs for the controllable gas bearing [78] have been tuned experimentally from waterfall diagrams. The control design was able to reduce the mass imbalance response for the investigated injection pressure.

1.3.2 Numerical Studies

This section covers the application of control in numerical studies where models derived from first principles have been used for design.

Cai et al. [79] proposed an adaptive back-stepping control law for a tilting pad oil bearing model to asymptotically regulate the rotor displacement despite the uncertainties in the coefficients of the lubricant film force. An implementation of the Reynolds equation allowed simulations to be performed. The mass imbalance is neglected, but the results show that the proposed adaptive controller significantly reduces the settling time of the rotor compared to the passive operation. Deckler et al. [80] consider design of an LQR for a tilting pad oil bearing. A simplified one-dimensional Reynolds equation was proposed with a solution scheme, where the linearised model may used for control design. Though the response of the non-linear and the linearised model differed significantly. A control design for a hydroactive tilting pad oil bearing in [10] aimed at designing the controller using the Reynolds equation. Here, the Reynolds equation was extended by a term to take the effects of the controllable lubrication into account. The linearised stiffness and damping coefficients were calculated, and the system was assumed linear in the frequency range of interest. A controller was designed to obtain a specified change in damping factor. Lihua et al. [21] considered control design for an aerodynamic tilting-pad gas bearing using piezo-actuated active pads. Decentralised PD controllers were designed to minimise the two-norm of weighted state and control output response. The numerical study showed that the vibration amplitude was reduced significantly over a wide frequency range. Mason et al. [53] synthesised both an LPV controller and a gain-scheduling control design between $\mathcal{H}_\infty$ controllers to reduce the mass imbalance response of a rotor supported by AMBs. Sawicki and Gawronski [81] consider the challenge of obtaining reduced order controllers from the generally high order controllers synthesised from models of flexible shafts. A flexible three-disk rotor system supported on anisotropic bearings is considered and a balanced truncation allows a reduction of the system model from 96 to 22 states. From this model, a state observer and a linear quadratic gaussian controller were designed to reduce the two-norm of the impulse response.

1.3.3 Experimental Model-Based Control

An early work in model-based control design considered $\mathcal{H}_\infty$ control design for an AMB system [82]. A central controller was calculated and the Youla-parameter was used to place controller poles on the imaginary axis to reject mass imbalance. One of the early results in control design for a rigid rotor supported by a hydroactive tilting pad oil bearing was developed in [40]. The Reynolds equation was formulated and extended by a term to take the effects of the controllable lubrication into account. A solution scheme is proposed and from the solutions, perturbation theory is used to obtain the linearised stiffness and damping coefficients. The model allowed tuning of a PD-controller and the controller parameters were tuned using a proposed scheme. In this scheme, the Reynolds equation was solved for a particular choice of gains. A controller was designed and was validated experimentally to halve vibrations for the investigated angular velocity. This design methodology may be applied if relatively few controller parameters must be tuned, but it is not easily used for more advanced controllers such as state-space based controllers. For a hydrodynamic tilting-pad oil bearing with embedded electromagnetic actuators [83], the linearised coefficients were extracted from the Reynolds equation and used for control design. An external shaker was mounted to excite the system with known forces to tune the model parameters. The model obtained was used for PD control design that reduced the peak vibration amplitude by up to 18% during run-up and by 11% for operation at constant speed.

Very recent advances in [42, 43] improved the modelling of the controllable gas bearing considered in this thesis. The improved model was shown to allow design of model based control. Here, a method was developed to obtain linear models from the Reynolds equation including the effects of the controllable lubrication. These effects may be included into the rotor FE model. The resulting linear model was then reduced significantly to allow design of a PID controller and an LQR with a Luenberger observer. The experimental results show that the controllers reduced the mass imbalance response sufficiently to allow operation across the two first critical speeds.

In [84] and [67] $\mathcal{H}_\infty$ controllers were designed for a rigid shaft supported by AMBs. In [67], an analytical rigid body model derived from first principles was compared to a finite element model obtained from Ansys and an identified LTI model. The latter model was used for $\mathcal{H}_\infty$ control design at the chosen rotor speed. The controllers were designed to obtain a low output sensitivity at low frequency and

minimise control activity at high frequency. The control performance deteriorated as the rotor speed increased from the original design condition, which highlights the need for models that may capture the parameter-varying nature of the rotating machine. More recently an identified LTI model has been used for robust control design for an AMB in [48]. In [85] LPV and $\mathcal{H}_\infty$ controllers were designed to reduce the mass imbalance response significantly at a particular angular velocity by placing under-damped poles in the controller at that particular frequency. The $\mathcal{H}_\infty$ controllers quickly became ineffective for mass imbalance reduction as the angular velocity was shifted away from the optimal condition. The LPV controller on the other hand was able to shift the frequency of the under-damped poles continuously to allow a continuous reduction of the mass imbalance. The work was extended in [52] by using a flexible shaft model. A switching law was proposed using the Youla parameter to gain-schedule between multiple unstable LPV controllers. Schlotter and Keogh [86] considered a rotor supported by AMBs and included the gyroscopic effects of the rotor to design controllers that minimised rotor displacements or bearing transmitted forces. In [87] a rotor supported by passive oil journal bearings was considered, where electromagnetic actuators were mounted to allow actuation of the shaft. The non-linear effects from the oil journal bearing were included by letting the corresponding stiffness and damping matrices be polynomials of the shaft angular velocity. An LPV controller was designed to minimise output effects of the mass imbalance inputs during run-ups and coast-downs.

The literature survey shows that applications of LPV control design have been limited to applications actuated by AMBs [86, 52, 85, 87] where the shaft angular velocity is the only scheduling parameter.

There have been few applications of adaptive control in rotordynamics [66, 88, 89] which propose various so-called open loop adaptive control strategies, but the inclusion of the control objectives into the adaptive controllers is a challenge.

1.4 Summary of Literature Survey

The literature survey shows that active control of bearings promises great advances in terms of vibration reduction, damping enhancement and extension of the operating range. While the modelling and control for rotating machinery supported by AMB is well established, the control designs for active bearings actuated by non-electromagnetic actuators is still in its early infancy. The control designs that have been validated experimentally are governed by decentralised experimentally-tuned

classical control. It is difficult to ensure that such control designs perform well across the range of the scheduling parameters. This highlights the need for control relevant models. The state-of-the-art models are often of too high complexity to be used for control design and may still suffer from parameter uncertainties, which makes them difficult to use for control system design. In this regard, system identification has proven itself a viable alternative for obtaining the models of rotating machinery supported by AMBs. It is therefore an interesting modelling approach for controllable gas bearings. The models should be able to capture the inherent parameter-varying machine dynamics, but the identification methods widely applied for AMBs have focussed on identification of LTI models. The identification of parameter-varying models is still a field with many open challenges, where the available solutions are often somewhat ad-hoc often requiring manual interaction.

1.5 Contributions of the Appended Publications

This section highlights the contributions from the appended papers. The contributions are included in chronological order.

The thesis has two novel contributions. One is that the dynamics of hydroactive gas bearings can be well-captured by LPV models and procedures have been proposed to identify such models in Papers A, C and G. A novel application of the runout-filter has been developed to eliminate mass imbalance to obtain measurements of the active response with micro-meter precision. The second contribution is the application of model-based control design for controllable air journal bearings. Here, the models identified have been shown useful for model-based control design of state-feedback control in Paper A, $\mathcal{H}_\infty$ control in Papers B, E and F, decentralised classical control in Papers C and D, LPV control in Paper E and gain-scheduled $\mathcal{H}_2$ control design in Paper G. The papers A-F include experimental validation from closed loop experiments.

1.5.1 Paper A - Experimental Grey Box Model Identification of an Active Gas Bearing

The conference paper [1] presents an identification approach for controllable journal bearings relying on grey-box modelling. To counteract the non-linear behaviour of the piezo-actuators, decentralised PID controllers are deployed and shown to obtain a linear behaviour of the controlled piezo-actuators. It is shown that the dynamics can be captured by linear time invariant models for a constant injection

pressure and angular velocity of the rotor. The method is used for identification of the rotating shaft, where a novel application of the run-out filtering is presented to filter out the mass imbalance response to obtain micro-meter precision measurements of the active response. A grey-box identification structure is proposed and shown to allow identification of the rotor-bearing dynamics of the controllable gas bearing. The actuator's dynamics is approximated as static. Models are identified over a small range of angular velocities to model the dynamics development. The application of a model-based state-feedback and observer-based control design for one angular velocity validates the suitability of the model for control. The control design is validated experimentally to increase the damping of the system by a factor nine, which is higher than expected.

1.5.2 Paper B - Modelling of Rotor-gas bearings for Feedback Controller Design

The conference paper [2] discusses challenges for control design using the state-of-the-art models derived from first principles versus control design from models obtained using system identification. The previous model from Paper A is extended by a dynamical actuator model of the closed-loop piezo-actuators. From experimentally-collected data, a model is identified and used for design of an $\mathcal{H}_\infty$ controller to increase the damping of the system using the mixed sensitivity approach. The parameter-varying effects are included as parameter uncertainty to prove closed-loop stability of the controller over the desired operating range. Experimental closed loop results verify that the damping factor is increased by a factor three which is very close to the expected increase.

1.5.3 Paper C - Modelling and identification for control of gas bearings

The journal paper [3] presents an experimental technique for "in situ" identification of low complexity models of a rotor–bearing–actuator system and demonstrates identification over relevant scheduling parameter ranges of angular velocity and gas injection pressure. The paper can be seen as an extension of the modelling from Papers A and B, where the previous models are improved significantly by the inclusion of time delays. The delays are included into the model as first order Padé approximations to allow identification with readily available grey-box tools. Decentralised PD controllers are employed for control of the piezo-actuators and are validated from experiments to allow linear modelling of the closed-loop system. The identified models

are interpolated as functions of the scheduling parameters to obtain an LPV model that captures the dominant dynamics. The approach is shown to be easily applied and to suit subsequent control design. Based on the identified models, decentralised proportional control is designed and shown to obtain the required damping in theory and in a laboratory test rig. The experimental open and closed-loop results are shown to match very well with the ones from the model.

1.5.4 Paper D - Experimental Investigations of Decentralised Control Design for The Stabilisation of Rotor-Gas Bearings

The conference paper [4] further explores control design using the models identified from Paper C. The models are validated from experimentally collected impulse responses. A decentralised strategy is pursued using classical controllers. The root locus analysis shows that two different control solutions are feasible for the dampening the first two eigenfrequencies of the gas bearing in the horizontal and vertical directions. The root locus analysis further shows that it is possible with a proportional controller to obtain a critically damped system, which is validated experimentally in Paper C. Hardening and softening P-lead controllers are designed based on the models experimentally identified, and salient features of both controllers are discussed. Both controllers are implemented and validated on the physical test rig. Experimental closed loop results confirm the validity of the proposed approach and show good agreement between the measurements and the model predictions.

1.5.5 Paper E - Enhancing Damping of Gas Bearings Using Linear Parameter-Varying Control

The journal paper [5] addresses the enhancement of the damping properties of active gas bearings over desired intervals of operating conditions. An LPV model of the gas bearing test rig is identified. The LPV model is used for design of an LPV control that guarantees a high damping over the desired range of operation. An $\mathcal{H}_\infty$ controller is designed for comparison. Both controllers significantly enhance the damping of the gas bearing over the scheduling parameter range. The performance of the controllers is compared both theoretically and experimentally. The LPV controller in general shows a somewhat better performance and requires less control effort than the $\mathcal{H}_\infty$ controller. This improved performance should be compared to the increased complexity in design and implementation which must be judged for the specific application.

1.5.6 Paper F - Gas Bearing Control for Safe Operation in Critical Speed Regions - Experimental Verification

The conference paper [6] further explores the capabilities of the controllers designed in Paper E for extending the operating range of the rotating machine. The damping enhancement provided by the controller reduces the disturbance amplification near the natural frequencies. Using the LPV model from Paper C and the $\mathcal{H}_\infty$ design methods as presented in Paper E, active lubrication techniques are proposed to enhance the damping, which in turn reduces the vibrations to a desired safe level. The control design is validated experimentally on a laboratory test rig, and shown to allow safe operation for angular velocities up to, in and above the two first critical speeds, which significantly extends the operating range. The controller is found to reduce vibrations sufficiently to allow operation in the regions of the two first critical speeds. This allows an extension of the operating range of angular velocity by 70%.

1.5.7 Paper G - Gain-Scheduled Control Using State-Space Interpolation - An Application to Hydroactive Gas Bearings

The conference paper [7] presents the design of gain-scheduled control for gas bearings. Here, local $\mathcal{H}_2$ controllers are synthesised and the continuously gain-scheduled controller is obtained from subsequent state-space interpolation. The paper presents a simplification to the previous model identification from Paper C where the local models can be identified in one step and with a sixth order state-space model structure. The reduced order local models avoid the need for time delays and are shown to obtain the same accuracy as the previous models. The model parameters are shown to develop continuously with the scheduling parameters to allow LPV modelling of the rotating machine. The paper uses the proposed LPV model to design low-order controllers to reject the mass imbalance, regulate the disc position and enhance the damping using a limited control effort. The state-space interpolated controller is shown superior for rejection of mass imbalance compared to controllers which schedule with the Youla parametrisation. Our proposed gain-scheduling approach avoids the increase of state-space controller order associated to the Youla parametrisation.

1.6 Structure of the Thesis

The remainder of the thesis is structured as follows: Chapter 2 provides a short summary of system identification of linear models and the extension to identification of LPV models and presents the identification of the controllable gas bearing. Chapter 3 describes the control design for active bearings. The main methods that have been applied for control design for the controllable bearings are briefly revisited followed by a description of the control objectives and challenges. Selected closed loop experimental results with the proposed control designs are presented. In Chapter 4 conclusions are drawn and future aspects are given.

Chapter 2

Identification of Controllable Bearings

This chapter provides a short summary of system identification of linear models and the extension to identification of linear parameter-varying (LPV) models and presents the identification of the controllable gas bearing.

System identification is the field of building mathematical models or estimating model parameters of a system of interest from observed data [45]. Such models can have low complexity and can yet provide a convenient basis for synthesising controllers [46]. They can avoid the high order associated with mechanical models based on first principles to include only the phenomena relevant for the control design. System identification is therefore an attractive means for obtaining control relevant models of controllable bearings.

The chapter first summarises the well-established identification of linear time-invariant (LTI) models and shows an example of LTI model identification of the controllable gas bearing test rig. Then, the challenges of extending LTI identification to LPV systems are presented in Section 2.2 followed by the three gas bearing models in Section 2.3 proposed in Papers A, C and G. Section 2.4 presents a brief discussion of the method and some guidelines. Section 2.5 includes an example of the identification of one of the proposed parameter-varying models. Section 2.6 presents solutions to counteract the non-linear behaviour of the piezo-actuators and the runout filtering to obtain only the active response from the piezo-actuators.

2.1 Summary of System Identification

The aim of system identification is to obtain a model $\mathfrak{M}$ of a system with the inputs $\mathbf{u}$ and $\mathbf{d}$ and the outputs $\mathbf{y}$. The inputs $\mathbf{u}$ are commonly chosen as the set of

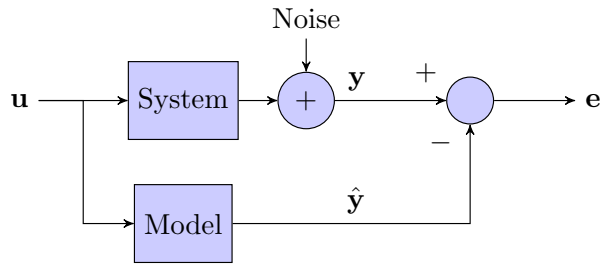

Figure 2.1: Identification overview. The model is chosen to minimise the simulation error $\mathbf{e}$ between the measurement $\mathbf{y}$ and the estimate $\hat{\mathbf{y}}$.

controllable inputs that can be manipulated, whereas the inputs $\mathbf{d}$ are commonly denoted by disturbances. These disturbances may stem from uncontrollable forces acting on the system from e.g. mass imbalance and measurement noise. The disturbances are often fully or partially unknown, and it is therefore of interest to obtain measurements with a minimal effect from these disturbances. A common method is the prediction error method (PEM) where parameters are estimated by minimising a residual. The simulation error [45] is a suitable residual choice for the controllable gas bearing since it is possible to reduce the disturbance effects in the measured data significantly. The simulation error is defined as the signal norm of the difference between the measured output $\mathbf{y}$ and the output of the model $\hat{\mathbf{y}}$ simulated with the input $\mathbf{u}$ as shown in Figure 2.1.

Denote the input (vector) by $\mathbf{u}_k$ and the measured output by $\mathbf{y}_k$ at sampling instant k at time $t = kT_s$ for $k \in \{1, ..., K\}$. Consider the model $\mathfrak{M}$ parametrised by a parameter vector $\boldsymbol{\theta}$. The model predicted output at time k is denoted by $\hat{\mathbf{y}}_k$. The residual to be minimised is denoted by $\mathbf{e}$ and is chosen as the simulation error[1]

$$\mathbf{e} = \mathbf{y} - \hat{\mathbf{y}} \tag{2.1}$$

The residual is calculated by simulating the model given the input sequence $\mathbf{u}$. The

[1]Instead of choosing the residual as the simulation error, it is commonly chosen to be the one-step prediction error defined as $\mathbf{e} = \mathbf{y}_k - \hat{\mathbf{y}}_{k|k-1}$, where $\hat{\mathbf{y}}_{k|k-1}$ denotes the estimated model output given all measurements up to sample $k-1$ [45]. A model that minimises the one-step prediction error is optimal for one-step prediction. Such models may not be good for simulation and vice versa.

optimal parameter is denoted by $\boldsymbol{\theta}^*$ and minimises the residual:

$$\boldsymbol{\theta}^* = \arg\min_{\boldsymbol{\theta}} \underbrace{\sum_{k=0}^{K} \|\mathbf{e}_k\|_2^2}_{\mathcal{J}(\boldsymbol{\theta})} \tag{2.2}$$

The minimisation of the cost function $\mathcal{J}(\boldsymbol{\theta})$ is a non-linear optimisation problem. It is therefore necessary to use iterative methods to estimate the optimal parameter set from a given initial estimate. The non-linear optimisation bears the risk that the optimisation converges to a local minimum. This risk is reduced by providing a good initial parameter estimate for the algorithm. The model quality must be assessed subsequently (prediction capabilities on validation data, significance of parameters, pole-zero cancellations). The order of the system is commonly unknown, and the selection of a model order can be an iterative process. The parameters are estimated from finite length data sequences which are affected by stochastic measurement noise. The parameter estimate will therefore itself be stochastic [45].

2.1.1 Goodness of Fit

The model quality is commonly quantified by the goodness of fit calculated as the normalized root mean square error of the residuals. The models have a goodness of fit value for each of the n output channels $\mathbf{y}_k = [y_{1,k}, ..., y_{n,k}]^{\mathrm{T}}$. The goodness of fit (or simply fit value) of channel n is calculated as

$$\text{fit}_n = 1 - \frac{\sum_{k=0}^{K} \|e_{n,k}\|_2}{\sum_{k=0}^{K} \|y_{n,k} - E(y_n)\|_2} \tag{2.3}$$

where $E(y_n)$ denotes the mean value of the measurements $y_{n,k}$ and $e_{n,k}$ is the n-th output channel of the simulation error as defined in (2.1). The fit value is defined on the interval $]-\infty, 1]$. If the residual is zero, the goodness of fit is $1 = 100\%$. The fit value is a measure to be used with care. A high fit on one data set does not guarantee a high fit on another data set collected from the same system near the same linearisation point if the model over-fits. To avoid such over-fitting to the data, it is a standard guideline to evaluate the fit value on a validation data set to ensure the fit values are similar. This validation data should be data that was not used for the identification.

2.1.2 Input Excitation

The data sets for identification should contain sufficient excitation of the input signals in the frequency range of interest. For control design it is important to excite the system in the frequency range of the crossover frequency which is rarely known prior to the control design. For the controllable gas bearing, this excitation is ensured by changing the position references for the piezo-actuators. Excitation signals such as pseudo-random binary signals (PRBSs) and chirp signals are effective for designing the frequency interval of excitation. In general, all piezo-actuators are excited simultaneously with independent signals for the horizontal and the vertical actuators. The amplitude of these excitation signals is a tuning parameter and a higher level can increase the quality of models by increasing the signal-to-noise ratio, which can increase the fit values as seen from (2.3). Too high levels however excite the system further away from the equilibrium point where it no longer behaves linearly or it could cause rotor-stator rub that damages the bearing surface.

2.1.3 Prefiltering

It is often beneficial to prefilter the data before the identification. This prefiltering can remove or reduce effects that the model is not able to predict. For the controllable gas bearing, prefiltering is applied to remove the mass imbalance response using the extended runout filter described in Section 2.6.2 and to remove biases from input and output signals. These biases are estimated from a short initial time-span for the identification data sets where the piezo-actuators positions are not changed.

2.1.4 LTI Identification of Controllable Gas Bearings

This section shows examples of identification of LTI models of the controllable gas bearing for two different operating conditions.

It has previously been shown for hydroactive oil film bearings [62] that the differences between the non-linear and linear model predictions can be significant. Our initial analyses in Paper A showed that the gas bearing dynamics for a constant operating condition can be approximated well by LTI models. This operating condition is determined by the combination of angular velocity and injection pressure. The paper further showed that the actuator dynamics can be captured with LTI models when local controllers are deployed to counteract the inherent non-linearities in the piezo-ceramics. The measurements collected for rotating operating conditions

include the response from *mass imbalance* that poses a challenge for the identification. A runout filter has been proposed in Paper A and C to remove the mass imbalance response offline from the identification measurements.

Two data sets collected for different operating conditions are included. The data sequences have a duration of approximately 8-12 seconds, where the piezo-actuators are commanded PRBS signals. The first is collected for the lowest injection pressure and zero angular velocity. For these data sets, the runout filter is not used, but the biases are removed. A model on the form presented in Section 2.3.3 has been identified for the data set. A part of the sequence is shown in Figure 2.2 along with the response of the identified model. During this part of the sequence, two steps are commanded to the vertical actuators (lowest plot). These steps mainly induce vibrations in the vertical disc direction (2^{nd} plot from above). Frequent steps are commanded to the horizontal actuators (4^{th} plot from above), which mainly cause horizontal disc vibrations, but also vertical disc vibrations with lower amplitude. The model is able to capture these cross-couplings and the fit values are $[88.8,\ 86.3]\%$. The fit values for a validation data set are $[89.7,\ 84.1]\%$, which is close to the identification fit values indicating that the model is able to predict the response well. One fit value is higher for the validation data than the identification data. This indicates a better signal to noise ratio in the validation data.

A similar data set has been collected for a higher angular velocity. Here, the runout filter has been applied to remove the mass imbalance response. Figure 2.13 shows a part of the data set before and after runout filtering. The mass imbalance vibrations have an amplitude of $9\mu m$ and have been reduced to $0.5\mu m$ by runout filtering. A model is identified from the data set and the model and measured responses are shown in Figure 2.3. Again a zoom is shown where two steps are commanded to the vertical actuators while frequent steps are commanded to the horizontal actuators. At higher angular velocities the cross coupling gains increase and it is evident that the vertical vibrations from the horizontal actuator steps are now more significant. The fit values are slightly lower ($[79.4,\ 77.4]\%$) due to the residual mass imbalance vibrations. The fit values for a validation data set are close to these values($[80.3,\ 76.5]\%$) indicating that the model is able to predict the response well. The optimal parameter sets for the data collected at lower and at higher angular velocities differ, which indicates the parameter-varying plant nature.

The following sections describe the LPV identification methods proposed for models that capture this parameter development.

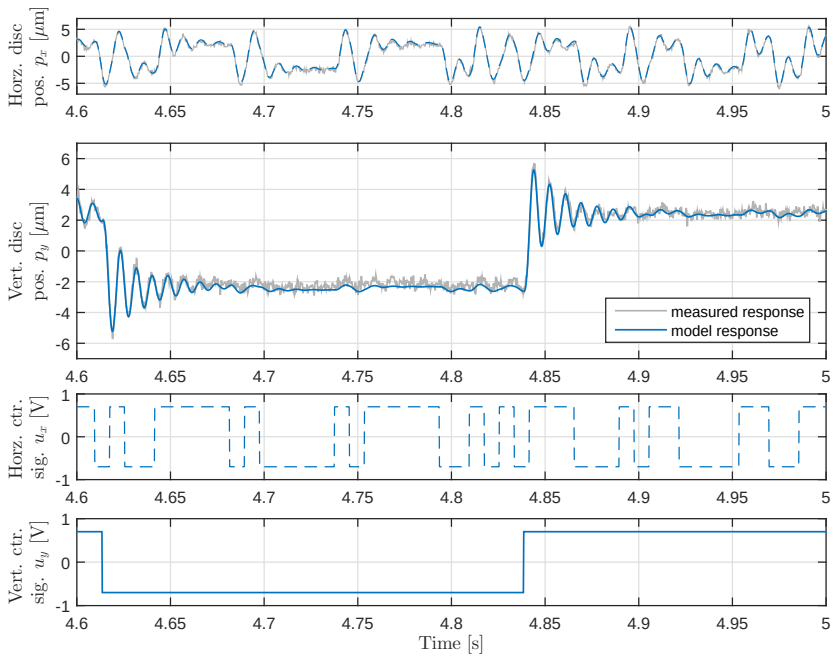

Figure 2.2: Identification data for low pressure and non-rotating shaft $\mathbf{q} = [0\text{krpm},\ 0.3\text{MPa}]$. Model goodness of fit: $[88.8,\ 86.3]\%$.

2.2 Identification of LPV Systems

The dynamics of the controllable gas bearing is a function of the operating condition defined by the combination of angular velocity and injection pressure. This project has developed methods for identification of LPV models that capture the dynamics well.

The LPV models are generally formulated in state-space descriptions where the state-space matrices are functions of the scheduling parameters denoted by $\mathbf{q}(t)$:

$$\mathbf{G}(\mathbf{q},t) = \left[\begin{array}{c|c} \mathbf{A}(\mathbf{q}) & \mathbf{B}(\mathbf{q}) \\ \hline \mathbf{C}(\mathbf{q}) & \mathbf{D}(\mathbf{q}) \end{array}\right], \tag{2.4}$$

The matrices $\mathbf{A}, \mathbf{B}, \mathbf{C}$ and $\mathbf{D}$ can be structured or fully populated. For the controllable gas bearing, the scheduling parameters are chosen as the operating condition defined by the angular velocity and the injection pressure.

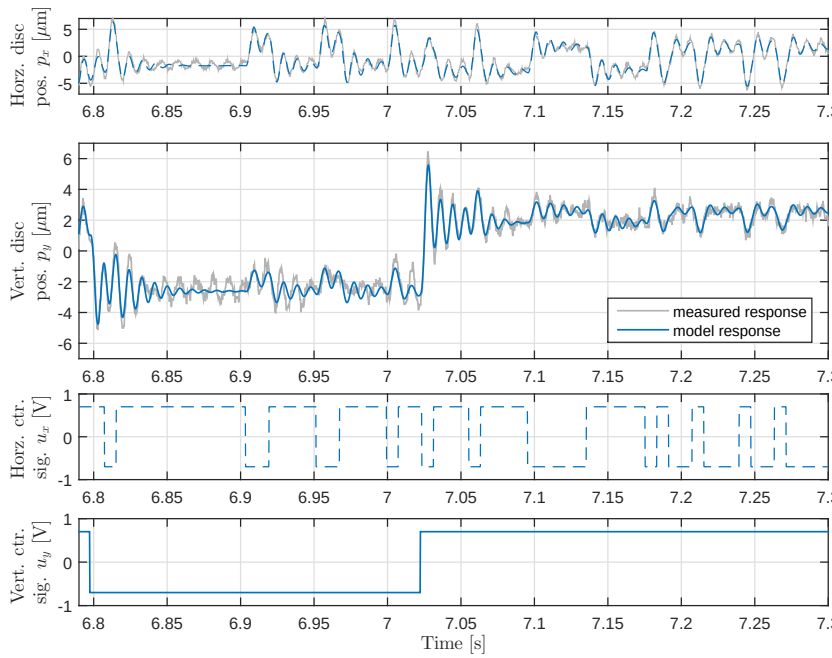

Figure 2.3: Identification data for low pressure and rotating shaft $\mathbf{q} = [5.3\text{krpm},\ 0.3\text{MPa}]$. Model goodness of fits: $[79.4,\ 77.4]\%$.

2.2.1 Local and Global Approach

The approaches for identification of LPV models of the form (2.4) from literature can be divided into two main categories [69] namely the local and the global. The global approaches aim to directly identify models on the form (2.4) from data sets with simultaneous excitation of both the system inputs and the scheduling parameters. The global approaches therefore require non-linear identification methods. They are therefore better suited for low order systems with only one or a few inputs, outputs and scheduling parameters. For the gas bearing, the global approaches require intractable amounts of data. Partly because the system has fast dynamics and the scheduling parameter can only be changed slowly and partly because a big amount of data is required to ensure sufficient excitation of both scheduling parameters, inputs and outputs.

The local approaches instead rely on identifying models of the system for multiple

constant values of the scheduling parameter $\mathbf{q}_i \in \mathbf{Q}$, in which case the model identification becomes LTI and the local model is:

$$\mathbf{G}(\mathbf{q}_i, t) = \left[\begin{array}{c|c} \mathbf{A}(\mathbf{q}_i) & \mathbf{B}(\mathbf{q}_i) \\ \hline \mathbf{C}(\mathbf{q}_i) & \mathbf{D}(\mathbf{q}_i) \end{array}\right] \tag{2.5}$$

From the local models, the LPV model can then be obtained. The local approaches can therefore divide the identification into multiple LTI identification tasks. A discussion of the method and its limitations is given in Section 2.4.

Local modelling approaches have shown fruitful results for modelling of the controllable gas bearing.

2.2.2 Model Order and Structure

It is standard knowledge from identification of LTI models that the order of the model must not be too high or low. Too low order models are not able to capture the dominant dynamics and too high order models over-fit in the sense that they will perform poorly for prediction on a validation data set. This challenge is multi-dimensional for LPV identification because the multiple local models to be identified must cohere, e.g. the number of poles and zeros must be constant, which is ensured by imposing a structure. The model structure must capture the dynamics in the desired scheduling parameter range. Furthermore, the model parameters develop adequately allow interpolation to develop an LPV model that captures the dynamics of the gas bearing.

Standard black-box identification methods are often not suitable for LPV identification. Matrix transfer function-based models such as ARX and ARMAX models tend to provide high order models for MIMO systems, and they tend to underestimate the damping due to their unrealistic noise models. The black-box state-space models can provide good local models with low order, but the models are usually obtained in different state-space realisations, and they are therefore not easily interpolated. The available techniques from literature [72, 71, 69, 73] have used black box identification methods and propose methods for transforming the models to suitable state-space representations to allow interpolation. They suffer from challenges with numerical conditioning [73] or low level of automation [71, 72, 69]. The methods are shown feasible for fairly small scale examples, but not much attention has been devoted to the the model structures to allow interpolation. Our experiences with locally identified black box models of the gas bearing show that the model parameters to not develop adequately over the scheduling parameter to provide LPV models

that capture the behaviour of the gas bearing. This project has therefore sought an alternative strategy for the development of LPV models.

2.3 Grey-Box LPV Identification

This project contributes with a local grey-box LPV identification method, where the local models are identified directly on a desired state-space form, such that certain model parameters can be interpolated to obtain the LPV model.

There are no analytical approaches for the selection of model structures for LPV identification described in literature. The modelling is therefore an iterative procedure, which is reflected in this work by the different models proposed. When an analytical model is available, it can be linearised to obtain these local models on a suitable structure, but this is generally not the case.

The models can capture the dominant dynamics of the controllable gas bearing in the frequency range of the two first natural frequencies, which are captured with mass-spring-damper like systems similar to (1.3). The model parameters can be identified with standard LTI grey-box identification tools using functions written as part of this project as shown in Section 2.1.4. The models avoid an over-parametrisation. The model parameters can therefore be identified for multiple different constant values of the scheduling parameters $\mathbf{q}_j$ for $j = \{1, ..., J\}$. Each of the n model parameters $\boldsymbol{\theta} = [\theta_1, ..., \theta_n]^{\mathrm{T}}$ have then been approximated as polynomials of the scheduling parameters. The varying parameters can be chosen as the unknown parameters of the grey-box model or a subset thereof. The method is not restricted to polynomials but the experimental results show that second order polynomials are well suited to avoid over- and under-fitting. The parameter-varying matrices then have the form:

$$\begin{aligned}
\alpha_1(\mathbf{q}) =& \theta_{1,0} + \alpha_{1,1} q_1 + \alpha_{1,2} q_2 + \alpha_{1,3} q_1^2 + \alpha_{1,4} q_2^2 + \alpha_{1,5} q_1 q_2 \\
&\vdots \\
\theta_n(\mathbf{q}) =& \theta_{1,0} + \alpha_{n,1} q_1 + \alpha_{n,2} q_2 + \alpha_{n,3} q_1^2 + \alpha_{n,4} q_2^2 + \alpha_{n,5} q_1 q_2
\end{aligned} \tag{2.6}$$

These polynomials are approximated with standard regression tools from the $j = \{1, ..., J\}$ estimates of each of the parameter $\theta_{n,j}$. The parameters $\alpha_{n,1}, ..., \alpha_{n,1}$ are chosen such that they minimise the cost function:

$$J_\theta(\mathbf{q}) = \sum_{n=1}^{N} \sum_{j=1}^{J} \|\theta_n(\mathbf{q}_j) - \theta_{n,j}\|_2^2 \tag{2.7}$$

The optimisation can be divided into linear N independent least squares problems, which can be solved analytically:

$$J_\theta(\mathbf{q}) = \sum_{n=1}^{N} J_{\theta_n}(\mathbf{q}), \quad J_{\theta_n}(\mathbf{q}) = \sum_{j=1}^{J} \|\theta_n(\mathbf{q}_j) - \theta_{n,j}\|_2^2 \tag{2.8}$$

The LPV model $\mathbf{G}(\mathbf{q}, t)$ on the form (2.5) is then derived from the estimated functions $\theta_n(\mathbf{q}_j)$. The following is an example for a first order system.

Example with First order System To exemplify the grey-box LPV identification approach, consider a first order system scheduled in one parameter q in the interval $q \in [q_{min}, q_{max}]$ with a parameter-varying gain and -pole. This system has a minimal state-space representation:

$$\left[\begin{array}{c|c} a(q) & b(q) \\ \hline 1 & 0 \end{array}\right] \tag{2.9}$$

The process is summarised in Figure 2.4 and is as follows.

The interval is gridded to cover the interval $Q = \{q_1, q_2, ..., q_j, ..., q_J\}$ and local LTI models on the form

$$\mathcal{M}_j = \left[\begin{array}{c|c} a_j & b_j \\ \hline 1 & 0 \end{array}\right] \tag{2.10}$$

are identified for a set of fixed values of the scheduling parameter $q \in Q$ to cover the desired interval. The varying parameters are a and b, which are interpolated from the estimates $\{a_1, a_2..., a_J\}$ and $\{b_1, b_2..., b_J\}$ using standard linear least squares regression tools, that minimise cost functions:

$$J_a(q) = \sum_{j=1}^{J} \|a(q_j) - a_j\|_2^2 \tag{2.11}$$

where a similar function $J_b(q)$ is minimised for b from which the LPV model (2.9) is derived.

Controllable Gas Bearing Models Three different continuous time models for grey-box LPV identification have been developed throughout the project and are denoted as Model 1,2 and 3.

- Model 1 includes a dynamical fourth order model of the rotor-bearing system and the actuator dynamics are approximated as static gains.

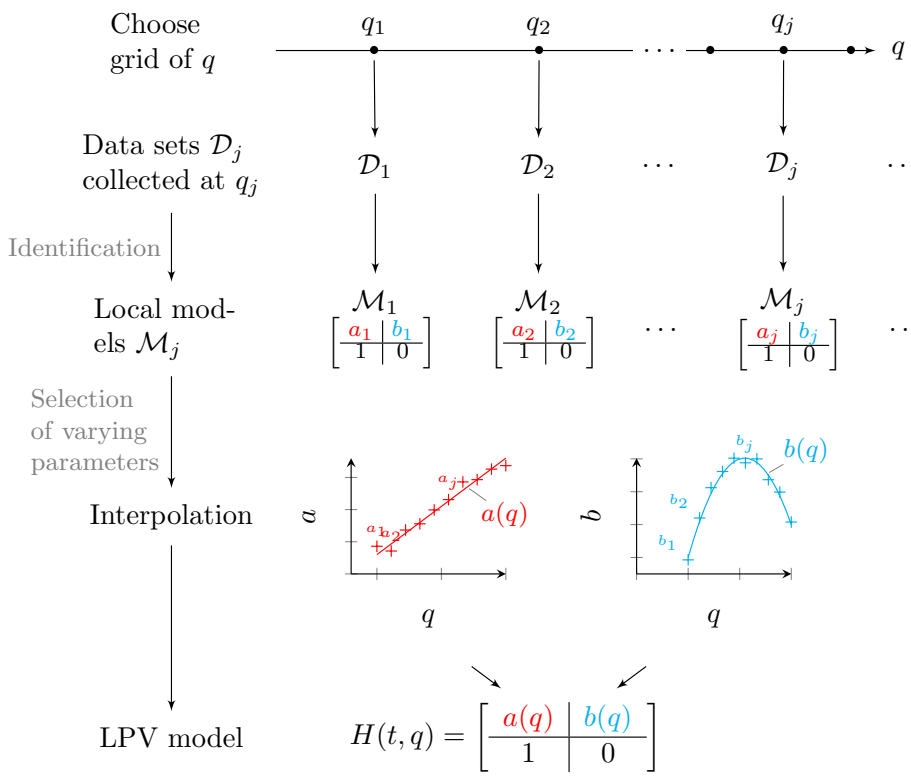

Figure 2.4: Summary of the state-space interpolation algorithm. Different data sets $\mathcal{D}_j$ are collected for constant values of the scheduling parameter q_j. From the data sets, models $\mathcal{M}_j$ are identified in a desired state-space realisation. the time-varying parameters (in this case a and b) are interpolated as functions of the scheduling parameter to obtain the LPV model.

- Model 2 includes both a fourth order model of the actuator dynamics and a sixth order model of the rotor-bearing dynamics, which are identified separately.

- Model 3 includes all the dynamics into one sixth order model to avoids the need of separating the identification in two.

The following sections describe the three models. Section 2.5 includes an example of the identification of model 3 on LPV form and a comparison of models 2 and 3.

2.3.1 Model 1

This section summarises model 1 presented in Paper A, which models the rotor-bearing system as a second order mass-spring-damper equivalent system:

$$\mathbf{G}_{rb}(t) = \left[\begin{array}{cc|cc} \mathbf{0} & \mathbf{I} & \mathbf{0} & \mathbf{0} \\ \boldsymbol{\mathcal{K}} & \boldsymbol{\mathcal{D}} & \boldsymbol{\mathcal{B}} & \boldsymbol{\mathcal{B}}_d \\ \hline \mathbf{I} & \mathbf{0} & \mathbf{0} & \mathbf{I} \end{array}\right] \tag{2.12}$$

where in the above the matrices to be identified are $\boldsymbol{\mathcal{K}}$, $\boldsymbol{\mathcal{D}}$, $\boldsymbol{\mathcal{B}}$, $\boldsymbol{\mathcal{B}}_d$, each fully populated and of dimension 2×2 and the initial state $\mathbf{x}_0$. The four inputs are the two controllable inputs $\mathbf{u}$ and the two disturbance inputs $\mathbf{d}$.

In this model, the actuator dynamics is neglected and approximated with a static gain $\mathbf{G}_{act}(s) = 2\mathbf{I}$.

The parameters to be interpolated are the elements of the stiffness and damping equivalents $\boldsymbol{\mathcal{K}}$, $\boldsymbol{\mathcal{D}}$ and the input gains $\boldsymbol{\mathcal{B}}$. A parameter-varying model was developed for a small range of angular velocities. The model was used for design of a state-feedback controller, with a Luenberger state observer in Paper A. The experimental closed loop results showed some deviation from the results expected from this model. The model was therefore improved in Paper C.

2.3.2 Model 2

This section summarises model 2 presented in Paper C, which is a cascading of the actuator model $\mathbf{G}_{act}$ and the rotor-bearing model $\mathbf{G}_{rb}$. These models are identified separately as shown in Figure 2.5. The rotor-bearing model is a 2 degree of freedom (DOF) mass-spring-damper system actuated through first order delays τ_x and τ_y. The two time delays are represented with first order Padé approximations to allow linear

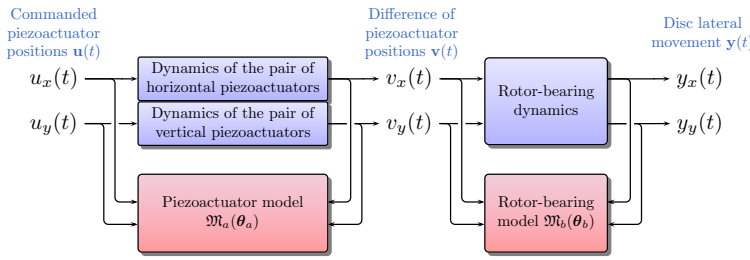

Figure 2.5: Overview of the system identification process. A perturbation of the commanded piezo-actuator positions perturbs both the piezo-actuators and the shaft and disc. An actuator model can the be identified from the $\{\mathbf{u}, \mathbf{v}\}$ data sets, and a rotor-bearing model from the $\{\mathbf{v}, \mathbf{p}\}$ data sets.

modelling. The final rotor-bearing model has the structure:

$$\mathbf{G}_{rb}(t) = \left[\begin{array}{ccc|c} \mathbf{0} & \mathbf{I} & \mathbf{0} & \mathbf{0} \\ \boldsymbol{\mathcal{K}} & \boldsymbol{\mathcal{D}} & 2\boldsymbol{\mathcal{B}}\boldsymbol{\mathcal{T}} & -\boldsymbol{\mathcal{B}} \\ \mathbf{0} & \mathbf{0} & -\boldsymbol{\mathcal{T}} & \mathbf{I} \\ \hline \mathbf{I} & \mathbf{0} & \mathbf{0} & \mathbf{0} \end{array}\right], \tag{2.13}$$

in which $\boldsymbol{\mathcal{K}}$, $\boldsymbol{\mathcal{D}}$ and $\boldsymbol{\mathcal{B}}$ are fully populated matrices that represent the equivalent stiffness, damping and input gain. The time delay approximations are included in the matrix $\boldsymbol{\mathcal{T}} = diag(2/\tau_x, 2/\tau_y)$, where the delays have the following state-space realisations:

$$G_{\tau_j}(t) = \left[\begin{array}{c|c} -2/\tau_j & 1 \\ \hline 4/\tau_j & -1 \end{array}\right], \quad j \in \{x, y\} \tag{2.14}$$

and can therefore be written

$$\mathbf{G}_{\boldsymbol{\tau}}(t) = \begin{bmatrix} G_{\tau_x}(t) & 0 \\ 0 & G_{\tau_y}(t) \end{bmatrix} = \left[\begin{array}{c|c} -\boldsymbol{\mathcal{T}} & \mathbf{I}_2 \\ \hline 2\boldsymbol{\mathcal{T}} & -\mathbf{I}_2 \end{array}\right], \tag{2.15}$$

A similar model can be set up for the PD-controlled piezo-actuator pairs. Each pair of piezo-actuators can be modelled as a second order low-pass filter. The piezo-actuator dynamics is written as transfer functions with gains $\kappa_{a,j}$ and two poles $p_{1,j}$, and $p_{2,j}$, where the subscript j refers to the pair of horizontal (x) or vertical (y) piezo-actuators. Considering the commanded reference position as input,

the piezo-actuator dynamics $\mathbf{G}_{act}$ then reads:

$$\begin{bmatrix} v_x(s) \\ v_y(s) \end{bmatrix} = \underbrace{\begin{bmatrix} G_{a,x}(s) & 0 \\ 0 & G_{a,y}(s) \end{bmatrix}}_{=\mathbf{G}_{act}} \begin{bmatrix} r_x(s) \\ r_y(s) \end{bmatrix}, \qquad G_{a,j}(s) = \frac{\kappa_{a,j}}{\left(\frac{1}{p_{1,j}}s+1\right)\left(\frac{1}{p_{2,j}}s+1\right)} \tag{2.16}$$

in which $G_{a,j}(s)$ is the second order filter of the specified form (2.16).

In this model, the parameters to be interpolated as function of the scheduling parameters are the time delays $\{\tau_x, \tau_y\}$ and the mass-spring-damper parameters $\{vec(\boldsymbol{\mathcal{K}}), vec(\boldsymbol{\mathcal{D}}), vec(\boldsymbol{\mathcal{B}})\}$. The actuator model is approximated as LTI.

Model 2 is obtained by cascading the actuator model (2.16) and the rotor-bearing model (2.13). This model can capture the dynamics very well but has a fairly high order.

2.3.3 Model 3

The simplified but yet accurate Model 3 was developed as part of the work related to Paper G. The work is summarised in Section 2.5 which shows that the local models can be identified directly in one step and that a sixth order model can provide a similar accuracy as Model 2.

The reduced model structure consists a parameter-varying mass-spring-damper system actuated through first order low-pass filters $h_j(s),\ j \in \{1,2\}$ with unit static gain to avoid over-parametrisation:

$$h_j(s) = \frac{p_j}{s+p_j} = \left[\begin{array}{c|c} -p_j & p_j \\ \hline 1 & 0 \end{array}\right], \quad j \in \{1,2\} \tag{2.17}$$

The chosen model structure can then be written

$$\mathbf{G} = \left[\begin{array}{ccc|c} \mathbf{0} & \mathbf{I} & \mathbf{0} & \mathbf{0} \\ \boldsymbol{\mathcal{K}} & \boldsymbol{\mathcal{D}} & \boldsymbol{\mathcal{B}} & \mathbf{0} \\ \mathbf{0} & \mathbf{0} & -\boldsymbol{\mathcal{P}} & \boldsymbol{\mathcal{P}} \\ \hline \mathbf{I} & \mathbf{0} & \mathbf{0} & \mathbf{0} \end{array}\right], \quad \boldsymbol{\mathcal{P}} = diag(p_1, p_2) \tag{2.18}$$

in which the parameters to be identified are $\boldsymbol{\theta} = [vec(\boldsymbol{\mathcal{K}}), vec(\boldsymbol{\mathcal{D}}), ..., vec(\boldsymbol{\mathcal{B}}), p_1, p_2]$. These are also the parameters to be interpolated.

2.4 Discussion

This section presents a discussion of the proposed grey-box identification method. The discussion is divided in topics.

Model range The method relies on regression for data collected in some interval of $\mathbf{q}$, and the model is not expected to be valid outside this interval. The identified models are therefore not able to replace the first principles models during the machine design phase, where it is necessary to evaluate the effects of changing parameters such as the bearing geometry. Care should be taken to avoid over-fitting to ensure that the model captures the parameter-variation inside the desired interval. High order polynomials should be avoided since they are usually poor for prediction between the investigated values used for interpolation.

Local approach limitations The proposed grey-box identification method belongs to the class of local LPV identification methods, and it is therefore limited to applications with slow parameter-variations. The method is not able to capture the effects from rate of change in the scheduling parameters.

Choice of $\mathbf{q}$ grid The grid of the scheduling parameter interval must not necessarily be evenly distributed, but a high density in one region of the scheduling parameter interval increase the accuracy of the interpolation in that region at the cost of accuracy in other regions. For the present project, it has generally been chosen to collect models in equidistantly gridded sets, and to collect at least two data sets at each scheduling parameter value to allow cross-validation of the models on similar data sets.

Model validation It is common to assess identified LTI models using tools such as autocorrelation analysis, spectral analysis of the residuals and parameter significance tests to assess whether the chosen model structure is too simple or too complicated. It may be that certain model parameters are insignificant or a higher order model is required to obtain a white residual.

These model changes are not easily assessed for LPV model identification since the model order is constrained to be the same for all models, and certain parameters may change sign over the scheduling parameter interval. The choice of model structure for LPV identification is a field that requires further treatment in research.

An increase of model order increases the order of the controller when modern control design techniques are applied. It is therefore of interest to obtain low order models. Correlation analyses of the residuals show that the model residuals are not white, but it has been chosen to avoid a further increase of the model orders.

2.5 Identification of Model 3 and Model Comparison

This section shows an example of identification of the parameter-varying Model 3 proposed in Paper G. The focus of the paper is on the design of gain-scheduled control, and the paper uses Model 3 from Section 2.3.3.

Model 3 is able to reduce the complexity compared to Model 2. The state-space order is reduced from 10 to 6, the new model avoids the need for parameter-varying time-delays, and the local models could be identified in one step. The optimal model order was assessed by identifying black-box state-space models using Matlab's `ssest` of different orders for three data sets collected at different values of the scheduling parameter. For each data set, a validation data set was available, from which we evaluated the goodness of fit. For the same data sets we identified a model on the form of Model 2. Table 2.1 summarises the goodness of fit-values for the different models in validation. The table shows that the validation fit increases significantly up to model order 6, from which the change is negligible. We then identified local black-box models from the same data sets used in Paper E collected in the grid points $q_1 \in \{0, 1, 2, 3, 4, 5, 6\}$ krpm, $q_2 \in \{0.3, 0.4, 0.5, 0.6, 0.7\}$ MPa. The parameters of the black-box model did not develop adequately to be interpolated[2]. We therefore began to investigate grey-box models of order 6 that were adequate for interpolation. These analyses led to Model 3. The corresponding validation fits for Model 3 are included in Table 2.1 and demonstrate that it obtains fit values similar to Model 2 indicating that no accuracy is lost. Models on the form of Model 3 were therefore identified for the collected data sets.

For the interpolation we only use 35 of the identified models. The remaining 34 models are used for model validation to ensure that the models predict well in these remaining points. The parameters to be interpolated are the four stiffness equivalents and similarly the four damping and input gain equivalents and the two poles:

$$\boldsymbol{\theta} = \{k_{xx}, k_{xy}, k_{yx}, k_{yy}, d_{xx}, \ ..., d_{yy}, b_{xx}, \ ..., b_{yy}, p_1, p_2\} \tag{2.19}$$

[2]Without any model transformations, the parameters did not appear to develop continuously. The methods proposed for transforming the models proposed in [73] were not applicable as the transformation matrices became singular. Attempts were also made to identify the models in discrete time, which improved the numerical conditioning sufficiently to obtain regular transformation matrices that allow usage of the SMILE technique [73]. The subsequent interpolation however revealed that the local models' behaviour was significantly different from the LPV model's behaviour in the same points. We contribute this to a high numerical parameter sensitivity in the sense that a small error in parameter-estimate significantly changes the input-output behaviour of the model.

Model order	`ssest 4`	`ssest 5`	`ssest 6`	`ssest 7`	ssest 8	Model 2	Model 3
Data sets collected at $q_1 = 0$krpm, $q_2 = 0.3$MPa:							
Horz. fit (%)	78.85	79.57	86.70	86.72	86.77	86.27	86.42
Vert. fit (%)	75.17	86.98	87.17	87.25	87.28	86.69	85.50
Data sets collected at $q_1 = 4.05$krpm, $q_2 = 0.5$MPa:							
Horz. fit (%)	70.41	74.20	86.40	86.49	86.40	85.57	86.01
Vert. fit (%)	73.03	87.08	87.50	87.50	87.54	85.91	86.87
Data sets collected at $q_1 = 4.2$krpm, $q_2 = 0.7$MPa:							
Horz. fit (%)	71.04	73.28	85.03	84.55	84.88	82.75	84.70
Vert. fit (%)	75.99	80.02	87.50	87.35	87.16	83.35	84.34

Table 2.1: Validation for n^{th} order black box models and two of the proposed grey-box models for selected local data sets.

The parameters are approximated with polynomials of $\mathbf{q}$, and it is found that a second order polynomial on the following form is suitable to identify the elements of $\boldsymbol{\theta} = [\theta_1, ..., \theta_i, \theta_I]$ on the form (2.6). The estimated model parameters as functions of $\mathbf{q}$ are shown in Figures 2.6, 2.7, 2.8 and 2.9. The figures show the points used for identification ($*$) and the ones used for validation ($\times$) and their polynomial surfaces along with the root mean square (RMS) error for the identification and the validation points. The difference between the RMS error for the identification data and the validation data is low, indicating that the models do not over-fit.

As shown from the figures, the second order polynomial surfaces capture the parameter development well. It may be possible to use a linear (first order polynomial) model in $\mathbf{q}$ to obtain an affine LPV model. Such a model could avoid the need for gridding in the LPV synthesis. In Paper G we used the SMILE technique [73] to obtain the LPV model, where the local models are transformed to coherent state-space bases. In the transformation, the structure of the model state-space matrices is lost. Polynomial surface estimates of the Model 1 are available in Paper A and for Model 2 in Paper C.

2.6 Practical Challenges

This section presents the solutions to practical challenges in the identification of the gas bearing dynamics. First is the inherent non-linearities of the piezo-actuators. These non-linearities are counteracted by decentralised controllers for each piezo-actuator. Second is the runout compensation to filter out the mass imbalance response

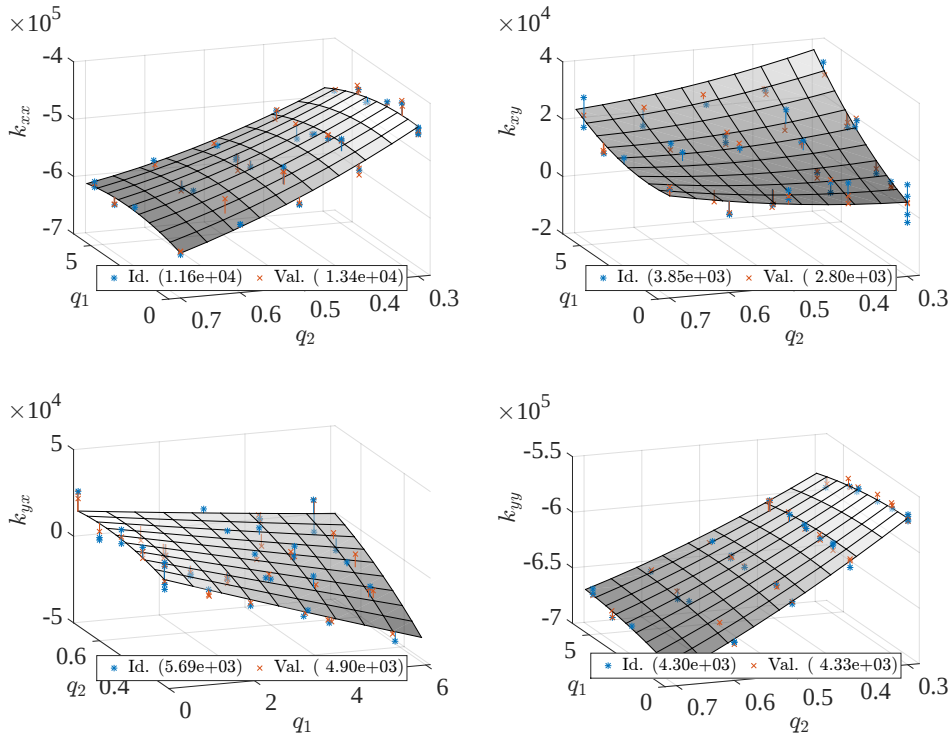

Figure 2.6: Stiffness equivalents $[N/(kg\,\mu m)]$ estimated as polynomial surfaces of the scheduling parameter. The RMS errors for identification and the validation data are written with the legend.

from the identification data.

2.6.1 Piezo-Actuators

The piezo-actuators are subject to hysteresis and creep. The hysteresis can be modelled with the Preisach model [90]. The creep and hysteresis can be compensated with iterative algorithms [91], but these methods are not easily applied and the resulting models are complex. To avoid the significant increase of complexity associated to the modelling of these non-linearities, it is of interest to counteract them using high-gain feedback controllers. This is treated in Paper C through the deployment of decentralised PD-controllers. The controllers are tuned experimentally and allow the piezo-actuators to track reference positions. The closed loop piezo-actuator dynamics

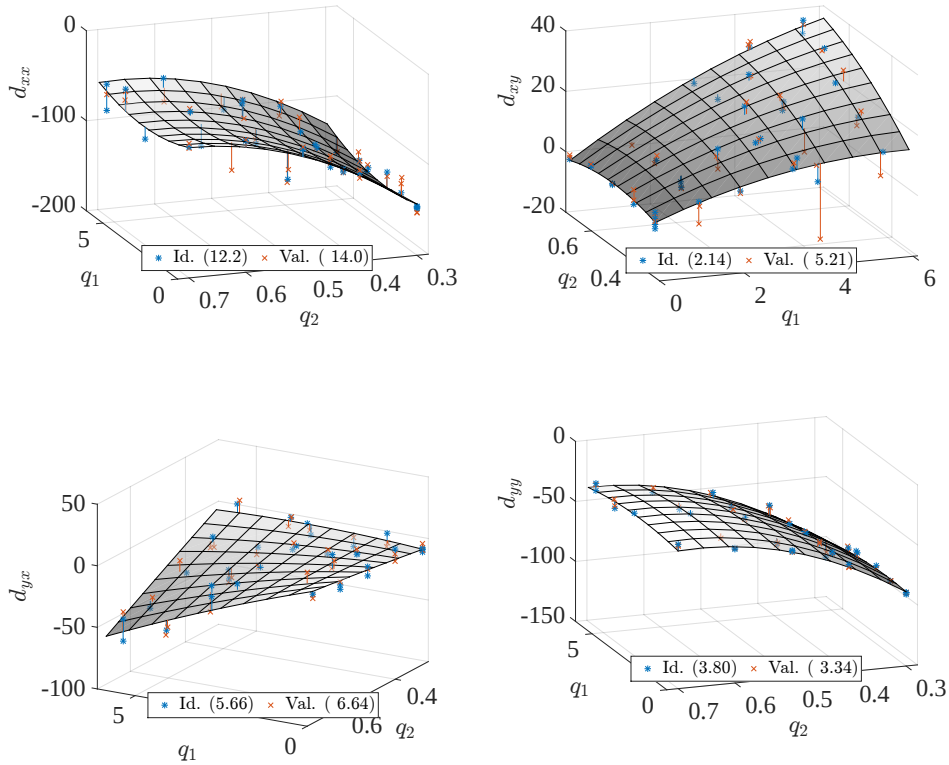

Figure 2.7: Damping equivalents $[Ns/(kg\ \mu m)]$ estimated as polynomial surfaces of the scheduling parameter. The RMS errors for identification and the validation data are written with the legend.

can then be captured by linear models. Figure 2.10 shows step responses of an open and closed loop piezo-actuator. The static equilibrium positions shown in Figure 2.11 reveal the hysteresis.

2.6.2 Runout Compensation

This section first summarises the standard runout compensation for rotating machinery and then presents the novel application of runout compensation for removing mass imbalance response to obtain the active response.

The disc movement is measured with eddy current sensors that induce electrical currents in the disc surface by a coil. This in turn induces currents in a second

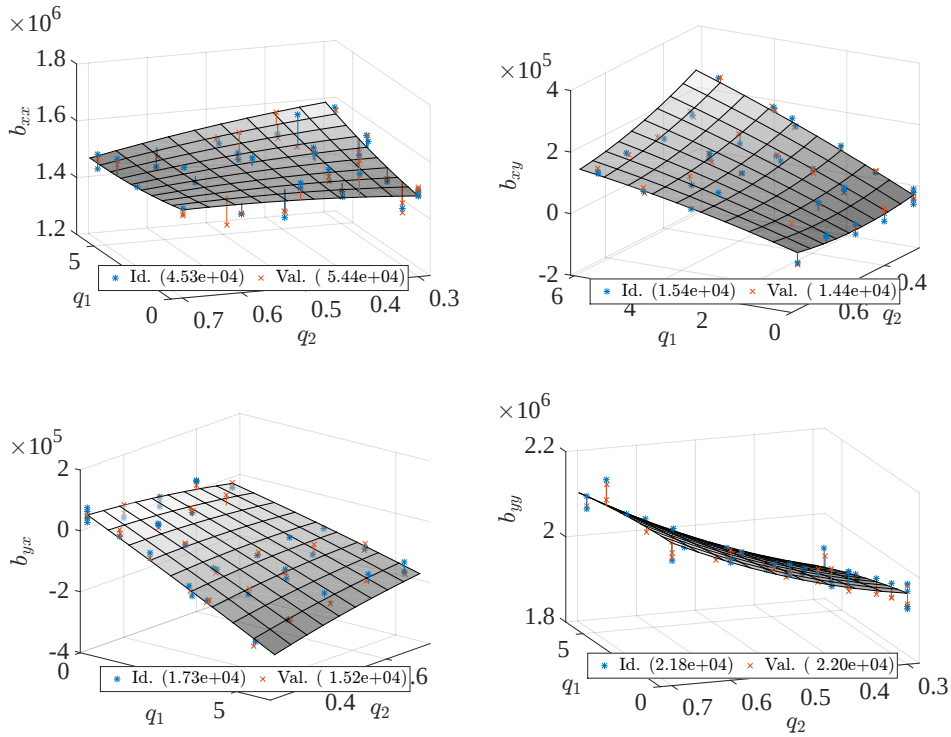

Figure 2.8: Input gain equivalents $[N/(kgV)]$ estimated as polynomial surfaces of the scheduling parameter. The RMS errors for identification and the validation data are written with the legend.

coil, from which the distance from the sensor to the disc is measured. These measurements are very accurate, but to obtain the required precision it is necessary to take imperfections in the disc into account. The imperfections include small scale electrical property variations and small scale deviations in the radius of the disc [92] and cause erroneous observations in the disc position denoted by runout. The runout is not caused by disc movement, therefore it is of interest to filter it out.

The runout is estimated from measurements collected at low angular velocity where the vibration amplitude is negligible (< 200rpm) and an example of measured response is shown in Figure 2.12. The runout estimate is a look-up table of the angular position and can be subtracted online to remove runout errors from the disc movement measurements. Figure 2.12 shows the uncompensated measurements

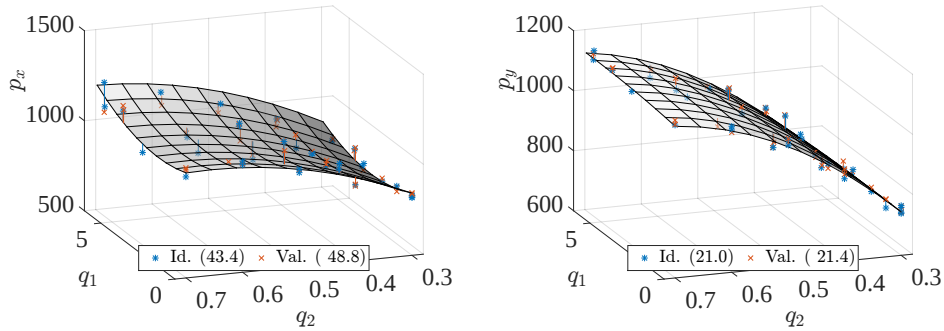

Figure 2.9: Real poles $[rad/s]$ estimated as polynomial surfaces of the scheduling parameter. The RMS errors for identification and the validation data are written with the legend..

for the two angular velocities $\Omega = 0$ rpm and $\Omega = 5$ krpm and the black lines are the corresponding estimated runouts. The estimate is obtained as the mean of the measurements collected at a particular angular position. This runout filtering is standard for rotating machinery.

As a novel application, we propose to use the same runout filtering method to partition the disc movement measurements into mass imbalance vibrations, runout errors and active response. This partitioning is particularly useful to obtain only the active response, i.e. the disc movement stemming from the actuation.

This requires estimation of the mass imbalance response. For a constant angular velocity, the disc movement signals enter a limit cycle induced by the mass imbalance. This limit cycle can be estimated from a data set collected at a desired constant angular velocity where the rotor is only excited by the mass imbalance. From the measurements the extended runout is estimated in the same way as the ordinary runout filter and generates a look-up table of the angular position. An example of identification data before and after runout compensation of the mass imbalance response is shown in Figure 2.13. The runout compensation of the mass imbalance filters out the mass imbalance and only the active response remains.

This filtering is described in Paper A and Paper C and can also be used for removing the mass imbalance for the closed-loop system as described in Paper E.

The compensation for run-out and mass imbalance significantly improves the signal quality and allows micrometer precision measurement of the response from perturbing the piezo-actuators.

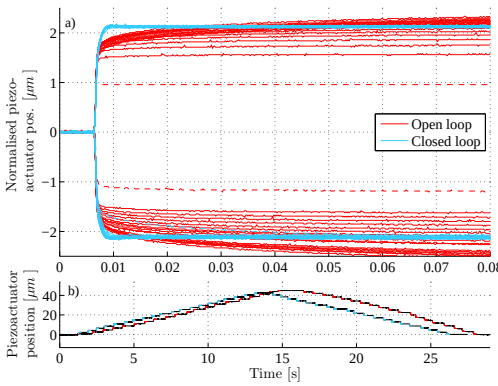

Figure 2.10: Open loop and PD-controlled piezo-actuator staircase responses. b) The piezo-actuator position during the staircase response. a) The individual steps without offsets in time and position. The PD-control reduces both hysteresis and creep effects that cause the open loop step responses to vary.

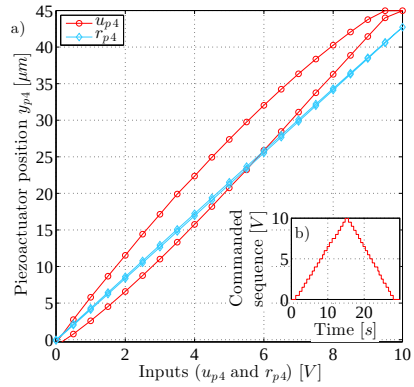

Figure 2.11: Hysteresis curves for piezo-actuator four for the open loop case and the closed loop case. The responses are collected for a staircase input shown in b). The PD-controller efficiently eliminates the hysteresis.

An alternative to the extended runout filtering is to use notch filters, but such filters remove both the mass imbalance and the active response within the range of the notch. Multiple notch filters would be required to filter out the synchronous vibrations and their higher order harmonic components. The extended runout filtering approach avoids the phase-shifts related to the frequency-based notch filtering approaches. The runout signals may change over time due to slow changes for example from magnetisation and small scratches in the disc surface, hence the runout estimate is updated occasionally.

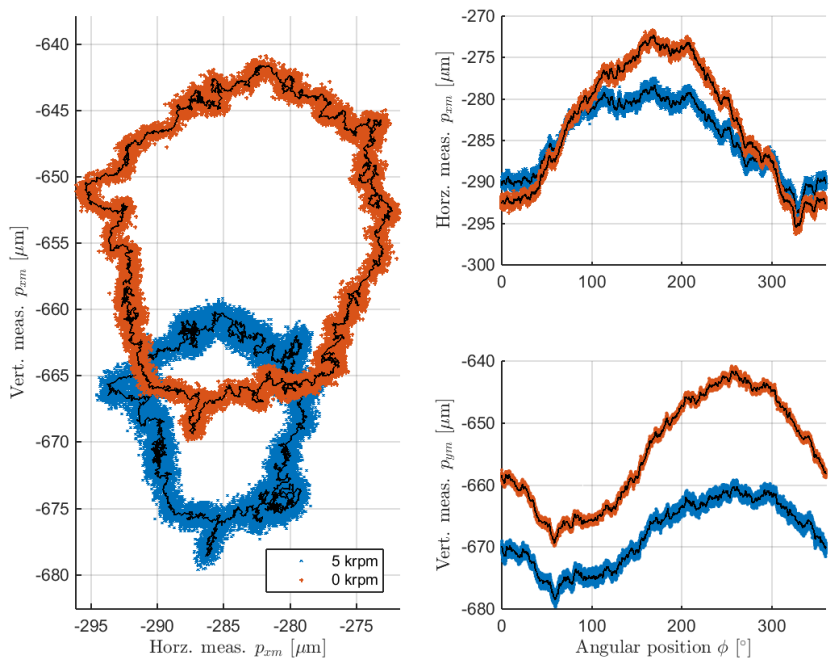

Figure 2.12: Runout estimation of disc movement signals. Position sensor signals seen both as an XY-plot and as functions of the angular position.

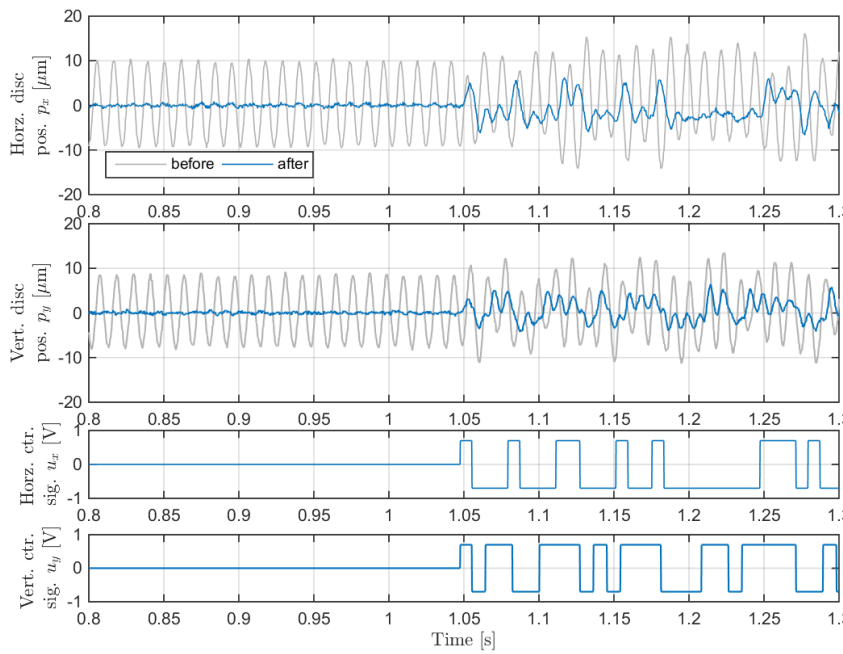

Figure 2.13: Identification data collected at $q_1 = 5$ krpm, $q_2 = 0.3$MPa before and after mass imbalance runout compensation. The runout compensation of the mass imbalance can filter out the mass imbalance such that only the active response remains. Before time $t = 1.045$s, the piezo-actuator positions are held constant. After this time the piezo-actuator positions are changed and cause disc vibrations.

Chapter 3

Control of Active Bearings

This chapter describes the control design for active bearings. The main methods that have been applied for control design for the controllable bearings are briefly revisited followed by a description of the control objectives and challenges. Finally, selected closed loop experimental results with the proposed control designs are presented.

The chapter first summarises the main methods employed for control design in Section 3.1. Then the control objectives for controllable gas bearings are presented in Section 3.2. Section 3.3 presents examples of control of the gas bearing test rig.

3.1 Control Design Methods

This section revisits the main methods that have been applied for control design during the project.

3.1.1 $\mathcal{H}_\infty/\mathcal{H}_2$ Control Design

The $\mathcal{H}_\infty/\mathcal{H}_2$ synthesis methods are attractive for their flexibility in control design, where many control objectives can be imposed by weighting functions. These weights can shape the frequency responses of the closed loop system, and the synthesis tools are readily available in standard numerical computing software such as Matlab.

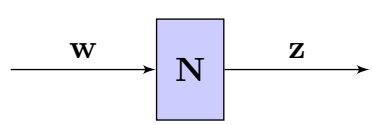

Figure 3.1: Stable LTI system **N**.

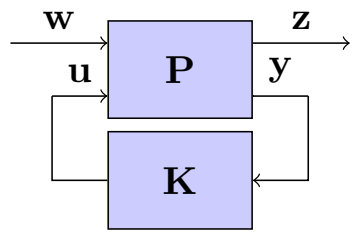

Figure 3.2: Block diagram of the closed loop system.

The methods minimise norms, where for a stable LTI system $\mathbf{N}(s)$, where $\mathbf{z}(s) = \mathbf{N}(s)\mathbf{w}(s)$ as in Figure 3.1, the $\mathcal{H}_\infty$ norm is defined:

$$\|\mathbf{N}\|_\infty = \sup_{0<\|\mathbf{w}\|_2<\infty} \frac{\|\mathbf{z}(t)\|_2}{\|\mathbf{w}(t)\|_2} \tag{3.1}$$

The synthesis of $\mathcal{H}_\infty$ and $\mathcal{H}_2$ controllers relies on the general control problem formulation from Figure 3.2 [93, Sec. 9.3] where a controller $\mathbf{K}$ is synthesised to have $\mathbf{u} = \mathbf{K}\mathbf{y}$. The controller may then guarantee that the gain (either $\mathcal{H}_\infty$ or $\mathcal{H}_2$ norm) from the exogenous inputs $\mathbf{w}$ to the exogenous outputs $\mathbf{z}$ is bounded by some value γ.

This generalised plant can emerge from weighting the plant $\mathbf{G}$ appropriately to form the generalised plant $\mathbf{P}$ with inputs $\mathbf{w}, \mathbf{u}$ and outputs $\mathbf{z}, \mathbf{y}$, where the exogenous inputs are $\mathbf{w}$ and the exogenous outputs are $\mathbf{z}$. The generalised plant can be written in state-space as:

$$\mathbf{P} = \left[\begin{array}{c|cc} \mathbf{A} & \mathbf{B}_1 & \mathbf{B}_2 \\ \hline \mathbf{C}_1 & \mathbf{D}_{11} & \mathbf{D}_{12} \\ \mathbf{C}_2 & \mathbf{D}_{21} & \mathbf{D}_{22} \end{array}\right] \tag{3.2}$$

The closed loop dynamics $\mathbf{N}$ can be written as a lower linear fractional transformation (LFT):

$$\mathbf{z} = \mathbf{N}\mathbf{w}, \quad \mathbf{N} = F_l(\mathbf{P}, \mathbf{K}) \tag{3.3}$$

The controller $\mathbf{K}$ is commonly found as the solution to two Riccati equations [94, 95]. Both synthesis methods ($\mathcal{H}_\infty$ and $\mathcal{H}_2$) result in full order controllers, where the state-dimension of the controller is equal to the state-dimension of the generalised plant.

The $\mathcal{H}_\infty$ synthesis seeks to minimise $\|\mathbf{N}\|_\infty$; hence the optimal controller $\mathbf{K}^*$ is

$$\mathbf{K}^* = \arg \min_{\mathbf{K} \text{ stabilises } \mathbf{P}} \|\mathbf{N}\|_\infty, \quad \gamma = \|\mathbf{N}\|_\infty \tag{3.4}$$

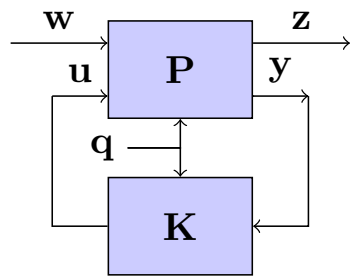

Figure 3.3: LPV control of parameter-varying plant.

The common optimisers use interior point methods to approximate the minimum γ^* iteratively, therefore a suboptimal value γ is found ($\gamma > \gamma^*$).

The $\mathcal{H}_2$ synthesis seeks to minimise the two-norm $\|\mathbf{N}\|_2$. This is equal to minimising the RMS value of $\mathbf{z}$ for the exogenous signal $\mathbf{w}$ being white noise with unit intensity. The $\mathcal{H}_2$ norm is defined:

$$\|N\|_2 = \sqrt{\frac{1}{2\pi}\int_{-\infty}^{\infty} \operatorname{tr}\left(\mathbf{N}(j\omega))^H \mathbf{N}(j\omega)\right) d\omega} \tag{3.5}$$

Unlike the $\mathcal{H}_\infty$ synthesis, the optimal $\mathcal{H}_2$ controller can be found uniquely from the solution to two Riccati equations.

3.1.2 LPV Control

The notion of $\mathcal{H}_2$ and $\mathcal{H}_\infty$ control can be extended to the class of LPV systems, where the state-space parameters of the plant $\mathbf{P}$ are function of the scheduling parameter $\mathbf{q}$ as in Figure 3.3. The scheduling parameter is assumed measurable in real time. The controller synthesis conditions will then be based on parametrised linear matrix inequalities (LMIs) [96, 97]. The plant in consideration has inputs $\left[\mathbf{w}^{\mathrm{T}}, \mathbf{u}^{\mathrm{T}}\right]^{\mathrm{T}}$ and outputs $\left[\mathbf{z}^{\mathrm{T}}, \mathbf{y}^{\mathrm{T}}\right]^{\mathrm{T}}$:

$$\mathbf{P}(\mathbf{q}) = \left[\begin{array}{c|cc} \mathbf{A}(\mathbf{q}) & \mathbf{B}_1(\mathbf{q}) & \mathbf{B}_2(\mathbf{q}) \\ \hline \mathbf{C}_1(\mathbf{q}) & \mathbf{D}_{11}(\mathbf{q}) & \mathbf{D}_{12}(\mathbf{q}) \\ \mathbf{C}_2(\mathbf{q}) & \mathbf{D}_{21}(\mathbf{q}) & \mathbf{0} \end{array}\right], \tag{3.6}$$

such that the external output $\mathbf{z}$ is $\mathbf{z} = \mathrm{LFT}(\mathbf{P}, \mathbf{K})\mathbf{w}$, and $\|\mathbf{z}\|_2 \leq \gamma \|\mathbf{w}\|_2$.

The goal is to synthesise a gain-scheduled controller $\mathbf{K}(\mathbf{q})$ with state-space reali-

sation

$$\mathbf{K}(\mathbf{q}) = \left[\begin{array}{c|c} \mathbf{A}_K(\mathbf{q}) & \mathbf{B}_K(\mathbf{q}) \\ \hline \mathbf{C}_K(\mathbf{q}) & \mathbf{D}_K(\mathbf{q}) \end{array}\right], \tag{3.7}$$

In the basic characterisation [75], a full-order LPV controller for the system (3.6) is found from the solution to the following two matrix inequalities for the decision variables $\hat{\mathbf{A}}_K(\mathbf{q})$,$\hat{\mathbf{B}}_K(\mathbf{q})$,$\hat{\mathbf{C}}_K(\mathbf{q})$,$\mathbf{D}_K(\mathbf{q})$, $\mathbf{X}(\mathbf{q})$,$\mathbf{Y}(\mathbf{q}), \gamma$ of appropriate dimensions:

$$\begin{bmatrix} \mathbf{X} & \mathbf{I}_{n_a} \\ \mathbf{I}_{n_a} & \mathbf{Y} \end{bmatrix} \succ 0$$

$$\begin{bmatrix} \dot{\mathbf{X}} + \mathbf{X}\mathbf{A} + \hat{\mathbf{B}}_K\mathbf{C}_2 + (\star) & \star & \star & \star \\ \hat{\mathbf{A}}_K^{\mathrm{T}} + \mathbf{A} + \mathbf{B}_2\mathbf{D}_K\mathbf{C}_2 & \mathbf{A}\mathbf{Y} + \mathbf{B}_2\hat{\mathbf{C}}_K + (\star) & \star & \star \\ \left(\mathbf{X}\mathbf{B}_1 + \hat{\mathbf{B}}_K\mathbf{D}_{21}\right)^{\mathrm{T}} & \left(\mathbf{B}_1 + \mathbf{B}_2\mathbf{D}_K\mathbf{D}_{21}\right)^{\mathrm{T}} & -\gamma\mathbf{I}_{n_w} & \star \\ \mathbf{C}_1 + \mathbf{D}_{12}\mathbf{D}_K\mathbf{C}_2 & \mathbf{C}_1\mathbf{Y} + \mathbf{D}_{12}\hat{\mathbf{C}}_K & \mathbf{D}_{11} + \mathbf{D}_{12}\mathbf{D}_K\mathbf{D}_{21} & -\gamma\mathbf{I}_{n_z} \end{bmatrix} \prec 0 \tag{3.8}$$

In the above, the dependency of the scheduling parameter $\mathbf{q}$ is omitted for simplicity. The star notation denotes $\mathbf{Z} + (\star) = \mathbf{Z} + \mathbf{Z}^{\mathrm{T}}$ [75] and $\mathbf{Z} \succ 0$ requires that all eigenvalues of $\mathbf{Z}$ have positive real parts. This problem is an LMI with infinite dimension, which can only be reduced to an LMI with finite dimension under certain conditions. For systems with affine parameter-dependency it is sufficient to evaluate the LMI over a polytope. For systems with polynomial parameter-dependency, a set of conditions are presented in [98], but this method is not easily applied. Alternatively when this is not the case, the LMIs (3.8) become tractable by the following propositions from [75]: 1) the matrix inequalities are evaluated over a finite grid $\mathbf{q} \in \mathbf{Q}_d$ of scheduling parameters covering the operating range; 2) the decision variables are constrained to functions of the scheduling parameter, e.g. a copy of the plant function dependency.

The resulting LMI is then solved over the design grid $\mathbf{q} \in \mathbf{Q}_d$. The solution is not guaranteed to be valid over the original set. It is therefore validated on a finer grid $\mathbf{q} \in \mathbf{Q}_v$.

The LMIs have been entered with YALMIP [99] and are solved over the design grid $\mathcal{Q}_d$ using MOSEK. A standard challenge in this regard is that MOSEK only solves nonstrict LMIs ($\mathbf{Z} \succeq 0$ and $\mathbf{Z} \preceq 0$). The LMIs (3.8) are required to be strict ($\mathbf{Z} \succ 0$ and $\mathbf{Z} \prec 0$) which is ensured by including a small positive scalar term $\epsilon > 0$ such that $\mathbf{Z} \succeq \epsilon$ and $\mathbf{Z} \preceq -\epsilon$.

Once the LMIs have been solved, the factorisation problem $\mathbf{I} - \mathbf{X}\mathbf{Y} = \mathbf{N}\mathbf{M}^{\mathrm{T}}$ must

be solved for some $\mathbf{N}(\mathbf{q})$ and $\mathbf{M}(\mathbf{q})$, and the controller parameters are then:

$$\mathbf{K}(\mathbf{q}) = \left[\begin{array}{c|c} \mathbf{A}_K(\mathbf{q}) & \mathbf{B}_K(\mathbf{q}) \\ \hline \mathbf{C}_K(\mathbf{q}) & \mathbf{D}_K(\mathbf{q}) \end{array}\right], \tag{3.9}$$

in which:

$$\begin{aligned} \mathbf{A}_K =& \mathbf{N}^{-1}\left(\mathbf{X}\dot{\mathbf{Y}} + \mathbf{N}\dot{\mathbf{M}}^{\mathrm{T}} + \hat{\mathbf{A}}_K - \mathbf{X}\left(\mathbf{A} - \mathbf{B}_2\mathbf{D}_K\mathbf{C}_2\right)\mathbf{Y}\right. \\ & \left. -\hat{\mathbf{B}}_K\mathbf{C}_2\mathbf{Y} - \mathbf{X}\mathbf{B}_2\hat{\mathbf{C}}_K\right)\mathbf{M}^{-\mathrm{T}} \\ \mathbf{B}_K =& \mathbf{N}^{-1}\left(\hat{\mathbf{B}}_K - \mathbf{X}\mathbf{B}_2\mathbf{D}_K\right) \\ \mathbf{C}_K =& \left(\hat{\mathbf{C}}_K - \mathbf{D}_K\mathbf{C}_2\mathbf{Y}\right)\mathbf{M}^{-\mathrm{T}}, \end{aligned} \tag{3.10}$$

and $\mathbf{D}_K$ is given from (3.8). The parameters are functions of the scheduling parameter $\mathbf{q}$, though the dependency is not stated explicitly. The evaluation of the matrices $\hat{\mathbf{A}}_K, \hat{\mathbf{B}}_K, \hat{\mathbf{C}}_K, \mathbf{D}_K$ and $\mathbf{X}, \mathbf{Y}$, and calculations of the controller matrices (3.10) have to be performed online for each scheduling sampling step, which is computationally heavy due to the two matrix inversions.

LPV synthesised controllers can be discretised systematically to allow implementation in standard computer control systems. Apkarian [100] proposed a trapezoidal LPV discretisation method for a general LPV state-space controller. The controller law at time kT_s defined by the controller state $\mathbf{g}_k$ and control signal $\mathbf{u}_k$ reads:

$$\begin{aligned} \mathbf{g}_{k+1} =& \left(\mathbf{I} - \tfrac{T_s}{2}\mathbf{A}_K(\mathbf{q}_k)\right)^{-1}\left(\mathbf{I} + \tfrac{T_s}{2}\mathbf{A}_K(\mathbf{q}_k)\right)\mathbf{g}_k + \\ & \sqrt{T_s}\left(\mathbf{I} - \tfrac{T_s}{2}\mathbf{A}_K(\mathbf{q}_k)\right)^{-1}\mathbf{B}_K(\mathbf{q}_k)\mathbf{y}_k \\ \mathbf{u}_k =& \sqrt{T_s}\mathbf{C}_K(\mathbf{q}_k)\left(\mathbf{I} - \tfrac{T_s}{2}\mathbf{A}_K(\mathbf{q}_k)\right)^{-1}\mathbf{g}_k + \\ & \left(\tfrac{T_s}{2}\mathbf{C}_K(\mathbf{q}_k)\left(\mathbf{I} - \tfrac{T_s}{2}\mathbf{A}_K(\mathbf{q}_k)\right)^{-1}\mathbf{B}_K(\mathbf{q}_k) + \mathbf{D}_K(\mathbf{q}_k)\right)\mathbf{y}_k \end{aligned} \tag{3.11}$$

The calculation of the controller matrix updates require the inversion of $\mathbf{N}, \mathbf{M}$ and the term $\left(\mathbf{I} - \frac{T_s}{2}\mathbf{A}_K(\mathbf{q}_k)\right)$. This is time consuming, and it may therefore be necessary to update the controller parameters with lower sampling period than the control signal update.

3.1.3 Gain-Scheduled $\mathcal{H}_2$ Control Design

The LPV synthesis methods provide a systematic approach for synthesising gain-scheduled controllers to address plant parameter variations, but they require a numerically well-conditioned low order generalised plant. The mentioned LPV synthesis techniques sufficed for the control design in Paper E, but it has not been

possible to synthesise an LPV controller for the more complex generalised plant proposed in Paper G. As an alternative approach for such systems, we proposed a gain-schedulling strategy in Paper G to obtain controllers with an LPV form. The method relies on synthesising a set of local linear $\mathcal{H}_2$ controllers for a generalised plant in LPV form over a grid of scheduling parameters in a desired range. The $\mathcal{H}_2$ controllers are synthesised from the solution of two Riccati equations and are therefore determined uniquely. Though it is not guaranteed, the state-space parameters of the controllers will often develop adequately to allow interpolation of these parameters. The synthesised controllers can then be interpolated using state-space interpolation to obtain an LPV controller. This is generally not the case for $\mathcal{H}_\infty$ controllers which are solved iteratively as discussed in Section 3.1.1. Instead, $\mathcal{H}_\infty$ controllers can be converted to a unique observer and state-feedback structure to allow interpolation of the state-feedback and observer feedback gains [101, 102]. The proposed interpolated $\mathcal{H}_2$ control design does not guarantee closed loop stability of the closed loop system, but the stability can be proven subsequently using Lyapunov theory. The technique resembles the interpolation method of the grey-box models described in Sec. 2.3 and may be summarised as follows:

- Set up the generalised plant $\mathbf{P}(\mathbf{q}, t)$ in LPV form such that the state-space parameters of $\mathbf{P}$ develops continuously in the scheduling parameters.
- For a grid of $i \in \{1, ..., I\}$ scheduling parameters $\mathbf{q}_i \in \{\mathbf{q}_1, ..., \mathbf{q}_I\}$, synthesise local $\mathcal{H}_2$ LTI controllers $\mathbf{K}_i(t)$.
- Use state-space interpolation to obtain $\mathbf{K}(\mathbf{q}, t)$
- Investigate closed loop stability

For the interpolation of the state-space parameters, standard regression tools such as linear least squares fitting is applicable. The standard guidelines to avoid over-parametrisation should be followed. We advice to use a fraction of the systems to estimate the interpolated parameters and the remaining to validate that the behaviour of the interpolated controller matches the one of the local linear controllers in the interpolation regions.

The proposed approach is very flexible since it is applicable for both continuous and discrete time systems and the generalised plant can be cast to include multiple control objectives. The resulting interpolated controllers have an LPV form and may readily be converted to discrete time using available methods from [100]. The

gain-scheduling proposed is limited to systems with slow parameter-variation. which can be quantified using the approach from [103]. As discussed in [102], the approach is limited to an appropriate interpolation of the control weights.

3.2 Control Objectives

The control objectives have generally focussed on the reduction of vibrations and the enhancement of damping.

The main control objective for rotating machinery is to avoid rub (rotor-stator contact). This simple objective becomes a challenge of disturbance rejection of mass imbalance and forces induced from other machines, especially in presence of time-varying system parameters. It is furthermore of interest to extend the operating range of the rotating machine to allow operation at higher angular velocities using control. These challenges are treated in the following sections.

3.2.1 Damping Enhancement

Sufficient damping levels are important for bearings [78, 83, 10, 40] to avoid the big disturbance amplifications associated to low-damped natural frequencies. A common guideline for rotating machinery is to avoid operation to within $\pm 15\%$ of the *critical speeds*. This restricts the operation, and we have sought to reduce the disturbance sensitivity in these critical speeds regions to extend the operating range of the controllable gas bearing.

To clarify the increase of damping from a control design perspective, consider the general linear control system shown in Figure 3.4. The system plant is denoted by $\mathbf{G}(s)$ and has controllable inputs $\mathbf{u}(s)$, and measured outputs $\mathbf{y}(s)$ affected by the unknown disturbance $\mathbf{d}(s)$. The disturbance enters the output through the unknown dynamics $\mathbf{G}_d(s)$. A feedback controller $\mathbf{K}(s)$ closes the loop. This disturbance description encompasses many situations, for instance, for an input disturbance $\mathbf{G}_d = \mathbf{G}$ and for an output disturbance $\mathbf{G}_d = \mathbf{I}$.

The output sensitivity is defined

$$\mathbf{S}_o(s) = (\mathbf{I} - \mathbf{GK})^{-1}, \tag{3.12}$$

and the input sensitivity is $\mathbf{S}_i(s) = (\mathbf{I} - \mathbf{KG})^{-1}$. These sensitivity functions are limited for stable closed loop systems by Bode's sensitivity integrals [104, 93] as discussed in Paper D, and a reduction of sensitivity in one frequency range comes at the cost of an increase of sensitivity in another range.

For the controllable gas bearing, the disturbances $\mathbf{d}(s)$ may stem from the mass imbalance and general forces from mechanical shocks. The models and experimental results [31] show that the disturbance forces are strongly amplified in the frequency range of the low-damped natural frequencies, and it is of interest to attenuate these disturbances.

The transfer function from the disturbance $\mathbf{d}(s)$ to the output $\mathbf{y}(s)$ is

$$\begin{aligned}\mathbf{y}(s) &= \mathbf{S}_o\mathbf{G}_d\mathbf{d}(s) \\ &= (\mathbf{I} - \mathbf{G}\mathbf{K})^{-1}\,\mathbf{G}_d(s)\mathbf{d}(s)\end{aligned} \tag{3.13}$$

This rather simple analysis shows that the effects of the disturbances on the output are diminished by a controller $\mathbf{K}$ that obtains a low sensitivity ($|\mathbf{S}_o(j\omega)|$ low for frequencies ω near the natural frequencies). Similarly, high sensitivities imply a disturbance amplification, which should be avoided.

The proposed control designs have focussed on enhancing the damping properties. In Papers B, E and F we propose $\mathcal{H}_\infty$ controllers designed from the mixed sensitivity setup, where the sensitivity $\mathbf{S}$ is weighted by $\mathbf{W}_p$. The weight $\mathbf{W}_p$ has a high amplitude in the regions of the natural frequencies to ensure a low disturbance sensitivity. In Paper E we propose an LPV controller for the gas bearing for enhancing the damping of the parameter-varying gas bearing. The controller is synthesised with the gridding procedure. Experimentally collected closed loop results confirm a strong enhancement of damping and a reduction of the mass imbalance vibration amplitude.

In Paper F we explored the capabilities of such damping enhancing controllers and showed that they significantly increase the allowed angular velocity and allow safe operation in the regions of the two first critical speeds.

Previous works [105, 52, 53, 54] have proposed controllers to attenuate the mass imbalance by placing zeros on the closed loop sensitivity at the angular frequency. In Paper G we proposed such a gain-scheduled control design which also enhances the damping. Here, the damping was enhanced by weighting the transfer function from an input disturbance to the system output $\mathbf{S_o}(\mathbf{s})\mathbf{G}(\mathbf{s})$.

3.2.2 Induced Vibrations

Many bearing applications are subject to externally induced vibrations. The nature of these disturbances is wide-spread. The disturbances could be sinusoidal vibrations induced from mass imbalance of other rotating machines connected mechanically to

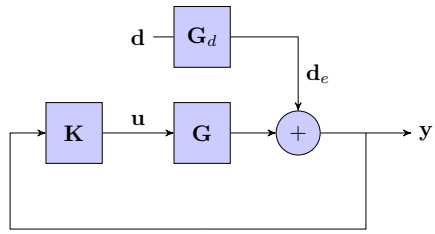

Figure 3.4: General Control diagram.

the rotating machine to be controlled. They may also stem from mechanical impacts with impulse or step-like nature in mobile applications (automotive, aeronautic or maritime). When the disturbances excite the system over a wide frequency range, they excite the under-damped natural frequencies of the rotating machine. Disturbances that periodically excite the system in these frequency ranges can cause catastrophically large amplifications.

3.2.3 Operating Mode and Parameter-Variations

Rotating machinery must be able to operate in different modes. During standard operation, the machine typically operates near a constant angular velocity and/or injection pressure. This operating condition is often not controlled and it may drift slowly. These parameter-variations change the gain and natural frequencies of the system. Bode diagrams of the gas bearing in Figure 3.5 characterise the effects of variation for the extrema of the open loop operating interval. Other modes are the transients during start-up, shut-down and set point changes. During these transients, the operating condition is increased or decreased from one set point to another.

These changes in operating condition change the dynamics and the equilibrium position of the rotor. The changes may cause the machine to operate in regions near the critical speeds.

A controller can then either be designed to work for a particular operating condition or for an interval of operating conditions. The early control designs in Papers A, C and D were designed for constant operating conditions without focus on robustness, and it was shown that the control performance deteriorated when the operating condition was changed. The control design in Paper B was proven robustly stable over an operating range. In the Paper F we used the controller to extend the operation interval of angular velocities of the gas bearing. Here, extrapolation of the

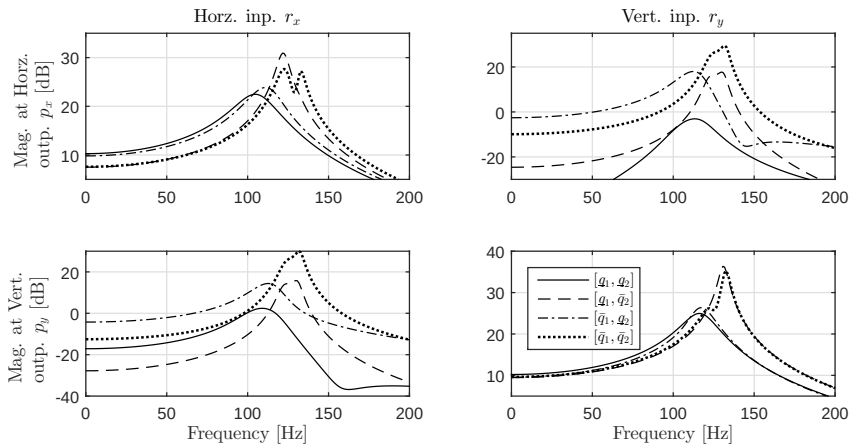

Figure 3.5: Bode diagrams of the gas bearing system for the scheduling parameter extrema.

LPV model predicted that the controller could operate safely in the regions of the mass imbalance. This prediction was validated experimentally.

3.2.4 Controllability and Observability Considerations

Placement of sensors and actuators is a challenge for rotating machinery with flexible rotors such as the controllable gas bearing test rig. If a sensor is placed in a node along the shaft for a given natural frequency, it becomes unobservable, similarly certain natural frequencies may become uncontrollable.

In the controllable gas bearing test rig considered, the position sensors are placed at the location of the disc, whereas it is critical to reduce the vibrations at the location of the gas bearing. A modeshape analysis shows that attenuation of vibrations at the disc corresponds to attenuation of vibrations at the bearing for the bending modes associated to the two first natural frequencies. This assumption has been validated from the experiments in Paper F, where the control reduced vibrations to allow crossing of and operation in the two first critical speeds. No sign of wear was found in subsequent analyses of the bearing surface. The topic of sensor and actuator placement has been treated in [32] and has not been investigated further in this project.

3.2.5 Equilibrium Position

The equilibrium position of the rotor is a function of the scheduling parameter. The measured disc position $\mathbf{p}$ can then be decomposed into a constant offset $\mathbf{p}_0$ and a time varying measurement $\delta\mathbf{p}$: $\mathbf{p}(t) = \mathbf{p}_0 + \delta\mathbf{p}(t)$. This offset is generally no problem for controllers that are to operate at a constant value of the scheduling parameter since the bias term $\mathbf{p}_0$ is easily estimated. It may become a challenge for controllers that are to operate at changing scheduling parameter values since the feedback control can change the equilibrium.

There are multiple controller strategies to tackle the parameter-varying bias term. When the scheduling parameter only varies little, the position offset can be estimated manually from offline data and subtracted online from the measurements to avoid a change of equilibrium position. This strategy was pursued in Papers A, B, C and D. Another solution is to design the controller with integral action to guarantee asymptotic regulation of the equilibrium position of the rotor. Such a solution usually comes at the cost of increased control complexity from an increase in controller order and from the implementation of an anti-windup scheme. The integral action comes at the cost of an increase in sensitivity in another frequency interval due to Bode's sensitivity integrals [104, 93]. A controller with integral action was proposed in Paper G, where the bandwidth of the integral action was chosen sufficiently low to avoid a significant sensitivity increase.

An alternative solution when the rotor equilibrium position is already far from the bearing is to design controllers with zero DC gain. Such a controller avoids to affect the rotor equilibrium position at the cost of poor disturbance rejection below a certain frequency.

In Paper F the controller was used to operate in the critical speed regions. Here, the rotor came close to the bearing housing due to the combination of changing equilibrium position and large amplitude vibrations. The rotor was moved away from the bearing housing by adding a bias signal to the control signal. This bias was chosen manually to steer the equilibrium position.

3.3 Examples of Damping Enhancing Control

This section shows a few control design results for damping enhancing control. First a short summary of the early results decentralised classical control designs, then the results obtained with modern control are summarised.

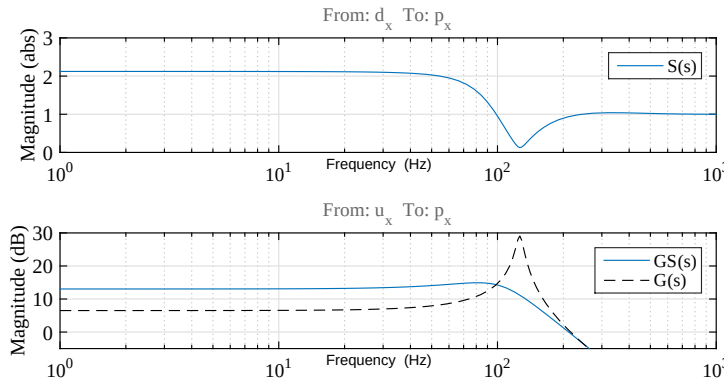

Figure 3.6: Sensitivity functions for the horizontal subsystem $\mathbf{S}_o = S(s)$, the system gain $G(s)$ and input disturbance gain $GS(s)$ using a proportional controller.

The early control designs we proposed for the gas bearing were classical decentralised proportional controllers. Model 2 was used for the control design for a constant scheduling parameter value. The cross couplings were assumed negligible, in which case the model reduces to two independent LTI models:

$$\mathbf{G} \approx \begin{bmatrix} G_{xx}(s) & 0 \\ 0 & G_{yy}(s) \end{bmatrix}, \tag{3.14}$$

in which $G_{xx}(s)$ represents the horizontal sub-system and $G_{yy}(s)$ represents the vertical one. Root locus analysis using the model showed that simple decentralised proportional control was able to critically damp the closed loop system. Such a controller was designed for both the horizontal and the vertical subsystem. The controller obtains a low output sensitivity near the natural frequencies as shown in Figure 3.6 and avoids high sensitivities in general. These controllers were implemented on the test rig. Experimentally collected closed loop impulse responses for varying proportional gains are shown in Figure 3.7. Comparisons with model simulations in Figure 3.8 validate that the experimental responses are in good agreement with the model predictions. These control designs are described further in Papers C and D. The root locus analysis further revealed that the critically damping controllers are very sensitive. A small change of the proportional control gain or a small modelling error of the static gain of the system significantly changes the damping factor in

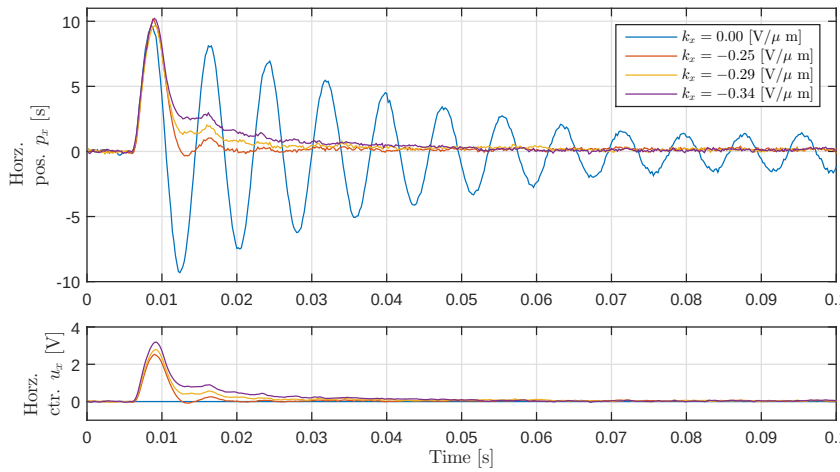

Figure 3.7: Horizontal impulse responses using proportional control. The controllers significantly enhance the damping.

these regions. The controllers are therefore not very robust towards changes in the scheduling parameter.

The Papers B, E and F focused on design of more robust damping enhancing controllers synthesised with robust control synthesis techniques. Here, the damping requirements were included in the mixed sensitivity setup [93] shown in Figure 3.9 where the $\mathcal{H}_\infty$ controllers were synthesised to minimise:

$$\mathbf{K}^* = \arg\min_{\mathbf{K}} \|\mathbf{N}\|_\infty, \quad \mathbf{N} = \begin{bmatrix} \mathbf{W}_p\mathbf{S} \\ \mathbf{W}_u\mathbf{K}\mathbf{S} \end{bmatrix}, \tag{3.15}$$

The damping was enhanced by choosing the performance weight $\mathbf{W}_p$ as inverse notch like filters. For the SISO case, the filter is $\mathbf{W}_p(s) = w_p(s)$ on the form:

$$w_p(s) = \frac{s^2 + 2\zeta_1\omega_p s + \omega_p^2 k_0}{s^2 + 2\zeta_2\omega_p s + \omega_p^2}, \tag{3.16}$$

The frequency of the notch ω_p is chosen as the under-damped natural frequencies of the gas bearing to obtain a high weight around these. The static gain filter is tuned by the constant k_0. The damping factors ζ_1 and ζ_2 are tuning parameters in the interval 0 to 1. The control sensitivity weight $\mathbf{W}_u$ is used to limit the control activity and is

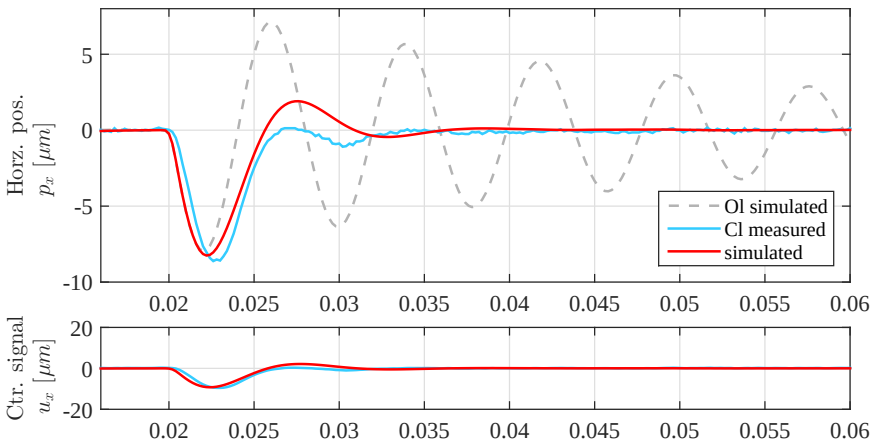

Figure 3.8: Impulse response of the model and measured impulse response for the horizontal shaft direction using proportional control.

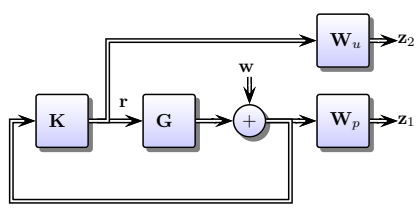

Figure 3.9: The augmented plant with controller for LPV controller design with performance weights $\mathbf{W}_p$ and controller sensitivity weight $\mathbf{W}_u$.

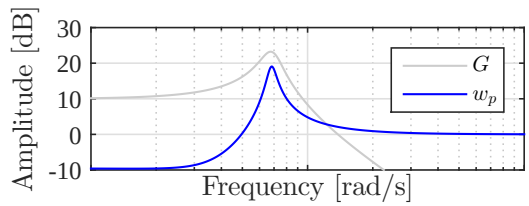

Figure 3.10: System gain and example of performance weight $w_p(s)$. The weight has a high amplitude near the resonance frequency of the system.

chosen as a first order high-pass filter from [93, Sec. 2, Eq. (2.72)]:

$$\mathbf{W}_u(s) = w_u(s), \quad w_u(s) = \frac{s/M_b + \omega_b}{s + \omega_b A_b}, \tag{3.17}$$

where the low frequency gain is $1/A_b$, the high frequency gain is $1/M_b$, and the approximate crossover frequency is ω_b.

An example of performance weight is shown in Figure 3.10.

The control design is proposed in Paper E, where further details are provided. Here, the controller was shown very robust towards variations in the scheduling parameters, and the damping enhancing controller provided a strong increase in damping of the closed loop system across the operating range and was shown to reduce the mass imbalance significantly. In the same paper, we proposed an extension of the design using the LPV system to obtain an LPV controller. The LPV controller was synthesised using the gridding approach [76] and is able to schedule the controller parameters according to the scheduling parameter values. Though not included in the paper, we also considered a proportional controller. The proportional controller was tuned to minimise the norm of impulse responses to achieve a dampening of the system. Impulse responses for the open loop and the closed loop system using different controllers are shown in Figure 3.11 for the scheduling parameter extrema. The open loop responses vary due to the difference in scheduling parameters. The proportional control is only able to increase the damping for some values of the scheduling parameter. The $\mathcal{H}_\infty$ controller enhances the damping well for the investigated scheduling parameter values, though the LPV controller provides the best damping enhancement across the scheduling parameter values.

In Paper F we further explored the capabilities of the proposed $\mathcal{H}_\infty$ controller

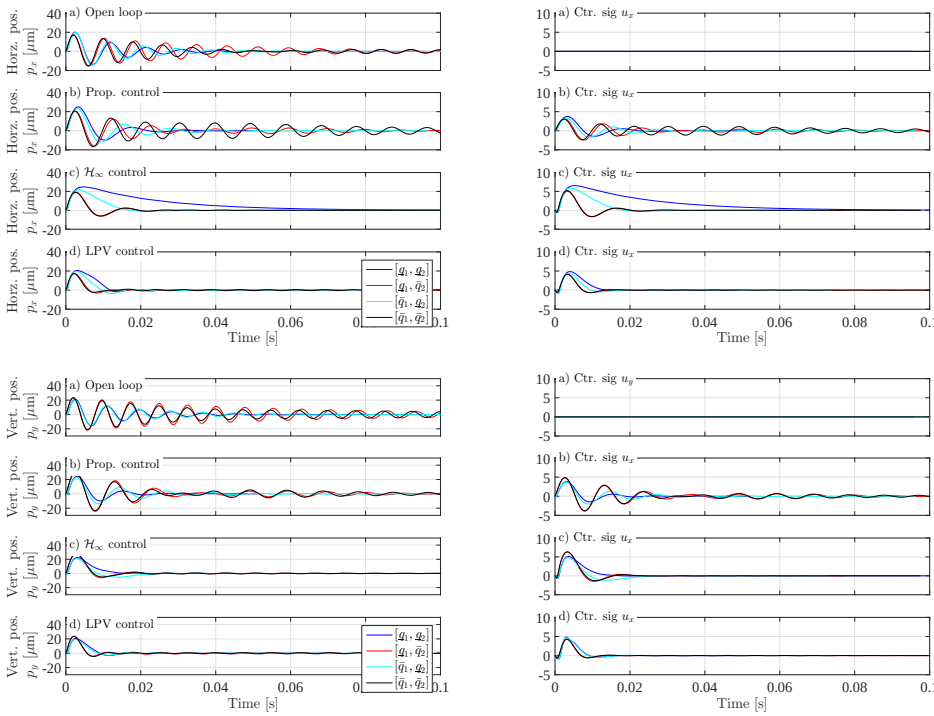

Figure 3.11: Simulated horizontal impact responses for the scheduling parameter extrema in the three cases: a) open loop, b) Proportional control, c) $\mathcal{H}_\infty$ control, d) LPV control. Figures to the right show corresponding control signals.

to extend the angular velocity range of safe operation. In these regions, open loop operation is not possible, and there was therefore no model available. The LPV model was therefore used in extrapolation beyond the range where it was expected to be valid. Such extrapolation provides no guarantees, but the resulting estimates of the expected vibration levels indicated the controller would allow significant extension. The experimental results confirmed that the controller reduced vibrations sufficiently to operate safely in the regions below, in, and above the two first critical speeds of the controllable gas bearing. A slow run-up of the open and closed loop system are shown Figure 3.12. The open loop experiment was stopped when the disc vibrations grew above a threshold to prevent damage to the test rig. The closed loop experiment was stopped when the actuators came close to saturation. The controller allowed a 70% increase of the angular velocity compared to open loop. Later simulations

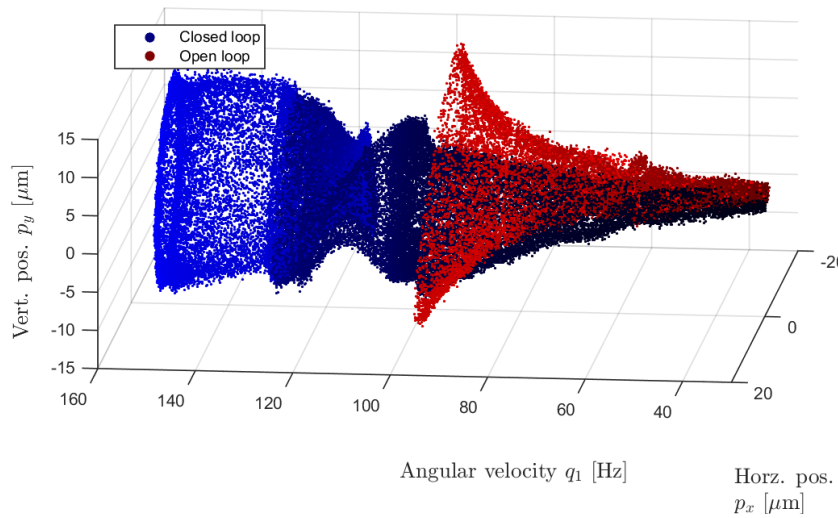

Figure 3.12: Slow run-up of the open and closed loop system with damping enhancing $\mathcal{H}_\infty$ controller. Around $94Hz$, the vibrations in the open loop case exceed the threshold for safe open loop operation. The controller allows significant extension of the interval of angular velocities where the machine can be operated.

indicate that it is possible to increase the angular velocity even further, since the actuator saturation should not cause instability.

Chapter 4

Conclusion

Controllable gas bearings with radial injection offer a very low rotor-bearing friction and a sufficient load carrying capacity. In their passive form, they suffer from poor damping properties. This project investigated the possibility of increasing the damping of controllable bearings using model-based control. A challenge in this regard is the design of control systems. High-speed rotating machines with flexible shaft and controllable journal bearings are complex systems, whose dynamics is generally modelled by means of partial differential equations naturally arising from the physics governing the system behaviour. Those models are not easily made suitable for the design of control systems, which is instead preferably based on low order models that capture the essential dynamics in focus of the control objectives. The project has demonstrated that low-order linear parameter-varying models are able to capture the dominant dynamics of a rotating machine with controllable journal bearings. The project has contributed with a linear parameter-varying (LPV) identification approach for rotating machinery. The project has shown fruitful results in using model-based control to enhance characteristics of the rotating machine:

- The experimental results from the active gas bearing test rig prove that the methods developed are easily applicable to rotating machines supported by controllable bearings. For design of feedback control, the proposed LPV identification approach bypasses the necessity of developing the complicated models derived from first principles and axioms of mechanics. The models were identified "in situ" without knowing the exact geometry of the machine to be modelled.

- The proposed LPV identification method relies on grey-box modelling and has

been used to successfully develop accurate linear models of an entire rotor-bearing-actuator-sensor system from experimental data. The identified models had a suitable complexity to capture the essential dynamics and to suit the subsequent control design.

- The models were formulated in state-space parametrisations that avoided over-parametrisation. Multiple local models could therefore be interpolated to derive LPV models. These LPV models described the behaviour of the rotor-bearing system over the desired operating range defined by the combination of injection pressure and angular velocity. The LPV model preserved important system characteristics in terms of eigenvalues, static gains and damping factors.

- A novel application of the runout filter was shown to improve the quality of the position measurements by filtering out mass unbalance and runout to allow micrometer precision measurement of the active response to improve the identification.

Several model-based controllers have been designed from the developed LPV models to improve the dynamics of the controllable gas bearing. Experimental closed loop results with the proposed control designs confirmed that the models are well able to predict the closed loop behaviour of the controllable gas bearing. The model-based control designs included:

- **Classical controllers designed from root loci**. The proportional controllers were able to critically damp the two first natural frequencies of the gas bearing.

- **LPV and $\mathcal{H}_\infty$ control**. The LPV and $\mathcal{H}_\infty$ controllers were designed with the mixed sensitivity setup, where a suitable choice of weights was shown to provide the desired level of damping, and shown to perform well over a desired operating range. The project has showed that damping enhancing $\mathcal{H}_\infty$ controllers could extend the operating range of angular velocity by 70% at the investigated injection pressure. The machine could therefore operate safely in and above the regions of the two first critical speeds.

- **Gain-scheduled $\mathcal{H}_2$ control** A gain-scheduling approach was proposed using state-space interpolation of local $\mathcal{H}_2$ controllers. The method was shown to avoid the increase of state-space order and preserve a high performance in the interpolation region for mass imbalance rejection for controllable gas bearings. A suitable choice of state-space representation allowed synthesising

$\mathcal{H}_2$ controllers whose parameters developed continuously in the scheduling parameter to allow interpolation.

4.1 Future Perspectives

- **Further increase of angular velocity** The project has proven that it was possible to significantly increase the angular velocity. It is of interest to increase it even further to allow operation in the range where the gas bearing becomes open loop unstable. In this regard it will be necessary to further investigate sub-synchronous whirl and instability

- **Sub-synchronous whirl and instability** For higher angular velocities Ω, the shaft begins to whirl with a frequency of approximately 0.42Ω. These oscillations are denoted as sub-synchronous whirl and are known to set on when the angular velocity approaches the double of the first critical speed. For an even further increase of the angular velocity, the rotor-bearing dynamics becomes unstable. Postponing the onset of whirl and instability is of major interest to further extend the range of safe operation. The non-linear whirl oscillations require further modelling to understand the phenomenon. The proposed controllers are expected to work well since they obtain a low sensitivity in the frequency range of the whirl oscillations. Further experimental investigations are needed.

- **Modelling** The modelling of controllable journal bearings is still a field with challenges to be solved. The proposed LPV identification is only able to model the system for slow time-variation of the parameters. The global identification approaches currently require too large amounts of data.

- **Control** This thesis has investigated a few model-based control designs. The grey-box models developed provide a strong foundation for future testing of the vast literature of control. Our initial investigations in Paper F allowed a safe crossing of and operation in the two first critical speeds. The test rig has been further developed in the mean time and controller is expected to allow an even further increase of the angular velocity.

- **LPV control** The methods for synthesising LPV controllers still suffers from challenges with numerical conditioning and the guaranteed performance is

lost with the gridded design procedure. Further development of the synthesis methods is required to overcome these limitations.

- **Grey-box identification of other bearings** The grey-box models and control designs proposed have potentials to also be used for other controllable bearings. Controllable bearings lubricated with oil [106] have similar challenges for modelling and they are subject to similar parameter-variations with oil injection pressure, angular velocity and temperature. Similarly controllable foil bearing designs are emerging where piezoactuators can change the geometrical shape of the foils.

- **Test rig sensitivity** It is currently difficult to ensure the test rig is reassembled in the exact same manner after maintenance disassembly. Small changes in gains and natural frequencies are observed after those dis-assemblies and reassemblies. The mechanical re-design of the test rig is beyond the scope of this thesis. Instead the model has been re-identified after these reassemblies. This sensitivity is probably a consequence of the low tolerances, and is a topic to be addressed in the further development.

- **Improving the state-space interpolation** The proposed state-space interpolation seeks to minimise the norm between the model parameters of the local models and the LPV model. An alternative approach that could improve the modelling, it may be possible to obtain better LPV models by minimising the norm of the frequency responses or time response of the difference between the local models and the LPV model evaluated in the corresponding scheduling parameters.

- **Parameter sensitivity for discrete time LPV** For LPV identification of discrete time models, we have generally observed a high "numerical sensitivity", in the sense that a small error in a parameter estimate significantly changes the input-output behaviour of the system. This numerical sensitivity might in particular be a challenge for systems sampled with high frequency. This phenomenon requires further research.

Appendix A

Experimental Grey Box Model Identification and Control of an Active Gas Bearing

From: Vibration Engineering and Technology of Machinery. Ed. by J. Sinha. Springer, 2014
The paper has been reformatted to for the thesis.
Lukas Roy Svane Theisen*[1], Fabián G. Pierart[2],
Henrik H. Niemann[1], Ilmar F. Santos[2] , Mogens Blanke[1]

[1]Dept. of Electrical Engineering and [2]Dept. of Mechanical Engineering
Technical University of Denmark, DK 2800 Kgs. Lyngby, Denmark
Email: Email: lrst@elektro.dtu.dk, fpvas@mek.dtu.dk, hhn@elektro.dtu.dk, ifs@mek.dtu.dk, mb@elektro.dtu.dk

Abstract:
Gas bearings have inherent dynamics that gives rise to low damping and potential instability at certain rotational speeds. Required damping and stabilization properties can be achieved by active flow control if bearing parameters are known. This paper deals with identification of parameters in a dynamic model of an active gas bearing and subsequent control loop design. A grey box model is determined based on experiments where piezo actuated valves are used to perturb the journal and hence excite the rotor-bearing system. Such modelling from actuator to output is shown to efficiently support controller design, in contrast to impact models that focus on resonance dynamics. The identified model is able to accurately reproduce the lateral dynamics of the rotor-bearing system in a desired operating range, in this case around the first two natural frequencies. The identified models are validated and used to design a model-based controller capable of improving the damping of the gas bearing. Experimental impact responses show an increase in damping by a factor nine for the investigated conditions.

Key words: System Identification, Active Gas Bearings, Experimental Techniques, Modelling, Rotordynamics.

A.1 Introduction

Passive and active gas bearings are receiving growing attention for their high speed operation capabilities. Passive gas bearings offer advantages of high speed operation, low friction, and clean and abundant air as lubricant; however they suffer from low damping and vibration instabilities [34, 35, 78].

There are two main approaches to increase damping and stability; one is through foil bearings [17, 13, 107, 108, 14, 15] that rely on friction between bumps and foil. Such a solution is relatively cheap, but the friction coefficient is a design challenge [17]. The other approach is via mechatronic solutions, which offer robustness and adaptability. Actively controlled gas bearings using piezo actuation [78] and active inherent restrictors [28, 29] is a promising mechatronic machine element approach to support clean and high speed solutions. An example of adjustable hybrid lubrication given in [109], proposes a rule based control strategy, where changing conditions caused changed critical speeds, which allowed them to cross the first critical speed. The design of model based controllers for gas bearings requires models that catch the dynamic behavior of the journal in the frequency range where control is needed. A model for control design should in a sufficiently simple manner describe the relation from piezo actuator electrical input to journal position.

The design of actively lubricated gas bearings relies on usage of the Reynolds equation, which models the behaviour of the compressible lubricant between the journal and the housing. The rotating journal in the gas bearing is then modelled as a mass subject to the force from the compressed air in the bearing. The Reynolds equation is solved to obtain a pressure distribution, which is integrated to obtain the aerodynamic forces. An input-output-model (IO model) was developed in [41] using a first order principles model to incorporate the behaviour of the piezo-electric valves into the Reynolds equation. This model catches well the behaviour of the bearing over a wide range of parameters but has too high complexity to be directly used for model based control. Another common approach is using a 2 DOF coupled mass-spring-damper system where parameters are experimentally identified from impacts. This model however does not properly describe the interaction of the pressurized air actively lubricating the journal, which is required for a model based controller

design.

The present contribution adopts a systematic data based method for modelling of a gas bearing with external inputs and identifies low-order dynamical models that are shown to be adequate for model based controller design. The models are shown to describe the behaviour of the rotor-gas bearing system with high accuracy.

The paper is structured as follows; A brief description of the controllable gas bearing setup is first described. Section A.3 presents the grey box model chosen and identification of its parameters is carried out based on experiments that cover the operational range of the bearing. The identified models are used for design of a model based controller to enhance damping properties. Special techniques to handle actuator hysteresis is discussed. Finally, an experimental characterization is done of the piezo actuated valves and the high closed loop damping is validated.

A.2 Experimental Setup of Gas Bearing

The experimental setup at hand is shown in Fig. A.1: A flexible journal (a) is supported by both a ball bearing (d) and the controllable gas bearing (b). A disc (c) is mounted in one end to preload the journal. The horizontal and vertical journal positions (ϵ_x, ϵ_y) are measured at the disc location $(\cdot)_d$ using eddy current sensors (e). Disc deflections $(\cdot)_d$ are easily mapped to bearing deflections $(\cdot)_b$ under assumption of a rigid shaft, and the transformation then reads $\epsilon_{xb} = \kappa\epsilon_{xd}$, in which $\kappa = 0.625[m/m]$ is the fractional position of the gas bearing along the length of the journal relative to the disc. The angular position of the journal ϕ is measured by an optical encoder. A more thorough description of the setup is available in [78].

The gas bearing is controllable by injection of pressurized air through the opening and closing of four piezo actuated valves positioned as shown in Fig. A.1. Each valve is controlled by a voltage $u_{p,i} \in [u_{p,min};\ u_{p,max}],\ i \in \{1, 2, 3, 4\}$, with limits $u_{p,min} = 0\ V, u_{p,max} = 10\ V$, where $u_{p,min}$ corresponds to a fully opened valve and $u_{p,max}$ fully closed. The position of the valves is measurable in the interval $y_{p,i} \in [y_{p,min};\ y_{p,max}] = [0;\ 10]\ V,\ i \in \{1, 2, 3, 4\}$, and the expansion of the piezo actuator is proportional to the measured position with maximum expansion at $u_{p,max}$ is $y_{max} = 45\ \mu m$ which is approximately $10\ V$, but it is not known exactly. Hence all piezo positions are listed in Volts. Piezo ceramics are subject to nonlinearities in form of hysteresis [110], which gives a nonlinear input output relationship. This nonlinearity is addressed in Sec. A.4.1.

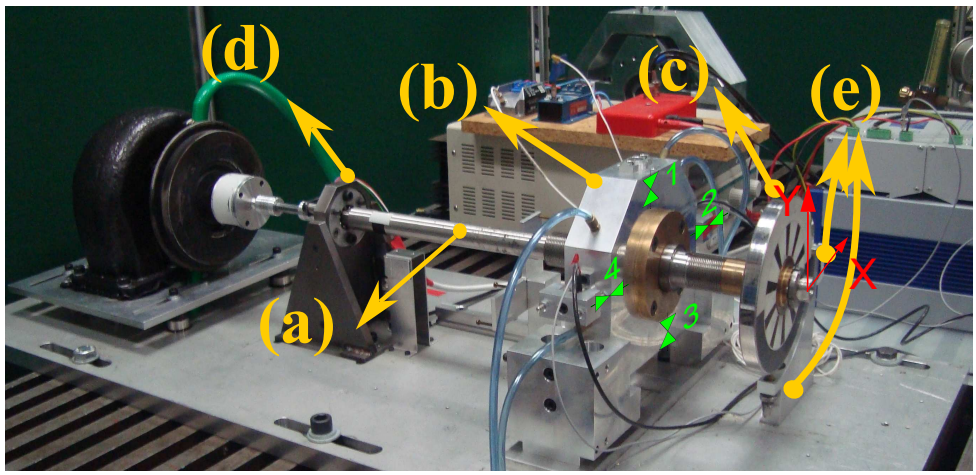

Figure A.1: The experimental bearing setup. A flexible shaft (a) is supported by both a ball bearing (d) and the controllable gas bearing (b) with four piezo actuated valves. A disc (c) is mounted in one end to preload the journal and displacement sensors (e) measure the lateral movement of the disc.

A.3 Experimental Identification of Gas Bearing Parameters

Modelling of controllable gas bearings still represents an open challenge. The approach pursued in this work is to some extent considered model free, as the developed models are found experimentally based on excitation of the rotor-gas bearing system by changing valve positions thereby perturbing the fluid film. A model is assumed with known structure, though unknown parameters. Identification of the parameters is then sought through grey box modelling. Standard means of model validation (sign test, residual analysis) are then used to assess over/ under parametrization of the model. The identified linear rotor-gas bearing models are found to have speed dependent parameters, hence polynomials parametrized in speed are fitted to allow a speed dependent model to be stated describing the gas bearing with the range of interest.
A common approach for modelling gas bearings is the linear mass-spring-damper-model. Using positions $p = [\epsilon_x, \epsilon_y]^{\mathrm{T}}$, with respective time derivatives $\frac{d}{dt}(\cdot) = \dot{(\cdot)}$

$$\mathcal{M}\ddot{p}(t) + (\mathcal{D} + \Omega\mathcal{G})\dot{p}(t) + \mathcal{K}\, p(t) = f(t), \quad p = [\epsilon_x, \epsilon_y]^{\mathrm{T}} \tag{A.1}$$

Mass Matrix	Stiffness matrix	Damping Matrix
$\mathcal{M} = \begin{bmatrix} m & 0 \\ 0 & m \end{bmatrix}$	$\mathcal{K} = \begin{bmatrix} k_{xx} & k_{xy} \\ k_{yx} & k_{yy} \end{bmatrix}$	$\mathcal{D} = \begin{bmatrix} d_{xx} & d_{xy} \\ d_{yx} & d_{yy} \end{bmatrix}$
	Input gain	Gyroscopic
$\mathcal{B}_d = \begin{bmatrix} b_{d,xx} & b_{d,xy} \\ b_{d,yx} & b_{d,yy} \end{bmatrix}$	$\mathcal{B}_p = \begin{bmatrix} b_{xx} & b_{xy} \\ b_{yx} & b_{yy} \end{bmatrix}$	$\mathcal{G} = \begin{bmatrix} 0 & g_{xy} \\ -g_{xy} & 0 \end{bmatrix}$

Table A.1: Structure of system matrices.

where $f(t)$ is the force, Ω is the rotation speed and the matrices have structures as listed in Tab. A.1. This models the gas bearing behaviour in a neighbourhood of the 1st and 2nd critical speeds and suggests a model structure.

The force $f(t)$ is the sum of external forces from disturbances, residual mass unbalance $f_u(t)$ and forces from the piezo actuators $f_p(t)$.

The modelling of equivalent applied force from the piezo valves is no trivial task. An approach presented in [41] uses a nonlinear state space model with states being position, and velocity of the piezo ceramic, and pressure in the chamber between the journal and bearing housing. The mentioned model however contains a coupling to the pressure of the lubricant, which in this case is not measured, making it challenging to use. Instead the approach pursued in the present work is taken from electromagnetically actuated bearings, in which opposing actuators are coupled pairwise (i.e. valves $\{1, 3\}, \{2, 4\}$ move oppositely). The gain from this approach is twofold: The coupled valves counteract possible nonlinear gains, and transforms the system from an overactuated (more control inputs than controlled outputs) to a fully actuated (equal number of control inputs and controlled outputs).
Due to piezo valves hysteresis which is shown later in Sec.A.4.1 to be approximately 15%, the valve input voltage is not suitable input for identification of linear models. Instead the piezo valve positions are used as model inputs for identification; more precisely the IO model input vector is chosen to be the difference of horizontal and vertical valve positions:

$$u(t) \triangleq [u_x(t), u_y(t)]^{\mathrm{T}} = [y_{p,2}(t) - y_{p,4}(t), y_{p,1}(t) - y_{p,3}(t)]^{\mathrm{T}} \tag{A.2}$$

The equivalent force acting on the journal is assumed linear i.e. $f_p(t) = \mathcal{B}_p u(t)$, where the structure of the input gain $\mathcal{B}_p$ is listed in Tab. A.1.
Considering only the active forces $f(t) = f_p(t)$, and reformulating to a unit mass

equation, the model reads:

$$\ddot{p}(t) + D\dot{p}(t) + Kp(t) = Bu(t) \tag{A.3}$$

where $D \triangleq \mathcal{M}^{-1}(\mathcal{D} + \Omega\mathcal{G})$, $K \triangleq \mathcal{M}^{-1}\mathcal{K}$, and $B \triangleq \mathcal{M}^{-1}\mathcal{B}_p$. Since a model structure is known (though the parameters are not), identification of the rotor bearing system parameters is sought through grey box modelling, which (using a suitable model structure and given reasonable initial parameter estimates) catches well both the stationary and dynamical behaviour of the bearing. The grey box modelling is eased by reformulation of the dynamics Eq.(A.3) to state space form, where a suitable choice of states is $x = [\epsilon_x, \epsilon_y, \dot{\epsilon}_x, \dot{\epsilon}_y]^{\mathrm{T}}$. The measurement noise and errors from simplified model are modelled as additive noise $d(t)$ entering both output and states with a disturbance input gain $\mathcal{B}_d$ and the chosen state space formulation of Eq. (A.1) then reads:

$$\begin{aligned} \dot{x}(t) &= \mathcal{A}x(t) + \mathcal{B}u(t) + \mathcal{B}_d d(t), \quad x(0) = x_0 \\ p(t) &= \mathcal{C}x(t) + d(t) \end{aligned} \tag{A.4}$$

where the system-, input gain-, and output matrix are

$$\mathcal{A} = \begin{bmatrix} 0 & I \\ -K & -D \end{bmatrix}, \quad \mathcal{B} = \begin{bmatrix} 0 \\ B \end{bmatrix}, \quad \mathcal{B}_d = \begin{bmatrix} 0 \\ B_d \end{bmatrix}, \quad \mathcal{C} = \begin{bmatrix} I & 0 \end{bmatrix}, \tag{A.5}$$

where in the above the matrices to be identified are $\hat{K}$, $\hat{D}$, and $\hat{B}$, $\hat{B}_d$ $\hat{x}_0$ with structure as listed in Tab. A.1.

The parameters of (A.5) are identified by recasting the problem to a model parametrized in $\hat{\theta} \triangleq \{\hat{D}, \hat{K}, \hat{B}, \hat{x}_0, \hat{B}_d\}$ as $\mathfrak{M}(\theta)$, where the parameters to be identified are:

$$\hat{\mathcal{A}}(\theta) = \begin{bmatrix} 0 & 0 & 1 & 0 \\ 0 & 0 & 0 & 1 \\ -\hat{K}_{xx} & -\hat{K}_{xy} & -\hat{D}_{xx} & -\hat{D}_{xy} \\ -\hat{K}_{yx} & -\hat{K}_{yy} & -\hat{D}_{yx} & -\hat{D}_{yy} \end{bmatrix}, \quad \hat{\mathcal{B}}(\theta) = \begin{bmatrix} 0 & 0 \\ 0 & 0 \\ \hat{B}_{xx} & \hat{B}_{xy} \\ \hat{B}_{yx} & \hat{B}_{yy} \end{bmatrix}, \tag{A.6}$$

$$\hat{\mathcal{B}}_d(\theta) = \begin{bmatrix} 0 & 0 \\ 0 & 0 \\ \hat{B}_{d,xx} & \hat{B}_{d,xy} \\ \hat{B}_{d,yx} & \hat{B}_{d,yy} \end{bmatrix}, \quad \mathcal{C} = \begin{bmatrix} 1 & 0 & 0 & 0 \\ 0 & 1 & 0 & 0 \end{bmatrix}, \quad x(0) = \hat{x}_0(\theta) \tag{A.7}$$

The model then reads

$$\mathfrak{M}(\theta) : \begin{cases} \dot{x}(t) = \hat{\mathcal{A}}(\theta)x(t) + \hat{\mathcal{B}}(\theta)u(t) + \hat{\mathcal{B}}_d(\theta)d(t), \quad \hat{x}(0) = \hat{x}_0(\theta) \\ p(t) = Cx(t) + d(t) \end{cases} \tag{A.8}$$

A.3.1 Description of Experiments

The choice of input signal for system identification is an open challenge, but should certainly excite the system dynamics sufficiently in the frequency range of interest, i.e. up to 200 Hz covering the first two natural frequencies. For identification of the above model, control signals are designed manually to excite simultaneously both the horizontal and vertical lateral rotor dynamics. Such input sequences are applied to the bearing, during 15 data sequences of $10s$ duration, with four different journal rotational velocities in the interval $[2.9; 6.0]krpm$. During the experiments the gas injection pressure is kept constant at $P_{inj} = 8.0bar$ and sampling is made with $f_s = 5kHz$. The horizontal and vertical valves are excited horizontally by a square input signal, while the vertical dynamics are excited by pseudo-random stepwise motion. Figure A.2 shows measured input and output sequence of one of the 15 experiments.

A.3.2 Prefiltering

Before system identification, the measured journal positions are preprocessed (filtered) in two steps: First step is to remove the stationary run-out and mass unbalance response. For this purpose a 10s data sequence is collected without any system excitation. This allows generation of a compensator function $\mathcal{F}(\phi)$ mapping positions as a function of encoder angle ϕ. The direct measurement $(\cdot)_r$ can then be converted to smoothed position $(\cdot)_s$ using the filtering $(\cdot)_s = (\cdot)_r - \mathcal{F}(\phi)$. The filtered positions can then be seen as deviations from the mass unbalance response. Second step consists of a low pass filtering is applied using a second order Butterworth filter, with cutoff frequency $f_0 = 1000Hz$ being approximately five times faster than the bearing poles to be identified.

A.3.3 Parameter Identification using Prediction Error Method

The optimal model $\mathfrak{M}(\theta^\star)$ is chosen as the minimum of the cost function $W(\theta) \triangleq \sum_{t=1}^{N} e(t)^{\mathrm{T}} e(t)$, where the prediction error e is defined as the difference between the measured and the estimated output $e(t) \triangleq y(t) - \hat{y}(t)$. The minimum is sought using the prediction error method (PEM) [45], such that the optimal parameter set reads:

$$\theta^\star = \min_{\theta} W(\theta) \tag{A.9}$$

The optimization is nonlinear and to ensure convergence to the optimal parameter set, good initial parameter estimates are required for $\hat{K}_{xx}, \hat{K}_{yy}, \hat{D}_{xx}, \hat{D}_{yy}, \hat{B}_{xx}, \hat{B}_{yy}$.

These initial estimates are found as preidentified parameters describing the horizontal and vertical dynamics as 1-DOF mass-spring-damper systems individually. The estimates for all parameters (incl. the cross coupling gains) are then iteratively refined and identification is terminated when the improvement of error norm is less than bound $Q = 0.01$ indicating the optimization has reached a minimum. Figure A.3 shows the identified equivalents of stiffness, damping and input gains for each of the 15 data sets along with a function fitted to the estimates. The identified parameters are very consistent for measurements made at the same rotational speed.

Figure A.2 shows that the linear models, to a very high extent, catch the behaviour of the journal. A sign test is performed to assess over parametrization of the model. This test proves that identified parameters within 1 standard deviation σ of the estimate $\pm 1\sigma$ are sign consistent (i.e. 0 is not in the interval, and the parameter estimate is therefore sign consistent). Analysis of the residuals between the measurements and the identified model $\varepsilon \triangleq y - \hat{y}$ shown in Fig. A.2 shows the residuals are not white noise as they should optimally be, and indicates presence of nonlinearities or higher order dynamics not caught by the linear model. The residual however is bounded by $|\varepsilon| \leq 1.4\ \mu m$, which indicates low magnitude of the neglected dynamics. Higher operation speeds will most likely require higher order models, though for the considered operation range the identified models are deemed sufficient.

The identified parameters $\hat{D}, \hat{K}, \hat{B}$ are used to fit speed varying quadratic polynomials to parameters $(\cdot)_{jk}$ of the form:

$$(\cdot)_{jk}(\Omega) = \alpha_{(\cdot),jk}\Omega^2 + \beta_{(\cdot),jk}\Omega + \gamma_{(\cdot),jk}, \tag{A.10}$$

with coefficients as listed in tab. A.3. The identified equivalent model then reads:

$$\begin{bmatrix} 1 & 0 \\ 0 & 1 \end{bmatrix} \begin{bmatrix} \ddot{\epsilon}_x(t) \\ \ddot{\epsilon}_y(t) \end{bmatrix} + \begin{bmatrix} \hat{D}_{xx}(\Omega) & \hat{D}_{xy}(\Omega) \\ \hat{D}_{yx}(\Omega) & \hat{D}_{yy}(\Omega) \end{bmatrix} \begin{bmatrix} \dot{\epsilon}_x(t) \\ \dot{\epsilon}_y(t) \end{bmatrix} + \begin{bmatrix} \hat{K}_{xx}(\Omega) & \hat{K}_{xy}(\Omega) \\ \hat{K}_{yx}(\Omega) & \hat{K}_{yy}(\Omega) \end{bmatrix} \begin{bmatrix} \epsilon_x(t) \\ \epsilon_y(t) \end{bmatrix} = \begin{bmatrix} \hat{B}_{xx}(\Omega) & \hat{B}_{xy}(\Omega) \\ \hat{B}_{yx}(\Omega) & \hat{B}_{yy}(\Omega) \end{bmatrix} \begin{bmatrix} u_x(t) \\ u_y(t) \end{bmatrix} \tag{A.11}$$

From each experiment, an estimate of the first and second critical speeds are directly calculable from the identified parameters as the system poles (the eigenvalues of $A(\theta)$). Figure A.4 shows the obtained estimates of the two complex pole pairs $p_{1,2}, p_{3,4}$ listed in the form $p_{1,2} = -\omega_{1,2}\left(\zeta_{1,2} \pm j\sqrt{\zeta_{1,2}^2 - 1}\right)$, having natural frequencies ω and damping factors ζ. The standard deviation of estimate of natural frequencies are $\sigma_{\omega,1,2} = 1.22\ Hz$, $\sigma_{\omega,3,4} = 0.51\ Hz$, and of damping factors $\sigma_{\zeta,1} = 2.8 \cdot 10^{-3}[-]$, $\sigma_{\zeta,3} = 5.1 \cdot 10^{-3}[-]$.

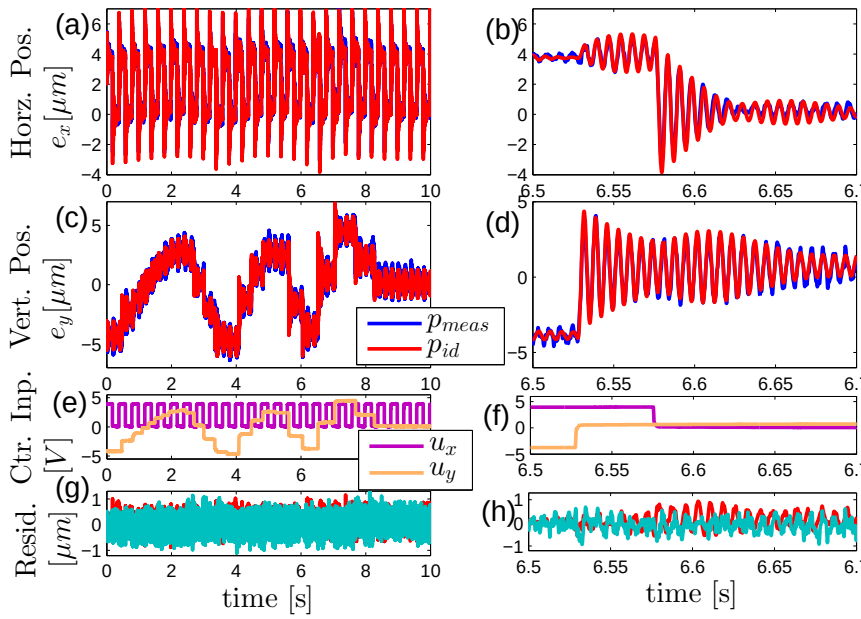

Figure A.2: (a),(c) and (b),(d) show an entire sequence and a time zoom of preprocessed measured and identified lateral journal positions $p_{meas} = [\epsilon_x, \epsilon_y]$, $p_{id} = [\hat{\epsilon}_x, \hat{\epsilon}_y]$ used for system identification, excited by the valve positions u_x, u_y shown in (e) and (d). (g) and (h) show the residual $e = p_{meas} - p_{id}$.

The identified parameters are shown for a unit mass bearing, but could be converted to real stiffness, damping and input gains on the assumption that the known mass of the journal m is equal to the equivalent mass.

A.4 Observer Based Controller Design

The undesirably low damping characteristics of the gas bearing can be addressed by model based control. This section shows design of a discrete time state feedback controller designed to increase closed loop damping of the gas bearing. The controller is to be implemented on a computer, hence the identified dynamics Eq. A.4 from an experiment at $6.0\ krpm$ are converted to discrete time using zero order hold with sampling time $T_s = 0.2ms$ to obtain the discrete time system, sampled at $x_k \triangleq x(kT_s)$

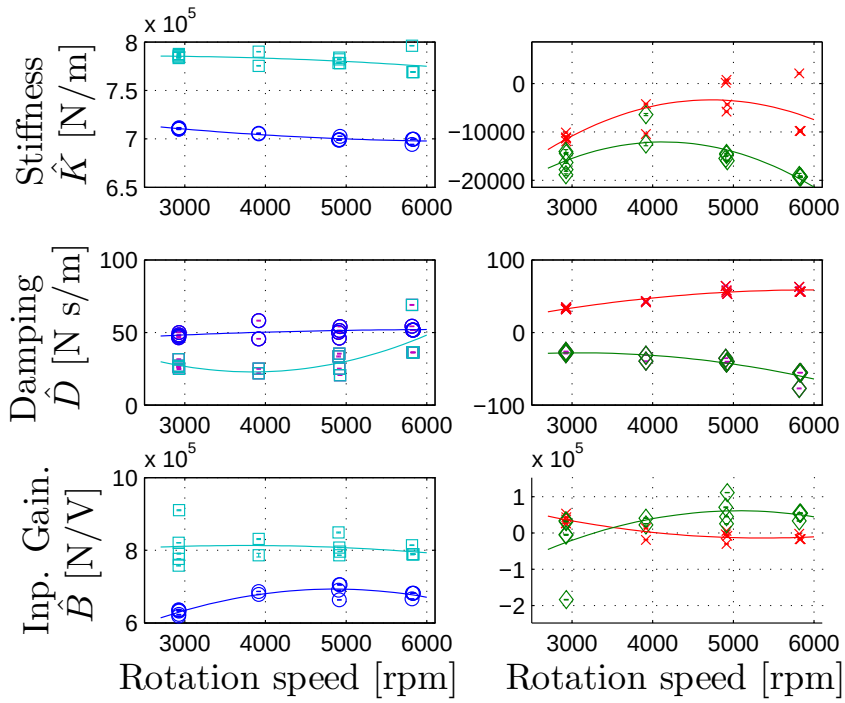

Figure A.3: Identified equivalent stiffness $\hat{K}$: $\{\hat{k}_{xx}, \hat{k}_{xy}, \hat{k}_{yx}, \hat{k}_{yy}\}$,damping $\hat{C}$: $\{\hat{c}_{xx}, \hat{c}_{xy}, \hat{c}_{yx}, \hat{c}_{yy}\}$, and input gain $\hat{B}$: $\{\hat{b}_{xx}, \hat{b}_{xy}, \hat{b}_{yx}, \hat{b}_{yy}\}$. $\circ$ $(\hat{\cdot})_{xx}$ $\diamond$ $(\hat{\cdot})_{xy}$ $\times$ $(\hat{\cdot})_{yx}$, $\square$ $(\hat{\cdot})_{yy}$. Identified equivalents are shown for a unit mass. Speed varying quadratic polynomials (solid lines) have been fitted to measurements.

:

$$\begin{aligned} x_{k+1} &= Fx_k + Gu_k + G_d d_k \\ y_k &= Cx_k + d_k, \end{aligned} \tag{A.12}$$

where the discrete time system matrices F, G are listed in Tab. A.2. Increasing the damping is pursued using a pole placement controller, which requires state feedback. Alternatively an LQR or other optimal controller could have been used. Since only position is measured, a discrete time full order observer is designed to estimate the states $\hat{x}$ given the control input u_k and the position measurement p_k. Designing the state feedback gain K_{sb} and the observer gain L can be done independently. The latter is chosen to have sufficiently fast observer poles.

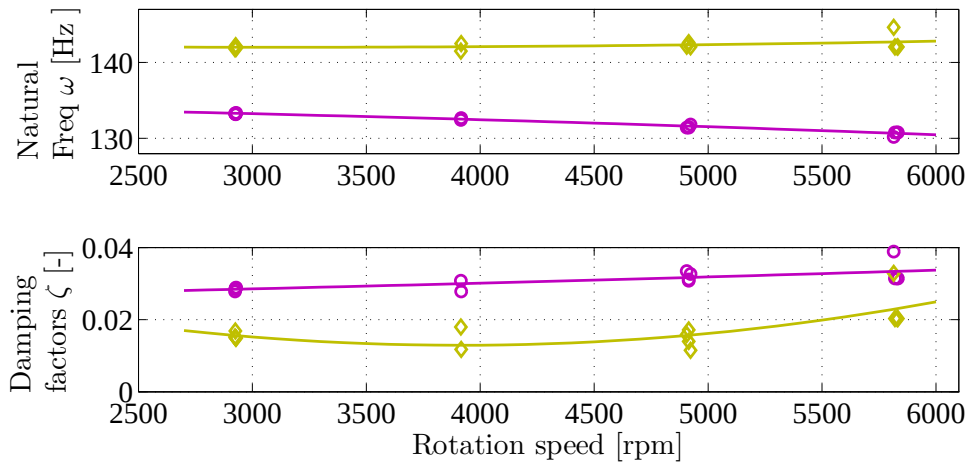

Figure A.4: Identified natural frequencies ○ $\omega_{1,2}$, ◇ $\omega_{3,4}$ (1st and 2nd critical speeds) and associated damping factors $\zeta_{1,2}, \zeta_{3,4}$. Speed varying quadratic polynomials (solid lines) have been fitted to measurements.

The state feedback gain K_{sb} is designed by pole placement [111] to increase the damping of the closed loop system by placing the discrete time closed loop poles $p_{d,cl}$ related to the discrete time open loop poles $p_{d,ol}$ according to $p_{d,cl} = Re(p_{d,cl}) + j\frac{1}{2}Im(p_{d,cl})$. This ensures a decent increase of damping. The control law then reads:

$$u_{f,k} = -K_{sb}\,\hat{x}_{k|k} \tag{A.13}$$

A.4.1 Experimental Piezo Actuator Characterization

The piezo ceramic hysteresis poses a challenge in controller design. A characterization of the hysteresis is developed by applying a stairwise increasing and then decreasing input voltage to a piezo valve. Figure A.6 shows measured equilibrium positions as function of applied input voltage. Unfortunately the position exceeds the saturation limit of the measurement equipment ($10V$), thus some of the hysteresis curve cannot be recovered. It is evident though, that the equilibrium position can change $\approx 15\%$ due to the hysteresis. Seeking to counteract valve hysteresis and increase performance, local PD controllers are designed with discrete time gains $K_P = 18.2[V/V], K_D = -0.187[Vs/V]$. The valve positions are controlled towards

reference positions $r_{p,i}$. Applying a similar staircase input as position reference to the controlled valve, the equilibrium positions from Fig. A.6 are obtained. The PD control both counteracts the hysteresis and gives a desirable valve DC-gain close to unity. For control purposes, the PD controlled valves also make it reasonable to neglect valve dynamics. A block diagram of the closed loop system is shown in Fig. A.5.

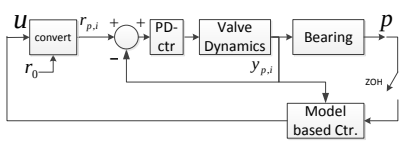

Figure A.5: Block diagram of the closed loop system.

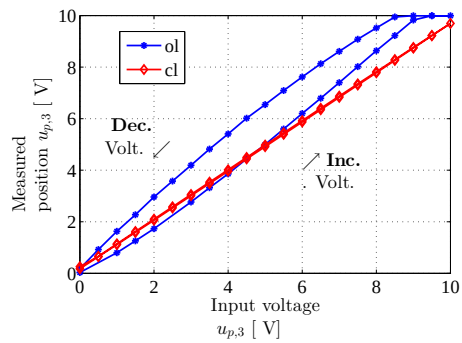

Figure A.6: Hysteresis plot of meas. valve pos. $y_{p,3}$ vs inp. voltage in open loop (ol) $u_{p,3}$, and PD-contr. closed loop reference $r_{p,3}$ (cl).

A.4.2 Experimental Impact Response using Damping Increasing Controller

The designed controller is implemented and an impulse impact is applied both to the controlled and uncontrolled gas bearing. Figure A.7 shows the comparison of the open and closed loop system subject to manually induced impulse impacts with the journal rotating at $\Omega_t = 4.1\ krpm$. The position measurements have been post-filtered to remove stationary run-out and mass unbalance response to allow visualization of the impact response, hence the control input variation. Quantitatively the response magnitudes are not directly comparable as the impacts were forced manually, but qualitatively the increased damping is certainly clear. The logarithmic decrement method gives from $\epsilon_y(t)$ the damping to be increased from 0.0159 to 0.139 - almost a factor nine.

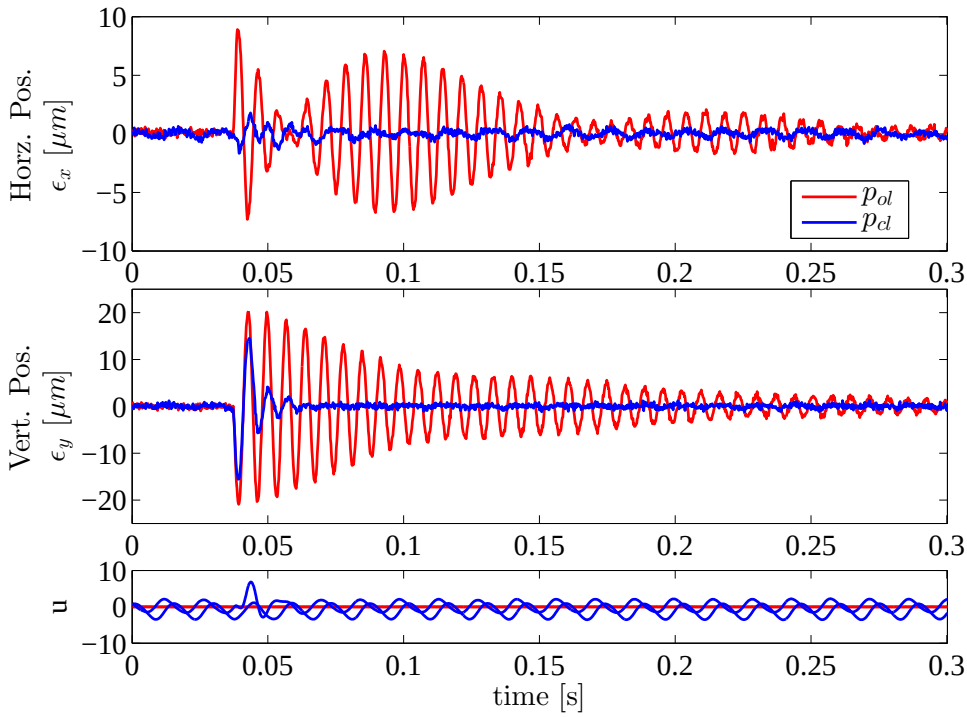

Figure A.7: Open and closed loop impact responses at rotation speed $\Omega_i = 4.1\ krpm$. Shown positions are smoothed to highlight transient response. The controller increases the damping by almost a factor 9.

A.5 Conclusion & Future Aspects

Grey box modelling was used successfully to develop accurate linear models of a rotor-gas bearing system based on experimental measurements. It was shown that it is possible to perturb the fluid film via active lubrication and extract relevant rotor-gas bearing model parameters based on input output relationships. The typical low damping properties of gas bearings could be significantly improved using the active lubrication principle. For a constant angular velocity of 4.1 krpm the damping was improved by a factor nine. Additional tests will be carried out in higher angular velocities in the near future. Future effort will focus on controller design addressing the speed dependent parameter variation.

Parameter		Parameter	
$L = \begin{bmatrix} 0.0605 & -0.0006 \\ -0.0015 & 0.0720 \\ 39.9112 & 2.1157 \\ -3.9433 & 49.9684 \end{bmatrix}$		$K_{sb} = \begin{bmatrix} -0.7584 & -0.0131 \\ 0.0480 & -0.7212 \\ 0.0001 & -0.0001 \\ 0.0000 & 0.0001 \end{bmatrix}^{\mathrm{T}}$	
$F = \begin{bmatrix} 0.9863 & 0.0003 & 0.0002 & 0.0000 \\ 0.0003 & 0.9842 & -0.0000 & 0.0002 \\ -136.5 & 2.7635 & 0.966 & 0.0089 \\ 2.960 & -156.7 & -0.0184 & 0.9606 \end{bmatrix}$		$G = \begin{bmatrix} 0.0132 & 0.0007 \\ -0.0003 & 0.0161 \\ 130.96 & 7.4100 \\ -3.8668 & 159.96 \end{bmatrix}$	

Table A.2: Discrete time system, observer and controller parameters.

$\hat{K}$	α	β	γ
$\hat{K}_{xx}(\Omega)$	$9.78 \cdot 10^{-4}$	-12.9	$7.4 \cdot 10^{5}$
$\hat{K}_{xy}(\Omega)$	$-2.66 \cdot 10^{-3}$	21.97	$-5.743 \cdot 10^{4}$
$\hat{K}_{yx}(\Omega)$	$-2.511 \cdot 10^{-3}$	23.72	$-5.94 \cdot 10^{4}$
$\hat{K}_{yy}(\Omega)$	$-7.821 \cdot 10^{-4}$	3.607	$7.814 \cdot 10^{5}$
$\hat{D}$	α	β	γ
$\hat{D}_{xx}(\Omega)$	$-3.37 \cdot 10^{-7}$	$4.3 \cdot 10^{-3}$	38.56
$\hat{D}_{xy}(\Omega)$	$-4.26 \cdot 10^{-6}$	0.026	-68.84
$\hat{D}_{yx}(\Omega)$	$-2.77 \cdot 10^{-6}$	0.03324	-41.09
$\hat{D}_{yy}(\Omega)$	$5.418 \cdot 10^{-6}$	-0.04158	102.6
$\hat{B}$	α	β	γ
$\hat{B}_{xx}(\Omega)$	-0.017	165.6	$2.91 \cdot 10^{5}$
$\hat{B}_{xy}(\Omega)$	-0.019	192.4	$-4.3 \cdot 10^{5}$
$\hat{B}_{yx}(\Omega)$	$8.5 \cdot 10^{-3}$	-91.46	$2.31 \cdot 10^{5}$
$\hat{B}_{yy}(\Omega)$	$-4.0 \cdot 10^{-3}$	29.98	$7.57 \cdot 10^{5}$

Table A.3: Polynomial coefficients for fitted estimates Acc. to Eq. (A.10).

A.6 Appendix

The appendix lists system parameters in Tables A.3, A.2.

Appendix B

Modelling of Rotor-gas bearings for Feedback Controller Design

From: Journal of Physics: Conference Series (Online) 570 (2014)
The paper has been reformatted to for the thesis.
Lukas R. S. Theisen, Henrik Niemann*

Department of Electrical Engineering, Technical University of Denmark, Elektrovej, Bld. 326, 2800 Kgs. Lyngby, Denmark

Abstract:
Controllable rotor-gas bearings are popular offering adaptability, high speed operation, low friction and clean operation. Rotor-gas bearings are however highly sensitive to disturbances due to the low friction of the injected gas. These undesirable damping properties call for controllers, which can be designed from suitable models describing the relation from actuator input to measured shaft position. Current state of the art models of controllable gas bearings however do not provide such relation, which calls for alternative strategies. The present contribution discusses the challenges for feedback controller design using the state of the art method, and an alternative data driven modelling approach is pursued based on Grey-Box system identification. The method allows development of models of the rotor-gas bearing suitable for controller design, which can be identified from data over the range of operation and are shown to accurately describe the dynamical behaviour of the rotor-gas bearing. Design of a controller using the identified models is treated and experiments verify the improvement of the damping properties of the rotor-gas bearing.

*Corresponding author. E-mail: lrst@elektro.dtu.dk

B.1 Introduction

Controllable gas bearings are popular for offering high speed operation at low friction using clean and abundant air as a lubricant. Design of such rotor-gas bearing systems has been the topic of a previous PhD project [31] from the Mechanical Engineering department at the Technical University of Denmark (DTU). A result of the work is a piezo actuated rotor-gas bearing test rig. A controller is however required to improve the poor damping properties, and a collaborative PhD has begun between the department of Mechanical Engineering and the Electrical Engineering control engineering group to further explore the design of such controllers. This paper provides an overview of the work so far of the collaborative PhD.

State of the art models of rotor-gas bearings [78, 31] rely on solving the Reynolds equation to model the pressure distribution of the fluid film. Morosi [31] included the effect of the piezo actuated valves into the Reynolds equation, and used it to develop a model of a short rigid rotor-gas bearing actuated by piezo valves based on this modified Reynolds equation (MRE). This model was used to manually tune the parameters of a decentralised controller. Recent work in print has however shown that alternative models of the flow in the valves are required to make the model reflect reality. The MRE requires iteratively solving causing an unknown analytical relation from input to the valves to displacement of the rotating shaft, which leaves the model unsuitable for design of model based controllers. This PhD project has therefore investigated development of such suitable models using system identification, e.g. in [1], which showed that linear models identified from experimental data could describe the gas bearing behaviour. Models were identified over a range of rotational velocities, where the parameters were found using Grey-Box system identification. The present contribution makes use of the same bearing model and extends the results by also modelling the actuator dynamics.

The present contribution provides an overview of the progress in developing models and their usage for feedback controller design of the rotor-gas bearing from experimental data over the desired operational range determined by rotational velocity and injection pressure. The paper is structured as follows: A brief overview of the experimental test rig is given in Sec. B.2, followed by an overview of the current state of the art model and its challenges. Section B.4 shows formulation of the Grey-box model and its parameters are identified from experiments. The identified model is used in Sec. B.5 to design a controller capable of increasing the damping properties of the rotor-gas bearing and experiments in Sec. E.5 verify the capabilities

of the designed controller.

B.2 Experimental Setup of Rotor-Gas Bearing

The experimental setup at hand is shown in Fig. B.1: a turbine driven flexible shaft (a) is supported by both a ball bearing (d) and the controllable gas bearing (b), in which pressurised air is injected through four piezo actuated valves numbered as shown. The manometric injection pressure P_I of the pressurised air is measured by a mechanical gauge before splitting up to the four actuators. The absolute pressure in the valves P_{abs} is assumed to be the sum of the measured pressure P_I and the atmospheric pressure P_{atm}. A disc (c) is mounted in one end to pre-load the journal. The horizontal and vertical shaft deflections (e_x, e_y) are measured at the disc location using eddy current sensors (e) in the coordinate frame specified in the figure. The angular position of the shaft ϕ is measured by an optical encoder. The pressurised air generates a thin layer of fluid film in the $25\mu m$ thin gap between the shaft and the bearing housing. For a range of conditions, the fluid film generates restoring forces and thereby keeps the shaft levitating in a stable equilibrium. A more thorough description of the setup is available in [78].

The piezo-electric valves are subject to hysteresis and creep effect [91]. To counteract the hysteresis, decentralised PD-controllers are deployed, effectively reducing the position uncertainty by counteracting the hysteresis. The controlled valves are commanded reference positions $r_{p,i} \in [0; 10]V$, and the corresponding valve positions $y_{p,i} \in [0; 10]V$ are measured ranging from open valve $(0V)$ to closed valve $(10V)$. The valves are controlled pairwise as if there was just a single horizontal and a vertical valve commanded position reference $r(t) \triangleq [r_x(t), r_y(t)]^{\mathrm{T}}$, which is mapped as a reference to the individual valves according to the law from $r(t) \to r_p(t)$, similarly the lumped valve position vector $u(t)$ is defined as a function of the individual valve positions:

$$r_p(r_x(t), r_y(t)) = \begin{bmatrix} r_{p,1}(t) \\ r_{p,2}(t) \\ r_{p,3}(t) \\ r_{p,4}(t) \end{bmatrix} = \begin{bmatrix} r_0 + r_y(t) \\ r_0 + r_x(t) \\ r_0 - r_y(t) \\ r_0 - r_x(t) \end{bmatrix}, \quad u(t) \triangleq \begin{bmatrix} u_x(t) \\ u_y(t) \end{bmatrix} = \begin{bmatrix} y_{p,2}(t) - y_{p,4}(t) \\ y_{p,1}(t) - y_{p,3}(t) \end{bmatrix} \tag{B.1}$$

This makes the valves cooperate and reduces the system from an over-actuated to a fully actuated. In addition the constant offset $r_0 = 5V$ ensures the largest dynamical range.

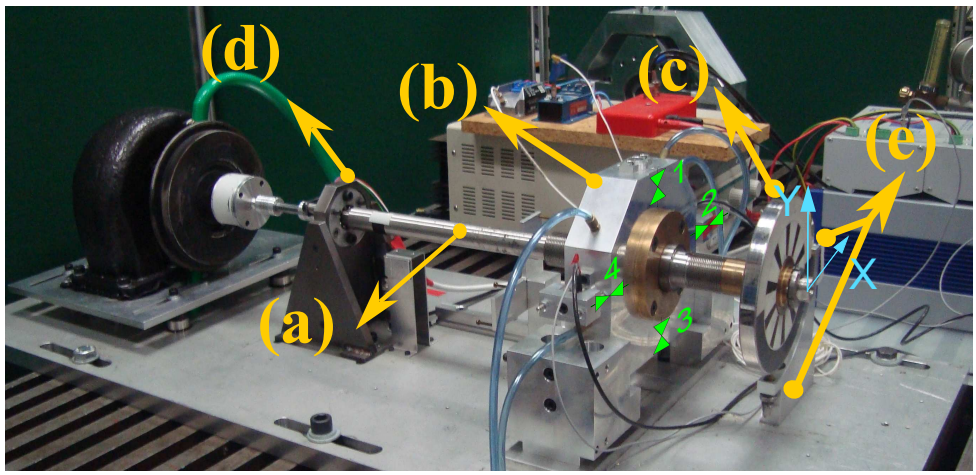

Figure B.1: The experimental bearing setup. A flexible shaft (a) is supported by both a ball bearing (d) and the controllable gas bearing (b) with four piezo actuated valves. A disc (c) is mounted in one end to pre-load the journal and displacement sensors (e) measure the lateral movement of the disc.

B.3 Rotor-gas Bearing Modelling Using Finite Element Models and the Modified Reynolds Equation

Current state of the art models of the rotor-gas bearing [41, 31] consist of two sub-models: A Finite Element model of the flexible shaft and a model of the thin layer of fluid film. This section provides an overview of these two models and their challenges.

B.3.1 The Modified Reynolds Equation

The Modified Reynolds equation [31] is used for modelling the behaviour of the thin layer of fluid film in the rotor-gas bearing. By a set of assumptions, a partial differential equation can be made, modelling the pressure p as a function of the fluid film thickness h, which varies along with the shaft position in the bearing and time t can then be set up:

$$\frac{\partial}{\partial \mathsf{y}}\left(\mathsf{ph}^3\frac{\partial \mathsf{p}}{\partial \mathsf{y}}\right)+\frac{\partial}{\partial \mathsf{z}}\left(\mathsf{ph}^3\frac{\partial \mathsf{p}}{\partial \mathsf{z}}\right)=6\mu U\frac{\partial(\mathsf{ph})}{\partial \mathsf{y}}+12\mu\frac{\partial(\mathsf{ph})}{\partial t}+12\mathsf{p}V_I \tag{B.2}$$

where the fluid film coordinate frame $(\mathsf{x}, \mathsf{y}, \mathsf{z})$ chosen is: x the radial coordinate directed towards the centre of the shaft, y the circumferential coordinate and z being the axial coordinate. μ is the viscosity of the gas, U is the linear velocity of the rotating shaft at the bearing housing, V_I is the velocity profile of the injected gas assumed to be parabola shaped with a linear pressure drop along the length of the valves; Work in print however shows this does not model the flow well. The flow is assumed laminar, which is reasonable given the small thickness of the fluid film. The MRE has no known analytical solution, but discretisation in a fine grid allows an iterative solution to be found from a good initial solution guess. This provides the pressure profile, which upon integration provides the horizontal and vertical forces from the fluid film acting on the flexible shaft $F_{be} = [F_{X,be},\ F_{Y,be}]^{\mathrm{T}}$.

B.3.2 Finite Element Modelling of Flexible Shaft

The flexible shaft can then be modelled using a finite element (FE) method, where the shaft is divided into n_e sections, which can bend and rotate relative to each other around the $n_n = n_e + 1$ nodes connecting the sections giving four degrees of freedom (DOFs) per node. Given the geometry of the shaft and its material properties, the stiffness of each section can be approximated, the mass of each section can be calculated and the forces from each section acting on the other sections can then be expressed as a $n_n \cdot 4$ coupled differential equations with the linear and angular displacements from a horizontal and a vertical axis $q_F = [q_1,\ q_2, \ldots, q_{4n_n}]^{\mathrm{T}}$ with corresponding time derivatives $\dot{q}_F$. The model is formulated using the mass matrix M_F, the stiffness matrix K_F, the gyroscopic matrix G_F and the damping matrix D_F:

$$M_F\ddot{q}_F(t) + (D_F - \Omega G_F)\dot{q}_F(t) + K_F q_F(t) = f_F(t), \quad q_F = [q_1,\ q_2, \ldots, q_{4n_n}]^{\mathrm{T}} \tag{B.3}$$

where in the above $f_F(t)$ is the external forces acting on each node of the FE model from the fluid film, external disturbances etc.. Using the linearised stiffness and damping forces from the MRE bearing model, the FE model predicts the eigenfrequencies within $\pm 5\%$ in the stationary case over a wide range of injection pressures and rotational velocities.

The requirement of this iteratively solved pressure profile for every configuration however leaves the model unable to describe the relation from actuator input voltage to shaft displacement on a form suitable for controller design. The time dependent MRE still remains to be coupled to the FE shaft model and validated experimentally, before the relation from input voltage to shaft displacement can be approximated

and put on an analytical form. This shows the need for alternative approaches to develop models for feedback controller design, which do not depend on the solution of the MRE.

B.4 A System Identification Approach - Data Driven Modelling

The modelling of rotor gas bearings still represents an open challenge. This section shows a heuristics based model approach, where basic knowledge from rotor-dynamics provides the basis for formulation of a model. The model parameters are then identified from experimental data, where the piezo-valves perturb the rotor-gas bearing. The method allows development of accurate models able to describe the rotor-gas bearing dynamics.

The measurement of the valve positions allows dividing the modelling in two: an actuator sub-model to model the valve dynamics from commanded valve reference position to valve position, and a bearing sub-model to model the relation from valve position to shaft deflection. The parameters of the identified models allow formulation of a global model.

B.4.1 Grey-Box Model of Gas Bearing

In a rotational range around the first two eigenfrequencies, the rotor gas bearing system consisting of the flexible shaft and the gas-bearing can be modelled as a 2 DOF coupled mass-spring damper system. Let $p = [e_x, e_y]^{\mathrm{T}}$ be the position vector consisting of horizontal and vertical shaft displacements, and denote time derivatives $\frac{d}{dt}(\cdot) = \dot{(\cdot)}$. The model then reads

$$\mathcal{M}\ddot{p}(t) + (\mathcal{D} - \Omega\mathcal{G})\dot{p}(t) + \mathcal{K}\, p(t) = \mathcal{B}_p u(t), \quad p = [e_x, e_y]^{\mathrm{T}}, \tag{B.4}$$

in which Ω is the rotation speed, $\mathcal{M}$ is the diagonal mass matrix, $\mathcal{D}$ is the damping matrix, $\mathcal{G}$ is the antisymmetric gyroscopic matrix, and $\mathcal{K}$ is the stiffness matrix, all with dimension 2×2. The right hand side should include external forces $f(t)$ acting on the rotor-gas bearing, which include: forces from mass unbalance, forces from the piezo valves and forces from external impacts. Section B.4.4 shows how the mass unbalance response is filtered out. In [1] it was shown reasonable to assume the actuator force proportional to the valve position with gain $\mathcal{B}_p$, of dimension 2×2 and the model therefore reduces to Eq. B.4. The model is reformulated to state space form to ease the Grey-Box modelling. A suitable choice of states is the deflection and

velocity of the shaft $x \triangleq [e_x, e_y, \dot{e}_x, \dot{e}_y]^{\mathrm{T}}$. The measurement noise and errors from simplified model are modelled as additive noise $d(t)$ entering both output and states with a disturbance input gain $\mathcal{B}_d$ and the chosen state space formulation of Eq. (B.4) then reads:

$$\begin{aligned} \dot{x}(t) &= \mathcal{A}x(t) + \mathcal{B}u(t) + \mathcal{B}_d d(t), \quad x(0) = x_0 \\ p(t) &= \mathcal{C}x(t) + d(t) \end{aligned} \tag{B.5}$$

where the system-, input gain-, and output matrix are

$$\mathcal{A} = \begin{bmatrix} 0 & I \\ -K & -D \end{bmatrix}, \quad \mathcal{B} = \begin{bmatrix} 0 \\ B \end{bmatrix}, \quad \mathcal{B}_d = \begin{bmatrix} 0 \\ B_d \end{bmatrix}, \quad \mathcal{C} = \begin{bmatrix} I & 0 \end{bmatrix}, \tag{B.6}$$

where $D \triangleq \mathcal{M}^{-1}(\mathcal{D} - \Omega\mathcal{G})$, $K \triangleq \mathcal{M}^{-1}\mathcal{K}$, and $B \triangleq \mathcal{M}^{-1}\mathcal{B}_p$ are the matrices to be identified along with disturbance gain B_d, and initial value x_0, each with four parameters giving 20 unknowns in total. The parameters of (B.6) are identified by recasting the problem to a model parametrized in $\hat{\theta}_b \triangleq \{\hat{D}, \hat{K}, \hat{B}, \hat{x}_0, \hat{B}_d\}$ as $\mathfrak{M}_b(\theta)_b$. Each matrix $\hat{D}, \hat{K}, \hat{B}, \hat{B}_d$ has four elements denoted by small letters and subscripts xx, xy, yx, yy. The model then reads

$$\mathfrak{M}_b(\theta_b) : \begin{cases} \dot{x}(t) = \mathcal{A}(\theta_b)x(t) + \mathcal{B}(\theta_b)u(t) + \mathcal{B}_d(\theta_b)d(t), \quad x(0) = x_0(\theta_b) \\ p(t) = \mathcal{C}x(t) + d(t) \end{cases} \tag{B.7}$$

B.4.2 Grey-Box Model of Lumped Actuators

This section formulates a similar model of the lumped PD-controlled piezo valves. The closed loop horizontal and vertical lumped valve can each be modelled as a second order low-pass filter. The valve dynamics can be seen as transfer functions with two poles $p_{1,j}$, and $p_{2,j}$, where j refers to the horizontal valve x or vertical valve y and gain $\kappa_{a,j}$. Considering only the commanded reference position as input, the dynamics then read:

$$\begin{bmatrix} u_x(s) \\ u_y(s) \end{bmatrix} = \begin{bmatrix} H_{a,x}(s) & 0 \\ 0 & H_{a,y}(s) \end{bmatrix} \begin{bmatrix} r_x(s) \\ r_y(s) \end{bmatrix}, \qquad H_{a,j}(s) = \frac{\kappa_{a,j}}{\left(\frac{1}{p_{1,j}}s + 1\right)\left(\frac{1}{p_{2,j}}s + 1\right)} \tag{B.8}$$

in which $H_{a,j}(s)$ is the second order filter of the specified form. The model can be formulated in the same structure as Eq. B.7, exploiting that cross coupling terms $k_{xy}, k_{yx}, d_{yx}, d_{xy}, b_{yx}, b_{xy}, b_{p,yx}, b_{p,xy}$ are zero. Reformulating this to a Grey-box

model and estimating the initial valve states x_a and a similar disturbance gain d_a, the model then reads

$$\mathfrak{M}_a(\theta_a): \begin{cases} \dot{x}_a(t) = \mathcal{A}(\theta_a)x_a(t) + \mathcal{B}(\theta_a)r(t) + \mathcal{B}_{d,a}(\theta_a)d_a(t), \quad x_a(0) = x_{a0}(\theta_a) \\ u(t) = \mathcal{C}_a x_a(t) + d_a(t) \end{cases} \tag{B.9}$$

Estimating the gains, poles, initial state and disturbance gain, the actuator model thus only has 12 parameters being:

$$\theta_a \triangleq [\underbrace{k_{a,xx},\ k_{a,yy},\ b_{a,xx},\ b_{a,yy},\ d_{a,xx},\ d_{a,yy}}_{\text{valve coefficients}},\ \underbrace{b_{da,xx},\ b_{da,yy}}_{\text{disturbance gains}},\ \underbrace{x_{a1,x0},\ x_{a2,x0},\ x_{a3,x0},\ x_{a4,x0}}_{\text{initial state}}]^{\mathrm{T}}, \tag{B.10}$$

and a similar actuator model $\mathfrak{M}_a(\theta_a)$ has been formulated.

B.4.3 Description of Experiments

The model should represent the rotor-gas bearing over the range of operational conditions, which are defined by two main characteristics: rotational speed Ω and injection pressure P_I, which can vary within $\Omega \in [0; 6]krpm$ and $P_I \in [3; 7]bar$ respectively. This identification over the whole operational range will be available in [3], where the coefficients are estimated from data sets collected from a grid of injection pressures and rotational velocities representing the range of interest. Here a selected example is chosen $\bar{\Omega} = 0rpm$ and $\bar{P}_I = 4.0bar$. During data collection all variables were sampled at f_s=5kHz. A pseudo random binary sequence commanded as reference for the lumped valves $r(t)$ ensured excitation of the system and hence identifiability of the parameters. The input stepped from -1 to 1 at random sampling instants. The lumped valve references $r(t)$ and measured lumped valve positions $u(t)$ were logged as input and output for the actuator sub-model and the lumped valve positions $u(t)$ and the shaft displacement $p(t)$ as input and outputs for the bearing model.

B.4.4 Prefiltering

Before identification, the data sets are prefiltered using a run-out filter $\mathcal{F}_r$, which filters out the response from surface unsmoothness and mass unbalance response. This is calculated from a data set collected at each operational condition, where the

shaft is not excited, which allows generation of the response as function of encoder angle $\mathcal{F}_r(\phi)$. The offset of both inputs and outputs estimated as mean of the first 2000 samples are subtracted from the data sets. A median filter of size 3 is used to smooth out noise from the shaft position measurements.

B.4.5 Identification

The parameters of both the actuator sub-model and the bearing sub-model are identified using the prediction error method [45], and initial guesses of the parameters are obtained from previous identified models. The model update iterations were stopped when the relative improvement norm was less than 10^{-4} indicating convergence.

Both the actuator model $\mathfrak{M}_a$ and the bearing model $\mathfrak{M}_b$ are then identified from the respective data sets. The actuator sub-models are found to be fairly constant over the investigated range of interest, and a nominal actuator model G_{act} is chosen. The bearing model parameters however vary with both injection pressure and rotational velocity as expected from [31]. The model residuals are expected to be white noise, which is not the case as shown in Fig. B.2 (d) and (h). The norm of the residual however is small indicating low importance of the residual dynamics.

Cascading of the bearing model and the actuator model provides the total rotor-gas bearing model: $G_p(s) = G_{bear}(s)G_{act}(s)$.

B.5 H_∞ Control

A suitable control strategy such as the mixed sensitivity-approach can improve the poor damping characteristics of the rotor-gas bearing. The identified model is used for design of such a controller.

The H_∞ controller $K_\infty(s)$ has been designed using the stacked requirements $||N||_\infty = \max_\omega \bar{\sigma}(N(j\omega)) < 1$;, where $N = [W_pS, W_uK_\infty S]^{\mathrm{T}}$. The controller is designed for a model identified at $P_I = 7bar, \Omega = 4000rpm$. The chosen weights W_p and W_u shown in Fig. B.3 ensure an increase in damping without counteracting low frequency disturbances such as changes in equilibrium position due to changing operational condition. The controller obtained using the specified weights is reduced from 24 states to a fourth order controller $K_\infty(s)$ using Gramian-based input/output balancing. The reduction factor in sensitivity towards disturbances is determined

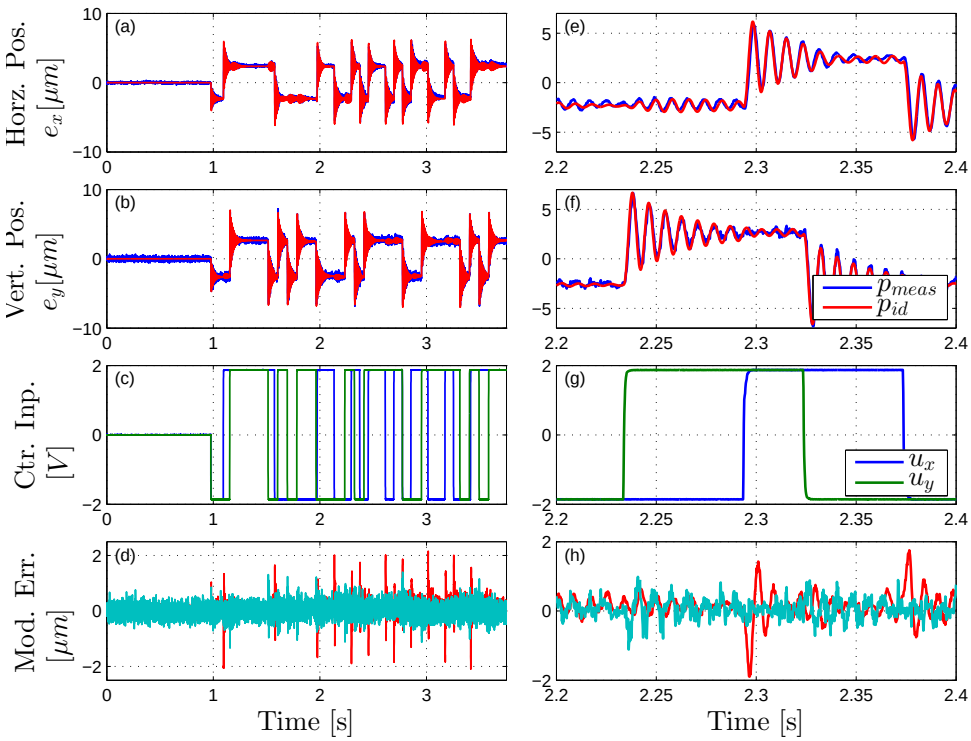

Figure B.2: Example of an identification of data set collected at $P_I = 4bar, \Omega = 0rpm$. The valve positions $[u_x, u_y]$ exciting the bearing shown in c) excite the bearing dynamics causing deflection of the shaft. a) and b) show this measured deflection $p_{meas} = [e_x, e_y]$ and the predicted using the identified model $p_{id} = [\hat{e}_x, \hat{e}_y]$ subject to valve excitation. d) shows the residual between identified and measured response $\varepsilon = p_{meas} - p_{id}$. Subplots e, f, g and h show corresponding time zooms.

from the output sensitivity calculated as:

$$S_o(s) \triangleq (\mathbb{I}_2 + G_p(s)K_\infty(s))^{-1} \tag{B.11}$$

The reassembled bearing model [3] is used to assess performance of the controller over the range of operation. This model is developed from identified models from data collected over a range of injection pressures $(P_I \in [3;7]bar)$ and rotational speeds $(\Omega \in [0;6]krpm)$ and describes the rotor-gas bearing behaviour over the wide range of operational conditions. Figure B.4 shows the output sensitivity of the closed loop system for different randomly chosen operational points models within the operational range. The sensitivity is reduced in the desired frequency range from $[70:190]Hz$ by a factor three to nine, though at the cost of an increased sensitivity of a factor 1.2 at low frequencies, and a peak sensitivity around $280Hz$ of a factor 1.8, which is affordable.

Discretisation of the controller to $K_\infty(z)$ using a Tustin-approximation allows implementation on the rotor-gas bearing test-rig, and the frequency response in Fig. B.5 shows the desirable capabilities of the controller: at low frequencies and DC the controller is not active, only in an interval around the critical frequencies is the controller active.

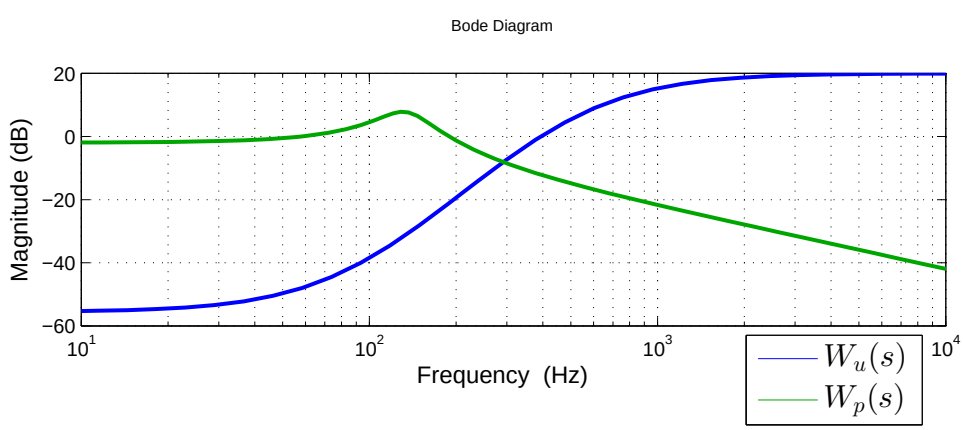

Figure B.3: Weights $W_p(s)$ and $W_u(s)$ for mixed sensitivity controller design

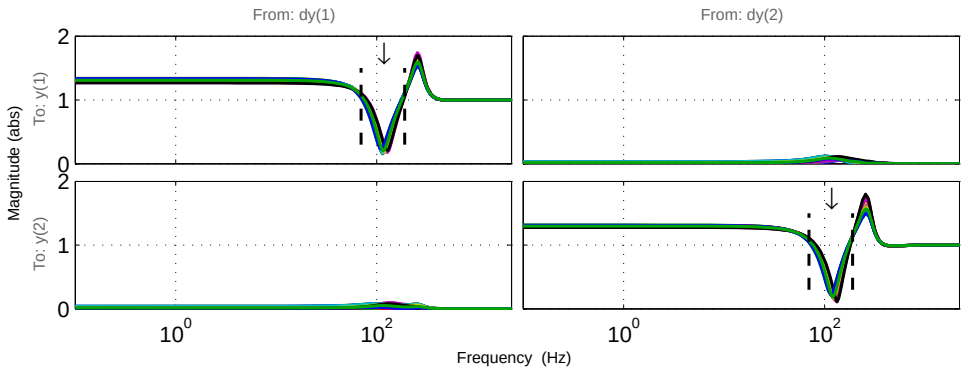

Figure B.4: Output sensitivity $S_o(s)$ for $N_r = 30$ realizations of the rotor-gas bearing within the operational. The black arrow and lines mark the frequency interval where the sensitivity is reduced.

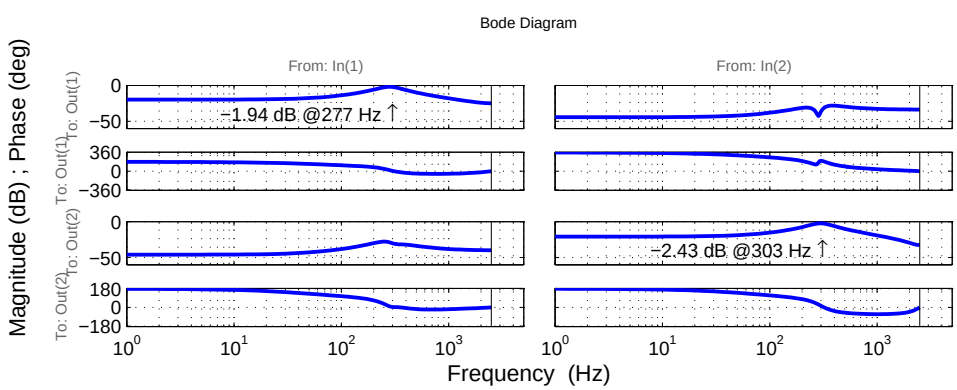

Figure B.5: Frequency response of controller $K(z)$

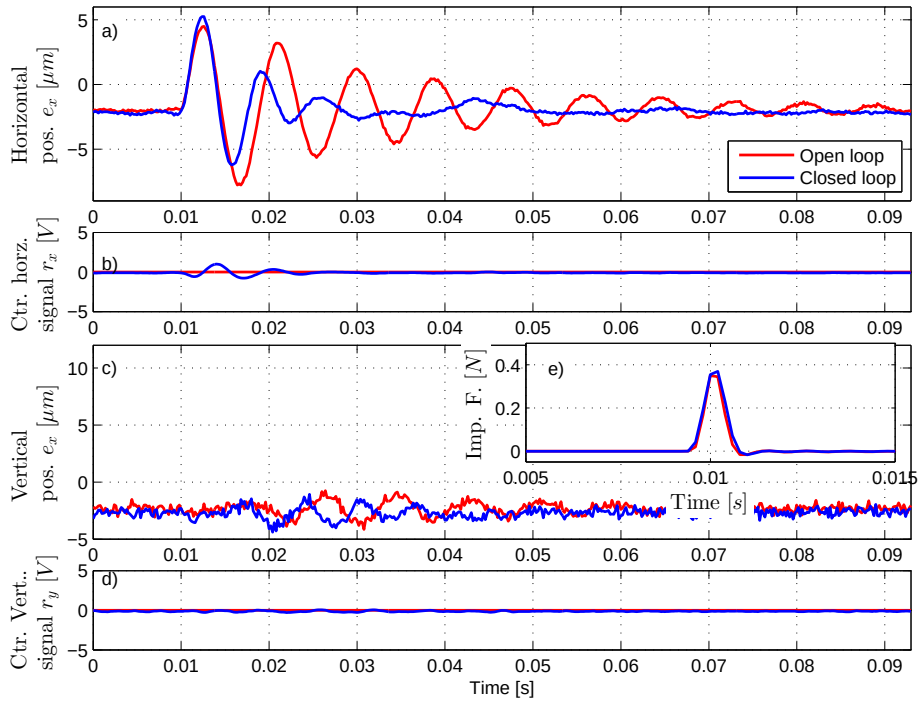

Figure B.6: Horizontal impact response without and with the designed controller at$\bar{P}_I = 4bar$, $\bar{\Omega} = 0rpm$. Impact occurs close to time $t = 0.01s$. a and c show measured deflections, b and d show commanded valve positions and e shows the measured impact force.

B.6 Experimental Results

The controller is implemented on the rotor-gas bearing system, and impacts are applied to the rotor-gas bearing both with the controller on and off. Figure B.6 shows a horizontal impact response at $\bar{P}_I = 4bar$, $\bar{\Omega} = 0rpm$: using the robust controller, the horizontal damping is found increased from 0.0567 to 0.173 - a factor three. A vertical impact in Fig. B.7 shows similar increase in damping. Horizontal and vertical impacts at higher pressure $\bar{P}_I = 7bar$ show a damping increase by a factor six from 0.0282 to 0.1668, which is within the expected range of damping increase predicted by the sensitivity function. Equivalent results can be obtained for non zero rotational velocities.

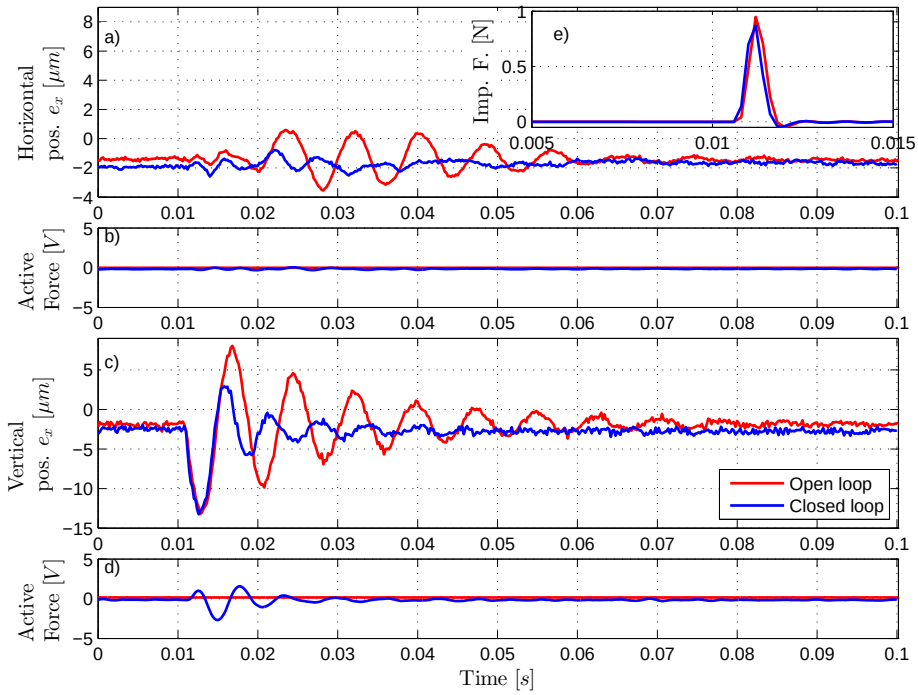

Figure B.7: Vertical impact response without and with the designed controller at $\bar{P}_I = 4bar$, $\bar{\Omega} = 0rpm$. Impact occurs close to time $t = 0.01s$. a and c show measured deflections, b and d show commanded valve positions and e shows the measured impact force.

B.7 Conclusion

Two Grey-box models were developed modelling the actuators and bearing dynamics for a rotor-gas bearing, and successfully used to identify model parameters describing the relation from commanded to measured valve position, and from valve position to shaft displacement of the rotor-gas bearing. A mixed sensitivity controller was designed to stabilise the rotor-gas, and its increase in damping was validated experimentally for chosen conditions.

Acknowledgments

The Danish Ministry of Science, Innovation and Higher Education is gratefully acknowledged for the support to the FTP research project 12-127502.

Appendix C

Modelling and Identification for Control of Gas Bearings

From: Mechanical Systems and Signal Processing 70–71 (2016), pp. 1150–1170
The paper has been reformatted to for the thesis.
Lukas R. S. Theisen[1], Hans H. Niemann[1], Ilmar F. Santos[2], Roberto Galeazzi[1], Mogens Blanke[1,3]

[1]Dept. of Electrical Engineering and [2]Dept. of Mechanical Engineering
Technical University of Denmark, DK 2800 Kgs. Lyngby, Denmark
[3]AMOS CoE, Institute for Technical Cybernetics
Norwegian University of Science and Technology, NO 7491 Trondheim, Norway
Email: {lrst,hhn,mb,rg}@elektro.dtu.dk, ifs@mek.dtu.dk

Abstract:
Gas bearings are popular for their high speed capabilities, low friction and clean operation, but suffer from poor damping, which poses challenges for safe operation in presence of disturbances. Enhanced damping can be achieved through active lubrication techniques using feedback control laws. Such control design requires models with low complexity, able to describe the dominant dynamics from actuator input to sensor output over the relevant range of operation. The mathematical models based on first principles are not easy to obtain, and in many cases, they cannot be directly used for control design due to their complexity and parameter uncertainties. As an alternative, this paper presents an experimental technique for "in situ" identification of low complexity models of the entire rotor-bearing-actuator system. Using grey-box identification techniques, the approach is shown to be easily applied to industrial rotating machinery with gas bearings and to allow for subsequent control design. The paper shows how piezoelectric actuators in a gas bearing are efficiently used to perturb the gas film for identification over relevant ranges of rotational speed and gas injection pressure. Parameter-varying linear models are found to capture the dominant dynamics of the system over the range of operation.

Based on the identified models, decentralised proportional control is designed and is shown to obtain the required damping in theory as well as in a laboratory test rig.

C.1 Introduction

Passive and active gas bearings are receiving growing attention for their high speed operation capabilities. While passive gas bearings offer advantages of high speed operation, low friction, and clean and abundant air as lubricant, they suffer from low damping and vibration instabilities [34, 35, 36]. The damping and stability properties can be improved by two methods. One is through foil bearings [13, 14, 15] that exploit friction between bumps and foil. Such solutions are relatively cheap, but friction is a significant design challenge [17]. An alternative is to use a mechatronic approach in the form of active control of the gas bearing using piezo actuation [78] or active inherent restrictors [28]. The controllers for such systems could be tuned experimentally, with the uncertainty and lack of quality assurance this method implies, or they could be stringently designed based on dynamic models with documentable performance properties. The latter requires a suitable model, which in a simple manner describes the relation from actuator input to measured output, representing the dynamics of the journal in the frequency range where control is needed. Concerning modelling, air-injection actuators have only received sparse attention. In contrast, electromagnetical actuators and oil bearings have been well covered. Modelling and a linear parameter varying control design were presented for a rotor supported by an oil bearing and an electromagnetically actuated bearing in [87], which showed ability to reduce vibrations and to allow rub-free crossing of the first resonance frequency. Current state of the art models of controllable gas bearings rely on solving the modified Reynolds equation [36], which emerges from including the external controllable lubricant injection into the Reynolds equation. No general closed analytical solutions exist for the equation considering bearings with finite dimension. Solutions are therefore found iteratively over time, and the input-output relationship between piezoactuator and rotor lateral displacement is not easily derived. Literature has therefore generally presented experimentally tuned controllers, e.g. in [78]. Some authors have proposed on-off control rules [109], where the opening of the valves changed the journal pressure, which in turn changed the critical speeds, allowing the rotor to cross them safely. Such approach, however, does not improve the damping characteristics of the gas bearing.

Models suitable for controller design can be developed using system identification.

Such models can have low complexity and can yet provide a convenient basis for synthesising controllers [46]. Such models can leave out the details and high order associated with mechanical models based on first principles. Only few results exist for controllable gas bearings, whereas the literature is rich on active magnetic bearings (AMB). AMBs have inherently unstable dynamics [63, 64, 65] and therefore require stabilising controllers. For the non-rotating case, the horizontal and vertical AMB dynamics are uncoupled, therefore a model is developed for each of the two directions. In [50] and [64], a frequency based identification approach was used to develop black-box models of a rotor supported by AMBs. This allowed development of high order continuous time models for a non-rotating shaft supported by AMBs, which sufficed for controller design. In [49], a frequency based method was proposed for identification of the transfer function matrix model of a non-rotating shaft supported by AMBs. The method consisted of steps identifying the submodels separately and finally combining them together. In [63], a similar approach was proposed and deliberately poor controllers were used to allow identification of the poles on the real axis, which are in general not easily identified. In [48], a predictor-based subspace identification algorithm was proposed to identify the dynamics of a non-rotating AMB system, and the obtained model was used to design robust controllers. In [66] a simple black-box model was proposed to represent the vertical displacement of a simple non-rotating rigid shaft supported by AMBs, where the model parameters were estimated online. In [47], an iterative frequency based joint identification/controller design scheme for a non-rotating shaft supported by AMBs was applied using an LQ criterion.

Controllable gas bearings differ from AMBs in the sense that gas bearings can be designed to be open loop stable, hence open loop identification schemes can be used. The lateral dynamics is though coupled due to aero-static effects even in the non-rotating case. Recent work [1] showed that grey-box system identification could be a means to develop such models. The main contribution of this work relies on: a) grey-box identification to develop low complexity models of the entire rotor-bearing-actuator system and b) extension of the early results from [1] by investigating the system dynamics as function of both gas injection pressure and rotational speed, which are the two main variables that influence system dynamic behaviour when the static load and the bearing geometry are kept constant [41]. The earlier models from [1] need to be extended to include the dynamics of the piezoelectric actuators and to capture the delay between the displacement of the piezoelectric actuator and the pressure build-up in the journal. The experimental procedure is developed aiming at

industrial applications to complex rotating systems supported by gas bearings, where first principles modelling is rarely simple and accurate enough for controller design.

The paper is structured as follows: a brief overview of the experimental test rig is given in Sec. C.2. The piezoelectric actuators are then characterised. The static gain from piezoactuator position to disc position is experimentally characterised. Section C.3 presents an experimentally-based model of the rotor-bearing system obtained for a set of operational conditions through grey-box identification techniques. Regression techniques are used in Sec. C.4 to fit polynomial surfaces to experimental data and build a linear parameter varying model of the entire controllable rotor-bearing system, which captures the essential behaviour across the operational range. Section C.5 presents the design of a decentralised proportional controller to confirm the suitability of the identified models for controller design and the results are experimentally verified. Sections E.6 and C.7 evaluate critically the results, showing that the controller enhances the damping properties of the gas bearing as expected.

Notation

The paper uses upper case bold letters for matrices $\mathbf{A}$, lower case bold letters for vectors $\mathbf{a}$ and non-bold letters for scalars a or A. When relevant, clear distinctions are made to address time signals $a(t)$ and the Laplace transformed $a(s)$. Units for rotational speeds are listed in revolutions per minute $(1rpm = 1/60Hz)$, and pressures are listed in bar $(1bar = 100,000Pa)$.

C.2 Experimental Setup of Controllable Gas Bearing Test Rig

The experimental controllable gas bearing setup at hand is shown in Fig. C.1. It consists of a turbine (1) driving a flexible shaft (2) supported by both a ball bearing (3) and the controllable gas bearing (4), in which pressurised air is injected through four piezoactuated injectors numbered as shown. The injection pressure P_{inj} is measured by a mechanical gauge before splitting up to the four piezoactuators. A disc (5) is mounted in one end to pre-load the journal. The horizontal and vertical disc movement $\mathbf{p} \triangleq [p_x, p_y]^{\text{T}}$ is measured at the disc location using eddy current sensors (6) in the coordinate frame specified in the figure. The angular position of the rotor ϕ is measured by an optical quadrature encoder (7). The position of the i-th piezoactuator can be controlled through a voltage input $u_{p,i} \in [0; 10]V$, where an increasing voltage expands the piezostacks by up to $45\ \mu m$, which closes the injector.

Test rig dimension	Bearing length $[mm]$	Bearing diameter $[mm]$	Shaft length $[mm]$	Shaft mass $[kg]$	Disc diameter $[mm]$	Disc mass $[kg]$	Orifice diameter $[mm]$
Value	40	40	500	2.04	140	1.5	2

Table C.1: Controllable gas bearing test rig parameters.

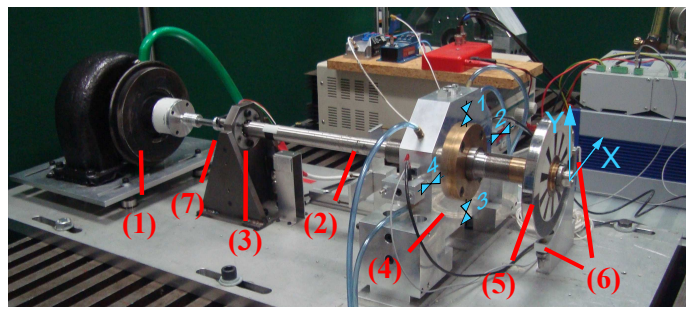

Figure C.1: The experimental controllable gas bearing setup. A turbine (1) drives a flexible shaft (2), which is supported by both a ball bearing (3) and the controllable gas bearing (4) with four piezoactuated injectors. A disc (5) is mounted in one end to preload the journal and displacement sensors (6) measure the lateral movement of the disc in the shown reference frame. A quadrature encoder (7) measures the angular position.

Figure C.2 shows a CAD drawing of the test rig, where the gas bearing is cut in half to visualise the control mechanism. The nominal clearance of the gas bearing is $25\ \mu m$. Given the right conditions of sufficient injection pressure and sufficiently low rotational speed, the gas film generates restoring forces and thereby keeps the rotor levitating about a stable equilibrium, and opening or closing an injector perturbs the gas film. Physical dimensions of the test rig are shown in Table C.1. All measurements are sampled with period $T_s = 0.2\ ms$. A detailed description of the setup is available in [31].

The piezoelectric stacks in the piezoactuators have two inherent nonlinear phenomena [91, 112]: creep and hysteresis. Hysteresis causes uncertainties in the piezoactuator position, which is a challenge for modelling and control. To counteract these nonlinear effects, decentralised PD-controllers are deployed. The controllers allow piezoactuator i, $i \in \{1, 2, 3, 4\}$ to track a reference position $r_{p,i}$. This is described in detail in C.8, and it is shown, that the closed loop piezoactuator dynamics can be captured by linear models, which is pursued further in Sec. C.3.7.

The four piezoactuators are available to control the shaft displacement in x and

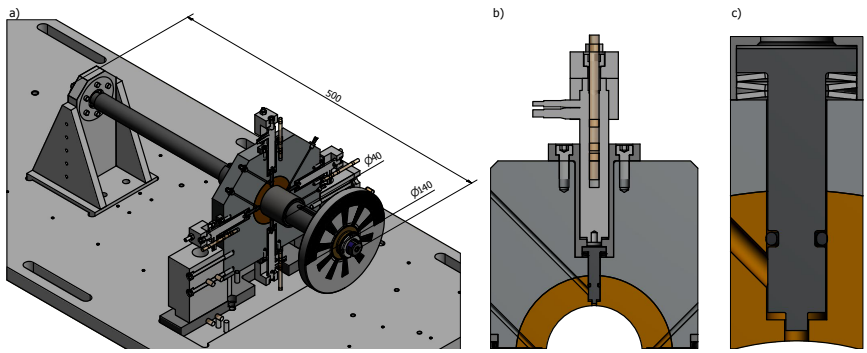

Figure C.2: CAD drawing of the test rig: a) the test rig with the controllable gas bearing cut in half. Major dimensions are included in millimetre $[mm]$. b) zoom of a piezoactuator. The piezo electric stack pushes a pin, which controls the injector opening. c) zoom of the injector pin and journal.

y. Individual control of the piezoactuators gives the challenge of control allocation. Instead they are pairwise controlled using a differential principle. Piezoactuator reference positions $\mathbf{r}(t) \triangleq [r_x(t), r_y(t)]^{\mathrm{T}}$ are commanded using:

$$\begin{aligned} r_{p,1}(t) &= r_0 + r_y(t) & r_{p,2}(t) &= r_0 + r_x(t), \\ r_{p,3}(t) &= r_0 - r_y(t) & r_{p,4}(t) &= r_0 - r_x(t), \end{aligned} \tag{C.1}$$

i.e. one reference signal r_x is sent to the pair of piezoactuators mounted horizontally, and one reference signal r_y is sent to the pair mounted vertically as shown in Fig. C.3. The constant offset r_0 is chosen to ensure the largest dynamical range avoiding actuator saturation. The individual piezoactuator positions are similarly mapped to a vector containing the difference of piezoactuator positions $\mathbf{u}(t)$:

$$\mathbf{u}(t) \triangleq [u_x(t), u_y(t)]^{\mathrm{T}} = [y_{p,2}(t) - y_{p,4}(t), y_{p,1}(t) - y_{p,3}(t)]^{\mathrm{T}} \tag{C.2}$$

The measurements of this difference of piezoactuator positions combined with the measurement of lateral disc movement allows modelling of actuator and bearing dynamics as individual linear subsystems. A rotor-bearing model is set up to describe the dynamics from piezoactuator position to lateral disc movement $[p_x, p_y]^{\mathrm{T}}$. An actuator model is set up to describe the relation from commanded piezoactuator positions $[r_x, r_y]^{\mathrm{T}}$ to piezoactuator position $[u_x, u_y]^{\mathrm{T}}$. The measured inputs and outputs of each subsystem are used to identify models as shown in Fig. C.4. The entire rotor-bearing-actuator model $\mathbf{G}$ is then obtained as the interconnection of the

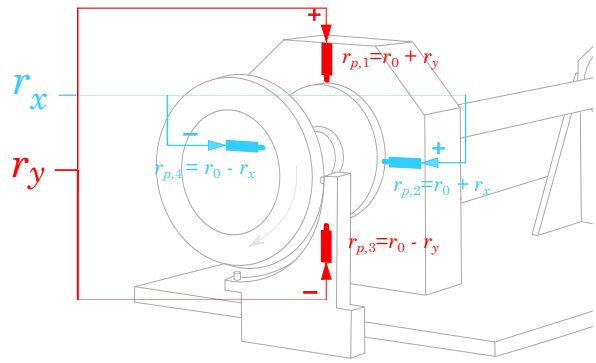

Figure C.3: The piezoactuators are controlled pairwise using a differential principle. A reference signal r_x is sent to the pair of piezoactuators mounted horizontally, and a reference signal r_y is sent to the pair mounted vertically.

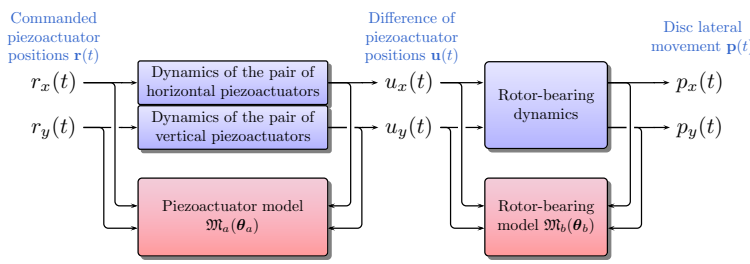

Figure C.4: Overview of the system identification process. A perturbation of the commanded piezoactuator positions perturbs both the piezoactuators and the shaft and disc. An actuator model can the be identified from the $\{\mathbf{r}, \mathbf{u}\}$ data sets, and a rotor-bearing model from the $\{\mathbf{u}, \mathbf{p}\}$ data sets.

rotor-bearing model $\mathbf{G}_{rb}$ and the actuator model $\mathbf{G}_{act}$:

$$\mathbf{G} = \mathbf{G}_{rb}\mathbf{G}_{act} \tag{C.3}$$

The individual models are derived in the following sections.

C.3 Experimentally-Based Modelling Aided by Grey-Box Identification

This section presents a low-complexity linear dynamical model describing the controllable gas bearing and rotor dynamics. The proposed model is shown to capture

the dominant dynamics well, and its simplicity makes it suitable for controller design. The model parameters are found from experimental data using grey-box system identification [45]. Experiments performed over the operating range allow the description of the overall dynamic behaviour of the controllable gas bearing. Multiple data sets collected at each operational condition are used for cross-validation ensuring the quality of the identified models.

C.3.1 Static Input-Output Gain Modelling of Rotor-Bearing

The presence of nonlinear phenomena in the shaft actuation is assessed by the collection of a staircase response, where a stepwise increasing voltage is applied to the commanded piezoactuator positions $\mathbf{r}$, followed by a stepwise decreasing voltage. The response allows the generation of a steady state gain mapping showing shaft equilibrium position $\mathbf{p}$ as a function of the difference of piezoactuator positions $\mathbf{u}$. Figure C.5 shows such a mapping for the injection pressure $\bar{P}_{\text{inj}} = 6\ bar$, and the rotational speed $\bar{\Omega} = 0\ rpm$. The linear relation from inputs to outputs is evident. Cross-coupling gains from the aerostatic effect are also present in the system, though with small influence. This analysis shows no evidence of hysteresis or other nonlinear phenomena affecting the shaft position. Similar results are obtained for other injection pressures and rotation speeds, though with varying slopes and equilibrium position. The error in equilibrium position from approximating the static gain linear is less than $0.95\ \mu m$ over the range of applied inputs with root mean square errors $[\sigma_{g0,xx}, \sigma_{g0,xy}, \sigma_{g0,yx}, \sigma_{g0,yy}]^{\mathrm{T}} = [0.44, 0.037, 0.059, 0.21]^{\mathrm{T}} \mu m$. Therefore linearity is a reasonable approximation.

C.3.2 Grey-Box Model of Rotor-Bearing System

A combined model of the rotor and the gas bearing can be set up as a 2 DOF coupled mass-spring-damper equivalent in a neighbourhood around the two first eigenfrequencies. For given constant shaft rotational speed $\Omega = \bar{\Omega}$ and injection pressure $P_{\text{inj}} = \bar{P}$, the model reads:

$$\boldsymbol{\mathcal{M}}\ddot{\mathbf{p}}(t) + (\boldsymbol{\mathcal{D}} + \bar{\Omega}\boldsymbol{\mathcal{G}})\dot{\mathbf{p}}(t) + \boldsymbol{\mathcal{K}}\mathbf{p}(t) = \mathbf{f}(t), \tag{C.4}$$

where $\boldsymbol{\mathcal{M}} = \mathrm{diag}(m, m)$ is the mass matrix, $\boldsymbol{\mathcal{D}}$ is the damping matrix, $\boldsymbol{\mathcal{G}}$ represents the antisymmetric gyroscopic effect, and $\boldsymbol{\mathcal{K}}$ is the stiffness matrix, all of dimension 2×2. The matrices $\boldsymbol{\mathcal{D}}, \boldsymbol{\mathcal{G}}$, and $\boldsymbol{\mathcal{K}}$ are known to vary with injection pressure and rotational speed. The right hand side of Eq. C.4 includes external forces $\mathbf{f}(t)$ acting

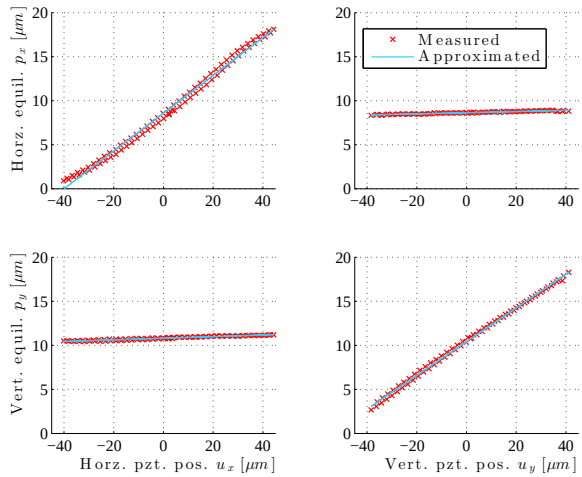

Figure C.5: Steady state characterization of input-output gains at $\bar{P}_{\text{inj}} = 6bar$, $\bar{\Omega} = 0rpm$: the experimental data reveal a linear mapping from $\mathbf{u}$ to lateral disc position $\mathbf{p}$.

on the shaft, which includes mass unbalance, external disturbances and active forces controlled with help of the piezoactuators. Section C.3.5 shows how to subtract the response from the unknown mass unbalance. Thus, by ensuring no impacts occur during collected data sets, only the response from active forces remain. These are not easily modelled due to the compressibility of air, which causes memory effect as known from Cummins equation [113]. The memory effect can effectively be modelled as time delays $\boldsymbol{\tau} = [\tau_x, \tau_y]^{\mathrm{T}}$ from piezoactuator position to force applied on the shaft. Section C.3.1 showed that the disc lateral movement could be approximated proportional to $\mathbf{u}$, and it is therefore reasonable to assume that the active forces are also proportional to the delayed signal $\mathbf{u}_\tau(t) \triangleq [u_x(t-\tau_x), u_y(t-\tau_y)]^{\mathrm{T}}$ with a gain $\boldsymbol{\mathcal{B}}_p$:

$$\boldsymbol{\mathcal{M}}\ddot{\mathbf{p}}(t)+(\boldsymbol{\mathcal{D}}+\bar{\Omega}\boldsymbol{\mathcal{G}})\dot{\mathbf{p}}(t)+\boldsymbol{\mathcal{K}}\mathbf{p}(t) = \boldsymbol{\mathcal{B}}_p\mathbf{u}_\tau(t), \quad \mathbf{u}_\tau(t) \triangleq [u_x(t-\tau_x), u_y(t-\tau_y)]^{\mathrm{T}} \quad \text{(C.5)}$$

This suggests a model structure for identification. With a model structure known, the identification of the rotor-bearing system parameters is sought through grey-box identification. The grey-box modelling is eased by reformulation of the dynamics Eq. C.5 to state space form, where a suitable choice of states is the lateral movement and velocity of the disc $\mathbf{x} \triangleq [p_x, p_y, \dot{p}_x, \dot{p}_y]^{\mathrm{T}}$. The output is $\mathbf{y}_b = \boldsymbol{\mathcal{C}}\mathbf{x} = \mathbf{p}$. The very simple model structure inevitably gives rise to modelling errors, which are included as process noise $\mathbf{v}(t)$. Measurement noise is modelled as an additive signal $\mathbf{w}(t)$.

This combination of process noise and measurement noise can be reduced to one equivalent noise term $\mathbf{d}_b(t)$ entering both the state and the output equation [45]. Therefore model errors and measurement noise are included as a stochastic additive signal $\mathbf{d}_b(t)$ entering both through an input gain $\boldsymbol{\mathcal{B}}_d$ and the measurements directly:

$$\begin{aligned} \dot{\mathbf{x}}(t) &= \boldsymbol{\mathcal{A}}\mathbf{x}(t) + \boldsymbol{\mathcal{B}}\mathbf{u}_\tau(t) + \boldsymbol{\mathcal{B}}_d\mathbf{d}_b(t), \quad \mathbf{x}(0) = \mathbf{x}_0, \\ \mathbf{y}(t) &= \boldsymbol{\mathcal{C}}\mathbf{x}(t) + \mathbf{d}_b(t), \end{aligned} \tag{C.6}$$

where the system-, input gain-, and output matrix are:

$$\boldsymbol{\mathcal{A}} = \begin{bmatrix} \mathbf{0} & \mathbf{I} \\ \mathbf{K} & \mathbf{D} \end{bmatrix}, \quad \boldsymbol{\mathcal{B}} = \begin{bmatrix} \mathbf{0} \\ \mathbf{B} \end{bmatrix}, \quad \boldsymbol{\mathcal{B}}_d = \begin{bmatrix} \mathbf{0} \\ \mathbf{B}_d \end{bmatrix}, \quad \boldsymbol{\mathcal{C}} = \begin{bmatrix} \mathbf{I} & \mathbf{0} \end{bmatrix}, \tag{C.7}$$

and $\mathbf{D} \triangleq -\boldsymbol{\mathcal{M}}^{-1}(\boldsymbol{\mathcal{D}} + \bar{\Omega}\boldsymbol{\mathcal{G}})$, $\mathbf{K} \triangleq -\boldsymbol{\mathcal{M}}^{-1}\boldsymbol{\mathcal{K}}$, and $\mathbf{B} \triangleq \boldsymbol{\mathcal{M}}^{-1}\boldsymbol{\mathcal{B}}_p$ are matrices to be identified along with the disturbance gain $\mathbf{B}_d$. $\mathbf{0}$ and $\mathbf{I}$ are zero-, and identity matrices respectively. $\mathbf{K}$, $\mathbf{D}$ and $\mathbf{B}$ are thus equivalent to stiffness, damping and input gain scaled by the mass matrix. In other words, $\boldsymbol{\mathcal{M}}$ is assumed to be the identity matrix. The equivalent stiffness therefore has units $[N/(kgm)]$, the equivalent damping has units $[Ns/(kgm)]$ and the equivalent input gain has units $[N/(kgm)]$, and they are simply referred to as stiffness, damping and input gain. Using only the measured piezoactuator position as input, the model in the Laplace domain reads:

$$\begin{bmatrix} p_x(s) \\ p_y(s) \end{bmatrix} = \underbrace{\overbrace{\begin{bmatrix} G_{b,xx}(s) & G_{b,xy}(s) \\ G_{b,yx}(s) & G_{b,yy}(s) \end{bmatrix}}^{\triangleq \mathbf{G}_b(s)} \overbrace{\begin{bmatrix} e^{-\tau_x s} & 0 \\ 0 & e^{-\tau_y s} \end{bmatrix}}^{\triangleq \mathbf{G}_\tau(s)}}_{\triangleq \mathbf{G}_{rb}(s)} \begin{bmatrix} u_x(s) \\ u_y(s) \end{bmatrix}, \tag{C.8}$$

in which $\{G_{b,xx}, G_{b,xy}, G_{b,yx}, G_{b,yy}\}$ are the individual transfer functions, and τ_x and τ_y are the delays from the pressure build-up in the gas film active forces. The time delay $\boldsymbol{\tau}$ is small, but not negligible. It is not easy to estimate directly; hence a first order Padé approximation is used instead, which gives:

$$\mathbf{G}_\tau(s) \approx \mathbf{G}_{\tilde{\tau}}(s) \triangleq \begin{bmatrix} G_{\tilde{\tau},x}(s) & 0 \\ 0 & G_{\tilde{\tau},y}(s) \end{bmatrix}, \quad G_{\tilde{\tau},j}(s) \triangleq \frac{1 - \frac{\tau_j}{2}s}{1 + \frac{\tau_j}{2}s}, \tag{C.9}$$

Equation C.9 has an equivalent state space description with state vector denoted $\mathbf{x}_\tau$, and matrices $\boldsymbol{\mathcal{A}}_\tau, \boldsymbol{\mathcal{B}}_\tau, \boldsymbol{\mathcal{C}}_\tau, \boldsymbol{\mathcal{D}}_\tau$. The controllable rotor-bearing model emerges from

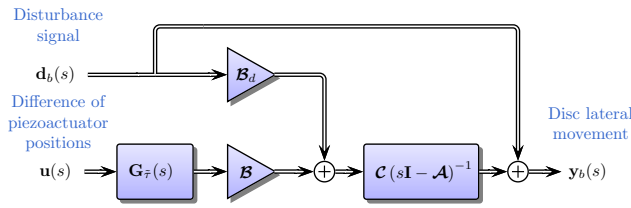

Figure C.6: Overview of the rotor-bearing model: the difference of piezoactuator positions $\mathbf{u}$ enters as input into the Padé approximated delays modelling the fluid memory effect. The signal $\mathbf{d}_b$ models the differences between measured and model response including measurement noise.

substitution of the Padé approximated time delay Eq. C.9 into Eq. C.6:

$$\begin{aligned}\overbrace{\begin{bmatrix}\dot{\mathbf{x}}(t)\\ \dot{\mathbf{x}}_\tau(t)\end{bmatrix}}^{\triangleq\dot{\mathbf{x}}_b(t)} &= \overbrace{\begin{bmatrix}\mathcal{A} & \mathcal{B}\mathcal{C}_\tau\\ \mathbf{0} & \mathcal{A}_\tau\end{bmatrix}}^{\triangleq\mathcal{A}_b}\overbrace{\begin{bmatrix}\mathbf{x}(t)\\ \mathbf{x}_\tau(t)\end{bmatrix}}^{\triangleq\mathbf{x}_b(t)} + \overbrace{\begin{bmatrix}\mathcal{B}\mathcal{D}_\tau\\ \mathcal{B}_\tau\end{bmatrix}}^{\triangleq\mathcal{B}_b}\mathbf{u}(t) + \overbrace{\begin{bmatrix}\mathcal{B}_d\\ \mathbf{0}\end{bmatrix}}^{\triangleq\mathcal{B}_{d,b}}\mathbf{d}_b(t), \quad \mathbf{x}_b(0)=\mathbf{x}_{b0}\\ \mathbf{y}_b &= \overbrace{\begin{bmatrix}\mathcal{C} & \mathbf{0}\end{bmatrix}}^{\triangleq\mathcal{C}_b(t)}\mathbf{x}_b(t)+\mathbf{d}_b(t),\end{aligned} \tag{C.10}$$

where $\mathbf{x}_b$ is the concatenated state vector, $\mathcal{A}_b, \mathcal{B}_b, \mathcal{B}_{d,b}$ and $\mathcal{C}_b$ are the state space matrices. Figure C.6 shows an overview of the rotor-bearing model. The signal $\mathbf{d}_b$ models the differences between measured and model response.

The parameters of Eqs. C.7 and C.9 in Eq. C.10 are identified by recasting the problem to a model parametrised in $\boldsymbol{\theta}_b \triangleq \{\mathbf{K}, \mathbf{D}, \mathbf{B}, \boldsymbol{\tau}, \mathbf{B}_d, \mathbf{x}_{b0}\}$ as $\mathfrak{M}_b(\boldsymbol{\theta}_b)$. Each matrix $\mathbf{K}, \mathbf{D}, \mathbf{B}, \mathbf{B}_d$ has four elements denoted by small letters and subscripts xx, xy, yx, yy, e.g. $\mathbf{K} = \begin{bmatrix}k_{xx} & k_{xy}\\ k_{yx} & k_{yy}\end{bmatrix}$. The initial state $\mathbf{x}_{b0}$ has six elements denoted by $\hat{x}_{j,0},\ j \in \{1,2,3,4,5,6\}$. The corresponding estimates are $\hat{\boldsymbol{\theta}}_b \triangleq \{\hat{\mathbf{K}}, \hat{\mathbf{D}}, \hat{\mathbf{B}}, \hat{\boldsymbol{\tau}}, \hat{\mathbf{B}}_d, \hat{\mathbf{x}}_{b0}\} = \left[\hat{k}_{xx}, \hat{k}_{xy}, \hat{k}_{yx}, \hat{k}_{yy}, \hat{d}_{xx}, \ldots, \hat{x}_{6,0}\right]^{\mathrm{T}}$. The model then reads:

$$\mathfrak{M}_b(\boldsymbol{\theta}_b): \begin{cases}\dot{\mathbf{x}}_b(t) = \mathcal{A}_b(\boldsymbol{\theta}_b)\mathbf{x}_b(t) + \mathcal{B}_b(\boldsymbol{\theta}_b)\mathbf{u}(t) + \mathcal{B}_{d,b}(\boldsymbol{\theta}_b)\mathbf{d}_b(t), \quad \mathbf{x}_b(0) = \mathbf{x}_{b0}(\boldsymbol{\theta}_b)\\ \mathbf{y}_b(t) = \mathcal{C}_b\mathbf{x}_b(t) + \mathbf{d}_b(t)\end{cases} \tag{C.11}$$

C.3.3 Grey-Box Model of Piezoactuators

A similar model can be set up for the PD-controlled piezoactuator pairs. Each pair of piezoactuators can be modelled as a second order low-pass filter. The piezoactuator dynamics is written as transfer functions with gains $\kappa_{a,j}$ and two poles $p_{1,j}$, and $p_{2,j}$, where the subscript j refers to the pair of horizontal (x) or vertical (y) piezoactuators. Considering the commanded reference position as input, the piezoactuator dynamics $\mathbf{G}_{act}$ then reads:

$$\begin{bmatrix} u_x(s) \\ u_y(s) \end{bmatrix} = \underbrace{\begin{bmatrix} G_{a,x}(s) & 0 \\ 0 & G_{a,y}(s) \end{bmatrix}}_{\triangleq \mathbf{G}_{act}} \begin{bmatrix} r_x(s) \\ r_y(s) \end{bmatrix}, \qquad G_{a,j}(s) = \frac{\kappa_{a,j}}{\left(\frac{1}{p_{1,j}}s+1\right)\left(\frac{1}{p_{2,j}}s+1\right)} \tag{C.12}$$

in which $G_{a,j}(s)$ is the second order filter of the specified form. The piezoactuator dynamics can also be written in state space form as a grey-box structure similar to Eq. C.6 with state vector $\mathbf{x}_a$. Let define an equivalent modelling error term $\mathbf{d}_a$ entering as input along with the commanded piezoactuator positions $\mathbf{r}$. The output is $\mathbf{u}$, and the unknown parameters are:

$$\boldsymbol{\theta}_a \triangleq [p_{1,x},\, p_{1,y},\, p_{2,x},\, p_{2,y},\, \kappa_{a,x},\, \kappa_{a,y},\, x_{a1,0},\, x_{a2,0},\, x_{a3,0},\, x_{a4,0}]^{\mathrm{T}}, \tag{C.13}$$

thus the actuator model $\mathfrak{M}_a(\boldsymbol{\theta}_a)$ has been set up, which reads:

$$\mathfrak{M}_a(\boldsymbol{\theta}_a): \begin{cases} \dot{\mathbf{x}}_a(t) = \boldsymbol{\mathcal{A}}(\boldsymbol{\theta}_a)\mathbf{x}_a(t) + \boldsymbol{\mathcal{B}}(\boldsymbol{\theta}_a)\mathbf{r}(t) + \boldsymbol{\mathcal{B}}_{d,a}(\boldsymbol{\theta}_a)\mathbf{d}_a(t), \quad \mathbf{x}_a(0) = \mathbf{x}_{a0}(\boldsymbol{\theta}_a) \\ \mathbf{u}(t) = \boldsymbol{\mathcal{C}}_a\mathbf{x}_a(t) + \mathbf{d}_a(t) \end{cases} \tag{C.14}$$

C.3.4 Description of Experiments

The sought model should represent the controllable gas bearing over the entire operating range. Previous work [41] show that the gas bearing coefficients mainly depend on two parameters: the rotational speed Ω and injection pressure P_{inj}, which can vary within $\Omega \in [0;6]krpm$ and $P_{\text{inj}} \in [3;7]bar$. Locally valid models can therefore be identified from data sets collected over a grid of these two parameters. Grid points are chosen in the sets $\bar{P}_{\text{inj}} \in \{3,4,5,6,7\}bar$ and rotational speeds $\bar{\Omega} \in \{0,4,6\}krpm$. Five to six data sets are collected at each grid point $(\bar{P}_{\text{inj}}, \bar{\Omega})$, and a model is identified from each data set. During the collected data sets, identifiability of the parameters is ensured by commanding a pseudo-random binary sequence (PRBS)

to the piezoactuators $\mathbf{r}(t)$, where the inputs are stepped randomly and mutually independently from $-1V$ to $1V$ at fixed sampling instants. The eigenfrequencies are very under-damped, and care should be taken to avoid rub due to over-excitation. The piezoactuator position references $\mathbf{r}(t)$ and measured difference of piezoactuator positions $\mathbf{u}(t)$ are logged as input and output respectively for the actuator submodel and $\mathbf{u}(t)$ and the lateral disc movement $\mathbf{p}(t)$ are logged as input and outputs for the rotor-bearing model.

C.3.5 Prefiltering

Prefiltering is required before carrying out the identification to remove offsets, response from run-out, and mass unbalance from the raw position measurements $\mathbf{p}_{raw}$. A data set is collected at each investigated operational condition $(\bar{P}_{\text{inj}}, \bar{\Omega})$. Each data set allows generation of a filter $\boldsymbol{\mathcal{F}}_r$ to remove run-out and unbalance response from the lateral disc movement measurements. During these experiments, the piezoactuators are kept stationary, which allows mapping of the measured response $\mathbf{p}_{raw}$ as function of the angular position of the rotor ϕ. Thereby the filtered lateral disc movement is $\mathbf{p}(t) = \mathbf{p}_{raw}(t) - \boldsymbol{\mathcal{F}}_r(\phi(t))$. For the signals collected for identification, the mean lateral disc position is subtracted from each data set, and a median filter of size 3 is used to reduce measurement noise from the disc movement measurements. The compensation for run-out and unbalance significantly improves the signal quality and allows micrometer precision measurement of the response from perturbing the piezoactuators.

C.3.6 Identification of Rotor-Bearing Models

The optimal rotor-bearing model $\mathfrak{M}_b(\boldsymbol{\theta}_b^\star)$ from each data set is chosen as the one associated with the minimum cost of a prediction error cost function $W_b(\boldsymbol{\theta}_b) \triangleq \sum_{t=1}^{N} \boldsymbol{\epsilon}(t)^{\mathrm{T}} \boldsymbol{\epsilon}(t)$, where the prediction error $\boldsymbol{\epsilon}$ is defined as the difference between the one step ahead measured and the predicted output $\boldsymbol{\epsilon}(t) \triangleq \mathbf{p}(t) - \hat{\mathbf{p}}(t)$. The minimum is sought using the prediction error method (PEM) [45], such that the optimal parameter set reads:

$$\boldsymbol{\theta}_b^\star = \min_{\boldsymbol{\theta}_b} W_b(\boldsymbol{\theta}_b) \tag{C.15}$$

The model update iterations should stop when the parameter estimates converge. This convergence is decided when the relative improvement norm is less than the bound 10^{-4}. A rotor-bearing model $\mathfrak{M}_b(\hat{\boldsymbol{\theta}}_b)$ is identified from each data set $\{\mathbf{u}(t), \mathbf{p}(t)\}$.

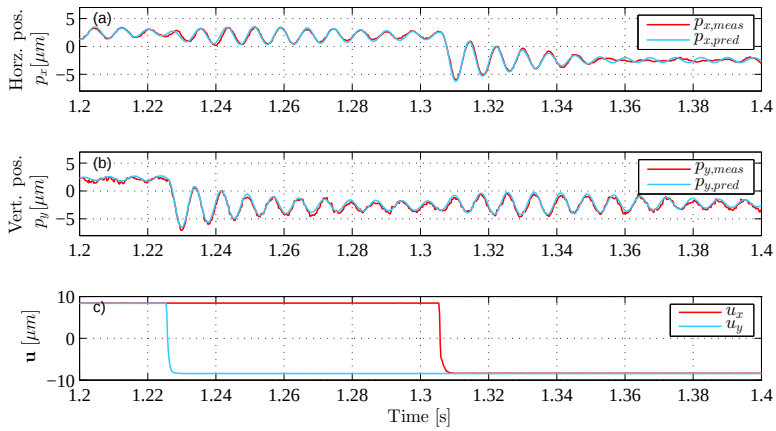

Figure C.7: Example of identification from data set collected at $\bar{P}_{\text{inj}} = 5bar, \bar{\Omega} = 6.0krpm$, here a zoom in time interval in the interval $t \in [1.2 : 1.4]s$. The piezoactuator positions $[u_x, u_y]$ shown in c) cause disc vibrations. The lateral disc movement $\mathbf{p}_{meas} = [p_x, p_y]$ and the simulated movement using the identified model $\mathbf{p}_{pred} = [\hat{p}_x, \hat{p}_y]$ subject to same excitation is shown in a) and b). The model predicts both the direct and the cross coupling oscillations.

The identified model is simulated using the measured input sequence to generate the model predicted response to allow comparison. Figure C.7 shows an example of measured lateral disc movement $\mathbf{p}_{meas} = [p_{x,meas}, p_{y,meas}]^{\mathrm{T}}$ and their predicted $\mathbf{p}_{pred} = [p_{x,pred}, p_{y,pred}]^{\mathrm{T}}$ for a part of one of the 86 data sets. A step signal commanded to the piezoactuators in one direction generates disc vibrations in both orthogonal directions due to the cross-coupling effect from the gas film forces and the gyroscopic moment. The identified model predicts direct and cross-coupling oscillations well. All the available data sets give similar results.

The fourteen key parameters being stiffness, damping, input gain and time delay estimates are comparable across identified models, and they determine the eigenfrequencies, the static gains and delays of the models. Parameters such as the initial state $\hat{\mathbf{x}}_{b0}$, and disturbance gain $\hat{\mathbf{B}}_{d,b}$ are more descriptive for the particular dataset and are not relevant to compare across identified models. The key parameters are treated further in Sec. C.4.

Param.	$p_{1,x}\ \left[\frac{rad}{s}\right]$	$p_{2,x}\ \left[\frac{rad}{s}\right]$	$p_{1,y}\ \left[\frac{rad}{s}\right]$	$p_{2,y}\ \left[\frac{rad}{s}\right]$	$\kappa_{a,x}\ \left[\frac{m}{m}\right]$	$\kappa_{a,y}\ \left[\frac{m}{m}\right]$
Value	3078	8143	2452	6494	1.863	1.865

Table C.2: Actuator model parameters.

C.3.7 Identification of Actuator Models

The actuator dynamics is identified using the same procedure as in Sec. C.3.6. An actuator model $\mathfrak{M}_a(\hat{\boldsymbol{\theta}}_a)$ is identified from each data set $\{\mathbf{r}(t), \mathbf{u}(t)\}$. Figure C.8 shows the estimated gains and poles $\{\kappa_x, \kappa_y, p_{1,x}, p_{2,x}, p_{1,y}, p_{2,y}\}$ of the identified models using Eq. C.12 across the data sets. The actuator parameters do not vary over the range of injection pressure and rotational speed, but there are outliers in the pole and gain estimates. There are two main reasons for this. The well damped actuator dynamics does not show clear resonances. Further, the step frequency of the excitation signals is low compared to the dynamics of the piezoactuators. Higher frequent stepping intervals in the PRBS signals would however excite the underdamped eigenfrequencies of the bearing dynamics and cause big amplitude shaft oscillations.

Since the actuator dynamics are found to be independent of rotational speed and injection pressure, a nominal model is chosen as the one with the highest mean of fit-percentages in cross-validation. This is No. 39, which has parameters listed in Table C.2.

C.3.8 Model Cross-Validation

The quality of the identified models is assessed by cross-validating them on other data sets collected at similar operational conditions.

A simulation compares how well each identified model is at predicting the response for a cross-validation data set. Model j identified from dataset j is validated on dataset $j+1$ collected at the same rotational speed and injection pressure. Figure C.9 shows a histogram of the cross-validation fits. The horizontal fit mean value is $\mu_{bh} = 81.1\%$ and its standard deviation is $\sigma_{bh} = 2.66\%$, and the vertical fit mean value is $\mu_{bv} = 85.1\%$ and its standard deviation is $\sigma_{bv} = 3.37\%$. These are high fit percentages indicating the models can well describe the behaviour of the rotor-bearing system. The simulation residual $\boldsymbol{\epsilon}(t)$ defined as the difference between measured response $\mathbf{p}$ and predicted response $\hat{\mathbf{p}}(\hat{\boldsymbol{\theta}}_b)$ should ideally be white noise. This is not the case, and the residual will to some extent be cross-correlated with the inputs.

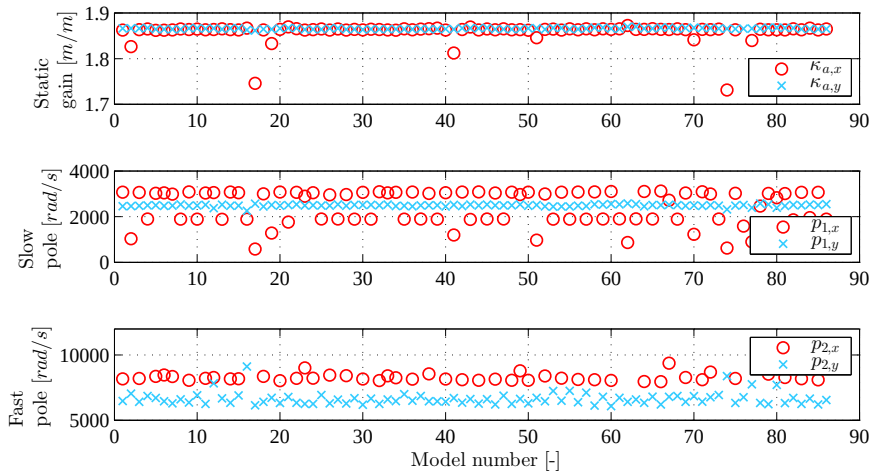

Figure C.8: Estimated gains $\kappa_{a,x}, \kappa_{a,y}$, slow poles $p_{1,x}, p_{1,y}$, and fast poles $p_{2,x}, p_{2,y}$ of the actuator models from Eq. C.12 across the models identified from different data sets.

This is a penalty of the simple model structure. The infinity norm of the residuals is, however, small for all 86 datasets, indicating good significance of the results.

Similar analysis is made for the piezoactuator submodel. The piezoactuator model is cross-validated against the other piezoactuator datasets. The results are shown in Fig. C.10. The actuator horizontal fit mean value is $\mu_{ah} = 98.34\%$ and its standard deviation is $\sigma_{ah} = 0.074\%$, whereas the fit percentages for the pair of vertical piezoactuators have $\mu_{av} = 99.42\%$ and its standard deviation is $\sigma_{av} = 0.058\%$. The lower horizontal fits match well with the bigger variation in parameters of the horizontal piezoactuators from Fig. C.8.

C.4 Linear Parameter Varying Model of Rotor-Bearing System

The locally identified models provide the basis for construction of a parametrised rotor-bearing model valid over the operating range. The model is developed in three steps: the first step is the approximation of each key parameter from the 86 parameter estimates onto smooth surfaces. These individually approximated terms are used in the second step to assemble a linear parameter varying model of the rotor-bearing system parametrised in speed and injection pressure. The last step is to cascade the linear parameter varying model with the piezoactuator model to obtain the model of the entire rotor-bearing-actuator system. The steps are elaborated in the following.

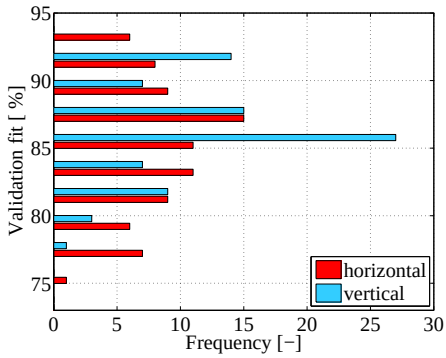

Figure C.9: Cross-validation fit percentages of the horizontal and vertical residuals in validation of the identified bearing submodels cross-validated on other data sets.

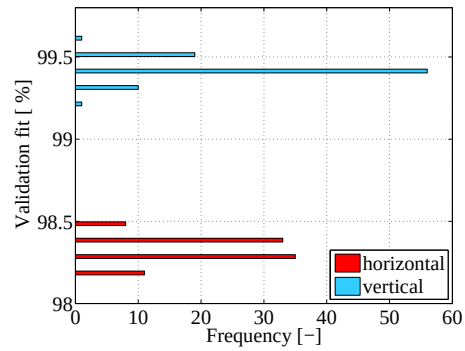

Figure C.10: Horizontal and vertical validation fit percentages of the identified actuator submodels cross-validated on other data sets.

The rotor-bearing model parameters are expected to depend continuously on injection pressure and rotational speed. Each key parameter is therefore approximated onto a polynomial surface. A second order polynomial is chosen to avoid over-fitting. Thereby the identified stiffness, damping and gain matrix coefficients $(\cdot)_{ij}$, where $(\cdot) \in \{k, c, b\}$ and $i, j \in \{x, y\}$ (e.g. k_{xy}) and the time delays τ_x and τ_y are modelled as:

$$\begin{aligned} k_{ij}(\Omega, P_{\text{inj}}) =& k_{0,ij} + k_{1,ij}P_{\text{inj}} + k_{2,ij}\Omega + k_{3,ij}\Omega P_{\text{inj}} + k_{4,ij}P_{\text{inj}}^2 + k_{5,ij}\Omega^2 \\ c_{ij}(\Omega, P_{\text{inj}}) =& c_{0,ij} + c_{1,ij}P_{\text{inj}} + c_{2,ij}\Omega + c_{3,ij}\Omega P_{\text{inj}} + c_{4,ij}P_{\text{inj}}^2 + c_{5,ij}\Omega^2 \\ b_{ij}(\Omega, P_{\text{inj}}) =& b_{0,ij} + b_{1,ij}P_{\text{inj}} + b_{2,ij}\Omega + b_{3,ij}\Omega P_{\text{inj}} + b_{4,ij}P_{\text{inj}}^2 + b_{5,ij}\Omega^2 \\ \tau_i(\Omega, P_{\text{inj}}) =& \tau_{0,i} + \tau_{1,i}P_{\text{inj}} + \tau_{2,i}\Omega + \tau_{3,i}\Omega P_{\text{inj}} + \tau_{4,i}P_{\text{inj}}^2 + \tau_{5,i}\Omega^2 \end{aligned} \tag{C.16}$$

This describes a surface in space, whose cross-sections are a parabola. The parameters of the polynomial models are fitted using linear least squares and the calculated regression coefficients are listed in table C.6. Note the units of the stiffness, damping and input gain equivalents as described in Sec. C.3. The stiffness coefficients $\{\hat{k}_{xx}, \hat{k}_{xy}, \hat{k}_{yx}, \hat{k}_{yy}\}$ are shown in Fig. C.11 along with their polynomial approximations. Similarly Figs. C.12 and C.13 show the estimated damping coefficients and input gains with the corresponding polynomial approximations. The variation of each key parameter's estimate for a fixed operational condition is small, indicating a good consistency across different data sets.

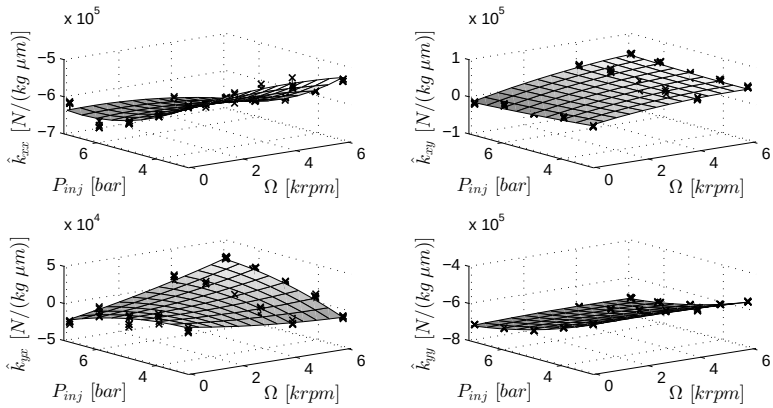

Figure C.11: Identified stiffness coefficients as function of injection pressure P_{inj} ($1bar = 0.1MPa$) and rotational speed Ω, along with 2^{nd} order polynomial fit, assisting lines indicate 3D location of the parameter estimates.

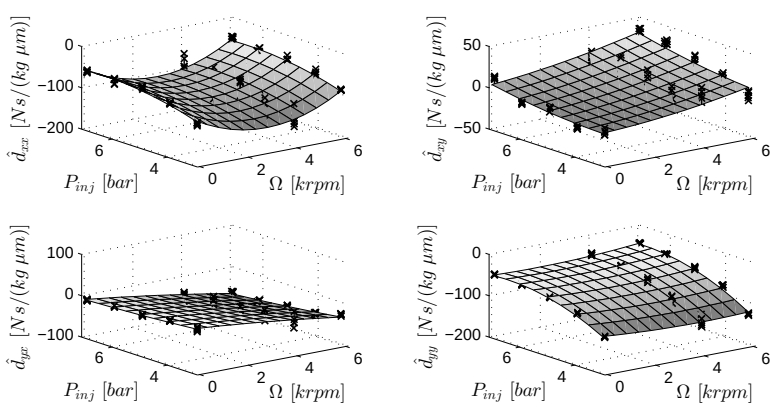

Figure C.12: Identified damping coefficients as function of injection pressure P_{inj} ($1bar = 0.1MPa$) and rotational speed Ω, along with 2^{nd} order polynomial fit, assisting lines indicate 3D location of the parameter estimates.

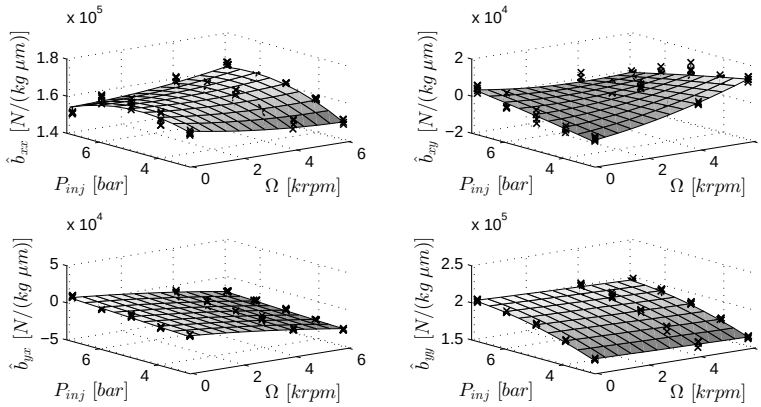

Figure C.13: Identified input gain coefficients as function of injection pressure P_{inj} ($1bar = 0.1MPa$) and rotational speed Ω, along with 2^{nd} order polynomial fit, assisting lines indicate 3D location of the parameter estimates.

Figures C.14 and C.15 show comparisons of the estimated time delays between the identified models and their polynomial approximations. It is interesting to note that the delay is bigger in the horizontal direction. The RMS deviation for horizontal and vertical time delays are $\Delta\tau_{x,RMS} = 0.088ms$, $\Delta\tau_{y,RMS} = 0.041ms$. Compared to the sampling period of $T_s = 0.2ms$, the variation in estimated time delays is small, and since their identification is not easy due to the combination of dynamics and time delays, the results are considered good. It is evident that for increasing pressure the time delay drops, which intuitively makes sense: a larger pressure allows a faster pressure build-up.

All parameters (stiffness, damping, gain terms and time delays) have been parametrised in the same manner. This in turn allows for the assembly of the linear parameter varying model:

$$\begin{aligned}\dot{\mathbf{x}}(t) =& \boldsymbol{\mathcal{A}}(\Omega, P_{\text{inj}})\mathbf{x}(t) + \boldsymbol{\mathcal{B}}(\Omega, P_{\text{inj}})\mathbf{u}_{\tilde{\tau}}(t, \Omega, P_{\text{inj}}) \\ & \mathbf{u}_{\tilde{\tau}} \triangleq [u_x(t - \tau_x(\Omega, P_{\text{inj}})), u_y(t - \tau_y(\Omega, P_{\text{inj}}))]^{\mathrm{T}} \\ \mathbf{y}(t) =& \boldsymbol{\mathcal{C}}\mathbf{x}(t)\end{aligned} \tag{C.17}$$

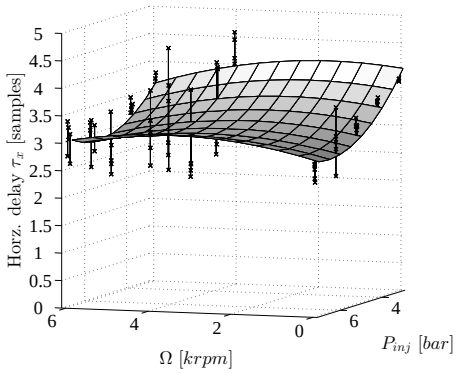

Figure C.14: Identified and linear parameter varying model horizontal time delay $[samples@5kHz]$ between Eq. C.17 over varying speed and injection pressure, $(1bar = 0.1MPa)$.

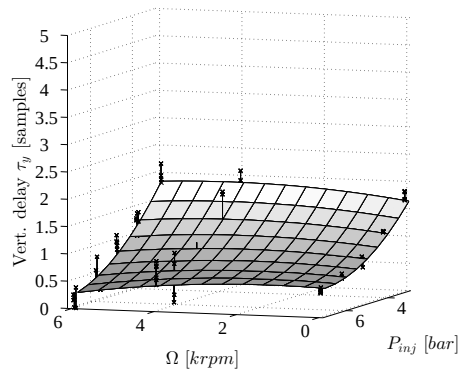

Figure C.15: Identified and linear parameter varying model vertical time delay $[samples@5kHz]$ between Eq. C.17 over varying speed and injection pressure.

Where the parameters from Eq. C.16 are used to assemble the matrices:

$$\begin{aligned}\boldsymbol{\mathcal{A}}(\Omega, P_{\text{inj}}) = &\underbrace{\begin{bmatrix}\mathbf{0} & \mathbf{I}\\ \mathbf{K}_0 & \mathbf{D}_0\end{bmatrix}}_{\boldsymbol{\mathcal{A}}_0} + \underbrace{\begin{bmatrix}\mathbf{0} & \mathbf{0}\\ \mathbf{K}_1 & \mathbf{D}_1\end{bmatrix}}_{\boldsymbol{\mathcal{A}}_1} P_{\text{inj}} + \underbrace{\begin{bmatrix}\mathbf{0} & \mathbf{0}\\ \mathbf{K}_2 & \mathbf{D}_2\end{bmatrix}}_{\boldsymbol{\mathcal{A}}_2} \Omega + \underbrace{\begin{bmatrix}\mathbf{0} & \mathbf{0}\\ \mathbf{K}_3 & \mathbf{D}_3\end{bmatrix}}_{\boldsymbol{\mathcal{A}}_3}\\ &+ \Omega P_{\text{inj}} + \underbrace{\begin{bmatrix}\mathbf{0} & \mathbf{0}\\ \mathbf{K}_4 & \mathbf{D}_4\end{bmatrix}}_{\boldsymbol{\mathcal{A}}_4} P_{\text{inj}}^2 + \underbrace{\begin{bmatrix}\mathbf{0} & \mathbf{0}\\ \mathbf{K}_5 & \mathbf{D}_5\end{bmatrix}}_{\boldsymbol{\mathcal{A}}_5} \Omega^2,\\ \boldsymbol{\mathcal{B}}(\Omega, P_{\text{inj}}) = &\begin{bmatrix}\mathbf{0}\\ \mathbf{B}(\Omega, P_{\text{inj}})\end{bmatrix},\\ \mathbf{B}(\Omega, P_{\text{inj}}) = &\mathbf{B}_0 + \mathbf{B}_1 P_{\text{inj}} + \mathbf{B}_2 \Omega + \mathbf{B}_3 \Omega P_{\text{inj}} + \mathbf{B}_4 P_{\text{inj}}^2 + \mathbf{B}_5 \Omega^2,\\ \boldsymbol{\tau}(\Omega, P_{\text{inj}}) = &\boldsymbol{\tau}_0 + \boldsymbol{\tau}_1 P_{\text{inj}} + \boldsymbol{\tau}_2 \Omega + \boldsymbol{\tau}_3 \Omega P_{\text{inj}} + \boldsymbol{\tau}_4 P_{\text{inj}}^2 + \boldsymbol{\tau}_5 \Omega^2\end{aligned} \tag{C.18}$$

This linear parameter varying model has rotational speed and injection pressure as scheduling parameters, and for constant parameters $(\Omega, P_{\text{inj}}) = (\bar{\Omega}, \bar{P}_{\text{inj}})$, the bearing transfer function can then be defined:

$$\begin{aligned}\mathbf{G}_{rb}(s, \bar{\Omega}, \bar{P}_{\text{inj}}) = &\mathbf{G}_b(s, \bar{\Omega}, \bar{P}_{\text{inj}}) \mathbf{G}_{\tilde{\tau}}(s, \bar{\Omega}, \bar{P}_{\text{inj}}),\\ \mathbf{G}_b(s, \bar{\Omega}, \bar{P}_{\text{inj}}) = &\boldsymbol{\mathcal{C}} \left(s\mathbf{I} - \boldsymbol{\mathcal{A}}(\bar{\Omega}, \bar{P}_{\text{inj}})\right)^{-1} \boldsymbol{\mathcal{B}}(\bar{\Omega}, \bar{P}_{\text{inj}})\end{aligned} \tag{C.19}$$

The linear parameter varying model in Eq. C.17 is valid if it preserves the main characteristics for the rotor-bearing system such as natural frequencies, damping factors and static gains $\mathbf{G}_{dc} = \mathbf{G}_{rb}(0, \bar{\Omega}, \bar{P}_{\text{inj}}) = \left[\begin{smallmatrix} g_{xx} & g_{xy} \\ g_{yx} & g_{yy} \end{smallmatrix}\right]$. These characteristics can be directly calculated from the experimentally identified models and compared to those of developed model $\mathbf{G}_{rb}(s, \bar{\Omega}, \bar{P}_{\text{inj}})$. The identified models have two pairs of complex conjugate eigenvalues, which can be listed as two natural frequencies ω_1, ω_2 and corresponding damping factors ζ_1, ζ_2. Figure C.16 shows a comparison of the natural frequencies ω_1 and ω_2 between the linear parameter varying model and the identified rotor-bearing models. The quality of the linear parameter varying model is quantified by the deviation defined for a given pressure $\bar{P}_{\text{inj}}$ and rotational speed $\bar{\Omega}$ as the difference between the identified parameter and parameter predicted using Eq. C.16. The RMS deviation for the first and 2nd eigenvalue pairs are $\Delta\omega_{1,RMS} = 1.13Hz$, $\Delta\omega_{2,RMS} = 0.58Hz$ respectively.

Figure C.17 shows a comparison of the damping factors of the eigenvalues. The RMS deviation for the damping factors of the first and 2nd eigenvalue are $\Delta\zeta_{1,RMS} = 0.0104[-]$ and $\Delta\zeta_{2,RMS} = 0.0063[-]$. The damping factors are in general more uncertain, which makes the polynomial approximation more uncertain. It is evident that the results collected at $\bar{\Omega} = 4krpm$ are in general more uncertain than results collected at other operational conditions. The measurement quality of the lateral disc movement relies on the quality of the filter to remove run-out and unbalance, which in turn relies on a well defined stationary mass unbalance orbit. This is not the case for the results collected around $4krpm$, where small deviations occur in the orbit, indicating non-synchronous vibration. The filter is therefore not able to eliminate the mass unbalance response. The static gain matrix is shown in Fig. C.18 along with the static gains of the identified models. The maximum observed deviation is $0.016\ m/m$, and the standard deviation for each gain is $[\sigma_{g,xx}, \sigma_{g,xy}, \sigma_{g,yx}, \sigma_{g,yy}]^{\mathrm{T}} = [0.0031,\ 0.0022,\ 0.0027,\ 0.0031]^{\mathrm{T}} m/m$.

The entire model results from cascading the linear parameter varying model with the piezoactuator model Eq. C.12:

$$\mathbf{G}(s, \bar{\Omega}, \bar{P}_{\text{inj}}) = \mathbf{G}_{rb}(s, \bar{\Omega}, \bar{P}_{\text{inj}})\mathbf{G}_{act}(s), \tag{C.20}$$

which is readily evaluated for a given operational condition.

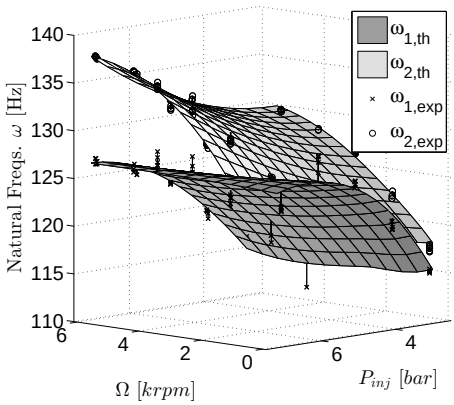

Figure C.16: Natural frequencies of the experimentally identified models and the linear parameter varying model Eq. C.17 over varying speed and injection pressure, $(1bar = 0.1MPa)$.

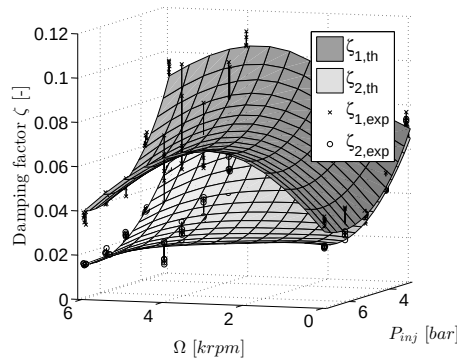

Figure C.17: Damping factors of experimentally identified models and the linear parameter varying model Eq. C.17 over varying speed and injection pressure, $(1bar = 0.1MPa)$.

C.5 Decentralised P-control of Controllable Gas Bearing

The poor damping properties of the controllable gas bearing can be improved by means of active control. A P-controller is designed using the proposed model, which strongly increases the closed loop damping factor. Figure C.19 provides an overview of the closed loop system. Experimental results for selected operational conditions validate the strong damping enhancement. Comparisons show a good agreement between the simulated and measured response, and confirms suitability of the identification procedure.

The identified models show that the direct couplings from horizontal/vertical piezoactuator to horizontal/vertical disc movement have gains an order of magnitude larger than the cross coupling gains. This makes decentralised control a feasible option. The controller should improve the damping properties and reject disturbances in a frequency range around the under-damped eigenfrequencies. Our recent work [4] show, that this is possible with a proportional controller, where an interval of positive feedback gains provide damping injection. Therefore a proportional controller is designed for the horizontal and vertical directions to improve the damping properties.

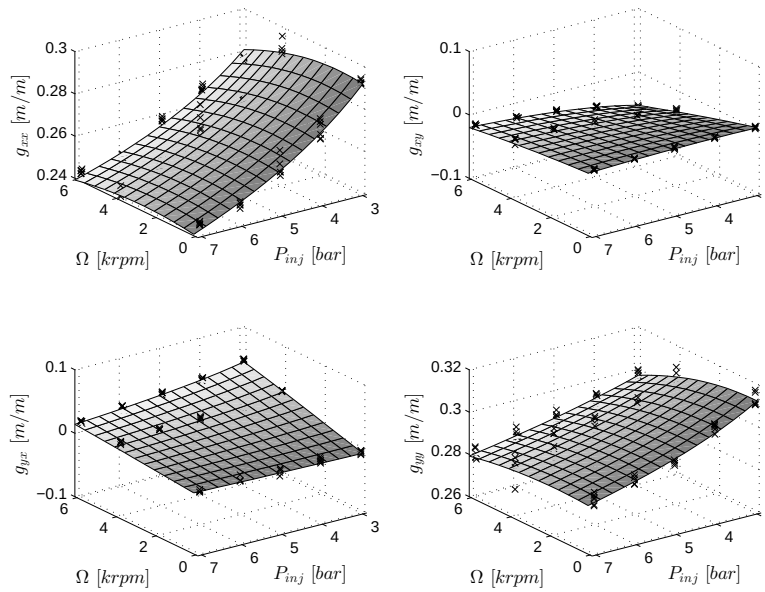

Figure C.18: Comparison of static gains between experimentally identified models and the linear parameter varying model Eq. C.17 over varying speed and injection pressure.

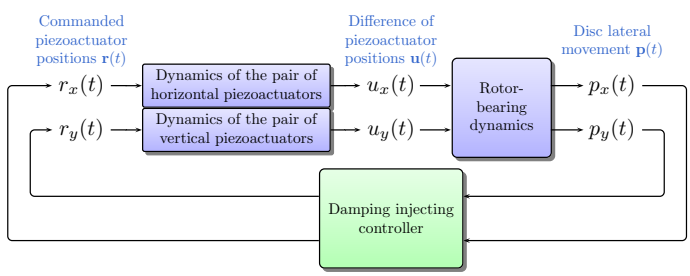

Figure C.19: Block diagram of the closed loop system. The horizontal piezoactuators are decoupled from the vertical ones. The lateral disc movement is used by the feedback controller to generate piezoactuator reference positions.

The control law is $\mathbf{r}(s) \triangleq \mathbf{K}_{pl}(s)\mathbf{p}(s)$, where the controller $\mathbf{K}_{pl}$ has the form:

$$\mathbf{K}_{pl}(s) \triangleq \begin{bmatrix} \kappa_x & 0 \\ 0 & \kappa_y \end{bmatrix} H_{lp}(s) \tag{C.21}$$

The controller parameters to be tuned are the proportional gains κ_x and κ_y. An n_K-th order lowpass filter $H_{lp}(s)$ is inserted to reduce controller sensitivity towards high frequency oscillations. The developed model Eq. C.20 provides an excellent basis for offline design, which avoids the risk of instability during online tuning. Upon closing the loop with the controller $\mathbf{K}_{pl}$, the output sensitivity $\mathbf{S}_o$ and closed loop controller sensitivity $\mathbf{K}_{pl}\mathbf{S}_o$ can be calculated, where:

$$\mathbf{S}_o(s) \triangleq (\mathbf{I}_2 - \mathbf{G}(s)\mathbf{K}_{pl}(s))^{-1}. \tag{C.22}$$

The output sensitivity $\mathbf{S}_o$ and closed loop controller sensitivity $\mathbf{K}_{pl}\mathbf{S}_o$ are useful tools for tuning the controller gains. The output sensitivity both allows evaluation of the reduction in sensitivity in the desired frequency range, while at the same time evaluating the increase in sensitivity at other frequencies. Similarly the closed loop controller sensitivity $\mathbf{K}_{pl}\mathbf{S}_o$ allows inspection of the required control effort. The controller design produces positive feedback and the choices $\kappa_x = 1.1250\ m/m$,$\kappa_y = 0.99\ m/m$, increases the damping factor by a factor 9.0 and 14.5 respectively. A first order low-pass filter $H_{lp}(s) \triangleq p_{lp}/(s+p_{lp})$ with bandwidth $p_{lp} = 1000\ Hz$ is used to avoid counteraction of high frequency disturbances. The output sensitivity and closed loop controller sensitivity shown in Fig. C.20 reveal the desirable properties: the sensitivity is greatly reduced close to the resonance frequencies, thus increasing horizontal and vertical damping. This comes at the cost of a disturbance amplification for low frequencies in the horizontal direction. An increase in sensitivity in some frequency interval is unavoidable due to Bode's sensitivity integral [104], and this is affordable as the mass unbalance response at these frequencies is low. Figure C.21 shows the open loop magnitude response $\mathbf{p}(s) = \mathbf{G}(s)\mathbf{r}(s)$ compared to the closed loop input disturbance response $\mathbf{p}(s) = \mathbf{S}_o(s)\mathbf{G}(s)\mathbf{r}(s)$. The reduction in peak gain is evident.

C.5.1 Experimental Results

The increase in damping is experimentally validated by comparing the lateral disc response to impulse excitation with and without the controller proposed. Both the horizontal and vertical controllers are simultaneously active. An impact hammer

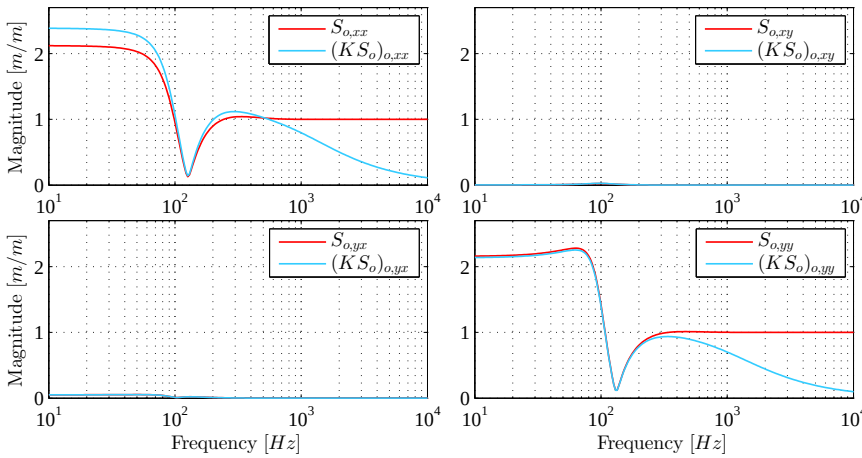

Figure C.20: Output sensitivity $\mathbf{S}_o$ and closed loop controller sensitivity $\mathbf{K}_{pl}\mathbf{S}_o$ for the controller $\mathbf{K}_{pl}$.

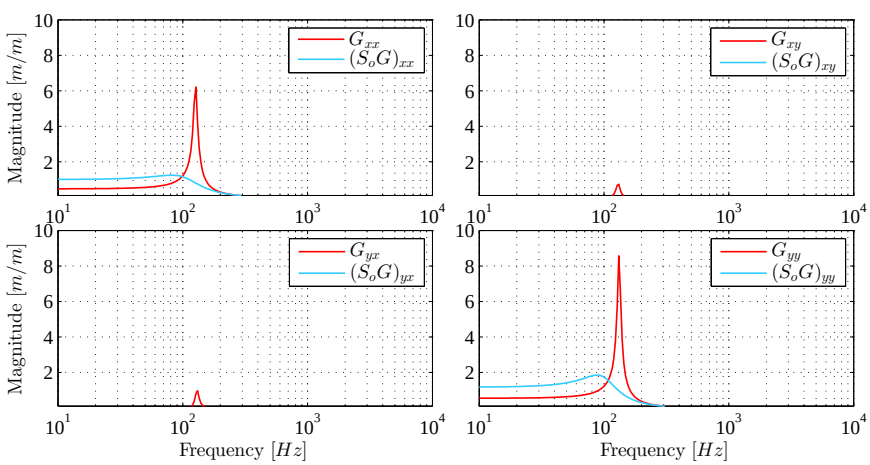

Figure C.21: Bode magnitude diagram for the open loop system $\mathbf{G}$ and closed input disturbance response $\mathbf{S}_o\mathbf{G}$ for the controller $\mathbf{K}_{pl}$.

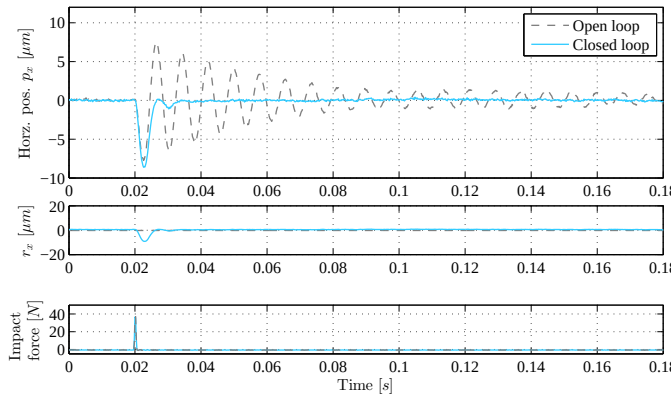

Figure C.22: Horizontal open and closed loop impact responses and measured impact forces.

is used to excite the shaft close to the controllable gas bearing while measuring the impact force to ensure equal excitation across the experiments to be compared. Figure C.22 shows the horizontal impact responses. Only the horizontal responses and control signals are shown as the controller almost eliminates cross-coupling oscillations. The increase in damping is evident. A vertical impact shown in Fig. C.23 reveals a similar performance as expected. The impact responses are fitted to a two degrees of freedom using the system identification procedure described in [1]. This allows comparison between the expected results using the model and the results obtained from experiments. The expected and obtained open loop natural frequencies $\omega_{1,ol}, \omega_{2,ol}$ and similarly closed loop natural frequencies $\omega_{1,cl}, \omega_{2,cl}$ are compared in Table C.3, and show good agreement. Table C.4 similarly compares the expected and obtained open loop damping factors $\zeta_{1,ol}, \zeta_{2,ol}$ and closed loop damping factors $\zeta_{1,cl}, \zeta_{2,cl}$. The results match within a factor two, which is considered a good agreement. A root locus analysis in [4], show that a small change in proportional gain results in a large change in damping factor for the gas bearing, similarly a small model uncertainty can cause a large damping factor uncertainty.

The measured impact responses are validated against the model using the following approach. An impact enters the rotor-bearing dynamics directly without the time delay and the piezoactuator dynamics, but it enters with a scaling factor g_f as the impact is a force signal $f(t)$, and the model input is a difference of piezoactuator positions. The impact response is thus given in the Laplace domain as $\mathbf{p}(s) = \mathbf{G}_b(s) g_f f(s)$ from Eq. C.8. This scaling factor is found using a linear least

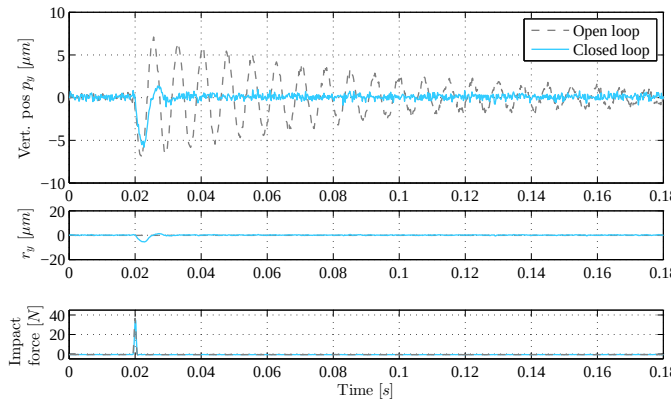

Figure C.23: Vertical open and closed loop impact responses and measured impact forces.

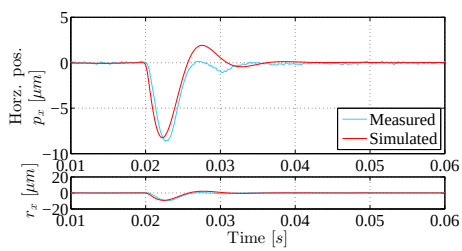

Figure C.24: Simulated and measured horizontal closed loop impact response.

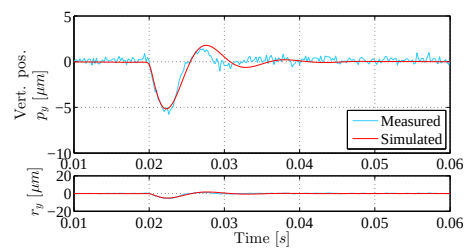

Figure C.25: Simulated and measured vertical closed loop impact response.

Natural frequency	$\omega_{1,ol}$ $[Hz]$	$\omega_{1,cl}$ $[Hz]$	$\omega_{2,ol}$ $[Hz]$	$\omega_{2,cl}$ $[Hz]$
Expected from model	126.6	99.9	132.1	105.1
Obtained Experimentally	126.3	89.9	134.4	111.6

Table C.3: Expected and obtained open loop natural frequencies $\omega_{1,ol}$, $\omega_{2,ol}$ and expected and obtained closed loop natural frequencies $\omega_{1,cl}$, $\omega_{2,cl}$.

squares on the measured and simulated non-scaled response. Figures C.24 and C.25 show comparisons of the measured and simulated horizontal and vertical impacts, which show great agreement.

The controller stabilises the controllable gas bearing for non-zero rotation speeds as well, which can be validated from the sensitivity function. This is proven for a

Damping factor	$\zeta_{1,ol}$ $[-]$	$\zeta_{1,cl}$ $[-]$	$\zeta_{2,ol}$ $[-]$	$\zeta_{2,cl}$ $[-]$
Expected from model	0.035	0.318	0.029	0.424
Obtained Experimentally	0.026	0.658	0.016	0.446

Table C.4: Expected and obtained open loop damping factors $\zeta_{1,ol}$, $\zeta_{2,ol}$ and expected and obtained closed loop damping factors $\zeta_{1,cl}$, $\zeta_{2,cl}$.

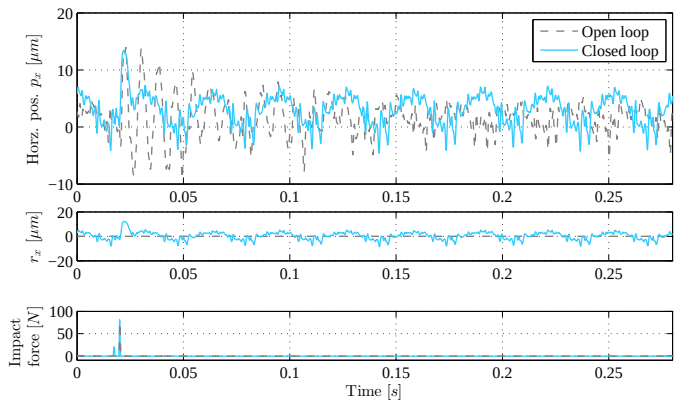

Figure C.26: Experimental open vs closed loop horizontal impact response at $\bar{\Omega} = 2.05\ krpm$.

rotational speed of $\bar{\Omega} = 2.05\ krpm$. Figures C.26 and C.27 show a horizontal and a vertical impact respectively. Here, the run-out filter has not been used to remove mass unbalance response. The mass unbalance response is more pronounced in the horizontal direction, still, the damping increase is evident.

The obtained controller performance is close to the expected. The results show, that the proposed modelling methodology can be used to develop accurate models, which can be used effectively for model based controller design.

C.6 Discussion

The presented approach offers a systematic procedure to model rotor-bearing systems. The models have low complexity, yet they suffice for controller design since they capture the essential dynamics. The procedure is general in the sense that in many real applications, the mathematical model does not describe the behaviour of the plant with sufficient accuracy, which makes the model difficult to use for model based controller design. The methodology of the grey-box identification

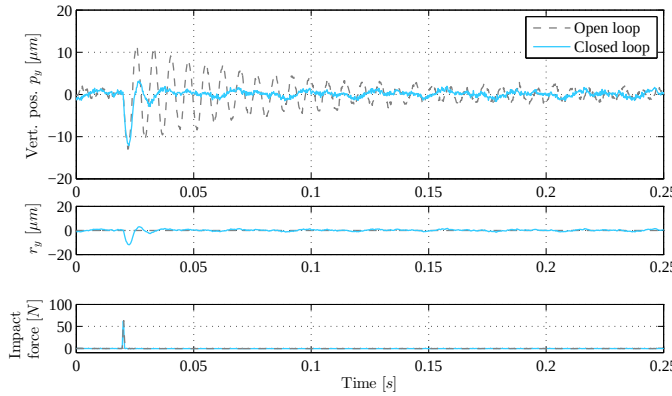

Figure C.27: Experimental open vs closed loop vertical impact response at $\bar{\Omega} = 2.05\ krpm$.

can be applied "in situ" and accurately identifies eigenfrequencies and damping factors, which are in general difficult to estimate for eigenfrequencies so closely placed. The suggested method does not require knowledge of the geometry of the test rig to be modelled, and it avoids solving the Reynolds equation, CFD methods and finite element modelling along with the time-consuming tuning required for these methodologies. The suggested method does not allow direct estimation of the gyroscopic effect nor the mass directly, nor are they necessary for control purposes. However, their effects are implicitly included in the identified parameters. The mass matrix can be estimated from impact responses with known impact forces. The proposed filter is capable of removing both run-out and mass unbalance, and it can be applied online. This gives the possibility of using the controller to counteract mass unbalance or to only be active when the disc deviates from the mass unbalance orbit. The grey-box method imposes a parameter structure, which allows comparisons of the grey-box model parameters across identified models. This is different from black-box models, where different sets of model parameters can represent the same system. The approach has potential of being extended to other types of controllable bearings. The method is general in the sense that influence from e.g. eccentricity or other factors could have been included by performing system identification for a range of those factors.

C.7 Conclusion

Grey-box modelling was used to successfully develop accurate linear models of an entire rotor-bearing-actuator system from experimental data. The models were identified "in situ" without knowing the exact geometry of the machine to be modelled, and the developed models were shown to be suitable for controller design due to their low complexity. The model was decomposed to two subsystems: an actuator dynamics and a rotor-bearings dynamics, where the subsystems were identified separately. It was found that incorporation of the air pressure build-up dynamics was necessary to match observed behaviour, which was accomplished by approximation of the unknown time delays. The approximated delays could then be included as parameters in the grey-box identification. A filter was shown to significantly improve the lateral disc movement measurement quality by filtering out mass unbalance and run-out to allow micrometer precision measurement. The locally identified models were used to derive a linear parameter varying model describing the behaviour of the rotor-bearing system over the operating range, defined by the combination of injection pressure and rotational speed. The linear parameter varying model preserved important system characteristics in terms of eigenvalues, static gains and damping factors. The model was shown to allow design of model based decentralised controllers, which greatly improved the damping properties of the controllable gas bearing. This increase was verified experimentally both for a non-rotating and for a rotating condition. All results were compared with experiments. The very good agreement between the model and the experiments confirmed the suitability of the approach.

Acknowledgements

The Danish Ministry of Science, Innovation and Higher Education is gratefully acknowledged for the support to the FTP research project 12-127502. A thanks also goes to John D'Errico for his Matlab function `polyfitn.m`.

C.8 Experimental Characterisation and Control of Piezoactuators

Piezoelectric stacks have two inherent nonlinear phenomena: creep and hysteresis. The creep effect causes slow expansion of the piezo stacks by a few percent over

Parameter	P_i $[m/m]$	z_1 $[rad/s]$	p_p $[rad/s]$
Piezoactuator 1	0.926	1996	101
Piezoactuator 2	0.927	1983	101
Piezoactuator 3	0.220	8349	101
Piezoactuator 4	0.640	2945	101

Table C.5: PD-controller parameters for piezoactuator controllers.

a time scale of minutes. This is very slow compared to the time constants of the controllable gas bearing. Hysteresis causes uncertainties in the piezoactuator position, which is a challenge for modelling and control. A staircase response is collected for each piezoactuator to characterise the hysteresis: a stepwise increasing voltage is applied to a piezoactuator, followed by a stepwise decreasing voltage. Plotting the stationary piezoactuator position after each step as function of the applied input voltage reveals the open loop hysteresis curve. This is shown in Fig. C.28 for piezoactuator number four. For the same input voltage, the piezoactuator position differs up to $8.4\mu m$ depending on the input history. Due to variations in the piezo ceramics, the characteristics and hysteresis curve for each piezoactuator vary. A PD-controller is tuned experimentally for each piezoactuator to counteract these nonlinear effects. The controlled piezoactuators are capable of tracking desired reference positions $r_{p,i}$, and the control law for piezoactuator i, $i \in \{1, 2, 3, 4\}$ reads:

$$u_{p,i}(s) = P_i \frac{s + z_i}{s + p_p}(r_{p,i}(s) - y_{p,i}(s)) \tag{C.23}$$

The proportional gains P_i and zeros z_i have different values to account for the variation of characteristics in each piezo stack. The values can be found in Table C.5. A staircase response is collected for the uncontrolled and the PD-controlled piezoactuator to show the tracking capabilities of the PD-controller. Figure C.28 shows the stationary piezoactuator positions for the closed loop case, and Figure C.29 shows the open loop and PD-controlled piezoactuator staircase responses. Without control, the static gain at each step varies due to the hysteresis, and the piezoactuator slowly creeps. The PD-controller reduces both hysteresis and creep effect and the PD-controlled step responses are uniform. The three dashed step responses differ notably. The dashed closed loop responses is the last decreasing step response, and in this case the actuator reached saturation, which deteriorates the performance. The two dashed open loop responses have a noticeable smaller step size, since in these cases the piezoactuator reaches maximum expansion.

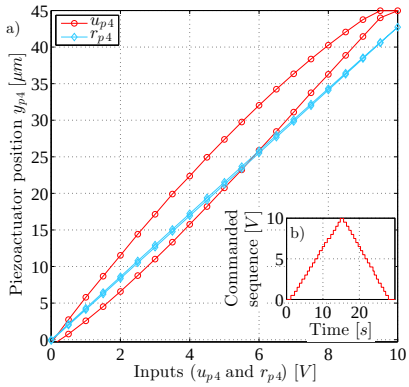

Figure C.28: a) Hysteresis curves for piezoactuator four for the open loop cases commanded the staircase sequence $u_{p,4}$ and the closed loop case commanded the position reference $r_{p,4}$. The responses are collected for a staircase input shown in b). The PD-controller efficiently eliminates the hysteresis.

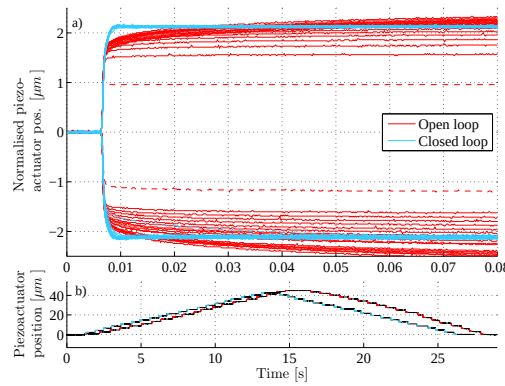

Figure C.29: Open loop and PD-controlled piezoactuator staircase responses. b) shows the piezoactuator position during the staircase response, and a) shows the individual steps, which were normalised by subtracting the offsets in time and position from each response. In the uncontrolled case, the stationary position varies due to hysteresis, and the piezoactuators creep. The PD-control reduces both hysteresis and creep effect.

C.9 Fitted Coefficients

Table C.6 contains the coefficients of fitted polynomials of the form Eq. C.16.

Stiffness	$k_{0,ij}\left[\frac{N}{g\cdot m}\right]$	$k_{1,ij}\left[\frac{N}{g\cdot m\cdot bar}\right]$	$k_{2,ij}\left[\frac{N}{g\cdot m\cdot rpm}\right]$	$k_{3,ij}\left[\frac{N}{g\cdot m\cdot bar\cdot rpm}\right]$	$k_{4,ij}\left[\frac{N}{g\cdot m\cdot bar^2}\right]$	$k_{5,ij}\left[\frac{N}{g\cdot m\cdot rpm^2}\right]$
k_{xx}	-3.168e+08	-9.758e+07	1.790e+04	-2.192e+03	7.472e+06	-1.462e+00
k_{xy}	4.020e+07	-1.023e+07	6.391e+03	1.256e+03	4.305e+05	-9.054e-01
k_{yx}	-9.321e+05	9.624e+06	-1.428e+04	2.880e+03	-1.782e+06	3.838e-01
k_{yy}	-2.832e+08	-1.026e+08	-4.493e+02	9.310e+02	5.845e+06	-7.379e-01
Damping	$c_{0,ij}\left[\frac{N\cdot s}{g\cdot m}\right]$	$c_{1,ij}\left[\frac{N\cdot s}{g\cdot m\cdot bar}\right]$	$c_{2,ij}\left[\frac{N\cdot s}{g\cdot m\cdot rpm}\right]$	$c_{3,ij}\left[\frac{N\cdot s}{g\cdot m\cdot bar\cdot rpm}\right]$	$c_{4,ij}\left[\frac{N\cdot s}{g\cdot m\cdot bar^2}\right]$	$c_{5,ij}\left[\frac{N\cdot s}{g\cdot m\cdot rpm^2}\right]$
d_{xx}	-1.855e+05	4.036e+04	-3.329e+01	1.003e-02	-3.149e+03	5.819e-03
d_{xy}	-6.016e+03	-3.643e+03	4.422e-01	3.002e-01	7.513e-02	3.918e-04
d_{yx}	3.087e+04	-8.330e+03	-3.198e+00	-5.626e-01	4.052e-02	-3.087e-01
d_{yy}	-2.673e+05	6.863e+04	-7.541e+00	7.258e-01	-5.339e+03	6.750e-04
Input gain	$b_{0,ij}\left[\frac{N}{g\cdot m}\right]$	$b_{1,ij}\left[\frac{N}{g\cdot m\cdot bar}\right]$	$b_{2,ij}\left[\frac{N}{g\cdot m\cdot rpm}\right]$	$b_{3,ij}\left[\frac{N}{g\cdot m\cdot bar\cdot rpm}\right]$	$b_{4,ij}\left[\frac{N}{g\cdot m\cdot bar^2}\right]$	$b_{5,ij}\left[\frac{N}{g\cdot m\cdot rpm^2}\right]$
b_{xx}	1.326e+09	1.294e+07	-4.671e+03	6.982e+02	-1.400e+06	1.962e-01
b_{xy}	-1.504e+07	3.229e+06	4.720e+03	-9.969e+02	-8.013e+04	2.687e-01
b_{yx}	-5.080e+06	1.514e+06	-2.549e+03	-5.538e+01	4.262e+04	-2.298e-01
b_{yy}	1.099e+08	2.427e+07	-5.691e+02	-9.093e+01	-1.545e+06	2.269e-02
Delays	$\tau_{0,i}\,[s]$	$\tau_{1,i}\left[\frac{s}{bar}\right]$	$\tau_{2,i}\left[\frac{s}{rpm}\right]$	$\tau_{3,i}\left[\frac{s}{bar\cdot rpm}\right]$	$\tau_{4,i}\left[\frac{s}{bar^2}\right]$	$\tau_{5,i}\left[\frac{s}{rpm^2}\right]$
τ_x	1.401e-03	-2.548e-04	2.348e-09	5.497e-09	1.941e-05	-5.711e-12
τ_y	7.799e-04	-1.890e-04	3.186e-08	-3.651e-09	1.325e-05	-2.466e-12

Table C.6: Coefficients of fitted polynomials of the form Eq. C.16 for the key parameter $(\cdot)_{ik}$.

Appendix D

Experimental Investigations of Decentralised Control Design for The Stabilisation of Rotor-Gas Bearings

From: Proceedings of the XVII International Symposium on Dynamic Problems of Mechanics. 2015
The paper has been reformatted to for the thesis.
Lukas R. S. Theisen[1], Roberto Galeazzi[1], Henrik Niemann[1] and Ilmar F. Santos[2]

[1]Dept. of Electrical Engineering and [2]Dept. of Mechanical Engineering, Technical University of Denmark, DK 2800 Kgs. Lyngby, Denmark
Email: {lrst,hhn,rg}@elektro.dtu.dk, ifs@mek.dtu.dk

Abstract:
Rotor-gas bearings are attracting increasing interest because of their high speed capabilities, low friction and clean operation. However, hydrostatic rotor-gas bearings show reduced damping characteristics, which makes it challenging to operate the rotating machine at and about the resonance frequencies. Active lubrication of the journal during operations could enhance the damping and stabilisation characteristics of the systems, and this could be achieved by means of stabilising controllers. This paper investigates the feasibility of using reduced order models obtained through Grey-Box identification for the design of stabilising controllers, capable of enabling the active lubrication of the journal. The root locus analysis shows that two different control solutions are feasible for the dampening of the first two eigenfrequencies of the rotor-gas bearing in the horizontal and vertical directions. Hardening and softening P-lead controllers are designed based on the models experimentally identified, and salient features of both controllers are discussed. Both controllers are implemented and validated on the physical test rig. Experimental results confirm the validity of the proposed approach.

D.1 Introduction

Gas bearings are receiving growing attention for their high speed operation capabilities, low friction, and clean and abundant air as lubricant. However, they suffer from low damping and vibration instabilities [34, 35, 78, 114]. The damping and stability properties require enhancement to allow a safe machine operation in presence of disturbances, especially close to the under-damped resonances. A mechatronic approach can provide such enhancement, while at the same time providing robustness and adaptability. The actuation for such a solution can be electromagnetic [49], which can be further combined with lubricated bearings [83] to exploit the beneficial features of both. Other actuations rely on the use of smart materials, e.g. using piezo-ceramics, where the piezo actuators can either be used as pushers on squirrel cages [19, 23], as pushers on active tilting pads [77] or as servo valves [78] controlling the air injection. In the latter approach, the injected air is both a lubricant and it provides the active forces. The controllers for the mentioned systems can either be experimentally tuned [78] or based on a model. The design of model based controllers for gas bearings requires models that catch the dynamic behaviour of the journal in the frequency range where control is needed. In [3] such a model has been developed exploiting Grey-Box identification techniques for a piezo actuated rotor-gas bearing. Using the fundamental knowledge of rotor-dynamics, a reduced order model was set up and a few key parameters sufficed to describe the dynamics of the bearing for given injection pressure and rotational velocity. Experiments run at a range of different operational conditions in terms of injection pressure and rotational velocity allowed identification of locally valid models of the rotor-gas bearing providing estimates of the unknown parameters, which allowed the formulation of a model valid over the investigated operational range.

This paper investigates the feasibility of using this low complexity model for the design of control systems capable of enhancing the closed-loop damping characteristics by means of active lubrication of the journal. The root locus method is exploited to analyse the spectrum of possible control strategies. Two different control solutions appear to be feasible for the dampening of the first two eigenfrequencies of the rotor-gas bearing in the horizontal and vertical directions. Hardening and softening decentralised P-lead controllers are designed based on the models experimentally identified, and their stabilizing characteristics are analysed both in the frequency and time domain. Both controllers are then implemented and validated on the physical test rig. Experimental results confirm the validity of the proposed approach.

The paper is structured as follows. Section D.2 describes the experimental test rig. Section D.3 briefly reviews some of the findings about the system modelling presented in [3]. Section D.4 discusses the design of the two decentralized controllers for damping injection, and the respective features are analysed. Section D.5 makes a comparative analysis of the numerical and experimental results. Last, some conclusions are drawn in Section D.6.

D.2 Experimental Setup of Rotor-Gas Bearing Test Rig

The experimental setup at hand shown in Fig. D.1 consists of: a turbine driven flexible shaft (a) supported by both a ball bearing (d) and the controllable gas bearing (b), in which pressurised air is injected through four piezo actuated valves numbered as shown. The manometric injection pressure P_{inj} of the pressurised air is measured by a mechanical gauge before splitting up to the four actuators. The absolute pressure in the valves P_{abs} is assumed to be the sum of the measured pressure and the atmospheric pressure P_{atm}. A disc (c) is mounted on one end to pre-load the journal. The horizontal and vertical shaft deflections $\mathbf{p} \triangleq [p_x, p_y]^{\text{T}}$ are measured at the disc location using eddy current sensors (e) in the coordinate frame specified in the figure. The angular position of the shaft ϕ is measured by an optical encoder. All values are sampled with period $T_s = 0.2ms$.

The position of the i-th valve can be controlled through a voltage input $u_{p,i} \in [0; 10]V$, where an increasing voltage causes the piezo stacks to expand up to $46\mu m$, which closes the valve. The exact expansion varies from stack to stack, and the measured valve positions $y_{p,i}$ are therefore given as voltages $y_{p,i} \in [0; 10]V$, where $0V$ corresponds to an open valve and $10V$ corresponds to a closed valve. Decentralised PD-controllers counteract hysteresis in the valves and control the valve positions, using one commanded valve position $r_x(t)$ for the horizontal valves, and one commanded valve position r_y for the vertical valves. This approach reduces the system from over- to fully actuated. The valves are therefore seen as a "lumped" horizontal valve and a lumped vertical, each having a valve position $[u_x, u_y]^{\text{T}} \triangleq [y_{p,2}(t) - y_{p,4}(t),\ y_{p,1}(t) - y_{p,3}(t)]^{\text{T}}$.

The pressurised air generates a $25\mu m$ thin layer of fluid film in the gap between the shaft and the bearing housing. Given the right conditions of sufficient injection pressure and sufficiently low rotational velocity, the fluid film generates restoring forces and thereby keeps the shaft levitating about a stable equilibrium position. Opening or closing a valve thus perturbs the fluid film. A more thorough description

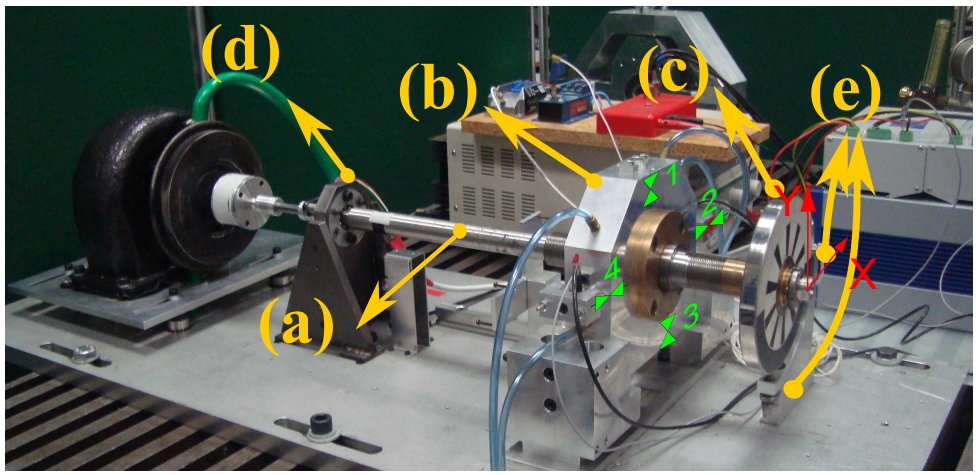

Figure D.1: The experimental rotor gas-bearing setup. A flexible shaft (a) is supported by both a ball bearing (d) and the controllable gas bearing (b) with four piezo actuated valves. A disc (c) is mounted on one end to preload the journal and displacement sensors (e) measure the lateral movement of the disc in the shown reference frame.

of the setup is available in [78].

D.3 Rotor-gas Bearing Model

[3] have identified reduced-order models for the rotor-gas bearing through an extensive experimental campaign, where data have been acquired at different injection pressures and rotational velocities. These models have the advantages of being low parametrised and locally well representing the dynamical behaviour of the system. Therefore they appear to be particularly suitable for model-based controller design.

The model is set up as the interconnection of two subsystems: the actuators and the bearing, as shown in Fig. D.2. The actuators subsystem models the dynamics of the PD-controlled piezo actuated lumped valves from commanded valve position $\mathbf{r}(t) = [r_x(t), r_y(t)]^{\mathrm{T}}$ to actual valve position $\mathbf{u}(t) = [u_x(t), u_y(t)]^{\mathrm{T}}$. The bearing model is parametrised in shaft rotational speed and injection pressure with input being the actual valve position $\mathbf{u}(t)$ and output being the shaft displacement $\mathbf{p}(t)$. The parameters defining the rotor-gas bearing operational conditions can vary in the following ranges: the rotational speed $\Omega \in [0; 6]\, krpm$, and the injection pressure

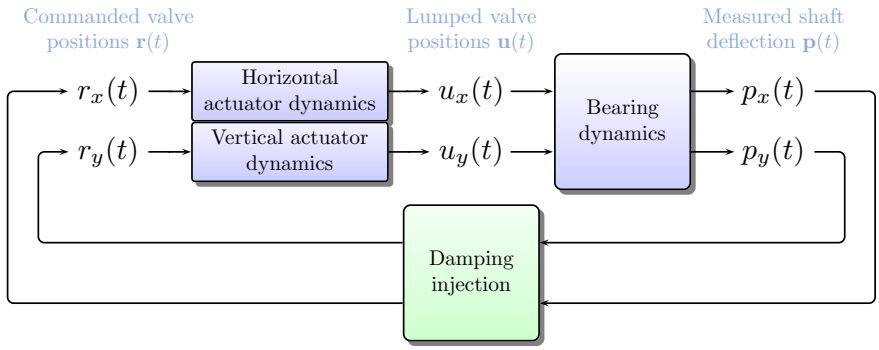

Figure D.2: Block diagram of the final system. The horizontal valves are decoupled from the vertical. The measured shaft deflections will be used for feedback controller design generating valve reference positions.

$P_{\text{inj}} \in [3; 7]\, bar$.

From an input-output perspective the entire model is given by

$$\mathbf{G}_p(s) = \mathbf{G}_{bear}(s)\mathbf{G}_{act}(s), \tag{D.1}$$

where $\mathbf{G}_{bear}(s)$ is the transfer function matrix from valve position $\mathbf{u}$ to shaft displacement at the disc location $\mathbf{p}$, and $\mathbf{G}_{act}(s)$ is the transfer function matrix from commanded valve position $\mathbf{r}$ to valve position $\mathbf{u}$. The characteristics of the two transfer function matrices will be further discussed in the following sections.

D.3.1 Modelling of Actuators

The four PD-controlled piezo actuated valves are controlled pairwise, where the two horizontal valves are controlled as one lumped valve, and similarly for the vertical valve. This is described further in [3]. Each pair of valves are modelled as a second order lowpass filter with two real poles $p_{1,j}$, and $p_{2,j}$ and a stationary gain $\kappa_{a,j}$, where j refers to the horizontal valve x or vertical valve y. The dynamics then reads:

$$\begin{bmatrix} u_x(s) \\ u_y(s) \end{bmatrix} = \underbrace{\begin{bmatrix} G_{a,x}(s) & 0 \\ 0 & G_{a,y}(s) \end{bmatrix}}_{\triangleq \mathbf{G}_{act}(s)} \begin{bmatrix} r_x(s) \\ r_y(s) \end{bmatrix}, \qquad G_{a,j}(s) = \frac{\kappa_{a,j}}{\left(\frac{1}{p_{1,j}}s + 1\right)\left(\frac{1}{p_{2,j}}s + 1\right)} \tag{D.2}$$

in which $G_{a,j}(s)$ is the second order filter of the specified form. The poles are located at $p_{1,x} = 3078\, rad/s$,$p_{2,x} = 8143\, rad/s$, $p_{1,y} = 2452\, rad/s$,$p_{1,x} = 6494\, rad/s$. The gains are $\kappa_{a,x} = 1.863\, V/V$, and $\kappa_{a,y} = 1.865 V/V$

D.3.2 Modelling of Bearing

The combination of flexible shaft and gas bearing can be modelled locally (for constant injection pressure and rotational velocity) as a 2 DOF coupled mass spring damper system combined with an input delay for each valve direction [3]. The bearing model input is the actual valve position $\mathbf{u}(s)$ and the output is the shaft displacement $\mathbf{p}(s)$. The model reads:

$$\begin{bmatrix} p_x(s) \\ p_y(s) \end{bmatrix} = \overbrace{\overbrace{\begin{bmatrix} G_{b,xx}(s) & G_{b,xy}(s) \\ G_{b,yx}(s) & G_{b,yy}(s) \end{bmatrix}}^{\triangleq \mathbf{G}_b(s)} \overbrace{\begin{bmatrix} e^{-\tau_x s} & 0 \\ 0 & e^{-\tau_y s} \end{bmatrix}}^{\triangleq \mathbf{G}_\tau(s)}}^{\triangleq \mathbf{G}_{bear}(s)} \begin{bmatrix} u_x(s) \\ u_y(s) \end{bmatrix}, \tag{D.3}$$

in which $\{G_{b,xx}, G_{b,xy}, G_{b,yx}, G_{b,yy}\}$ are the relevant transfer functions, and the delays model the pressure build-up transients. This is valid over a wide operational range as the model coefficients are parameterised in rotational speed and injection pressure. For constant $\Omega = \bar{\Omega}$ and $P_{\text{inj}} = \bar{P}_{\text{inj}}$, the transfer function can be written with a slight abuse of notation:

$$\mathbf{G}_{bear}(s) = \mathbf{G}_{bear}(\bar{\Omega}, \bar{P}_{\text{inj}}) \tag{D.4}$$

Choosing more specifically $\bar{P}_{\text{inj}} = 6bar, \bar{\Omega} = 0rpm$, the rotor-gas bearing will have two resonance frequencies ω_x, ω_y. The first $\omega_x = 126.5Hz$ is dominant in the horizontal direction, while the latter $\omega_y = 132.1Hz$ dominates the vertical direction. The corresponding damping factors are $\zeta_x = 0.035$ and $\zeta_y = 0.029$. Figure D.3 shows a Bode plot of the whole system G_p. The time delays at this operational condition are $\bar{\tau}_x = 0.57ms = 2.8T_s$, $\bar{\tau}_y = 0.123ms = 0.6T_s$. The time delay due to the pressure build-up is approximated using a first order Padé approximation

$$\mathbf{G}_\tau(s) \approx \mathbf{G}_{\tilde{\tau}}(s) \triangleq \begin{bmatrix} G_{\tau,x}(s) & 0 \\ 0 & G_{\tau,y}(s) \end{bmatrix}, \quad G_{\tilde{\tau},j}(s) \triangleq \frac{1 - \frac{\tau_j}{2}s}{1 + \frac{\tau_j}{2}s}, \tag{D.5}$$

The rotor-gas bearing model then reads

$$\mathbf{p}(s) \triangleq \mathbf{G}(s)\mathbf{r}(s) = \mathbf{G}_b(s)\mathbf{G}_{\tilde{\tau}}(s)\mathbf{G}_{act}(s)\mathbf{r}(s) \tag{D.6}$$

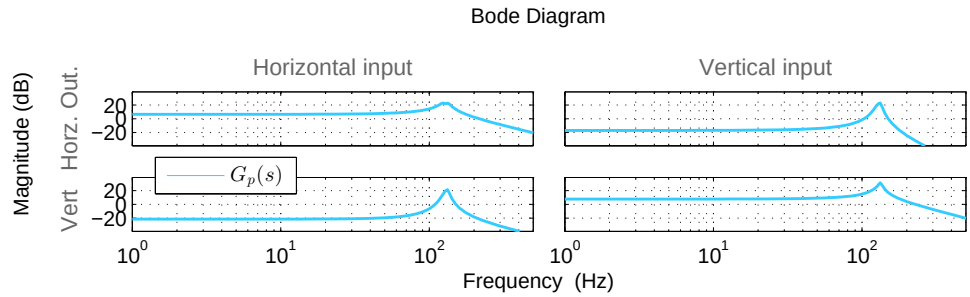

Figure D.3: Bode plot of the rotor-gas bearing from commanded valve position to shaft deflection. The system has one clear eigenvalue in each direction, with weaker cross couplings.

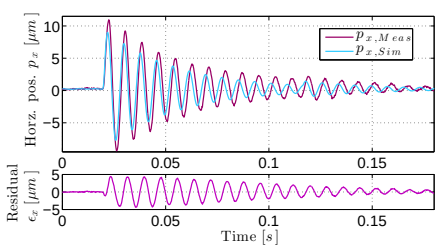

Figure D.4: Experimental model validation by horizontal impact response.

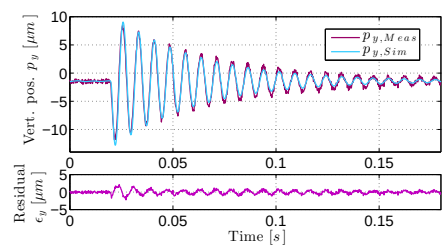

Figure D.5: Experimental model validation by vertical impact response.

D.3.3 Model validation

The bearing model is validated experimentally by impact responses. Application of a horizontal and a vertical impact allows the comparison of the measured and the simulated responses. Figure D.4 shows the comparison of the horizontal impact response and Fig. D.5 shows the comparison of the vertical impacts. The model deviation is more evident in the horizontal direction resulting in larger residuals defined as the difference between measured and simulated responses $\epsilon_j \triangleq p_{j,meas} - p_{j,sim}$.

D.4 Hardening and Softening Decentralised control of Rotor-gas Bearing

The reduced damping properties of the rotor-gas bearing can be improved by application of a suitable control strategy.

Problem statement *Given the open loop rotor-gas bearing input-output model* $\mathbf{p}(s) = \mathbf{G}(s)\mathbf{r}(s)$*, with* $\mathbf{p}(s)$ *and* $\mathbf{r}(s)$ *being the Laplace transforms of* $\mathbf{p}(t)$ *and* $\mathbf{r}(t)$*, design a control system that fulfils the following requirements:*

1. *To increase the damping and reject disturbances around the two first eigenfrequencies of the rotor-gas bearing system by at least a factor two while*

2. *using a sufficiently low control effort to avoid actuator wear.*

The rotor-gas bearing model Eq. D.6 (Fig. D.3) shows that the direct couplings from horizontal valves to horizontal shaft deflection (and similar for the vertical) have gains an order of magnitude larger than the cross coupling gains. This makes decentralised control a feasible option. The controller should improve the damping properties and reject disturbances in a frequency range around the first two eigenfrequencies. This can be achieved through the design of a P-lead controller. The horizontal and vertical P-lead controllers $K_{pl,x}$ and $K_{pl,y}$ thus form the controller $\mathbf{K}_{pl}$, such that:

$$\begin{aligned} \begin{bmatrix} r_x(s) \\ r_y(s) \end{bmatrix} &= -\mathbf{K}_{pl}(s) \begin{bmatrix} p_x(s) \\ p_y(s) \end{bmatrix}, \\ \mathbf{K}_{pl}(s) &\triangleq \begin{bmatrix} K_{pl,x}(s) & 0 \\ 0 & K_{pl,y}(s) \end{bmatrix} H_{lp}(s), \\ K_{pl,j}(s) &\triangleq \kappa_j \frac{\tau_j s + 1}{\alpha_j \tau_j s + 1}, \end{aligned} \tag{D.7}$$

in which the controller parameters to be tuned are the proportional gain κ_j, the time constant τ_j, and α_j. Each controller contains a lowpass filter $H_{lp}(s)$ to avoid too large high frequency gains. A choice of $H_{lp}(s)$ as a n_s-th order lowpass filter with bandwidth $b_{lp} = 1000Hz$,$n_s = 2$ and unity DC-gain gives sufficient results. The developed model Eq. (D.6) provides an excellent basis for off-line design, which avoids the risk of instability during on-line tuning. Upon closing the loop using the controller $\mathbf{K}_{pl}$, the output sensitivity $\mathbf{S}_o$ and closed-loop controller activity $\mathbf{K}_{pl}\mathbf{S}_o$ can

be calculated:

$$\mathbf{S}_o(s) \triangleq (\mathbf{I}_2 + \mathbf{G}(s)\mathbf{K}_{pl}(s))^{-1} \tag{D.8}$$

The output sensitivity $\mathbf{S}_o(s)$ and closed-loop controller activity $\mathbf{K}_{pl}\mathbf{S}_o(s)$ are useful tools for tuning the control system's gains, since they provide clear measures of the controller action over the desired range of frequencies. The fulfilment of requirement 1) implies that the output sensitivity close to the resonance frequencies ω_j satisfies $|S_o(\omega_j)|< 0.5$. Further, to avoid simply shifting the resonance, the peak should be sufficiently low, here chosen as $||S_o||_\infty \leq 1.6$. At lower and higher frequencies control effort is not desired.

The specifications can be achieved through two designs, which differ in the sign of proportional action. The natural approach is to establish a negative feedback control law, which implies that the sign of the proportional gain in Eq. (D.7) is positive, $\kappa_j > 0$. This is what we address as the *hardening decentralised controller*. An alternative approach, which still achieves the control objectives, is to establish a positive feedback by means of a negative proportional action, $\kappa_j < 0$. This is what we address as the *softening decentralised controller*.

The controller must satisfy the Bode sensitivity integral [104], which states that the sensitivity function $S(s)$ evaluated at $s = j\omega$ satisfies the following integral constraint $\int_0^\infty \ln|S(j\omega)|\, d\omega = 0$ which implies that any linear control law that reduces the sensitivity function in an interval must increase the sensitivity function in some other interval. Moreover, the presence of the time delays, modelled as first order non-minimum phase system, sets limitations on the achievable performance due to the interpolation constraints [93]: denote the right half plane zeros $z_m, m \in \{1, ..., M\}$. The sensitivity must then satisfy $S(z_m) = 1$.

A *hardening decentralized controller* places the sensitivity peak at the closed-loop eigenfrequency, which is higher than the open loop eigenfrequency. On the other hand,the *softening decentralized controller* places the sensitivity peak at a lower frequency. In this aspect, the time delay in the bearing dynamics plays an important role as it sets an upper bandwidth limit: using the hardening control approach it is not possible to achieve a sufficient reduction in sensitivity at the resonance frequency without it being at the cost of an unacceptably high sensitivity peak at higher frequencies. However, this is achievable using softening control. Evaluation of the sensitivity functions obtained through the *hardening decentralized controller* and the *softening decentralized controller* clearly confirm the analysis, and experimental results verify the sensitivity functions.

D.4.1 Controller Designs

The choice of gains for the controllers is no trivial task. Figure D.6 shows a root locus for the horizontal direction using only proportional gain κ_x. The gain must be within $\kappa_x \in [-0.47; 0.05]$ to avoid instability. For the hardening case, the controller soon destabilises the rotor-gas bearing, whereas for the softening case, proportional action alone is enough to achieve an increase in stabilisation. This is reflected in the choice of controller gains. The hardening and the softening controllers' parameters

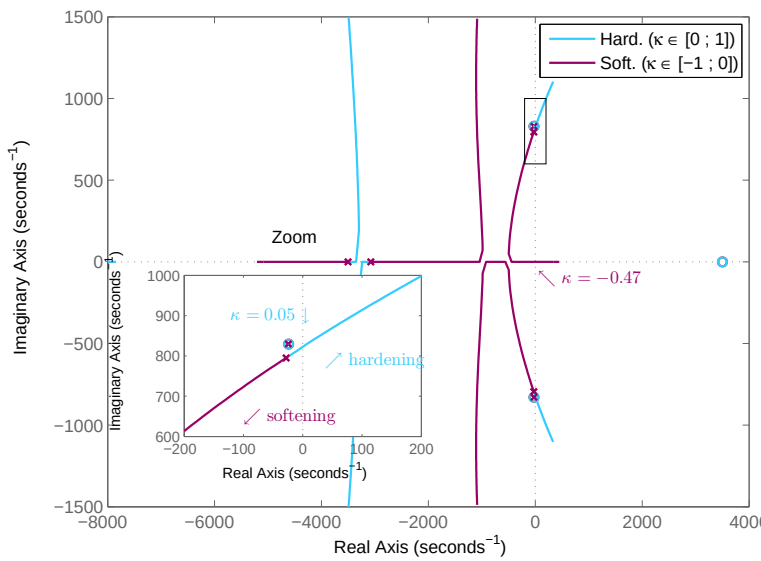

Figure D.6: Root locus for the horizontal direction using only proportional gain $\kappa \in [-1; 1]$.

are listed in Table D.1, and the respective Bode diagrams are shown in Fig. D.7. The lead action in the hardening case improves the damping characteristics, whereas for the softening controller the derivative action is minimal, and could in practice be neglected. Further, the root locus shows that positive proportional control can move the system eigenvalues to the real axis, thereby achieving a damping factor of 1. Experimental results validating this are available in [3]. Such a design however violates the sensitivity requirement $||S_o||_\infty \leq 1.6$ and is therefore not considered further here. The output sensitivities shown in Fig. D.8 validate that both designs achieve the specified sensitivity requirements.

For many applications controllers are used to provide sufficient damping to allow safe crossing of critical speeds. The main disturbance from mass unbalance thus

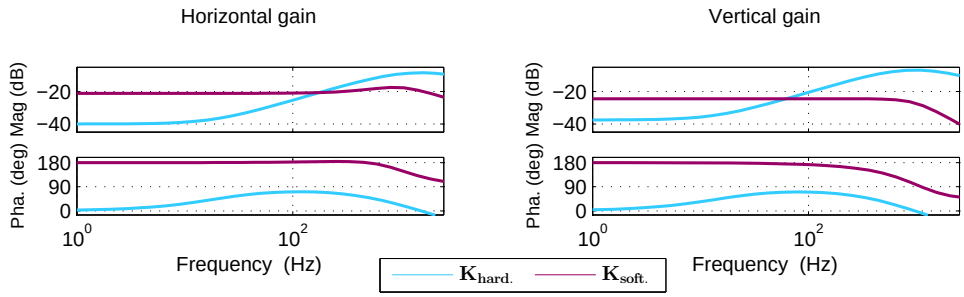

Figure D.7: Comparison of controller gains for the hardening and softening designs. left) $K_{Pl,x}(s)$, right) $K_{Pl,y}(s)$. Note the phase difference between the hardening and softening designs.

increases in frequency. Using the hardening controller design, these oscillations are attenuated at low frequencies, but are then amplified (compared to open loop) when the rotational speed becomes supercritical. This is avoided by the softening design, where the sensitivity reduces before the critical speed and remains low even in supercritical operation.

Table D.1: Controller parameters for controller of form Eq. (D.7)

Design	Gain κ_x $[V/\mu m]$	Gain κ_y $[V/\mu m]$	Time Const. τ_x $[ms]$	Time Const. τ_y $[ms]$	α_x $[-]$	α_y $[-]$
Hardening	0.0061	0.0133	20.8	11.3	0.0036	0.0148
Softening	−0.132	−0.090	0.30	0.0200	0.0077	0.0077

D.5 Experimental and Numerical Validation

This section presents validation of the controller designs. Both designs have been validated experimentally and numerically in the non-rotating case, and numerically for the vertical direction with a rotational speed of $\bar{\Omega} = 4.0krpm$.

D.5.1 Experimental and Numerical Validation - Non-Rotating Case

Both controllers have been discretised and implemented on the rotor-gas bearing system. Impact responses were collected both for the open and closed-loop bearing

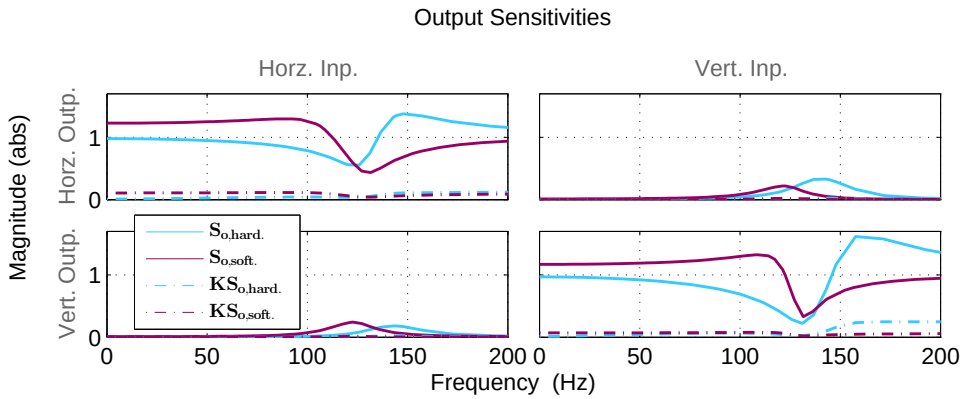

Figure D.8: Comparison of output sensitivities using the hardening and softening designs. The hardening design already achieves some performance for low rotational speeds ($|\mathbf{S}_{0,hard.}(0)|< 1$), whereas the softening amplifies disturbances at low frequencies ($|\mathbf{S}_{0,soft.}(0)|> 1$). Both controllers have decently small controller activities $\mathbf{KS}_o$

for both the horizontal (shown in Fig. D.10) and rhe vertical direction (shown in Fig. D.9). In both impact directions the softening controller achieves a clear damping increase. The hardening controller however only achieves a damping increase in the vertical direction. The unsatisfactory performance may well stem from the model discrepancies found in the horizontal open loop model validation. Figure D.11 shows individual comparisons between the measured and the simulated impact responses, where the model is simulated using the same impact force. The responses validate that the obtained performances are close to the predicted in all cases other than the horizontal hardening impact response. The revealed model deviation should be investigated further.

D.5.2 Numerical Validation - Rotating Case

The designed controllers have been tested in a rotating case as well by simulating impacts on the open-loop and closed-loop system with a rotational speed $\bar{\Omega} = 4.0\ krpm$. Figures D.12 and D.13 show simulated horizontal and vertical impact responses in 1) open loop and using 2) the hardening and 3) the softening controller design. Both controllers increase the damping compared to the open loop case with satisfactory performance. The modified dynamics due to the rotation however

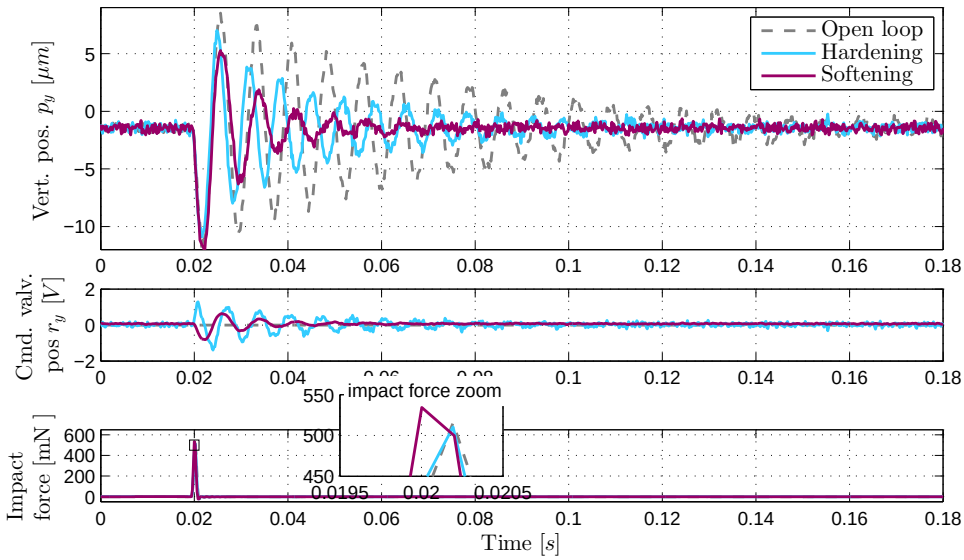

Figure D.9: Experimental comparison of vertical impact responses for cases: 1) without control, 2) using hardening, 3) using softening design.

benefits the hardening controller most in the vertical case, where it performs slightly better than the softening one. Closed-loop experimental results for rotating conditions are available in [3].

D.6 Conclusion

High-speed rotating machines with flexible shaft and gas bearings are complex systems, whose dynamics is generally modelled by means of partial differential equations naturally arising from the physics governing the system behaviour. Those models are not suitable for the design of control systems, which are instead preferably based on low order models that capture the essential dynamics in focus of the control objectives.

This paper has successfully investigated the feasibility of designing a control system for the stabilisation of a rotor-gas bearing based on a 2 degrees-of-freedom mass-spring-damper equivalent model, previously identified in [3]. Application of the root locus method pointed out the possibility of designing two types of decentralised

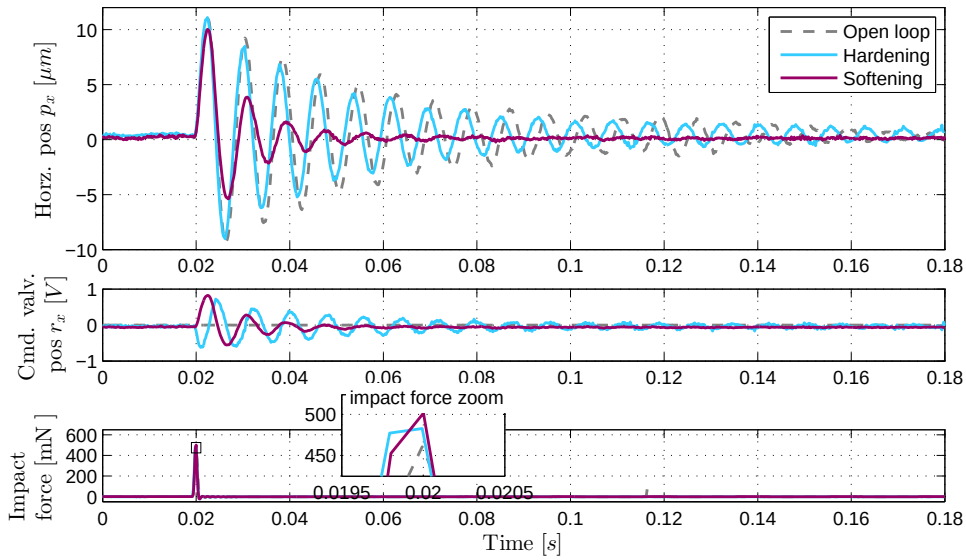

Figure D.10: Experimental comparison of horizontal impact responses for cases: 1) without control, 2) using hardening, 3) using softening design.

P-lead controllers, one determining a hardening of the closed-loop system, and one achieving a softening of the closed-loop system. Both controllers fulfil the control objectives. However, the decentralised softening controller showed better performance than the hardening one in terms of damping injection in both the horizontal and vertical directions.

The designed controllers have been successfully implemented and tested on the physical rotor-gas bearing test rig. The experimental results available for the non-rotating case are in very good agreement with the numerical simulations, especially for the softening controller. Numerical results validate damping enhancement for rotating conditions as well. This clearly confirms the feasibility of designing stabilising controllers for the rotor-gas bearing exploiting low complexity models obtained through system identification techniques.

ACKNOWLEDGMENTS

The Danish Ministry of Science, Innovation and Higher Education is gratefully acknowledged for the support to the FTP research project 12-127502.

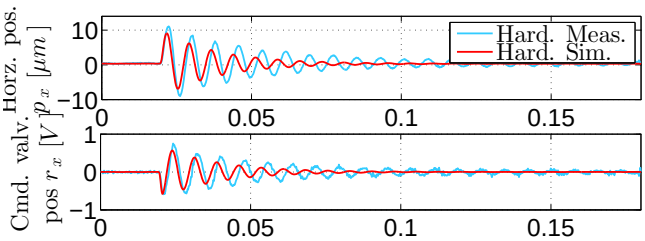

(a) Hardening controller - horizontal impact

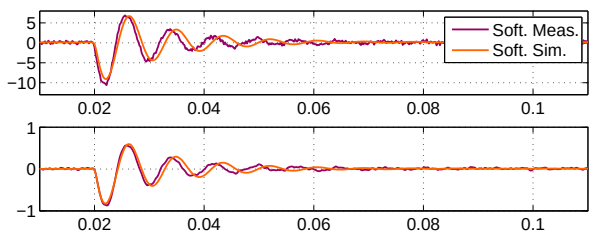

(b) Softening controller - horizontal impact

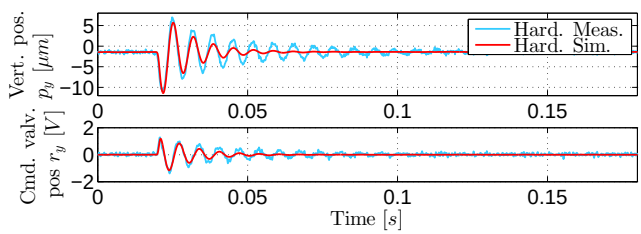

(c) Hardening controller - vertical impact

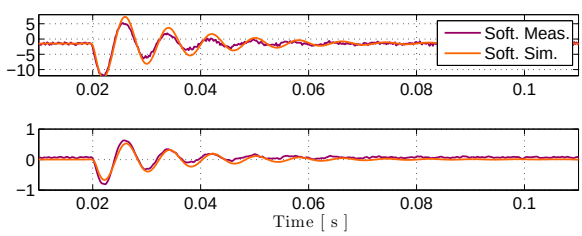

(d) Softening controller - vertical impact

Figure D.11: Experimental validation of controller designs by impact responses: measured impact vs simulated using the coresponding measured impacts from Fig. D.9.

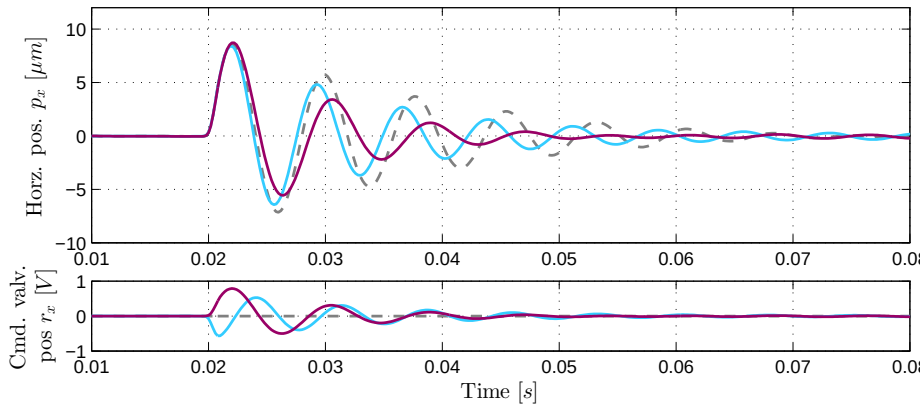

Figure D.12: Numerical validation for horizontal impact response at $\bar{\Omega} = 4.0\ krpm$ for cases: 1) without control, 2) using hardening, 3) using softening design.

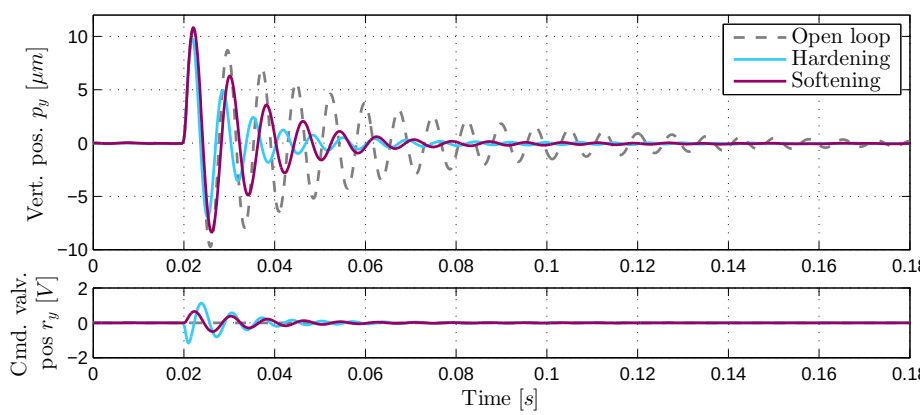

Figure D.13: Numerical validation for vertical impact response at $\bar{\Omega} = 4.0\ krpm$ for cases: 1) without control, 2) using hardening, 3) using softening design.

Appendix E

Enhancing damping of gas bearings using linear parameter-varying control

Submitted to Journal of Sound and Vibration (2016)
The paper has been reformatted to for the thesis.
Lukas R. S. Theisen[a**], Hans H. Niemann[a], Roberto Galeazzi[a], Ilmar F. Santos[b]
[*]Department of Electrical Engineering, Technical University of Denmark, Elektrovej, Bld. 326, 2800 Kgs. Lyngby, Denmark

Abstract:
Journal bearings can be lubricated through controllable injectors using pressurised fluids such as oil, water or air. The fluid viscosity determines the friction losses. Fluids with low viscosity reduce friction at the expense of poor damping properties, which pose challenges for safe operation of rotating machines in presence of disturbances. One advantageous design solution is to actively control the injection. The dynamics of rotating machinery is inherently parameter-varying. A controller should then be able to guarantee stability over the range of parameter variation of the machine. This paper addresses the enhancement of the damping properties of active gas bearings over a desired operating range using control. We propose a linear parameter-varying (LPV) control design that guarantees stability and performance over the desired operating range. For comparison we also propose an $\mathcal{H}_\infty$ controller optimised for the linearised plant. The performance of the controllers is compared numerically and experimentally. Both controllers are found to significantly enhance the damping of the gas bearing over the scheduling parameter range.

[*a]Dept. of Electrical Engineering and [b]Dept. of Mechanical Engineering, Technical University of Denmark, DK 2800 Kgs. Lyngby, Denmark. Email: {lrst,hhn,rg}@elektro.dtu.dk, ifs@mek.dtu.dk

E.1 Introduction

Industry is searching for methods to reduce losses and increase the performance of rotating machines. One of the main influencing factors is friction losses in the bearings [115]. The friction can be reduced by choosing lubricants with lower viscosity, which in turn results in poorer damping properties. Pressurised air indeed offers this low viscosity and increasing research activities are focussing on the design of gas bearings with controllable injection of pressurised air [20, 28, 41]. Those air bearings have been shown to have poor damping properties [34] that cause significant amplification of the induced vibrations from mass imbalance and external disturbances near the system resonance frequencies. Therefore it is of interest to find passive or active technological means capable of enhancing the damping to reduce the sensitivity towards disturbances. An attractive solution among the active means is represented by mechatronic systems where electromechanical actuators are embedded into the bearings with advanced control systems. A promising design solution is the active gas bearing where pressurised air is injected through controllable piezo-actuators [41, 78, 3]. Such a solution is attractive for a number of applications including compressors, atomisers and turbochargers, but the bearing development is still in its infancy. The first design solution was proposed in [37]. Later a solution was proposed with active inherent restrictors [28], and more recently with radial injection of pressurised air through piezo-actuated injectors [78]. The controllers for those active bearing designs have been tuned for a constant scheduling parameter defined by the combination of angular velocity and pressure of the injected air. The bearings are often employed in applications where drifts and changes occur in the scheduling parameters. A control system must therefore be able to guarantee stability and a certain level of performance over the operating range. Those control systems are preferable designed from low complexity models that capture the phenomena relevant for control design. In recent work [3], we proposed a linear parameter-varying (LPV) identification method that allowed identification of low-complexity models of the entire rotor-bearing actuator-sensor system. The models captured the dynamics of the machine and had a suitable complexity for control design [4]. The LPV identification bypassed the need for the first principles models [41, 42] based on the modified Reynolds equation [38]. Those models are often of a high complexity and the modelling of the air flow in the injectors may be subject to significant parameter uncertainties [44].

The LPV identification was used in [3] to identify the dynamics of a controllable

gas bearing test rig modelled with the shaft angular velocity and air injection pressure as scheduling parameters. Proportional controllers designed from the proposed model were able to improve the damping significantly for a given scheduling parameter. However, robustness was not in focus, and the controller's performance deteriorated as the operating conditions changed. Other previous control systems for gas bearings were as well designed without focus for robustness. The controllers were usually designed for a specific linearisation point with a constant scheduling parameter either using a linearised model [3, 42, 4] or tuned experimentally [37, 20, 78, 28]. The variations in the operating conditions that occur slowly over time will therefore result in performance degradation or, in extreme cases, in closed-loop instability. This calls for more advanced control systems that guarantee stability and a certain level of performance over a wide range of plant operation.

LPV control system design represents a suitable methodology when closed-loop stability and robust performance in the $\mathcal{H}_\infty$ sense need to be guaranteed over a wide range of operation, as shown in [76, 75, 33]. LPV control has been widely applied in active magnetic bearings (AMBs), conversely the research community seems to not have devoted the same attention to gas bearings due to the fact that active gas bearing technology is in its "infancy" in comparison to AMB technology. Our literature study shows that the application of LPV control for gas bearing is novel. The LPV review paper [33] devotes a section to AMBs and reports the first ten LPV papers for AMBs validated by high fidelity simulations or experimental results. LPV control of an oil bearing combined with an AMB was considered in [87]. In [85] an LPV controller was designed for an AMB to reject the synchronous mass imbalance response. The shaft was assumed rigid to neglect the flexible modes. The work was extended in [52] by using a flexible shaft model and a switching between multiple unstable LPV controllers was proposed. A similar procedure was used in [53]. The LPV controllers were compared in [52] and [53] to a set of narrow-band $\mathcal{H}_\infty$ controllers, which were optimised for mass imbalance rejection at a single angular velocity, and the LPV controller was shown superior in performance. The LPV designs mentioned place zeros on the closed-loop sensitivity functions at the known frequency location to reject the synchronous mass imbalance disturbance. In industrial environments, the machines may further be subject to significant disturbances from mechanical shocks and vibrations from other machinery. Such disturbances may act over a wide frequency range. Critical disturbances are those acting near the underdamped resonance frequencies where strong vibration amplifications occur. The impact of these disturbances can be diminished by proper shaping of the closed-loop sensitivity

function.

The present work addresses the enhancement of the damping properties of controllable journal bearings over a desired operating range using feedback control. We propose an LPV control design that is able to guarantee stability and performance for a rotating machine supported by controllable gas bearing. The rotating machine is scheduled on the shaft angular velocity and air injection pressure. The damping and noise rejection requirements are cast according to the mixed sensitivity setup where suitable performance weights are chosen to obtain controllers that significantly enhance the damping properties of the gas bearing over the selected operating range. An LPV control design is proposed to directly address the parameter dependency in the design by scheduling the controller's gains. For comparison an $\mathcal{H}_\infty$ controller is designed since it is a natural initial design choice which is simple yet robust. The same performance weights are used for designing both controllers to assess the advantages and disadvantages of the two control methods. The damping enhancement of the controllers is investigated and compared through simulations and experiments using a controllable gas bearing test rig. Here the responses to impulse excitations are investigated and used to quantify the performance of the controllers.

The paper is structured as follows: Section E.2 provides an overview of the experimental test rig and the identification-based gas bearing model. The LPV and the $\mathcal{H}_\infty$ controllers are designed in Section E.3. Their effectiveness is investigated through simulations in Section E.4 and in Section E.5 the controllers are validated experimentally over the selected operating range and their performance is quantified. A discussion of the results and some conclusions are drawn in Section E.6.

E.2 Gas bearing Test Rig

This section provides a brief description of the controllable gas bearing test rig. The interested reader is referred to [31] for a detailed analysis of the experimental setup and the corresponding identified LPV model.

E.2.1 Test Rig description

The gas bearing test rig consists of a flexible shaft supported by a ball bearing and the controllable gas bearing as shown in Figure E.1. A disc is mounted to preload the shaft, and the horizontal and vertical disc movements are measured with eddy-current sensors. The deviation from the equilibrium position is denoted by

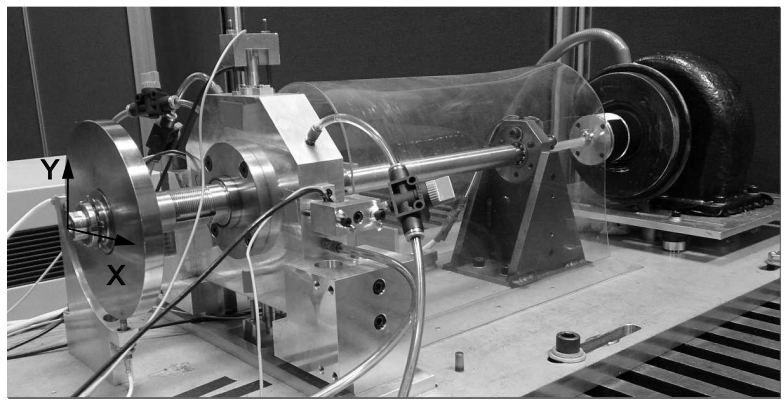

Figure E.1: Experimental gas bearing test rig. Four piezo-actuated injectors in the gas bearing control the injection of pressurised air and the lateral disc movement is measured with eddy-current sensors.

$\mathbf{p} = [p_x, p_y]^{\mathrm{T}}$, where the horizontal (x), and the vertical (y) shaft directions are as shown in the photo. The shaft is actuated by the injection of pressurised air through four controllable piezo-actuated injectors mounted in the gas bearing. The airflow generates a fluid film which provides a stable lifting force on the shaft. This fluid film gives rise to dynamics in the rotor-bearing coupling and its dynamics is a function of both the shaft angular velocity and the injection pressure [41]. The piezo-actuators have local high gain control loops as described in [3] to linearise their dynamics. The injectors are position-controlled in a pairwise differential mode. Thereby one piezo-actuator reference r_x is sent to control the position of the horizontal injectors and one reference r_y is sent to control the vertical ones. These references take values in the interval $[-5, 5]$ V, which corresponds to full-span motion of the piezo-actuator positions in the interval $[0, 45]$ μm. A turbine drives the shaft and an encoder measures the angular position ϕ, from which the angular velocity q_1 is calculated. The pressurised air to the gas bearing is supplied from a large pressure tank. In an industrial application, the injection pressure would be slowly time-varying. For the test rig at hand, a lever is mounted to allow manual control of the pressure variations. The injection pressure q_2 is measured before the airflow is split up to the four actuators.

Table E.1: Actuator Model Parameters. Poles $p_{1,x}, p_{2,x}, p_{1,y}, p_{2,y}$ are given in units krad/s. Gains are non-dimensional.

Parameter	$p_{1,x}$	$p_{2,x}$	κ_x	$p_{1,y}$	$p_{2,y}$	κ_y
Value	3.08	8.14	1.86	2.45	6.49	1.87

E.2.2 Gas bearing model

Gas bearing models derived from first principles [41, 42] rely on solution schemes to the nonlinear partial differential modified Reynolds equation[38]. Those methods often produce high order models and are subject to parameter uncertainty [42]. To avoid the need for those models, we instead adopt the grey-box identification procedure reported in [3] to obtain linear parameter-varying models of the test rig. The resulting model captures the dominant dynamics of the rotating machine and its low complexity suits the design of controllers [4]. The method from [3] is summarised in the following.

The LPV model has the scheduling parameter vector $\mathbf{q}$ whose components are the shaft angular velocity q_1 and the injection pressure q_2. The scheduling parameters can vary in the intervals $q_1 \in [\underline{q}_1,\ \bar{q}_1] = [0, 6]$ krpm, $q_2 \in [\underline{q}_2,\ \bar{q}_2] = [0.3, 0.7]$ MPa. Local LTI models are identified from data-sets collected in the grid points $q_1 \in \{0, 1, 2, 3, 4, 5, 6\}$ krpm, $q_2 \in \{0.3, 0.4, 0.5, 0.6, 0.7\}$ MPa. The local models are identified with a structure that allows interpolation of the model parameters to obtain the LPV model. The control input vector contains the position references sent to the piezoactuators $\mathbf{r} = [r_x, r_y]^{\mathrm{T}}$ and the output vector to be controlled is the lateral disc movement $\mathbf{p} = [p_x, p_y]^{\mathrm{T}}$. The control input was selected as a pseudo random step-wise excitation. The model is a cascading of two subsystems: the LTI actuator dynamics and the parameter-varying rotor-bearing dynamics. The actuator dynamics $\mathbf{G}_{act}$ in each direction is modelled as second order low-pass filters with real poles and a static gain:

$$\mathbf{G}_{act}(s) = \begin{bmatrix} G_{a,x}(s) & 0 \\ 0 & G_{a,y}(s) \end{bmatrix}, \quad G_{a,j}(s) = \frac{\kappa_{a,j}}{\left(\frac{1}{p_{1,j}}s+1\right)\left(\frac{1}{p_{2,j}}s+1\right)}, \quad j \in \{x, y\} \tag{E.1}$$

The actuator model parameters are listed in Table E.1.

The rotor-bearing dynamics is modelled as the interconnection of parameter-varying Padé approximated input delays and a second order parameter-varying mass-spring-damper system with stiffness, damping and input gains $\tilde{\boldsymbol{\mathcal{K}}}, \tilde{\boldsymbol{\mathcal{D}}}, \tilde{\boldsymbol{\mathcal{B}}}$ and a unit mass $\tilde{\boldsymbol{\mathcal{M}}}$. The stiffness equivalent, damping equivalent and an input gain

equivalents are then defined $\boldsymbol{\mathcal{K}} = \tilde{\boldsymbol{\mathcal{K}}}/\tilde{\boldsymbol{\mathcal{M}}}, \boldsymbol{\mathcal{D}} = \tilde{\boldsymbol{\mathcal{D}}}/\tilde{\boldsymbol{\mathcal{M}}}$ and $\boldsymbol{\mathcal{B}} = \tilde{\boldsymbol{\mathcal{B}}}/\tilde{\boldsymbol{\mathcal{M}}}$. If the state vector is chosen as the disc position $\mathbf{p}(t)$ and velocity $\dot{\mathbf{p}}(t)$, a state-space realisation reads:

$$\mathbf{G}_{rb}(t,\mathbf{q}) = \begin{cases} \begin{bmatrix} \dot{\mathbf{p}}(t) \\ \ddot{\mathbf{p}}(t) \end{bmatrix} = \begin{bmatrix} \mathbf{0} & \mathbf{I} \\ \boldsymbol{\mathcal{K}}(\mathbf{q}) & \boldsymbol{\mathcal{D}}(\mathbf{q}) \end{bmatrix} \begin{bmatrix} \mathbf{p}(t) \\ \dot{\mathbf{p}}(t) \end{bmatrix} + \begin{bmatrix} \mathbf{0} \\ \boldsymbol{\mathcal{B}}(\mathbf{q}) \end{bmatrix} \mathbf{u}_{rb}(t) \\ \mathbf{y}(\mathbf{t}) = \begin{bmatrix} \mathbf{I} & \mathbf{0} \end{bmatrix} \begin{bmatrix} \mathbf{p}(t) \\ \dot{\mathbf{p}}(t) \end{bmatrix} \end{cases} \tag{E.2}$$

The parameter-varying matrices are polynomials of the scheduling parameter vector $\mathbf{q} = [q_1,\ q_2]^{\mathrm{T}}$:

$$\begin{aligned} \boldsymbol{\mathcal{K}}(\mathbf{q}) =& \boldsymbol{\mathcal{K}}_0 + \boldsymbol{\mathcal{K}}_1 q_1 + \boldsymbol{\mathcal{K}}_2 q_2 + \boldsymbol{\mathcal{K}}_3 q_1^2 + \boldsymbol{\mathcal{K}}_4 q_2^2 + \boldsymbol{\mathcal{K}}_5 q_1 q_2 \\ \boldsymbol{\mathcal{D}}(\mathbf{q}) =& \boldsymbol{\mathcal{D}}_0 + \boldsymbol{\mathcal{D}}_1 q_1 + \boldsymbol{\mathcal{D}}_2 q_2 + \boldsymbol{\mathcal{D}}_3 q_1^2 + \boldsymbol{\mathcal{D}}_4 q_2^2 + \boldsymbol{\mathcal{D}}_5 q_1 q_2 \\ \boldsymbol{\mathcal{B}}(\mathbf{q}) =& \boldsymbol{\mathcal{B}}_0 + \boldsymbol{\mathcal{B}}_1 q_1 + \boldsymbol{\mathcal{B}}_2 q_2 + \boldsymbol{\mathcal{B}}_3 q_1^2 + \boldsymbol{\mathcal{B}}_4 q_2^2 + \boldsymbol{\mathcal{B}}_5 q_1 q_2, \end{aligned} \tag{E.3}$$

where $\boldsymbol{\mathcal{K}}_0, ..., \boldsymbol{\mathcal{K}}_5, ..., \boldsymbol{\mathcal{B}}_5$ describe the development within the operating range.

The two Padé approximated input delays τ_x in the horizontal actuation and τ_y in the vertical one are included in the identification and are as well parameter-dependent:

$$\begin{aligned} \tau_x(\mathbf{q}) =& \tau_{x,0} + \tau_{x,1} q_1 + \tau_{x,2} q_2 + \tau_{x,3} q_1^2 + \tau_{x,4} q_2^2 + \tau_{x,5} q_1 q_2 \\ \tau_y(\mathbf{q}) =& \tau_{y,0} + \tau_{y,1} q_1 + \tau_{y,2} q_2 + \tau_{y,3} q_1^2 + \tau_{y,4} q_2^2 + \tau_{y,5} q_1 q_2 \end{aligned} \tag{E.4}$$

The delay approximations have state-space realisations:

$$\begin{aligned} \mathbf{G}_{\boldsymbol{\tau}}(t,\mathbf{q}) &= \begin{bmatrix} G_{\tau_x}(t,\mathbf{q}) & 0 \\ 0 & G_{\tau_y}(t,\mathbf{q}) \end{bmatrix} \\ G_{\tau_j}(t,\mathbf{q}) &= \left[\begin{array}{c|c} -2/\tau_j(\mathbf{q}) & 1 \\ \hline 4/\tau_j(\mathbf{q}) & -1 \end{array}\right], \quad j \in \{x, y\} \end{aligned} \tag{E.5}$$

The Padé-approximated input delays and the stiffness, damping and input gain matrix are therefore functions of the scheduling parameter. Figure E.2 provides an overview of the model and the parameter-dependencies.

It is of interest to reduce the model order, since it reduces the controller order for synthesis with robust control techniques. We therefore use residualisation [93] to reduce the model from 10-th to 6-th order.

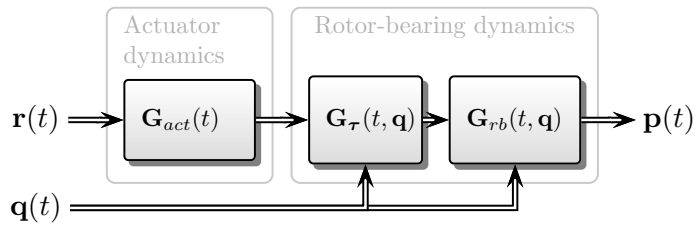

Figure E.2: Overview of the gas bearing model, which includes the actuator dynamics and parameter-varying rotor-bearing dynamics.

The gas bearing model can then be formulated in state-space as:

$$\mathbf{G}(t,\mathbf{q}) = \mathbf{G}_{rb}(t,\mathbf{q})\mathbf{G}_{\boldsymbol{\tau}}(t,\mathbf{q})\mathbf{G}_{act}(t) = \left[\begin{array}{c|c} \mathbf{A}_G(\mathbf{q}) & \mathbf{B} \\ \hline \mathbf{C} & \mathbf{0} \end{array}\right], \tag{E.6}$$

$$\mathbf{A}_g(\mathbf{q}) = \mathbf{A}_{g0} + \textstyle\sum_{n=1}^{N} f_n(\mathbf{q}) \cdot \mathbf{A}_{g,n}, \tag{E.7}$$

$$f_1 = q_1,\ f_2 = q_2,\ f_3 = q_1^2,\ f_4 = q_2^2,\ f_5 = q_1 q_2 \tag{E.8}$$

in which the basis functions f_n describe the parameter-dependency for $N = 5$. Since the parameters' variation is slow, it is reasonable to assume $\dot{\mathbf{q}} \approx \mathbf{0}$.

The LPV model is shown in [3] to preserve important properties (natural frequencies, damping factors and static gains) of the system within the desired range of the scheduling parameters. The shape of the time-varying parameters are shown in [3] as functions of the scheduling parameters. Here, the effects of parameter-variation are quantified by a set of derived parameters for the system. These parameters are chosen to describe the static gain matrix $\mathbf{G}(s,\mathbf{q})\big|_{s=0} = \left[\begin{smallmatrix} g_{xx} & g_{xy} \\ g_{yx} & g_{yy} \end{smallmatrix}\right]$ and the eigenvalues. The model has six eigenvalues: two related to the time delays and two complex pole pairs, which model the two first critical speeds of the rotor-bearing. The natural frequencies associated with the complex pole pairs are denoted ω_x and ω_y and their associated damping factors are ζ_x, ζ_y. Table E.2 provides the range of variation of the parameters considered showing that they all vary significantly across the operating range.

Figure E.3 shows how the frequency responses of the gas bearing system change when the scheduling parameters are at the extrema of the operating range ($[\underline{q}_1,\ \underline{q}_2]$, $[\underline{q}_1,\ \bar{q}_2], [\bar{q}_1,\ \underline{q}_2], [\bar{q}_1,\ \bar{q}_2]$). For high angular velocities, the cross coupling gains increase significantly. For high injection pressures, the natural frequencies increase and the damping decreases.

Table E.2: Derived parameter-variation

Parameter	interval	Deviation[a]
Horizontal natural frequency ω_x	$[657, 775]$ rad/s	15.2%
Vertical natural frequency ω_y	$[736, 832]$ rad/s	11.5%
Horizontal damping factor ζ_x	$[0.033, 0.12]$	73.2%
Vertical damping factor ζ_y	$[0.016, 0.092]$	82.7%
Horizontal delay τ_x	$[0.056, 0.41]$ ms	86.5%
Vertical delay τ_x	$[0.093, 0.46]$ ms	80.0%
Static gain g_{xx}	$[2.37, 3.27]$ μm/V	27.4%
Static gain g_{xy}	$[-0.01, 0.74]$ μm/V	101.5%
Static gain g_{yx}	$[-0.61, 0.14]$ μm/V	540.8%
Static gain g_{yy}	$[2.97, 3.24]$ μm/V	8.2%

[a]Deviation from the maximum value for variable $a \in [\underline{a}, \bar{a}]$ calculated as $100(\bar{a} - \underline{a})/\bar{a}$

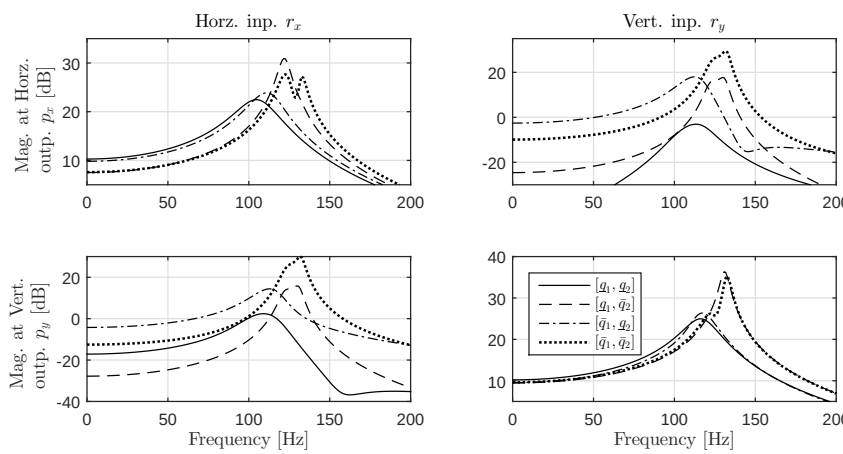

Figure E.3: Bode diagrams of the gas bearing system for the scheduling parameter extrema $[\underline{q}_1,\ \underline{q}_2], [\underline{q}_1,\ \bar{q}_2], [\bar{q}_1,\ \underline{q}_2], [\bar{q}_1,\ \bar{q}_2]$

E.3 Damping enhancing control of gas bearings

This section describes the design of the controllers. First a discussion is given of what is meant by damping enhancing control, followed by the design of the LPV controller and the $\mathcal{H}_\infty$ controller.

The gas bearing dynamics contains under-damped eigenfrequencies making it very sensitive to disturbances near the associated resonance frequencies. The impact of these disturbances can be diminished by proper shaping of the closed-loop sensitivity function. Consider the general control system from [93], the system output $\mathbf{y}(s)$ is:

$$\mathbf{y}(s) = \mathbf{G}(s)\mathbf{u}(s) + \mathbf{G}_d(s)\mathbf{d}(s) \tag{E.9}$$

in which $\mathbf{G}$ is the the plant to be controlled using the input $\mathbf{u}(s)$. The disturbances $\mathbf{d}(s)$ enter the output through the (generally unknown) dynamics $\mathbf{G}_d(s)$. When the loop is closed with the control law $\mathbf{u}(s) = \mathbf{K}(s)\mathbf{y}(s)$, the system output is

$$\mathbf{y}(s) = \mathbf{S}\mathbf{G}_d\mathbf{d}(s), \quad \mathbf{S}(s) = (\mathbf{I} - \mathbf{G}\mathbf{K})^{-1} \tag{E.10}$$

The analysis shows that the effects of the disturbances on the output in a specific frequency range $\omega \in \Omega$ are diminished by a controller $\mathbf{K}$ that obtains a low sensitivity $|\mathbf{S}(j\omega)| \ll 1$ in that range. Therefore the damping of the resonance frequencies is increased by reducing the sensitivity near the associated frequency.

E.3.1 LPV controller design

The LPV controller $\mathbf{K}$ should enhance the damping to reduce the disturbance sensitivity near the resonance frequencies and at the same time avoid wear of the actuator. These disturbance and noise rejection requirements can be cast according to the mixed sensitivity setup [93] which seeks to minimise:

$$\mathbf{K}(t, \mathbf{q}) = \min_{\mathbf{K}} \|\mathbf{N}\|_\infty, \quad \mathbf{N}(t, \mathbf{q}) = \begin{bmatrix} \mathbf{W}_p\mathbf{S} \\ \mathbf{W}_u\mathbf{K}\mathbf{S} \end{bmatrix}, \tag{E.11}$$

where the closed loop sensitivity functions are defined for constant $\mathbf{q} = \mathbf{q}_0$: $\mathbf{S}(s, \mathbf{q}_0) \triangleq (\mathbf{I}_{n_y} - \mathbf{G}(s, \mathbf{q}_0)\mathbf{K}(s, \mathbf{q}_0))^{-1}$ and $\mathbf{K}\mathbf{S}$, and they are shaped by the weight functions $\mathbf{W}_p$ and $\mathbf{W}_u$. The external output disturbance $\mathbf{w}$ and external outputs $\mathbf{z} = [\mathbf{z}_1^{\mathrm{T}}, \mathbf{z}_2^{\mathrm{T}}]^{\mathrm{T}}$ are augmented to the system to obtain the augmented plant as shown in Figure E.4. To enhance damping, the controller should therefore have high performance in the frequency range around the under-damped eigenfrequencies of the rotor-bearing

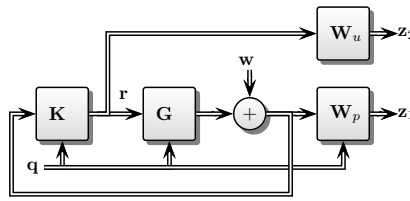

Figure E.4: The augmented plant with controller for LPV controller design with performance weights $\mathbf{W}_p$ and controller sensitivity weight $\mathbf{W}_u$.

$\omega_x(\mathbf{q})$ and $\omega_y(\mathbf{q})$. The performance filter is therefore chosen to contain inverse notch-like filters:

$$\mathbf{W}_p(s) = \text{diag}\left(w_{ph}(s,\mathbf{q}), w_{pv}(s,\mathbf{q})\right)) \tag{E.12}$$

in which w_{ph} and w_{pv} both have the form:

$$w_{ph}(s,\mathbf{q}) = \frac{s^2+2\zeta_1\omega_x(\mathbf{q})s+\omega_x(\mathbf{q})^2k_0}{s^2+2\zeta_2\omega_x(\mathbf{q})s+\omega_x(\mathbf{q})^2}, \tag{E.13}$$

$$w_{pv}(s,\mathbf{q}) = \frac{s^2+2\zeta_1\omega_y(\mathbf{q})s+\omega_y(\mathbf{q})^2k_0}{s^2+2\zeta_2\omega_y(\mathbf{q})s+\omega_y(\mathbf{q})^2} \tag{E.14}$$

The natural frequencies $\omega_x = \omega_x(\mathbf{q})$, $\omega_y = \omega_y(\mathbf{q})$ are chosen as the under-damped natural frequencies of the gas bearing to obtain a high weight around these. The weight at the resonance frequencies is a tuning parameter and an increased peak gain at the resonance frequency in general results in more damping. A few iterations showed that $\zeta_1 = 0.3$ and $\zeta_2 = 0.05$ provides a sufficient damping enhancement over the operating range. The peak gain is then 19 dB. The low sensitivity around the natural frequencies must come at the cost of increased sensitivity in another frequency range due to Bode's sensitivity integral [104]. Recent work [4] showed it is beneficial to place this sensitivity increase in the low frequency range where an amplification of disturbances is acceptable. The constant $k_0 = 1/3$ determines the low frequency weight. The control signal sensitivity weight $\mathbf{W}_u$ is chosen to penalise control action at high frequency control with the high-pass filter from [93]:

$$\mathbf{W}_u(s) = \mathbf{I}w_u(s), \quad w_u(s) = \frac{s/M_b + \omega_b}{s + \omega_b A_b}, \tag{E.15}$$

where the low frequency gain is $1/A_b$, $A_b = 10$, the high frequency gain is $1/M_b = 15$, and the approximate crossover frequency is $\omega_b = 2\pi 1000$ rad/s. The weight $\mathbf{W}_u$ and a realisation of the parameter-varying performance weight are shown in Figure E.5.

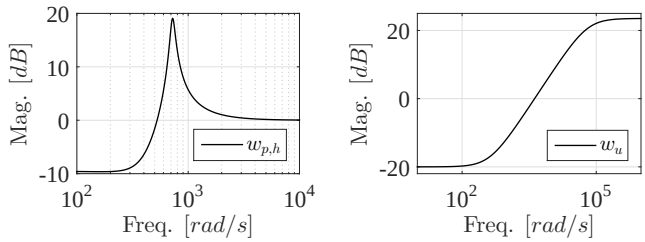

Figure E.5: Example of performance weight $w_{p,h}(s, \mathbf{q})$ as defined in (E.13) and controller sensitivity weight $w_u(s)$ as defined in (E.15) for scheduling parameter $\mathbf{q} = [2.87 \text{ krpm}, 0.51 \text{ MPa}]^{\mathrm{T}}$.

The augmented plant $\mathbf{P}$ has an LPV state-space realisation of 12^{th} order (6^{th} order system, 4^{th} order $\mathbf{W}_p$, 2^{nd} order $\mathbf{W}_u$):

$$\mathbf{P}(\mathbf{q}) = \left[\begin{array}{c|cc} \mathbf{A}(\mathbf{q}) & \mathbf{B}_1 & \mathbf{B}_2(\mathbf{q}) \\ \hline \mathbf{C}_1(\mathbf{q}) & \mathbf{D}_{11} & \mathbf{D}_{12} \\ \mathbf{C}_2 & \mathbf{D}_{21} & \mathbf{D}_{22} \end{array}\right], \tag{E.16}$$

in which the scheduling parameter-dependency can be formulated using the basis functions $f_n(\mathbf{q})$ defined in (E.8).

We use the guidelines from [33] to determine the synthesis method for the LPV controller. The scheduling parameter dependency is not affine and not on a linear fractional transformation form. The number of scheduling parameters is fairly low. For the present system, the guidelines then suggest to use the gridding-based LPV synthesis method [76]. A full-order LPV controller $\mathbf{K}(\mathbf{q})$ for the system $\mathbf{P}(\mathbf{q})$ (E.16) guarantees $\|\mathbf{z}\|_2 \leq \gamma \|\mathbf{w}\|_2$ if it is a solution to the following two matrix inequalities for the decision variables $\hat{\mathbf{A}}_K$,$\hat{\mathbf{B}}_K$,$\hat{\mathbf{C}}_K$,$\mathbf{D}_K$, $\mathbf{X}$,$\mathbf{Y}$, γ of appropriate dimensions for $\boldsymbol{\mathcal{T}}_1$ and $\boldsymbol{\mathcal{T}}_2$:

$$\boldsymbol{\mathcal{T}}_1 \succ 0, \quad \boldsymbol{\mathcal{T}}_2 \prec 0 \tag{E.17}$$

$$\mathcal{T}_1 = \begin{bmatrix} \mathbf{X} & \mathbf{I}_{n_a} \\ \mathbf{I}_{n_a} & \mathbf{Y} \end{bmatrix},$$

$$\mathcal{T}_2 = \begin{bmatrix} \mathbf{X}\mathbf{A} + \hat{\mathbf{B}}_K\mathbf{C}_2 + (\star) & \star & \star & \star \\ \hat{\mathbf{A}}_K^{\mathrm{T}} + \mathbf{A} + \mathbf{B}_2\mathbf{D}_K\mathbf{C}_2 & \mathbf{A}\mathbf{Y} + \mathbf{B}_2\hat{\mathbf{C}}_K + (\star) & \star & \star \\ \left(\mathbf{X}\mathbf{B}_1 + \hat{\mathbf{B}}_K\mathbf{D}_{21}\right)^{\mathrm{T}} & (\mathbf{B}_1 + \mathbf{B}_2\mathbf{D}_K\mathbf{D}_{21})^{\mathrm{T}} & -\gamma\mathbf{I}_{n_w} & \star \\ \mathbf{C}_1 + \mathbf{D}_{12}\mathbf{D}_K\mathbf{C}_2 & \mathbf{C}_1\mathbf{Y} + \mathbf{D}_{12}\hat{\mathbf{C}}_K & \mathbf{D}_{11} + \mathbf{D}_{12}\mathbf{D}_K\mathbf{D}_{21} & -\gamma\mathbf{I}_{n_z} \end{bmatrix} \tag{E.18}$$

The dependency of the scheduling parameters is omitted in the above. This problem is a linear matrix inequality (LMI) with infinite dimension, but becomes tractable by the following proposals from [75]: 1) the matrix inequalities are evaluated over a finite grid $\mathcal{Q}_d$ of scheduling parameters covering the operating range; 2) the decision variables are constrained to copy the non-linear plant function dependency:

$$\begin{aligned} \hat{\mathbf{A}}_K(\mathbf{q}) &= \hat{\mathbf{A}}_{K,0} + \sum_{n=1}^{N} f_n(\mathbf{q})\hat{\mathbf{A}}_{K,n}, \quad \hat{\mathbf{B}}_K(\mathbf{q}) = \hat{\mathbf{B}}_{K,0} + \sum_{n=1}^{N} f_n(\mathbf{q})\hat{\mathbf{B}}_{K,n} \\ \hat{\mathbf{C}}_K(\mathbf{q}) &= \hat{\mathbf{C}}_{K,0} + \sum_{n=1}^{N} f_n(\mathbf{q})\hat{\mathbf{C}}_{K,n}, \quad \mathbf{D}_K(\mathbf{q}) = \mathbf{D}_{K,0} + \sum_{n=1}^{N} f_n(\mathbf{q})\mathbf{D}_{K,n} \end{aligned} \tag{E.19}$$

In the above, $\hat{\mathbf{A}}_{K,n}, \hat{\mathbf{B}}_{K,n}, \hat{\mathbf{C}}_{K,n}$ and $\mathbf{D}_{K,n}$ are matrices to be determined in the LMI optimisation. The augmented systems (E.16) in the design grid must be in coherent state-space bases. To improve the numerical plant conditioning, it is balanced using one constant transformation matrix $\mathbf{T}_0$, such that $\begin{bmatrix} \mathbf{T}_0\mathbf{A}\mathbf{T}_0^{-1} & \mathbf{T}_0\mathbf{B} \\ \mathbf{C}\mathbf{T}_0^{-1} & \mathbf{0} \end{bmatrix}$ where $\mathbf{T}_0$ equalises the maximum row and column norms across the entire array of gridded augmented plants. The scaling matrix is found in Matlab with `ssbal.m`.

To obtain a controller which is practically valid (i.e. is not a function of the scheduling parameter derivatives, which are not measured), it is proposed in [75] to constrain either $\mathbf{X}$ or $\mathbf{Y}$ to be constant. All attempts trying to constrain $\mathbf{X}$ to a constant failed to provide a feasible LMI solution. We therefore choose $\mathbf{X}$ to be function of the scheduling parameters and $\mathbf{Y}$ to be constant:

$$\mathbf{X}(\mathbf{q}) = \mathbf{X}_0 + \sum_{n=1}^{N} f_n(\mathbf{q})\mathbf{X}_n, \quad \mathbf{Y} = \mathbf{Y}_0 \tag{E.20}$$

The resulting LMIs are then solved to minimise the objective function:

$$\min \left\{ \gamma + \varepsilon_T \sum_{n=0}^{N} \text{tr}(\mathbf{X}_n) + \text{tr}(\mathbf{Y}_0) \right\} \tag{E.21}$$

where the small constant $\varepsilon_T = 2.2 \cdot 10^{-16}$ is chosen to avoid numerically large values in $\mathbf{X}$ and $\mathbf{Y}$.

The LMIs are generated in Matlab with YALMIP [99], which only permits non-strict LMIs. The LMIs (E.18) are therefore restricted to:

$$\mathcal{T}_1 \succ \varepsilon, \quad \mathcal{T}_2 \prec -\varepsilon, \tag{E.22}$$

in which $\varepsilon > 0$ is some small positive number. Design iterations show that a value $\varepsilon = 1.5 \cdot 10^{-3}$ and a grid of 8×8 equidistant values of the scheduling parameter provides an adequate solution.

The LMIs are solved over the design grid $\mathcal{Q}_d$ using MOSEK to obtain an LMI solution satisfied for $\gamma = \gamma_d = 1.4987$. To ensure the performance over the whole scheduling parameter interval, the LMI solution must be validated over a finer validation grid $\mathcal{Q}_v$. It is common that the value γ_d must be increased for the LMI solution to be valid in the validation grid. In Figure E.6, we show how the performance γ_d varies over the scheduling parameter interval for a validation grid of 16×16 equidistant values of the scheduling parameters.

We refined the grid further to ensure the solution is valid. Figure E.7 shows the performance γ for varying sizes of the validation grid. The LMI solution is satisfied for $\gamma = 1.4995$.

From the solution, the factorisation problem $\mathbf{I} - \mathbf{XY} = \mathbf{NM}^{\mathrm{T}}$ must be solved for $\mathbf{N}(\mathbf{q})$ and $\mathbf{M}(\mathbf{q})$. We choose $\mathbf{M} = \mathbf{I}$ and $\mathbf{N}(\mathbf{q}) = \mathbf{I} - \mathbf{X}(\mathbf{q})\mathbf{Y}_0$. The controller parameters are calculated:

$$\mathbf{K}(\mathbf{q}) = \left[\begin{array}{c|c} \mathbf{A}_K(\mathbf{q}) & \mathbf{B}_K(\mathbf{q}) \\ \hline \mathbf{C}_K(\mathbf{q}) & \mathbf{D}_K(\mathbf{q}) \end{array}\right], \tag{E.23}$$

in which:

$$\begin{aligned} \mathbf{A}_K =& \mathbf{N}^{-1} \Big(\mathbf{X}\dot{\mathbf{Y}} + \mathbf{N}\dot{\mathbf{M}}^{\mathrm{T}} + \hat{\mathbf{A}}_K - \mathbf{X} \left(\mathbf{A} - \mathbf{B}_2 \mathbf{D}_K \mathbf{C}_2 \right) \mathbf{Y} \\ & - \hat{\mathbf{B}}_K \mathbf{C}_2 \mathbf{Y} - \mathbf{X} \mathbf{B}_2 \hat{\mathbf{C}}_K \Big) \mathbf{M}^{-\mathrm{T}} \\ \mathbf{B}_K =& \mathbf{N}^{-1} \left(\hat{\mathbf{B}}_K - \mathbf{X} \mathbf{B}_2 \mathbf{D}_K \right) \\ \mathbf{C}_K =& \left(\hat{\mathbf{C}}_K - \mathbf{D}_K \mathbf{C}_2 \mathbf{Y} \right) \mathbf{M}^{-\mathrm{T}}, \end{aligned} \tag{E.24}$$

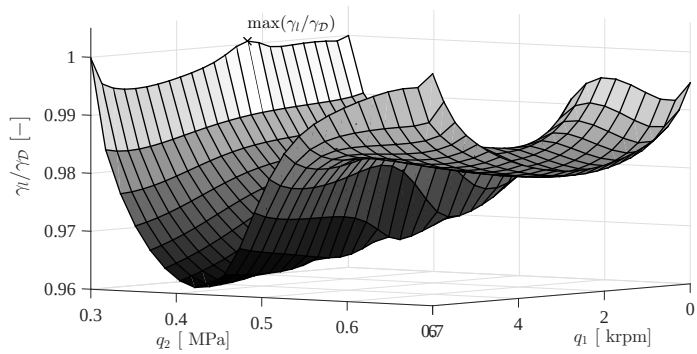

Figure E.6: Validation of LPV controller. Around $q_2 \approx 0.4$ MPa better performance is achieved than defined by γ_d whereas the limiting performance is obtained at $\mathbf{q} = [2.3 \text{ krpm}, 0.3 \text{ MPa}]^{\mathrm{T}}$, where $\max(\gamma)/\gamma_d = 1.00054$.

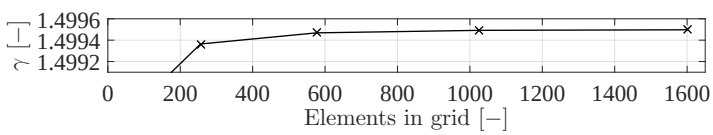

Figure E.7: Performance index for varying validation grid sizes. The performance converges as the grid size increases.

where the parameters are functions of the scheduling parameter. The evaluation of the matrices $\hat{\mathbf{A}}_K, \hat{\mathbf{B}}_K, \hat{\mathbf{C}}_K, \mathbf{D}_K$ and $\mathbf{X}, \mathbf{Y}$, and calculations of the controller matrices (E.24) have to be performed online for each scheduling sampling step, which is computationally heavy due to the two matrix inversions.

E.3.2 $\mathcal{H}_\infty$ controller design

The LPV controller can directly address the parameter-dependency though conservatism may be introduced by constraining the controller parameters to polynomial surfaces. A more simple controller which is able to include the multiple control objectives in the design is the $\mathcal{H}_\infty$ controller. This design methodology offers many possibilities. The parameter-varying dynamics could be modelled as uncertainties using e.g. multiplicative uncertainty. Such an approach tends to result in conservative

designs since performance is required in the frequency range of the under-damped eigenvalues where the gain varies strongly, so to guarantee robust performance; the controller could therefore not enhance the damping. An alternative and simpler approach is to design the controller for one operating condition to pursue a high damping increase for that nominal plant. This approach only guarantees stability for the design condition. The stability and performance must therefore be investigated over the selected operating range. The controller must be designed from a non-parameter-varying reference model which is chosen as the gas bearing model evaluated in the center operating condition $\mathbf{q}_0 = [3 \text{ krpm}, 0.5 \text{ MPa}]^{\mathrm{T}}$. The same mixed sensitivity setup for the LPV controller is used with the weights evaluated at $\mathbf{q}_{c0}$ to have $\mathbf{N}(s, \mathbf{q}_{c0}) = \mathbf{N}(s)$

$$\mathbf{K}(s) = \min_{\mathbf{K}} \|\mathbf{N}(s)\|_\infty, \quad \mathbf{N}(s) = \begin{bmatrix} \mathbf{W}_p(s)\mathbf{S}(s) \\ \mathbf{W}_u(s)\mathbf{K}(s)\mathbf{S}(s) \end{bmatrix}, \tag{E.25}$$

The controller will then be optimised for this particular operating condition. The controller $\mathbf{K}_\infty$ is synthesised with performance $\gamma_{\mathcal{H}_\infty} = 1.13$. The found γ is lower than the one found for the LPV controller and indicates the level of conservatism from constraining the LPV controller parameters. The stability and performance of the $\mathcal{H}_\infty$ controller over the operating range is then validated by calculating the closed-loop system over $\mathcal{Q}_v$, and it is found that the controller stabilises the gas bearing. The worst case performance index is found to be $\max\gamma = 2.28$ at $\mathbf{q} = [1.86 \text{ krpm}, 0.3 \text{ MPa}]^{\mathrm{T}}$. Figure E.8 shows the performance in the validation grid points of the $\mathcal{H}_\infty$- and the LPV controller. The LPV controller performance only varies little over the design interval. Based on the $\mathcal{H}_\infty$-performance values, the LPV controller in general outperforms the $\mathcal{H}_\infty$ controller except for a range around the design condition of the $\mathcal{H}_\infty$ controller. This is expected since the LPV controller gains are constrained to polynomial surfaces and similar results were found in [52, 53].

E.4 Numerical Controller Validation

The performance of rotating machinery is often assessed using impulse responses which effectively reveals under-damped modes by exciting the system over a wide frequency range. Such impulse responses have been generated for a fine grid of operating conditions. A constant impulse magnitude corresponding to a strong impact is chosen. Due to spacial limitations, only four are included in the paper as they are representative for the remaining impulse responses. The results shown are from

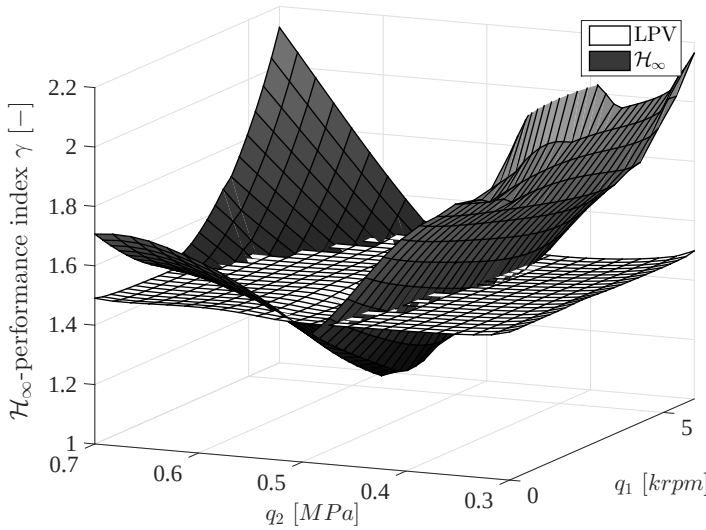

Figure E.8: Comparison of $\mathcal{H}_\infty$-performance index γ for LPV controller evaluated in the validation grid points $\mathbf{q}_l \in \mathcal{Q}_v$.

the four scheduling parameter extrema $\{[\underline{q}_1, \underline{q}_2]^{\mathrm{T}}, [\overline{q}_1, \underline{q}_2]^{\mathrm{T}}, [\underline{q}_1, \overline{q}_2]^{\mathrm{T}}, [\overline{q}_1, \overline{q}_2]^{\mathrm{T}}\}$. The impulse responses are compared for three different cases: a) open loop operation b) $\mathcal{H}_\infty$ controlled c) LPV controlled. Both output directions have been investigated over $\mathcal{Q}_v$ showing that the controller performance of the LPV and the $\mathcal{H}_\infty$ controller are similar in the vertical direction; whereas the horizontal direction shows more variation. Therefore only the horizontal results are shown. Figure E.9 shows the 3×4 impact responses. The impulse responses in the open loop case a) show differences in the natural frequency and the damping factor. The robust controller in case b) is able to enhance the damping but the LPV controller in case c) enhances the damping more for all investigated cases. The LPV controller does not alter the vibration period significantly. The oscillation magnitude is negligible after one period. The impact responses shown are of high magnitude, and controller saturation would occur in the the $\mathcal{H}_\infty$ controlled case as the control signal exceeds the saturation limits $r_x \in [-5, 5]$V and deteriorates the performance whereas the LPV control signal remains within the limits.

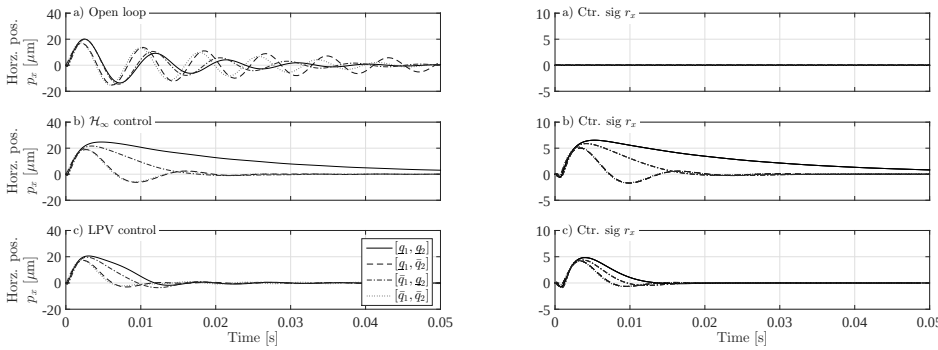

Figure E.9: Simulated horizontal impact responses for the scheduling parameter extrema in the three cases: a) open loop, b) $\mathcal{H}_\infty$ control, c) LPV control. Figures to the right show corresponding control signals.

E.5 Experimental Closed-Loop Results

This section presents experimental results validating the enhanced damping properties of the controllers designed. Experimental impact responses are collected and used to assess the performance of the controllers. The impact responses are compared for the open loop and the controlled cases. Finally, experiments have been performed during angular velocity transients to investigate the controllers' capabilities during scheduling parameter variations.

To allow implementation in the dSpace control system the controllers must be discretised. The $\mathcal{H}_\infty$ controller is converted to discrete time using a Tustin approximation. The LPV controller is discretised using the trapezoidal LPV discretisation method proposed in [100]. The calculation of the controller matrix updates requires the inversion of two matrices of dimensions 12×12, which is time consuming. We therefore update the control gains at a lower frequency as proposed in [85]. The equipment used allows the controller matrices to be updated with a sampling rate of 10 Hz while the control signal is updated with the sampling rate $f_s = 5$ kHz. The scheduling parameters change slowly on a time scale of seconds, the control matrix is updated 10 times faster.

E.5.1 Impact Responses

The controller performances are investigated experimentally with impulse responses similar to the ones in Section E.4 since they are effective for exciting the system eigenfrequencies. The shaft was therefore excited as close as possible to the gas bearing with an impact hammer which measures the applied force $f(t)$. To investigate the controller capabilities over the operating range such impulse responses were collected over a fine grid of operating conditions chosen as the combination of angular velocities $q_1 \in \{0, 1.5, 3, 4.5, 6\}$ krpm and injection pressures $q_2 \in \{0.3, 0.433, 0.567, 7\}$ MPa. This includes points different from the identification grid to validate the controller works in the interpolation regions too.

The impact response data collected for rotating conditions contains both the response from mass imbalance and from the shaft impact. The displayed data has therefore been filtered to remove the mass imbalance response. An example of data before and after filtering is shown in Figure E.10.

The experimental closed-loop results resemble the simulated and both controllers enhance the damping significantly. The experiments show that the LPV controller and the $\mathcal{H}_\infty$ controller achieve similar performance in the vertical shaft direction whereas the the differences are more evident in the horizontal direction. Due to the space restrictions all the $4 \times 5 \times 3$ impact responses cannot be shown in the paper, but Figure E.11 shows filtered horizontal impact responses for the open-loop, $\mathcal{H}_\infty$ controlled and the LPV controlled cases at the scheduling parameter extrema. The controllers enhance the damping in all cases. Four vertical impact responses at the operating conditions $q_1 \in \{1.5, 4.5\}$ krpm, $q_2 \in \{0.433, 0.567\}$ MPa are shown in E.7 to validate that the performance also is achieved in off-identification grid points.

It is desirable to quantify the controller performances both in terms of damping enhancement and noise rejection. A common approach is to estimate the damping factors using e.g. the logarithmic decrement. This approach is not suitable here since the controller increases the total system order by 12 and the impact responses cannot easily be decomposed. Therefore alternative approaches must be sought. When the damping is increased the impulse response decays faster hence the energy of the impulse response decreases. The magnitude of the response is proportional to the impact energy. The impulse responses are therefore quantified with the ratio of the disc displacement energy and the impact force energy denoted as V_p:

$$V_p = \frac{\|\mathbf{p}(t)\|_{\mathcal{L}2}}{\|f(t)\|_{\mathcal{L}2}} \tag{E.26}$$

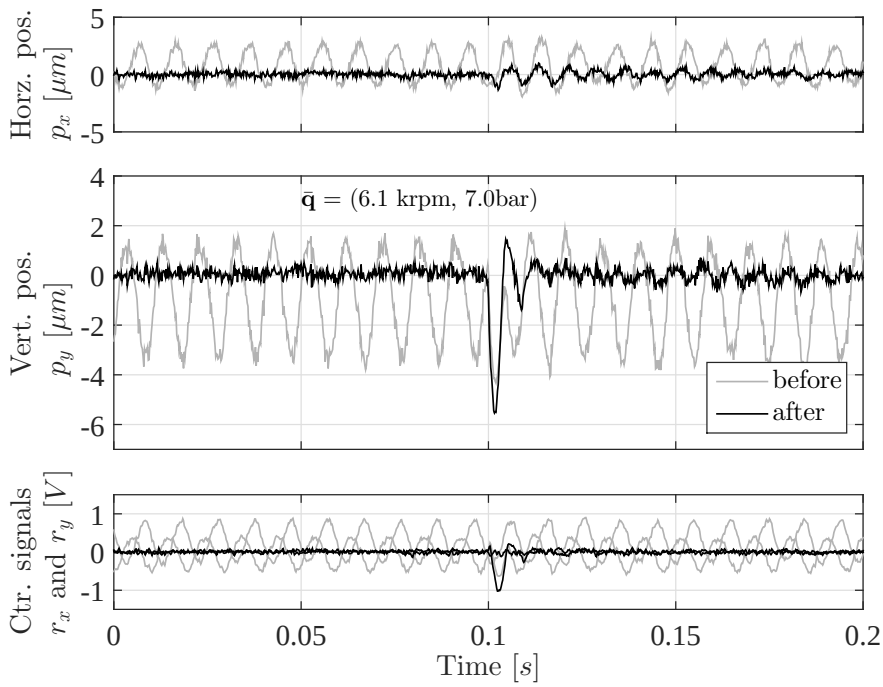

Figure E.10: Closed loop impact response at $\mathbf{q} = [6 \text{ krpm}, 0.7 \text{ MPa}]^{\mathrm{T}}$. To display the impact response, the data is filtered to remove the mass imbalance. This figure shows the data before and after runout-filtering, which filters out the mass imbalance response.

where the $\mathcal{L}2-$norm of a signal $\mathbf{a} = [a_1, a_2, ..., a_J]^{\mathrm{T}}$ sampled at instants kT_s, $k \in \{0, 1, ..., K\}$ is

$$\|\mathbf{a}(t)\|_{\mathcal{L}2} = \sqrt{\frac{1}{T_s} \sum_{k=0}^{K} \sum_{j=1}^{J} a_j^2(kT_s)} \tag{E.27}$$

The impact responses are defined as settled after $K = 500$ samples. Similarly, the control effort is quantified as the energy V_p defined as the ratio of the control signal displacement energy and the force energy:

$$V_r = \frac{\|\mathbf{r}(t)\|_{\mathcal{L}2}}{\|f(t)\|_{\mathcal{L}2}} \tag{E.28}$$

Multiple impact responses have been collected for each experimental grid point and the mean energy for the impact responses at the 20 experimental grid points is

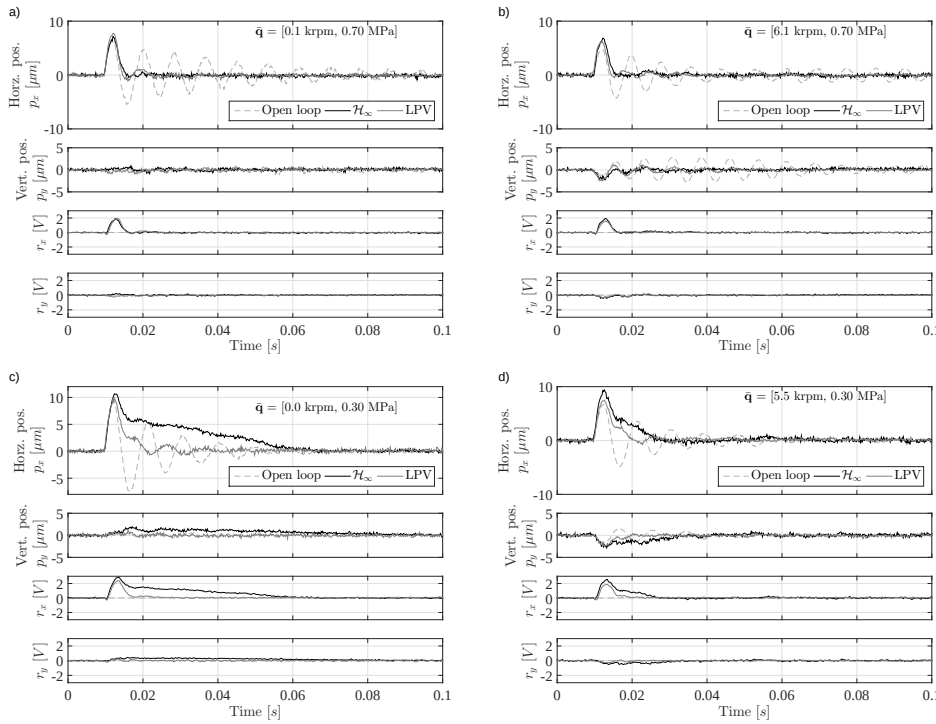

Figure E.11: Horizontal open loop and LPV closed loop impact responses at the scheduling parameter extrema: a) $\mathbf{q} = [0 \text{ rpm}, 0.7 \text{ MPa}]^{\mathrm{T}}$, b) $\mathbf{q} = [6 \text{ krpm}, 0.7 \text{ MPa}]^{\mathrm{T}}$, c) $\mathbf{q} = [0 \text{ rpm}, 0.3 \text{ MPa}^{\mathrm{T}}$, d) $\mathbf{q} = [5.5 \text{ krpm}, 0.3 \text{ MPa}]^{\mathrm{T}}$

shown in Figure E.12. The LPV controller reduces the response energy in all cases whereas the $\mathcal{H}_\infty$ controller reduces the energy at all operating conditions except experiment 1 at $\underline{\boldsymbol{q}} = [0.0 \text{ krpm}, 0.3 \text{ MPa}]$. This is in good agreement with the long settling time observed from Figure E.11.c.

The averages of control effort of the LPV controller and the $\mathcal{H}_\infty$ controller are shown in Figure E.13 which shows that the LPV controller generally has the lowest control effort. The means of the impact energies have been calculated over the experiments and Table E.3 summarises the results. The $\mathcal{H}_\infty$ controller in average reduces the impact energy for horizontal impacts to 51% compared to open-loop case and the LPV controller in average reduces the impact energy to 34%. Similarly for the vertical impacts, the the $\mathcal{H}_\infty$ controller reduces the impact energy to 25%, and

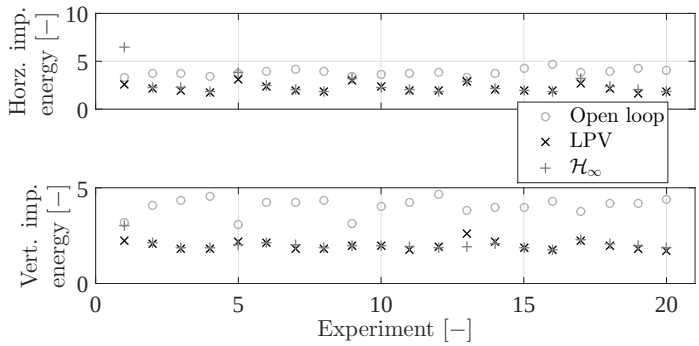

Figure E.12: Mean energy for the open and closed-loop impact responses calculated with (E.26).

Table E.3: Mean response energies of impact responses

	Open loop	LPV	$\mathcal{H}_\infty$
Horizontal impact energy:	14.94	5.08	7.63
Vertical impact energy:	16.51	4.00	4.20
Horizontal control energy:		0.30	0.53
Vertical control energy:		0.18	0.23

the LPV controller to 24%. This shows that the main benefits of the LPV control in this case is obtained in the horizontal shaft direction. The LPV controller reduces the control effort compared to the $\mathcal{H}_\infty$ controller to 57% for the horizontal impacts and 78% for the vertical ones.

The results are interesting since the $\mathcal{H}_\infty$ controller was tuned for one operating condition to pursue a high attenuation for the nominal plant. Figure E.8 shows that this comes at the cost of performance in the "global sense"since its performance deteriorates significantly over the operating range. A controller designed to guarantee robust performance would even locally be outperformed by the LPV controller. The approach pursued was very simple and the resulting controller was effective over the operating range.

E.5.2 Run-Up and Coast-Down

When the machine is started up (and shut down), faster variations occur in the angular velocity which is accelerated from zero to some operating speed (or vice

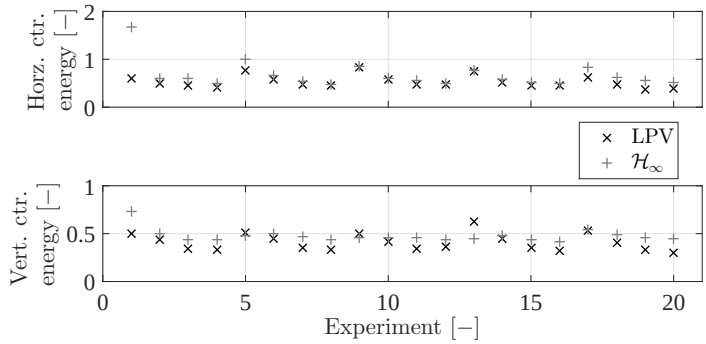

Figure E.13: The mean control efforts for closed-loop impact responses calculated with (E.28).

versa). The controllers designed are not guaranteed to work for changes in the scheduling parameters but simulations have shown the controller is effective in these scheduling parameter transients as well. Experiments have therefore been performed to display the controller capabilities during these transient modes. During the experiments the shaft is accelerated from 0 krpm to 6 krpm with a mean acceleration of 0.1 krpm/s. The turbine supply is then turned off and the shaft decelerates at a mean rate of 0.04 krpm/s. Figure E.14 shows the vibration amplitude during the run-up and following coast-down phase both for the open loop and the controlled gas bearing using both controllers. At low angular velocities the controllers amplify the vibrations within an acceptable level as expected. As the angular velocity increases the controllers reduce the vibration amplitude compared to open loop. In the vertical direction the LPV and the $\mathcal{H}_\infty$ controllers show equal performance in reducing the vibration amplitude. At 6 krpm the LPV controller reduces the vibration magnitude to 62.6%, whereas the $\mathcal{H}_\infty$ only reduces the vibration amplitude to 76.9% in the horizontal direction and 78% in the vertical direction. As desired both controllers use limited control efforts to avoid wear. The open loop experiments show vibration peaks in the horizontal and the vertical direction around angular velocities 3.69 krpm$(= 61.5$ Hz$)$ and 4.05 krpm$(= 67.5$ Hz$)$ and also at 2.34 krpm$(= 39.0$ Hz$)$ and 2.64 krpm$(= 44.0$ Hz$)$. These frequencies correspond to one half and one third of the first critical speeds. Such vibrations commonly indicate that the rotor is not accurately mounted in the gas bearing i.e. is misaligned. The misalignment is difficult to avoid in applications with low tolerances such as gas bearings. The misalignment causes excitation at integer-multiple of the angular velocity $(q_1, 2q_1, 3q_1, ...)$ [55, 56,

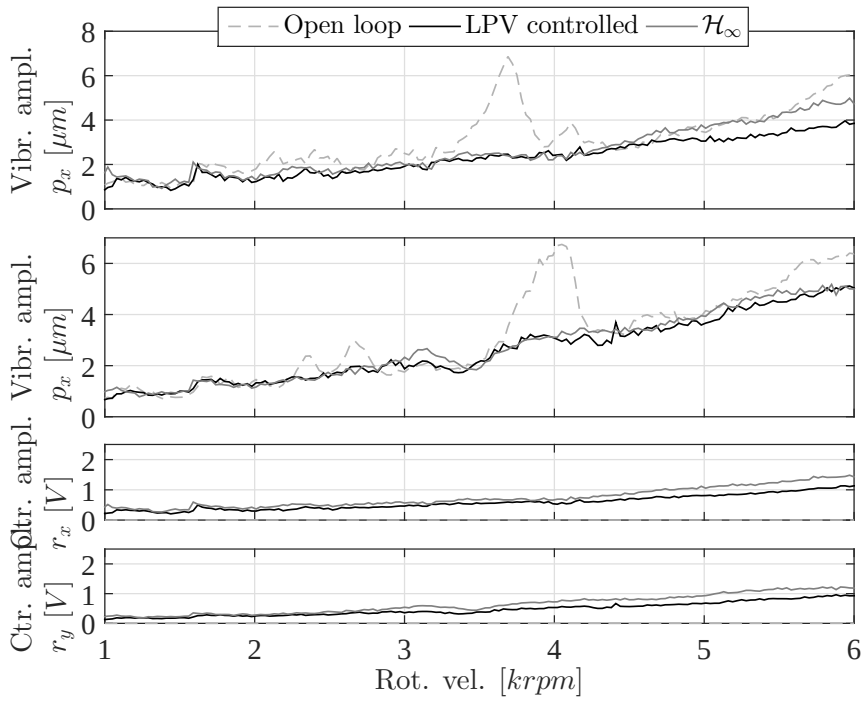

Figure E.14: Vibration amplitude in open loop and with LPV control during run-up and run-down in the interval $q_1 \in [0, 6]$ krpm at $q_2 = 0.7$ MPa

57]. Inspection of the frequency content supports the hypothesis of misalignment. The misalignment vibrations are significantly amplified around the under-damped eigenfrequencies. The controller therefore reduces these vibrations significantly. Since the system-gain in this frequency interval is high the controller does not require a significant effort to reduce the vibrations.

E.6 Conclusions and future aspects

This paper has presented control designs for enhancement of the damping properties of controllable journal bearings over their operating range. An LPV and an $\mathcal{H}_\infty$ controller were designed using the mixed sensitivity setup where a suitable choice of weights could provide the desired level of damping. The LPV control design is able to guarantee a certain level of performance over the desired scheduling parameter

range at the cost of an increased complexity in design. The $\mathcal{H}_\infty$ control design is simpler both in design and implementation and was designed for optimality for a given constant value of the scheduling parameter. Simulations and experimental closed loop results confirmed that both of the designed controllers were able to provide a significant enhancement of damping over the selected operating range. The LPV controller in general showed a somewhat better performance and required less control effort than the $\mathcal{H}_\infty$ controller. This improved performance should be compared to the strong increase in complexity in design and implementation which must be judged for the specific application.

The control design procedure was shown for a gas bearing system but has potential to be extended to other bearing designs as well, e.g. controllable oil bearings.

Acknowledgements

Elbert Hendricks is gratefully acknowledged for his feedback on the manuscript. The Danish Ministry of Science, Innovation and Higher Education is gratefully acknowledged for the support to the FTP research project 12-127502.

E.7 Vertical Impact Responses

This appendix contains the comparison of vertical impact responses of the LPV controlled and the open loop gas bearing for four non-identification operating conditions. During these experiments, the shaft was excited from the top of the shaft, and the first oscillation is therefore negative. The displayed responses have been filtered to remove the mass imbalance response. The responses are shown in Figure E.15. The controllers effectively enhance the damping.

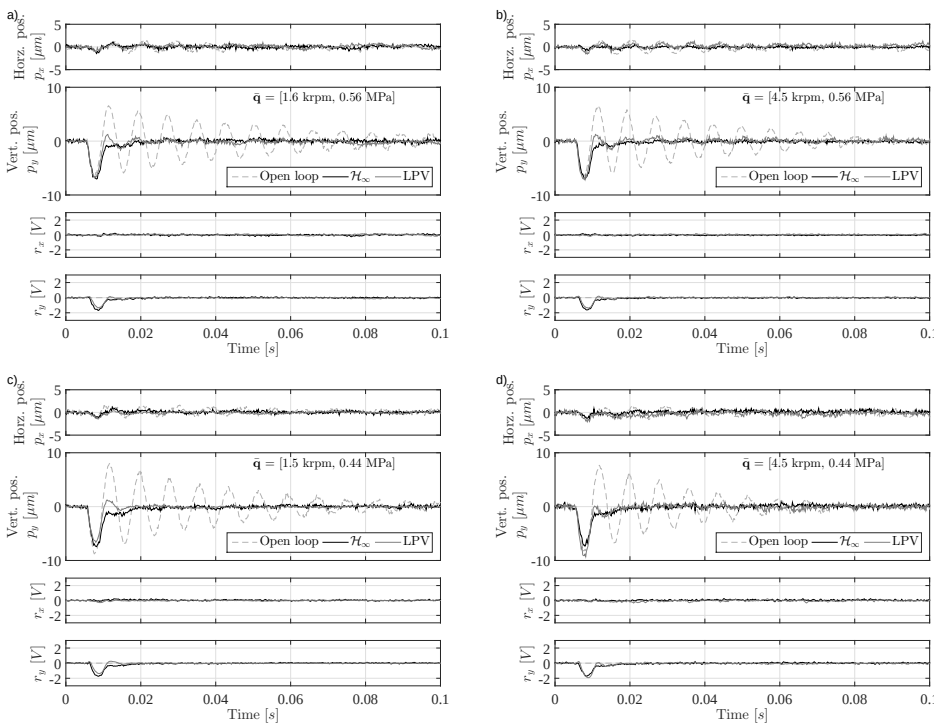

Figure E.15: Vertical open loop and closed loop impact responses at the four operating conditions $\{7, 9, 12, 14\}$: a) $\mathbf{q} = [1.5 \text{ krpm}, 0.57 \text{ MPa}]^{\mathrm{T}}$,b) $\mathbf{q} = [4.5 \text{ krpm}, 0.57 \text{ MPa}]^{\mathrm{T}}$,c) $\mathbf{q} = [1.5 \text{ krpm}, 0.43\text{MPa}]^{\mathrm{T}}$,a) $\mathbf{q} = [4.5 \text{ krpm}, 0.43 \text{ MPa}]^{\mathrm{T}}$

Appendix F

Gas Bearing Control for Safe Operation in Critical Speed Regions - Experimental Verification

From: Journal of Physics: Conference Series (Online) 659.1 (2015)
The paper has been reformatted to for the thesis.
Lukas R. S. Theisen[1], Hans H. Niemann[1], Roberto Galeazzi[1], Ilmar F. Santos[2]

[1]Dept. of Electrical Engineering and [2]Dept. of Mechanical Engineering
Technical University of Denmark, DK 2800 Kgs. Lyngby, Denmark
Email: {lrst,hhn,rg}@elektro.dtu.dk, ifs@mek.dtu.dk

Abstract:
Gas bearings are popular for their high speed capabilities, low friction and clean operation, but require low clearances and suffer from poor damping properties. The poor damping properties cause high disturbance amplification near the natural frequencies. These become critical when the rotation speed coincides with a natural frequency. In these regions, even low mass unbalances can cause rub and damage the machine. To prevent rubbing, the variation of the rotation speed of machines supported by gas bearings has to be carefully conducted during run-ups and run-downs, by acceleration and deceleration patterns and avoidance of operation near the critical speeds, which is a limiting factor during operation, specially during run-downs. An approach for reducing the vibrations is by feedback controlled lubrication. This paper addresses the challenge of reducing vibrations in rotating machines supported by gas bearings to extend their operating range. Using $\mathcal{H}_\infty$-design methods, active lubrication techniques are proposed to enhance the damping, which in turn reduces the vibrations to a desired safe level. The control design is validated experimentally on a laboratory test rig, and shown to allow safe shaft rotation speeds up to, in and above the two first critical speeds, which significantly extends the operating range.

F.1 Introduction

Gas bearings offer clean operation with low friction, but suffer from poor damping properties and require low clearances. Rotating machines supported by gas bearings are therefore very sensitive towards mass unbalance and disturbances. The natural frequencies especially become critical as they coincide with the rotation speed, where the mass unbalance response grows until the shaft rubs the bearing surface. Operation near the critical speeds is therefore avoided, which limits the usability of the machines. An ad-hoc approach to reduce vibrations when crossing the critical speeds, is to quickly accelerate rotation shaft across the critical speed before the full vibration amplitude is obtained. Such an approach however results in the "cat in the tree"-problem - it may be easy to get up, but difficult to get safely down again. Due to the low viscosity there are almost no friction losses, which in turn results in a slow deceleration of the shaft. This gives enough time for the undesired vibrations to build up.

For a given fixed machine design, the shaft vibrations can be reduced in two ways. Proper balancing of the shaft can drastically reduce mass unbalance, but not eliminate it. Further this obviously does not diminish sensitivity to external disturbances. Active lubrication techniques through feedback control represent a valid alternative approach, which can handle both mass unbalance and external disturbances. Feedback control has been widely applied to active magnetic bearing (AMB)-systems. Many authors have proposed various control designs, e.g. linear parameter-varying (LPV)-controllers to eliminate the mass unbalance response by placing closed-loop zeros in the sensitivity function at the shaft rotation speed. e.g. in [53, 85, 52]. Such controllers completely eliminate the mass unbalance at the cost of a high control effort. The use of phase shift filters has also been proposed in literature [116]. These mentioned approaches only reject disturbances at the rotational frequency.

Previous papers [3, 4, 78] on control of gas bearings have treated design of classical controllers, but none of these had sufficient robustness, and therefore were not able to reduce vibrations enough to allow a safe crossing of the critical speed. In [5] we proposed an $\mathcal{H}_\infty$ and an LPV controller to enhance the damping of the gas bearing. The controllers were found able to both reject the external disturbances and reduce the vibration amplitude within the considered operating range.

In continuation of that work, this paper explores further the capabilities of such designs. The same $\mathcal{H}_\infty$ setup is used to obtain a damping enhancing controller,

and the vibration reduction capabilities are investigated to extend the region of operation. The available model relies on open loop identification, which poses a challenge, since open loop operation is not possible in these regions. A controller is therefore required, which should again be validated from a model of the system at that particular operating condition. Instead, an alternative must be sought. Our approach therefore relies on designing a controller from the LPV model inside the identified region, and investigating the controller performance outside the identified region. The upper limits for safe rotation are investigated both for closed loop experiments and open loop experiments.

The paper is structured as follows. Section F.2 contains an overview of the test rig utilised for experimental validation and some highlights of the model of the gas bearing. The design of the $\mathcal{H}_\infty$ controller is detailed in Section F.3, and the available LPV model is used in extrapolation to provide an expectation of the controller performance for higher rotation speeds. This performance is investigated experimentally in Section F.4. Last, some conclusions are drawn and future aspects are discussed in Section F.5.

Notation

The paper uses upper case bold letters for matrices $\mathbf{A}$, lower case bold letters for vectors $\mathbf{a}$, the Laplace variable is denoted s. Continuous time signals are addressed $a(t)$. Signals in the Laplace domain are addressed $a(s)$, and sampled signals at time instants kT_s are denoted $a(kT_s)$. State-space dynamics is formulated in shorthand as $\mathbf{G} = \left[\begin{array}{c|c} \mathbf{A} & \mathbf{B} \\ \hline \mathbf{C} & \mathbf{D} \end{array}\right]$, which defines the state-space relation $\begin{bmatrix} \dot{\mathbf{x}} \\ \mathbf{y} \end{bmatrix} = \mathbf{G} \begin{bmatrix} \mathbf{x} \\ \mathbf{u} \end{bmatrix} = \left[\begin{array}{c|c} \mathbf{A} & \mathbf{B} \\ \hline \mathbf{C} & \mathbf{D} \end{array}\right] \begin{bmatrix} \mathbf{x} \\ \mathbf{u} \end{bmatrix}$. The identity matrix of size n is denoted $\mathbf{I}_n$. Shaft rotation speed units are given in Hz, though the common in rotordynamics is revolutions per minute: $(1\ Hz = 60\ rpm)$.

F.2 Controllable Gas Bearing

F.2.1 Test Rig

The experimental controllable gas bearing setup at hand is shown in Fig. F.1. It consists of a turbine (1) driving a flexible shaft (2) supported by both a ball bearing (3) and the controllable gas bearing (4), in which pressurised air is injected through four piezoactuated injectors numbered as shown. The injection pressure is constant $P_{\text{inj}} = 0.3\ MPa$, which is measured before splitting up to the four piezoactuators. The pressure is not controlled, but the variations are negligible. A disc (5) is mounted

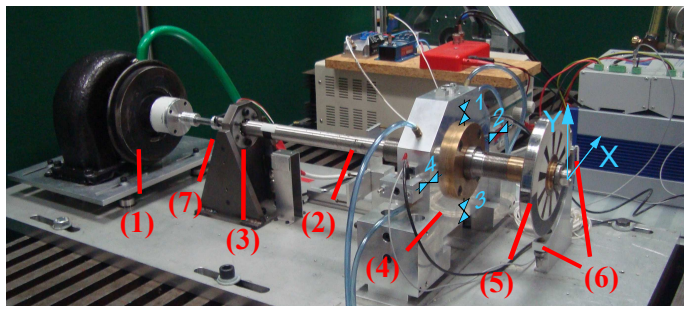

Figure F.1: The experimental controllable gas bearing setup. A turbine (1) drives a flexible shaft (2), which is supported by both a ball bearing (3) and the controllable gas bearing (4) with four piezoactuated injectors. A disc (5) is mounted in one end to pre-load the journal and displacement sensors (6) measure the lateral movement of the disc in the shown reference frame. A quadrature encoder (7) measures the angular position.

in one end to pre-load the journal. The horizontal and vertical disc movement $\mathbf{p} \triangleq [p_x, p_y]^{\mathrm{T}}$ is measured at the disc location using eddy current sensors (6) in the coordinate frame specified in the figure. For zero input and when the rotor is at stand still, the position is $\mathbf{p} = \mathbf{0}$. The angular position of the rotor ϕ is measured by an optical quadrature encoder (7), from which the rotation speed Ω is calculated. The injectors are controlled in a pairwise differential mode. Thereby one piezoactuator reference r_x is sent to control the position of the horizontal injectors, and one reference r_y is sent to control the vertical ones. These references are in intervals $[-5, 5]$ V, which corresponds to full-span motion of the piezoactuator positions in the interval $[0, 45]$ μm. The nominal clearance of the gas bearing is $25\ \mu m$. Given the right conditions of sufficient injection pressure and sufficiently low rotational speed, the gas film generates restoring forces and thereby keeps the rotor levitating about a stable equilibrium. All measurements are sampled with period $T_s = 0.2\ ms$. A detailed description of the setup is available in [31].

For equipment safety, the vibrations must be within a safety region, in this case chosen as a circle:

$$x_s = r \cdot cos(\theta) - x_0, \quad y_s = r \cdot sin(\theta) - y_0, \quad \theta \in [0, 2\pi[\ rad \tag{F.1}$$

Manual tests were performed to assess safe limits of the circle parameters, and the following were found sufficiently conservative: radius $r = 20\mu m$, and centre $x_0 = 10\mu m$, $y_0 = -3\mu m$. These limits are deliberately chosen to be conservative for equipment safety.

F.2.2 Gas Bearing Model

The gas bearing test rig is modelled using the linear parameter-varying (LPV)-identification approach from [3], where local LTI-models are identified from data collected in a grid of injection pressures and shaft rotation speeds. For the present work, the injection pressure is kept constant, and the model is then only function of the rotation speed. The identification grid contained six uniformly spaced shaft rotation speeds in the interval $\Omega \in [0, 92]\ Hz$. The model can be decomposed to a cascade coupling of the actuator dynamics $\mathbf{G}_{act}$, time delays $\mathbf{G}_{\boldsymbol{\tau}}$ and the rotor-bearing dynamics $\mathbf{G}_{rb}$:

$$\mathbf{G}(t, \Omega) = \mathbf{G}_{rb}(t, \Omega)\mathbf{G}_{\boldsymbol{\tau}}(t, \Omega)\mathbf{G}_{act}(t) \tag{F.2}$$

The actuator dynamics are independent of the scheduling parameter and have the following diagonal second order form with two real poles and a gain:

$$\begin{aligned} \mathbf{G}_{act}(s) &= \begin{bmatrix} G_{a,x}(s) & 0 \\ 0 & G_{a,y}(s) \end{bmatrix}, \\ G_{a,j}(s) &= \frac{\kappa_{a,j}}{\left(\frac{1}{p_{1,j}}s + 1\right)\left(\frac{1}{p_{2,j}}s + 1\right)}, \quad j \in \{x, y\} \end{aligned} \tag{F.3}$$

The rotor-bearing dynamics is modelled as the interconnection of a parameter-varying delay and a second order parameter-varying mass-spring-damper system. The latter has a state-space realisation:

$$\mathbf{G}_{rb} = \left[\begin{array}{cc|c} \mathbf{0}_2 & \mathbf{I}_2 & \mathbf{0}_2 \\ \mathcal{K}(\Omega) & \mathcal{D}(\Omega) & \mathcal{B}(\Omega) \\ \hline \mathbf{I}_2 & \mathbf{0}_2 & \mathbf{0}_2 \end{array}\right] \tag{F.4}$$

in which the parameter-varying matrices $\{\mathcal{K}, \mathcal{D}, \mathcal{B}\}$ are second order polynomials in the rotation speed Ω. The delays are second order polynomials in rotation speed, and finite models are obtained by a first order Padé approximation:

$$\begin{aligned} \mathbf{G}_{\boldsymbol{\tau}}(t, \Omega) &= \begin{bmatrix} G_{\tau_x(\Omega)}(t) & 0 \\ 0 & G_{\tau_y(\Omega)}(t) \end{bmatrix}, \\ G_{\tau_j(\Omega)}(t) &= \left[\begin{array}{c|c} -2/\tau_j(\Omega) & 1 \\ \hline 4/\tau_j(\Omega) & -1 \end{array}\right], \quad j \in \{x, y\} \end{aligned} \tag{F.5}$$

The natural frequencies of the LPV model change with rotation speed but are approximately $\omega_1 = 105\ Hz$ and $\omega_2 = 115\ Hz$. It is desired to extend the region of safe operation, which implies increasing the rotation speed to values outside

the identification region. The actuator dynamics contains only real poles acting at frequencies higher than $400Hz$. Since actuation in this range of frequencies is not desired, the actuator dynamics is approximated by a static gain. The gas bearing model is then of order $n = 6$.

The nominal model is chosen as the LPV model evaluated at $91\ Hz$.

$$\mathbf{G} = \mathbf{G}(t, \Omega)\Big|_{\Omega=91\ Hz} \tag{F.6}$$

The mass unbalance is not included in the model, but acts as a force on the shaft given by:

$$\mathbf{f}_u = m_u e_u \Omega^2 \begin{bmatrix} \sin(\Omega t + \varphi) \\ \sin(\Omega t - \pi/2 + \varphi) \end{bmatrix} \tag{F.7}$$

in which Ω is the shaft rotation speed, m_u is the unknown unbalance mass, and e_u is the unknown distance between the mass unbalance and the geometrical shaft centre, and φ is the phase of the disturbance. This can be modelled as an input disturbance in the gas bearing. The force from mass unbalance therefore grows by Ω^2 as the rotation speed increases, and the response is greatly amplified near the resonance frequencies. At this point, the mass unbalance remains largely unknown except for its frequency, which suffices for control design.

F.3 $\mathcal{H}_\infty$ Control Design

This section details the damping enhancing $\mathcal{H}_\infty$ control design from [5] to allow the safe crossing of the first two critical speeds by reducing the vibrations to be within the desired safety region from Eq. (F.1). These requirements are not easily included directly in the $\mathcal{H}_\infty$ setup especially since the mass unbalance is largely unknown. Instead, the controller $\mathbf{K}$ should enhance the damping and thereby reduce the gain magnitude at the resonance frequencies without wearing the actuator out. These disturbance and noise rejection requirements are formulated using the mixed sensitivity setup [93], which seeks to minimise:

$$\mathbf{K}^* = \arg\min_{\mathbf{K}} \|\mathbf{N}\|_\infty, \quad \mathbf{N} = \begin{bmatrix} \mathbf{W}_p\mathbf{S} \\ \mathbf{W}_u\mathbf{K}\mathbf{S} \end{bmatrix}, \tag{F.8}$$

where the closed loop sensitivity functions for a given $\Omega = \bar{\Omega}$ are :

$$\mathbf{S}(s, \bar{\Omega}) \triangleq (\mathbf{I} + \mathbf{G}\mathbf{K})^{-1} \tag{F.9}$$

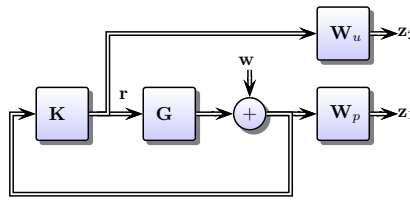

Figure F.2: The augmented plant with controller for LPV controller design with performance weights $\mathbf{W}_p$ and controller sensitivity weight $\mathbf{W}_u$.

and $\mathbf{KS}$ represents the control sensitivity. They are shaped by the weight functions $\mathbf{W}_p$ and $\mathbf{W}_u$. The external output disturbance $\mathbf{w}$ and external outputs $\mathbf{z} = [\mathbf{z}_1^{\mathrm{T}}, \mathbf{z}_2^{\mathrm{T}}]^{\mathrm{T}}$ are included into the system to obtain the augmented plant as shown in Fig. F.2. The controller then satisfies $\|\mathbf{N}\|_\infty < \gamma$.

To enhance damping, the controller should have high performance in the frequency range around the under-damped eigenfrequencies of the rotor-bearing ω_x and ω_y. The performance filter is therefore chosen to contain inverse notch like filters:

$$\mathbf{W}_p(s) = \mathrm{diag}\left(w_{px}(s), w_{py}(s)\right) \tag{F.10}$$

in which w_{px} and w_{py} both have the form:

$$w_{px}(s) = \frac{s^2 + 2\zeta_1\omega_x s + \omega_x^2 k_0}{s^2 + 2\zeta_2\omega_x s + \omega_x^2}, \quad w_{py}(s) = \frac{s^2 + 2\zeta_1\omega_y s + \omega_y^2 k_0}{s^2 + 2\zeta_2\omega_y s + \omega_y^2} \tag{F.11}$$

The natural frequencies ω_x, ω_y are chosen as the under-damped natural frequencies of the gas bearing to obtain a high weight around these. The weight at the resonance frequencies is set to 19 dB, which is obtained by the damping factors $\zeta_1 = 0.3$ and $\zeta_2 = 0.05$. The low sensitivity around the natural frequencies must come at the cost of increased sensitivity in another frequency range due to Bode's sensitivity integral [104]. It was argued in [4] to place this sensitivity increase in the low frequency range, where an amplification of mass unbalance and disturbances is acceptable. The constant $k_0 = 1/3$ determines the low frequency weight, and the sensitivity at low frequency is guaranteed to be less than γk_0. The control signal sensitivity weight $\mathbf{W}_u$ is chosen to penalise control action at high frequency. This is achieved with the high-pass filter from [93, Sec. 2, Eq. (2.72)]:

$$\mathbf{W}_u(s) = \mathbf{I} w_u(s), \quad w_u(s) = \frac{s/M_b + \omega_b}{s + \omega_b A_b}, \tag{F.12}$$

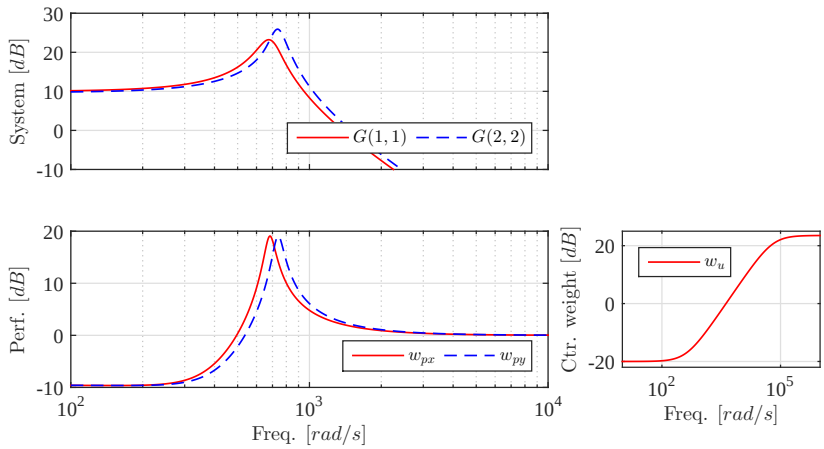

Figure F.3: System gain, performance weights $w_{px}(s)$, $w_{py}(s)$ as defined in Eq. (F.11) and controller sensitivity weight $w_u(s)$ as defined in Eq. (F.12). The two left plots share the frequency axis to show the performance weight peaks coincide with the natural frequencies.

where the low frequency gain is $1/A_b$, $A_b = 10$; the high frequency gain is $1/M_b = 15$, and the approximate crossover frequency is $\omega_b = 2000\pi$ rad/s. The weights are shown in Fig. F.3. Since $|\mathbf{S}| > 1$ for low frequencies, the controller amplifies mass unbalance for low rotation speeds, which is affordable, whereas at high rotation speeds, the vibrations are attenuated. A 12-th order $\mathcal{H}_\infty$ controller is synthesised with $\gamma = 1.15$ and the performance shown in Fig. F.4. At low frequencies up to above the first two critical speeds, the performance is limited by $\mathbf{S}$ as desired, whereas at high frequency, $\mathbf{KS}$ becomes limiting.

To allow implementation on the dSpace system, the controller is converted to discrete time using Tustin transformation and sampling frequency $f_s = 5\ kHz$.

F.3.1 Closed-Loop Performance Assessment Based on Extrapolated LPV Model

Since no gas bearing model is available for rotational speeds higher than 92 Hz, the performance of the controller is attempted to be assessed by means of model extrapolation from the identified LPV model. The performance assessment is strongly affected by the extrapolation, therefore the obtained results must be

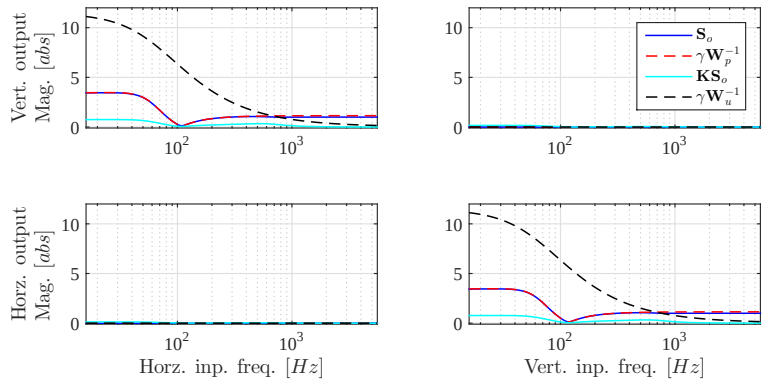

Figure F.4: Resulting sensitivity functions $\mathbf{S}$ and $\mathbf{KS}$ and corresponding inverse scaled weights $\gamma\mathbf{W}_p^{-1}$ and $\gamma\mathbf{W}_u^{-1}$. At low frequency, the performance closely follows the performance weight.

carefully interpreted. The LPV model Eq. (F.6) is extrapolated for various rotation speeds, and used to calculate the loop sensitivities using Eq. (F.9). The results are shown in Fig. F.5. In open loop, the input disturbances are greatly amplified near the resonances, whereas the closed loop disturbance functions $\mathbf{SG}$ show a significant reduction in disturbance gain as desired. The controller has low sensitivity near the resonance frequencies, and obtains $|\mathbf{S}| < 1$ in an interval above the resonance frequencies. This indicates that the controller reduces the mass unbalance both before and after the critical speeds are crossed. Investigations also show, that the control effort $\mathbf{KS}$ is sufficiently low. The performance analysis based on the extrapolated models suggests that the designed controller may succeed in increasing the system damping at and about the critical frequencies. The validity of these predictions needs to be verified experimentally, and this is shown in the following section.

F.4 Experimental Results

The results of the previous section should be investigated experimentally, both the open loop and the closed loop.

This is done by applying the controller at low speed, and then slowly accelerating the shaft while monitoring the vibration amplitude. A standard runout filter is applied to remove artefacts from the measurements from mechanical imperfections in the disk using the procedure described in [3]. At standstill, the rotor equilibrium position

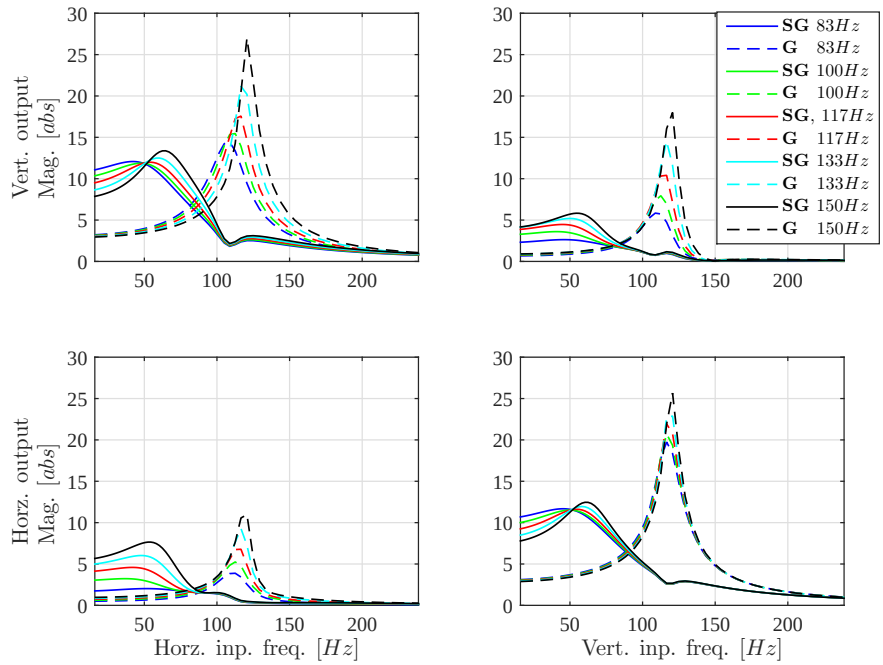

Figure F.5: Evaluation of open and closed loop input disturbance responses ($\mathbf{G}$, $\mathbf{SG}$) for different rotation speeds extrapolated with the LPV model. The model shows, that the controller reduce the peak gain significantly.

is below the geometric bearing centre [117]. The given shaft positions $\mathbf{p}$ correspond to deviations from the equilibrium position. Two different experiment types where performed to assess the upper limit of safe rotation speed: an open loop and a closed loop. To avoid rotor-bearing rubbing during experiments, the shaft rotation speed is increased slowly until the vibrations exceed the safety region. The vibrations of the open loop experiment are shown in Fig. F.6. At $\Omega = 94.8\ Hz$, the vibrations exceed the safety region, and the rotor reaches a speed of $\Omega = 97.5\ Hz$ before the experiment is stopped. The critical speeds can therefore not be crossed safely in open loop. During the closed loop experiment, the shaft is again accelerated slowly allow the vibrations to build up during the operation. A bias is applied to the control signal to allow a shift of the vibrations' centre. According to the model, the critical

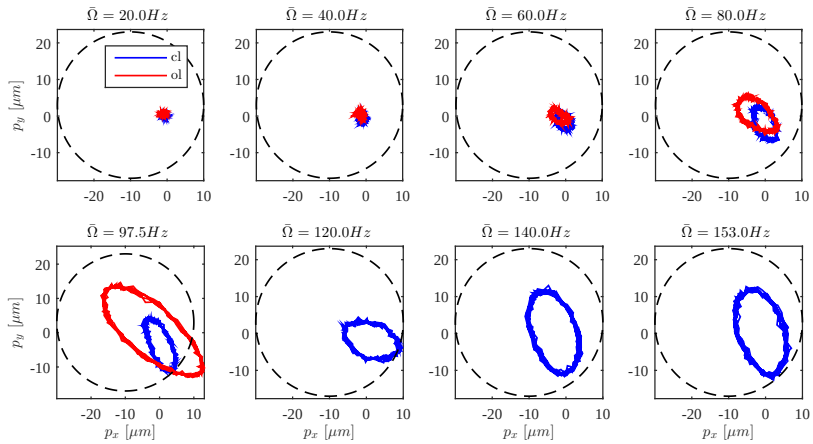

Figure F.6: Experimental measurements for various shaft rotation speeds. In open loop (ol), the vibrations exceed the limit of safe operation at $\Omega = 94.8\ Hz$. In closed loop (cl), the control reduces the vibrations and significantly increases this limit.

speeds are expected to be near $105\ Hz$ and $115\ Hz$. It is evident, that the shape of the vibrations changes near these speeds. These speeds are crossed very slowly to allow the vibrations to build up and validate, the critical speeds pose no challenge in closed loop. The rotation speed can therefore be increased even further. During the experiment, the rotor reaches a speed of $\Omega = 153\ Hz$ where the control signals approaches the level of saturation. Such saturation in best case deteriorates the performance, but potentially destabilises the system. It is therefore decided to stop the experiment.

The vibrations are often investigated in rotor-dynamics as function of the rotation speed in a waterfall diagram. This is obtained as the FFT of smaller sections of the data. Such a diagram is shown for the vertical shaft direction in Fig. F.7 for both the open loop and the closed loop case. The synchronous vibrations for $\Omega > 50Hz$ are significantly reduced in the closed loop case, and the critical speeds can therefore be crossed safely. It may be argued, that the approach of applying an input bias should also have been used in the open loop experiment, but the vibration amplitude would still quickly have grown exceeded the allowed vibration level.

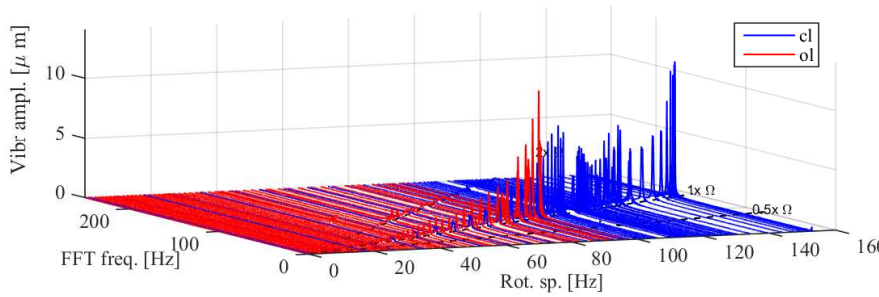

Figure F.7: Waterfall diagram for vertical shaft direction to investigate the frequency content of the vibrations. In open loop (ol) the synchronous vibrations grow fast as the critical speed is approached. In closed loop (cl), the vibrations are sufficiently attenuated to allow faster rotation speeds.

A later experiment was performed, where the rotor speed was increased even further up to $\Omega = 161.4\ Hz$, and the vibrations were within the desired level. This corresponds to an increase in operating range of approximately 70%.

F.5 Conclusions and Future Aspects

This paper investigated control designs to reduce the vibrations in rotating machinery supported by gas bearings. A controller was designed using the developed LPV model, and experimental results demonstrated the feasibility of using the controller to extend the operation range. The controller allowed rotation speeds up to, in and above the first two critical speeds, which extended the operation range by 70%. Future experiments will investigate the performance as the rotation speed is increased even further. In this region, sub-synchronous whirl dominates the response, and it is of interest to use controllers to postpone the onset of the whirl [31].

Appendix G

An Application of Gain-Scheduled Control Using State-Space Interpolation to Hydroactive Gas Bearings

Submitted for IEEE Multi-Conference on Systems and Control 2016 Buenos Aires, Argentina

The paper has been reformatted to for the thesis.

Lukas R. S. Theisen[1], Juan F. Camino[2], Hans H. Niemann[1]

[*]1 Automation and Control group, Department of Electrical Engineering, University of Denmark, 2800 Kgs. Lyngby, Denmark {lrst, hhn }@elektro.dtu.dk

[2] School of Mechanical Engineering, University of Campinas – UNICAMP, 13083-860 Campinas, SP, Brazil camino@fem.unicamp.br

Abstract:

Sinusoidal disturbances are common, especially in rotordynamics where mass imbalance causes undesirable vibrations. When the frequency of the disturbance is constant and known, it can be rejected using robust control techniques by including notches in the weights. For a known time-varying frequency, it is possible to design a gain-scheduled controller using multiple controllers optimised for a single frequency. Gain-scheduling strategies using the Youla parametrisation can guarantee stability at the cost of increased controller order and performance loss in the interpolation region. This paper contributes with a gain-scheduling strategy using state-space interpolation, which avoids both the performance loss and the increase of controller order associated to the Youla parametrisation. The proposed state-space interpolation for gain-scheduling is applied for mass imbalance rejection for a controllable gas bearing scheduled in two parameters. Comparisons against the Youla-based scheduling demonstrate the superiority of the state-space interpolation.

[*]The work was supported by the Danish Ministry of Science, Innovation and Higher Education through the FTP research project 12-127502. J. F. Camino is partially supported through grants from CAPES, FAPESP and CNPq Proc. 487101/2013-8

G.1 Introduction

Gain-scheduling is an attractive solution for rejection of time-varying sinusoidal disturbances. One application is in rotordynamics where mass imbalance causes undesirable vibrations. When the frequency of the disturbance is constant and known, it can be rejected using, for instance, $\mathcal{H}_2$ and $\mathcal{H}_\infty$ control techniques by including notches in the weights [52, 105]. For active magnetic bearings, disturbances with time-varying known frequency can be rejected by linear parameter-varying (LPV) control using parameter-varying notches [52, 53]. This motivates the use of gain-scheduling to allow high performance across the scheduling parameter interval. The LPV control can be conservative and in [5] for damping injection for gas bearings, we found that $\mathcal{H}_\infty$ controllers synthesised for local optimality in the scheduling parameter are locally able to outperform a synthesised LPV controller. This indicates conservatism in LPV control and demonstrates attractiveness of the locally synthesised linear controllers.

A basic gain-scheduling approach consists in an output interpolation strategy, where the controllers' outputs are weighted and summed. Thus for controllers K_1, K_2, the resulting controller becomes $K = \alpha K_1 + (1-\alpha)K_2)$. Such approach is shown in [118] to neither guarantee performance nor even stability. To ensure stability of the closed-loop system, the authors in [118] propose a solution based on the Youla-parametrisation. This approach increases the controller order, where for a system of order n_g, controller order n_k and for n_p scheduling parameters, the switched controller would be of order $n_g + 2^{n_p} n_k$. The basic output interpolation strategy and the one based on the Youla-parametrisation have the drawbacks of increasing the order of the resulting controller. A significant performance loss in the controller switching/interpolation region for rejection of sinusoidal disturbances is allowed by the gain-scheduling technique based on the Youla-parametrisation[52, 53] and using the basic output interpolation. This occurs because neither of the two strategies allow the the poles and zeros of the notches to develop continuously with the scheduling parameter. An alternative solution which can avoid the increase of controller order and performance loss is to gain-schedule by state-space parameter interpolation. Such approaches have been proposed in literature, for instance in [102, 119, 120, 103, 101, 121] and references therein. These approaches commonly rely on the design of local controllers which are optimal for a set of local models obtained for specific values of the scheduling parameter. These local controllers are represented in a suitable state-space representation and then interpolated to provide

the gain-scheduled controller. Strategies to represent plant and controller models in a coherent state-space form, such that interpolation techniques can be applied to generate LPV models, are provided in [71, 69, 73].

The works [101, 102] propose to synthesise $\mathcal{H}_\infty$ controllers, which can subsequently be written in observer and state-feedback structures. The LPV controller design proposed in [71], based on the original idea of interpolating local controller from [119], uses a decomposition of the local controllers into gains, poles and zeros, which can be approximated as functions of the scheduling parameters. In the second step, they are transformed to a parameter-varying state-space representation. Such an approach requires manual sorting of the poles and zeros and it is not easily applied for MIMO systems. A similar approach for gain-scheduled control of SISO LPV systems in [122] requires an a priori assumed structure, and allows requirements from Nyquist criteria to be included in the control parameter optimisation, but such approach is not easily extended to MIMO systems.

Though the controller interpolation strategies do not guarantee closed-loop stability in the initial design, it can be proved subsequently using Lyapunov theory or LFT techniques [120, 103, 121]. An LPV identification strategy in [72] suggests to use internally balanced state-space realisations to allow state-space interpolation. The state-space parameters will then usually develop continuously, except for a number of sign changes. The approach can require significant manual labour for systems of high order and/or when many local models must be used since many sign changes may occur. Another approach proposed for LPV identification is to transform the local models to a suitable state-space representation [69]. Here, a numerically well-balanced interpolated system is obtained by transforming the local systems to a coherent basis using the extended observability and controllability matrices. This method is not applicable when the resulting transformation matrices become singular. This can happen for full-order control designs for continuous time systems, where both the observability and the controllability matrices can be ill conditioned. The numerical condition is usually better for discrete time systems, but the model can be very sensitive to the subsequent interpolation in the sense that the time and frequency response of the interpolated controller will not match the one of the local linear controllers well.

We propose a state-space interpolation strategy for gain-scheduled control of MIMO systems with multiple scheduling parameters. The strategy avoids an increase in state-space order and it does not require manual sorting of poles and zeros. Furthermore, it can be applied effectively even when the interpolation approaches from

[69, 73] is not applicable for numerical reasons. Our strategy relies on synthesising $\mathcal{H}_2$ controllers directly in a suitable state-space representation, such that the controllers' state-space parameters can be directly interpolated. The effectiveness of the strategy is demonstrated in a design case for multi-objective control design for a controllable gas bearing test-rig.

The manuscript is structured as follows; Section G.2 presents an overview of the state-space interpolation techniques and its usage for the design of gain-scheduling. In Section G.3, the gain-scheduling approach is applied to the design of a multi-objective controller for a gas bearing test rig using a 6-th order model with two gain-scheduling parameters. In this step, local $\mathcal{H}_2$ controllers are designed and the gain-scheduling is performed using both the state-space interpolation and the Youla parameter-scheduling. In Section G.4, numerical simulations show the benefit of the proposed gain-scheduled controller design using both techniques. Finally conclusions are drawn in Section G.5.

G.2 State-Space Interpolation-Based Gain Scheduling

Many approaches exist for gain-scheduling. The interpolation of the controller's outputs is simple in implementation but it does not guarantee performance or stability in the interpolation regions. Youla parametrization based approaches [118, 123] guarantee stability at the cost of increased controller order, which grows rapidly with the number of scheduling parameters. The interpolation approaches proposed in [102, 72, 121, 71, 73] require that the controllers' state-space parameters can be well approximated as functions of the scheduling parameters. It allows the poles and zeros of the interpolated controller to develop continuously and at the same time avoids the increase in controller order. Closed-loop stability in the interpolation regions is not guaranteed with this approach, but it can easily be investigated using Lyapunov theory.

G.2.1 Overview of State-Space Interpolation

This section presents an overview of previous works in local LPV modelling approaches and gain-scheduling approaches.

State-space interpolation is the process of finding an LPV model (for the system plant or the controller) $\mathbf{G}(\mathbf{q}, t)$ from $i \in \{1, ..., I\}$ local LTI models $\tilde{\mathbf{G}}_i(t)$ of the system at the scheduling parameter $\mathbf{q}_i$. The local systems $\tilde{\mathbf{G}}_i(t)$ must be in a "suitable"

state-space representation $\mathbf{G}_i(t)$. The state-space interpolation approach can be summarized as follows:

1. Assume that for each $i \in \{1, ..., I\}$ scheduling parameter(s) $\mathbf{q}_i \in \{\mathbf{q}_1, ..., \mathbf{q}_I\}$, a realization of the plant the plant model $\tilde{\mathbf{G}}_i$ is available with order n_a and n_u inputs and n_y outputs

2. Ensure the systems are in "suitable" state-space representations denoted by $\mathbf{G}_i(t) = \left[\begin{array}{c|c} \mathbf{A}_i & \mathbf{B}_i \\ \hline \mathbf{C}_i & \mathbf{D}_i \end{array}\right]$. Denote their packed system matrices $[\mathbf{G}_i] \in \mathbb{R}^{L \times M}$, $L = (n_a + n_y)$, $M = (n_a + n_u)$:

$$[\mathbf{G}_i] = \begin{bmatrix} \mathbf{A}_i & \mathbf{B}_i \\ \mathbf{C}_i & \mathbf{D}_i \end{bmatrix}, \tag{G.1}$$

   denote the elements (state-space parameters) of $[\mathbf{G}_i]$ by $g_{lm,i}$, for $l \in \{1, ..., L\}$, $m \in \{1, ..., M\}$:

$$[\mathbf{G}_i] = \begin{bmatrix} g_{11,i} & \cdots & g_{1M,i} \\ \vdots & \ddots & \vdots \\ g_{L1,i} & \cdots & g_{LM,i} \end{bmatrix} \tag{G.2}$$

3. Approximate the state-space parameter estimates $g_{lm,1}, ..., g_{lm,i}, ..., g_{lm,I}$ onto functions $g_{lm}(\mathbf{q})$ of the scheduling parameter using the I estimates:

$$g_{lm}(\mathbf{q}) \text{ estimated from } \{g_{lm,1}, ..., g_{lm,i}, ..., g_{lm,I}\} \tag{G.3}$$

4. The LPV system $\mathbf{G}(\mathbf{q}, t)$ is then obtained from its packed form:

$$\begin{aligned} [\mathbf{G}(\mathbf{q})] &= \begin{bmatrix} g_{11}(\mathbf{q}) & \cdots & g_{1M}(\mathbf{q}) \\ \vdots & \ddots & \vdots \\ g_{L1}(\mathbf{q}), & \cdots & g_{LM}(\mathbf{q}) \end{bmatrix} \\ &= \begin{bmatrix} \mathbf{A}(\mathbf{q}) & \mathbf{B}(\mathbf{q}) \\ \mathbf{C}(\mathbf{q}) & \mathbf{D}(\mathbf{q}) \end{bmatrix} \end{aligned} \tag{G.4}$$

The question of how to obtain a "suitable" state-space representation is an open challenge. The authors in [73] show how to obtain a coherent state-space representation. The approaches employed in [3, 72, 71, 69] can be seen as alternative specific solutions. This challenge has been solved for a variety of cases for LPV identification using local approaches. The authors of [3] propose a grey-box model, where the parameters

are identified in a specific realisation such that the models are directly identified in the desired realisation, and the parameters therefore directly develop continuously. Here, a desired number of state-space parameters will be parameter-varying. The authors in [72] propose to transform locally identified models to internally balanced realisations. These realisations can differ by sign changes in the parameters which requires many manual changes of gains in the local models. The SMILE technique [69, 73] for LPV modelling uses state-space transformations of the local systems $\tilde{\mathbf{G}}_i$ using transformation matrices $\mathbf{T}_i$ to obtain the transformed systems $\mathbf{G}_i$. The transformation matrix $\mathbf{T}_i$ for system i is calculated from the observability matrices $\mathcal{O}_i$ of $\tilde{\mathbf{G}}_i$ (or alternatively controllability matrices) to obtain $\mathbf{T}_i = \mathcal{O}_1^{-1}\mathcal{O}_i$. Here, the reference model $\tilde{\mathbf{G}}_1$ is the one which maximises the observability (or controllability). This approach requires numerically well-conditioned plants to ensure invertibility of $\mathbf{T}_i$. This is not the case for the control design example in Section G.3 hence this method is not applicable.

G.2.2 Gain-Scheduled Control Using State-Space Interpolation

We propose to use the state-space interpolation technique for gain-scheduled control. A set of local linear controllers is designed for a set of scheduling parameters using $\mathcal{H}_2$-techniques. Our approach for obtaining the suitable state-space representation is to directly set up the generalised plant in a specific LPV state-space representation and then design the controllers.

The technique is summarised as follows:

- Set up the generalised plant $\mathbf{P}(\mathbf{q}, t)$ and ensure that the state-space parameters of $\mathbf{P}$ develops continuously in the scheduling parameters.
- For a set of $i \in \{1, ..., I\}$ scheduling parameters $\mathbf{q}_i \in \{\mathbf{q}_1, ..., \mathbf{q}_I\}$, synthesise local LTI controllers $\mathbf{K}_i(t)$ using $\mathcal{H}_2$ synthesis.
- Use state-space interpolation to obtain $\mathbf{K}(\mathbf{q}, t)$
- Investigate closed-loop stability

For the interpolation of the state-space parameters, standard regression tools such as linear least squares fitting can be applied. The standard guidelines to avoid over-parametrisation should be followed. We propose to take out a fraction of the systems to validate, that the behaviour of the interpolated controller matches the one of the local linear controllers in the interpolation regions.

The proposed approach is very flexible since it is applicable for both continuous and discrete time systems and the generalised plant can be cast to include multiple control objectives. In some cases for discrete time systems, we experienced a high parameter sensitivity in the sense that a small change error in the estimate of a state-space parameter can have a high effect on the dynamics. In these cases, the interpolated parameters appear to follow the desired values well, but the bode diagrams of the interpolated controllers are significantly different from the desired ones. Further, the resulting interpolated controllers have an LPV form and can be converted to discrete time using available methods from [100]. The gain-scheduling proposed is limited to systems with slow parameter-variation. which can be quantified using the approach from [103]. As discussed in [102], the approach is limited to an appropriate interpolation of the control weights. Instead of local $\mathcal{H}_2$ controllers, it is possible to use $\mathcal{H}_\infty$ synthesised controllers, but they are often obtained in non-coherent state-space realisations. It is then possible to transform the controllers to observer form with state feedback as proposed in [102].

The gain-scheduled interpolation proposed is not guaranteed to provide controllers whose parameters develop continuously, but this can easily be assessed from the parameter-development of the local controllers.

The next section shows the example application of the proposed state-space interpolation strategy for the design of a gain-scheduled control for a rotordynamical system.

G.3 Interpolation-Based Control for Hydroactive Gas Bearings

This section presents the application of the proposed gain-scheduled $\mathcal{H}_2$ control design for a hydro-active gas bearing test rig. Technical details of the test rig can be found in [31, 3]. Gas bearings are attractive for their low friction losses which generally come at the cost of poor damping characteristics. The low damping poses a challenge due to induced vibrations from the mass imbalance and from other machinery. Active control of the gas injection can increase the damping, by controlling the rotor position to avoid rotor-bearing rub and rejecting the mass imbalance. The gas bearing dynamics is a function of two scheduling parameters $\mathbf{q} = [q_1, q_2]^{\mathrm{T}}$, which are the angular velocity q_1 calculated from the encoder measurements and the injection pressure q_2. The fast dynamics of the gas bearing are in the scale of milliseconds, whereas the scheduling parameters change on a time scale of seconds. The rate of variation of the scheduling parameters is therefore negligible.

The hydro-active gas bearing shown in Fig. G.1 supports a rotating shaft by the injection of air through controllable injectors mounted in the bearing. The lateral (horizontal and vertical) disc movement, denoted by $\mathbf{y}(t) = [y_1(t), y_2(t)]^{\mathrm{T}}$, is measured with eddy current sensors. The disc equilibrium position is a function of the scheduling parameter. The shaft and disc are actuated using two pairs of piezo-actuators which are commanded by two position references $\mathbf{u}(t) = [u_1(t), u_2(t)]^{\mathrm{T}}$ in the interval -5V and $+5$V. The gas bearing test rig is modelled with inputs being the disturbance force from the mass imbalance $\mathbf{d}(t) = [d_1(t), d_2(t)]^{\mathrm{T}}$ and the piezo reference positions $\mathbf{u}(t) = [u_1(t), u_2(t)]^{\mathrm{T}}$ and outputs being the disc movement $\mathbf{y}(t)$. The state-space representation is given by:

$$\mathbf{G}(\mathbf{q}, t) = \left[\begin{array}{ccc|cc} \mathbf{0} & \mathbf{I} & \mathbf{0} & \mathbf{0} & \mathbf{0} \\ \mathbf{K}_m(\mathbf{q}) & \mathbf{D}_m(\mathbf{q}) & \mathbf{B}_m(\mathbf{q}) & \mathbf{B}_\mu & \mathbf{0} \\ \mathbf{0} & \mathbf{0} & -\mathbf{V}(\mathbf{q}) & \mathbf{0} & \mathbf{V}(\mathbf{q}) \\ \hline \mathbf{I} & \mathbf{0} & \mathbf{0} & \mathbf{0} & \mathbf{0} \end{array}\right], \tag{G.5}$$

The model can be seen as a 2 dof coupled mass-spring-damper system. This system is affected by mass imbalance $\mathbf{d}(t)$ and actuated through two independent first order low-pass filters. These filters are denoted by $h_1(\mathbf{q}, s) = \frac{v_1(\mathbf{q})}{s+v_1(\mathbf{q})}$ and $h_2(\mathbf{q}, s) = \frac{v_2(\mathbf{q})}{s+v_2(\mathbf{q})}$. and hence $\mathbf{V}(\mathbf{q}) = diag(v_1(\mathbf{q}), v_2(\mathbf{q}))$. The mass, stiffness, damping, and input gain of the mass-spring-damper system are denoted by $\boldsymbol{\mathcal{M}}, \boldsymbol{\mathcal{K}}, \boldsymbol{\mathcal{D}}, \boldsymbol{\mathcal{B}}$. The mass matrix is assumed identity $\boldsymbol{\mathcal{M}} = \mathbf{I}_2$, and the stiffness equivalent is then $\mathbf{K}_m(\mathbf{q}) = \boldsymbol{\mathcal{K}}(\mathbf{q})/\boldsymbol{\mathcal{M}}$, likewise the damping equivalent and the input gain are $\boldsymbol{\mathcal{D}}_m(\mathbf{q}) = \boldsymbol{\mathcal{D}}(\mathbf{q})/\boldsymbol{\mathcal{M}}$ and $\mathbf{B}_m(\mathbf{q}) = \boldsymbol{\mathcal{B}}(\mathbf{q})/\boldsymbol{\mathcal{M}}$. The mass imbalance gain is $\mathbf{B}_\mu = \boldsymbol{\mathcal{B}}_\mu/\boldsymbol{\mathcal{M}}$.

The parameter-dependent variables are denoted by $\boldsymbol{\theta} = [\theta_1, ..., \theta_m, ..., \theta_M]$ and include: the elements of $\mathbf{K}_m, \mathbf{D}_m, \mathbf{B}_m$ and v_1, v_2 whose parameters are described by 2^{nd} order polynomial surfaces such that each state-space parameter has the form $\theta_m(\mathbf{q}) = \alpha_{m0} + \alpha_{m,1}q_1 + \alpha_{m,2}q_2 + \alpha_{m,3}q_1^2 + \alpha_{m,4}q_2^2 + \alpha_{m,5}q_1q_2$. The mass imbalance is harmonic with the angular velocity of the shaft q_1 and has the form $\mathbf{d}(t) = k \times q_1^2[\cos(q_1 \times t), \sin(q_1 \times t)]^{\mathrm{T}}$, where k is a constant proportional to the imbalance mass and the distance between the shaft centre of mass and geometrical centre.

G.3.1 $\mathcal{H}_2$ Control Design

The controllers to be designed must be able to reduce the mass imbalance response, increase the damping, reject the noise and control the rotor position. These

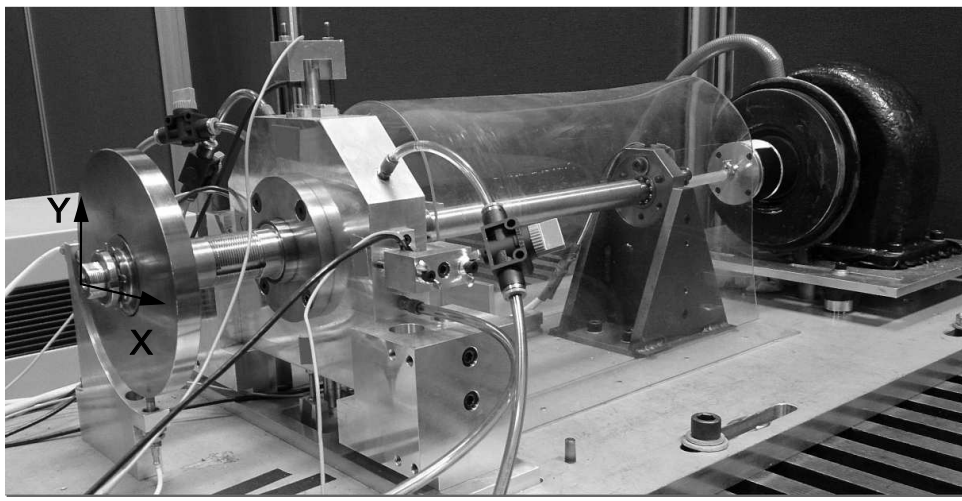

Figure G.1: The experimental controllable gas bearing setup. A disc is mounted on the flexible shaft to preload the journal and displacement sensors measure the lateral movement of the disc in the shown reference frame.

multiple requirements can be cast according to the $\mathcal{H}_2$ control framework to allow design of local LTI controllers.

- *Mass imbalance response*. To ensure mass imbalance attenuation, an angular velocity-dependent speed filter $\mathbf{W}_p$ is included.
- *Noise rejection*. The noise is rejected by weighing control signals at high frequency with the filter $\mathbf{W}_u$.
- *Rotor position control*. The rotor-position control is obtained by integrating the system's output weighted by a tuning parameter $\mathbf{W}_i$.
- *Damping*. The mass-spring-damper system contains two lightly-damped modes, one dominant in the horizontal, and one in the vertical shaft direction. These modes are damped by ensuring a sufficiently high minimum weight $\mathbf{W}_p$.

The generalised plant is setup according to the mentioned description as shown in Fig. G.2 with exogenous inputs being mass unbalance $\mathbf{w}_\omega \in \mathbf{R}^{2\times 1}$ and measurement noise $\mathbf{w}_n \in \mathbf{R}^{2\times 1}$ $\mathbf{w} = [\mathbf{w}_\omega; \mathbf{w}_n]$, and the two controllable inputs $\mathbf{u}$. The mass

imbalance is rejected using an approach inspired by [105]. An inverse notch filter $\mathbf{W}_p$ is chosen:

$$\begin{aligned} \mathbf{W}_p(q_1,t) &= \mathbf{I}_2 w_p(q_1,t) \\ w_p(q_1,s) &= \beta_0 \frac{s^2+2\zeta_1 q_1 s + q_1^2\kappa_0}{s^2+2\zeta_2 q_1 s + q_1^2} \end{aligned} \tag{G.6}$$

To ensure the continuity, the filter must be realised in a specific state-space representation chosen as:

$$w_p(q_1,t) = \left[\begin{array}{cc|c} 0 & 1 & 0 \\ -q_1^2 & -2\zeta q_1 & \beta_0 \\ \hline q_1^2\kappa_0 - q_1^2 & 2q_1(\zeta_1-\zeta) & \beta_0 \end{array}\right] \tag{G.7}$$

The parameters are chosen $\zeta_1 = 0.3$, $\zeta = 0.01$, $\beta_0 = 0.5$, $\kappa_0 = 0.5$.

The control effort is limited by the weight $\mathbf{W}_u$ chosen as the following high-pass filter:

$$\mathbf{W}_u(s) = \mathbf{I}_2 w_u(s), \quad w_u(s) = \frac{s/M_b + \omega_b}{s + \omega_b A_b}, \tag{G.8}$$

where the parameters are chosen $A_b = 10/11$, $1/M_b = 165$, and $\omega_b = 2\pi 11000$ rad/s. The measurement noise is rejected by $\mathbf{W}_n$, where a higher value results in less noise sensitivity. Here it is chosen $\mathbf{W}_n = 5 \times 10^{-4}\mathbf{I}_2$. The integral action to allow tracking of the rotor position is here obtained by augmenting the open loop system with integrators $\mathbf{G}^* = \frac{1}{s}\mathbf{G}$ whose output is included as an exogenous output weighted by $\mathbf{W}_i$. The bandwidth of the tracking can be tuned using the weight $\mathbf{W}_i$. Here the weight is chosen constant $\mathbf{W}_i = \mathbf{I}_2$, and increasing the weight increases the closed-loop control bandwidth. The controller to be applied to the system is then $\mathbf{K} = \frac{1}{s}\mathbf{K}^*$, where $\mathbf{K}^*$ is the synthesised controller.

The system has to operate in the interval $q_1 \in [1,\ 6]$ krpm $q_2 \in [0.3,\ 0.7]$ MPa. The number of local controllers should be sufficiently large to have enough models to use for the interpolation and some for validation [69]. Here, it is found that a grid of 10×10 equidistant values of the scheduling parameter $\mathbf{q}$ is sufficient. All the bode diagrams cannot be shown, but Fig. G.3 shows the Bode diagrams of the controller

$$\mathbf{K}(s) = \left[\begin{array}{cc} K_{11}(\mathbf{q}_0,s) & K_{12}(\mathbf{q}_0,s) \\ K_{21}(\mathbf{q}_0,s) & K_{22}(\mathbf{q}_0,s) \end{array}\right] \tag{G.9}$$

designed for $\mathbf{q}_0 = [5.72\text{krpm},\ 0.678\text{MPa}]$. The diagonal gains $K_{22}(\mathbf{q}_0,s)$,$K_{11}(\mathbf{q}_0,s)$ are approximately 20dB higher than the off-diagonal gains. The controller has an infinite static gain due to the integral action and high gains are obtained near the frequency of the mass imbalance to be rejected.

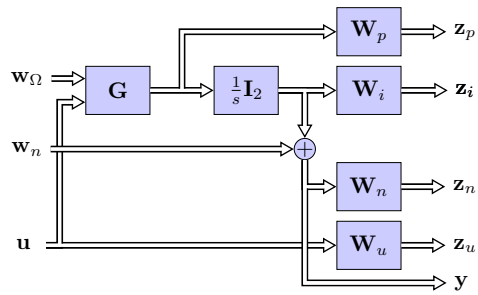

Figure G.2: Generalised plant for $\mathcal{H}_2$ control design

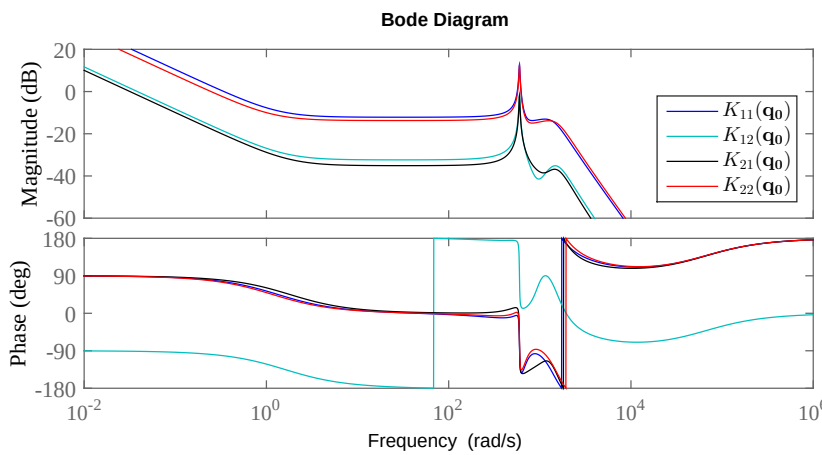

Figure G.3: Control gains $\mathbf{K}(\mathbf{q}_0)$ for $\mathbf{q}_0 = [5.72\text{krpm},\ 0.678\text{MPa}]$.

Once the local controllers are designed, the next step is to design the gain-scheduling. For the state-space interpolation, 66 of the local linear controllers $\mathbf{K}_i(t) = \left[\begin{array}{c|c} \mathbf{A}_i & \mathbf{B}_i \\ \hline \mathbf{C}_i & \mathbf{0} \end{array}\right]$, $i \in \{1, ..., 66\}$ are used for interpolation to obtain the LPV controller:

$$\mathbf{K}(\mathbf{q}, t) = \left[\begin{array}{c|c} \mathbf{A}(\mathbf{q}) & \mathbf{B}(\mathbf{q}) \\ \hline \mathbf{C}(\mathbf{q}) & \mathbf{0} \end{array}\right] \tag{G.10}$$

The parameter-dependency is modelled as an n^{th} order polynomial in $\mathbf{q}$ and the polynomial order is determined from a cost function of the remaining 34 validation

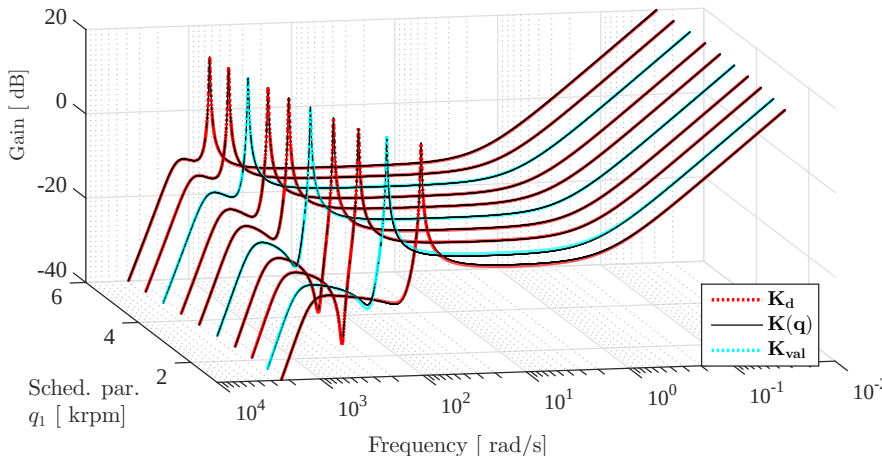

Figure G.4: Bode diagram of control gains $K_{11}(\mathbf{q}, s)$ for varying $q_1 \in [1,\ 6]$ krpm with $q_2 = 0.39$MPa. The gain of the interpolated controller $\mathbf{K}(\mathbf{q})$ resembles the bode diagrams of both the local controllers used for the interpolation $\mathbf{K}_d$ and the ones for validation $\mathbf{K}_{val}$.

controllers. Standard regression tools show that a 2^{nd} order polynomial in the scheduling parameters describes the parameter-variation well without over-fitting. The elements of $\mathbf{A}(\mathbf{q}), \mathbf{B}(\mathbf{q})$ and $\mathbf{C}(\mathbf{q})$ then have the form $\theta_m(\mathbf{q}) = \alpha_{m0} + \alpha_{m,1}q_1 + \alpha_{m,2}q_2 + \alpha_{m,3}q_1^2 + \alpha_{m,4}q_2^2 + \alpha_{m,5}q_1q_2$. The interpolated controller is obtained as described in Section G.2, and the remaining 34 local controllers are used to validate, that the behaviour of the interpolated controller evaluated in the validation points resembles behaviour of the local linear controllers as desired.

To validate that the interpolated controller's dynamics approximates the desired, the bode diagrams of the local controllers used for obtaining the interpolated controller have been compared with the bode diagrams of the interpolated controller and the local controllers or validation. Fig. G.4 shows the controllers' gains for varying q_1 with $q_2 = 0.39$MPa. The interpolated controller's gain follows closely the gains of the local controllers used for design and the ones used for validation as desired.

Stability of the closed-loop system can be proven using a similar approach as done in [121].

For comparison purpose, the gain scheduling control strategy based on Youla parameterization from [52] is used.

When the Youla parametrisation is used for gain-scheduling the approach is the following [118]. For the system $\mathbf{G}$ it is desired to gain-schedule between j different controllers $\mathbf{K}_j$. Choose one as the nominal controller $\mathbf{K}$. Assume there exists coprime factorisations of the system $\mathbf{G} = \mathbf{N}\mathbf{M}^{-1} = \tilde{\mathbf{M}}^{-1}\tilde{\mathbf{N}}$ and for the nominal controller $\mathbf{K} = \mathbf{U}\mathbf{V}^{-1} = \tilde{\mathbf{V}}^{-1}\tilde{\mathbf{U}}$ satisfying the double Bezout equation

$$\begin{bmatrix} \mathbf{I} & \mathbf{0} \\ \mathbf{0} & \mathbf{I} \end{bmatrix} = \begin{bmatrix} \tilde{\mathbf{V}} & -\tilde{\mathbf{U}} \\ -\tilde{\mathbf{N}} & \tilde{\mathbf{M}} \end{bmatrix} \begin{bmatrix} \mathbf{M} & \mathbf{U} \\ \mathbf{N} & \mathbf{V} \end{bmatrix} = \begin{bmatrix} \mathbf{M} & \mathbf{U} \\ \mathbf{N} & \mathbf{V} \end{bmatrix} \begin{bmatrix} \tilde{\mathbf{V}} & -\tilde{\mathbf{U}} \\ -\tilde{\mathbf{N}} & \tilde{\mathbf{M}} \end{bmatrix} \tag{G.11}$$

Then it is possible to switch from the nominal controller $\mathbf{K}$ to the controller $\mathbf{K}_i$ is performed using the Youla parameter $\mathbf{Q}_i$ calculated as:

$$\mathbf{Q}_i = \mathbf{M}^{-1}\mathbf{M}_i(\tilde{\mathbf{U}}_i\mathbf{V} - \tilde{\mathbf{V}}_i U) \tag{G.12}$$

When switching between J multiple controllers, the parameter is calculated:

$$Q = \sum_{j=1}^{J} \alpha_j Q_j \tag{G.13}$$

The parameters α_j can be chosen using the approach described in [124]. For operation e.g. in the centre between four design points $\mathbf{K}_1, \mathbf{K}_2, \mathbf{K}_3, \mathbf{K}_4$ we then choose the weights to be $\alpha_j = 1/4$. The resulting controller is guaranteed to be stable and is calculated as:

$$\mathbf{u} = (\mathbf{U} + \mathbf{M}\mathbf{Q})(\mathbf{V} + \mathbf{N}\mathbf{Q})^{-1}\mathbf{y} \tag{G.14}$$

This summarises the design of the state-space interpolated and the Youla gain-scheduled controllers.

G.4 Numerical Results

This section demonstrates the effectiveness of the state-space interpolated and the Youla-scheduled controllers through numerical simulations. The capability for mass imbalance rejection is analysed in the interpolation region using the designed controllers.

Measurement noise, coming from an experimentally recorded signal is applied during the simulation to show the noise rejection capabilities of the closed-loop system.

We include the interesting results obtained in the interpolation regions. Many simulations have been performed for a fine grid of scheduling parameters. The

system is simulated both in open loop and closed loop using the proposed state-space interpolated and the Youla scheduled controllers. In the interpolation regions, the controller generally operates between four locally designed controllers. The included results are obtained for operation in the centre between four control design points. From the responses in Fig. G.5, the mass imbalance rejection is evident using both controllers, though the state-space interpolated controller is superior. The horizontal and vertical responses are similar, thus only the horizontal is shown. Both controllers reject the noise well with similar control effort for the rejection of the mass imbalance. The proposed state-space interpolated controller rejects the mass imbalance well though the scheduling parameter is not in the set used for design. The controller scheduled with the Youla-parametrisation is less effective in rejecting the mass imbalance. Similar results are obtained regardless of the chosen grid for the scheduling parameter space.

The interpolated controller effectively rejects the mass imbalance with good performance even in the interpolation region. This is because the state-space interpolation allows the notch frequencies be adequately interpolated in contrast the the Youla-scheduled controller. This is demonstrated from an example in Fig. G.6, where the controller is desired to operate at $q_1 = 5.72$ krpm, $q_2 = 0.7$ MPa. This is in the centre between the two control design points $q_{1,\alpha} = 5.44$ krpm and $q_{1,\beta} = 6.00$ krpm for which controllers $\mathbf{K}_\alpha$ and $\mathbf{K}_\beta$ were designed. Gain-scheduling using the Youla-parametrisation from [118] results in the controller $\mathbf{K}(Q_{(\alpha+\beta)/2})$, where Q is the $Q_{(\alpha+\beta)/2} = (Q_\alpha + Q_\beta)/2$, which has a significantly reduced gain at the frequency of rotation. The interpolated controller $\mathbf{K}(\mathbf{q})$ maintains the high gain in this interpolation region. The gain of the Youla scheduled controller is very low at the frequency of the angular velocity. The reduced gain stems from the 180° phase shift near the notch gains as shown in Fig. G.3.

Damping of the closed loop system can be analysed from the impulse response. Here only the results using the state-space interpolated controller is included in Fig. G.7, which shows the damping has effectively been increased.

G.5 Conclusions

The paper proposed a gain-scheduling approach using state-space interpolation of local $\mathcal{H}_2$ controllers. The method was shown to avoid the increase of state-space order and preserve a high performance in the interpolation region for mass imbalance rejection for hydroactive gas bearings.

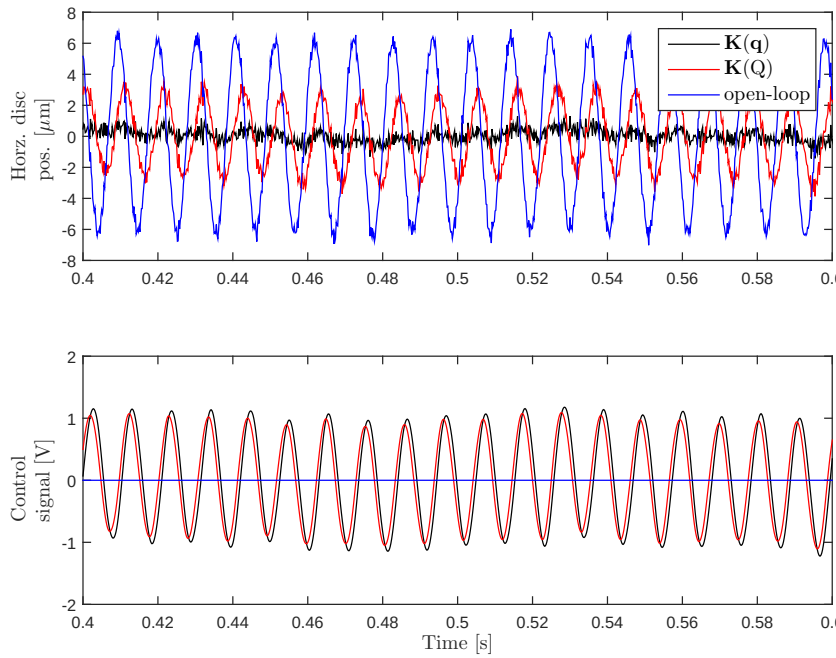

Figure G.5: Open and closed-loop response with measurement noise and mass imbalance for $\mathbf{q} = [5.72\text{krpm},\ 0.678\text{MPa}]$ using the proposed state-space interpolated controller $\mathbf{K}(\mathbf{q})$ and the Youla-scheduled controller $\mathbf{K}(Q)$.

It was demonstrated how a suitable choice of state-space representation allowed synthesising $\mathcal{H}_2$ controllers whose parameters developed adequately in the scheduling parameter to allow interpolation. The approach was applied for control of a gas bearing to reject the time-varying mass imbalance, increase the damping, reject measurement noise and allow control of the rotor-position. Numerical simulations where mass imbalance and recorded measurement noise sequences were added demonstrated the noise and mass imbalance rejection capabilities of the control design.

The proposed state-space interpolated gain-scheduling control design was compared against a controller scheduled on the Youla-parametrisation for rejecting mass imbalance and measurement noise. The two controllers used similar efforts, but the

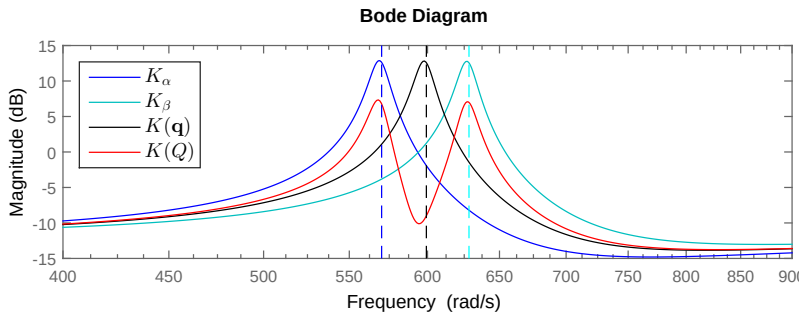

Figure G.6: Bode diagrams for the controllers $\mathbf{K}_\alpha$ and $\mathbf{K}_\beta$, the state-space interpolated controller $\mathbf{K}(\mathbf{q})$ and the Youla-scheduled controller $\mathbf{K}(Q)$.

proposed state-space interpolated controller was shown superior for rejecting mass imbalance in the interpolation region.

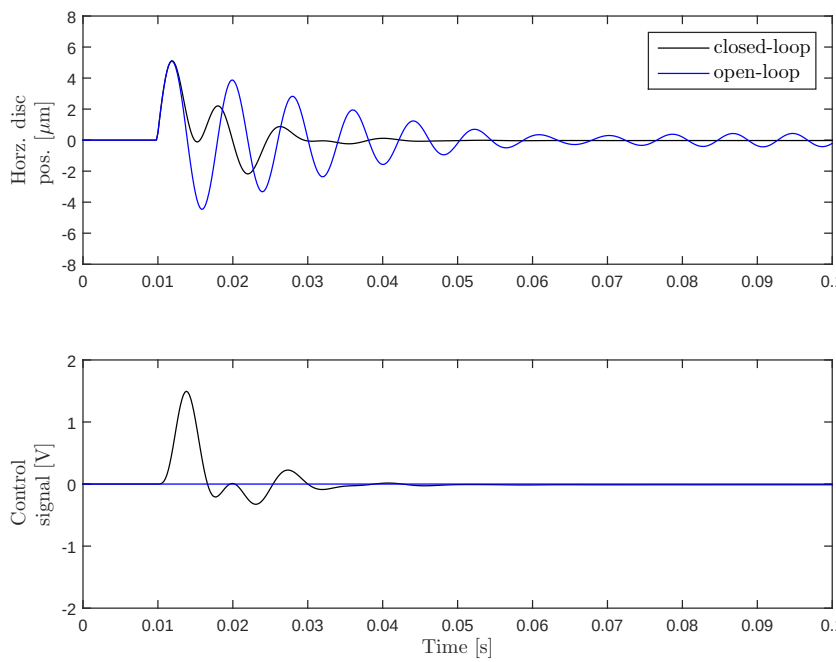

Figure G.7: Open and closed-loop horizontal impulse response for $\mathbf{q} = [5.72\text{krpm} 0.678\text{MPa}]$ using the proposed state-space interpolated controller $\mathbf{K}(\mathbf{q})$.

Appendix H

Experimental Facilities

This appendix describes the controllable gas bearing setup.

The experimental setup considered throughout the project consists of a *rotor* supported in one end by a ball bearing, and in the other end by an active gas *journal bearing* as shown in Figure H.1.

The main machine components are the rotor with a flexible shaft (a), on which a rigid disc is mounted (b). The rotor is supported in one end by a self aligning ball bearing (c) and in the other end by the active gas bearing (d). The shaft rotation is generated by the injection of pressurised air in the air turbine (e). The flexible coupling (f) transfers the rotational energy from the turbine to the rotor while reducing vibrations from the turbine. This laboratory test rig resembles a typical industrial rotating machine. Major dimensions of the test rig are listed in Table H.1.

In the controllable gas bearing, four piezo-actuated injectors are mounted as shown in Figure H.2 to push plastic pins. These pins control the control the injection flow of pressurised air. The pressurised air enters the bearing housing, where it

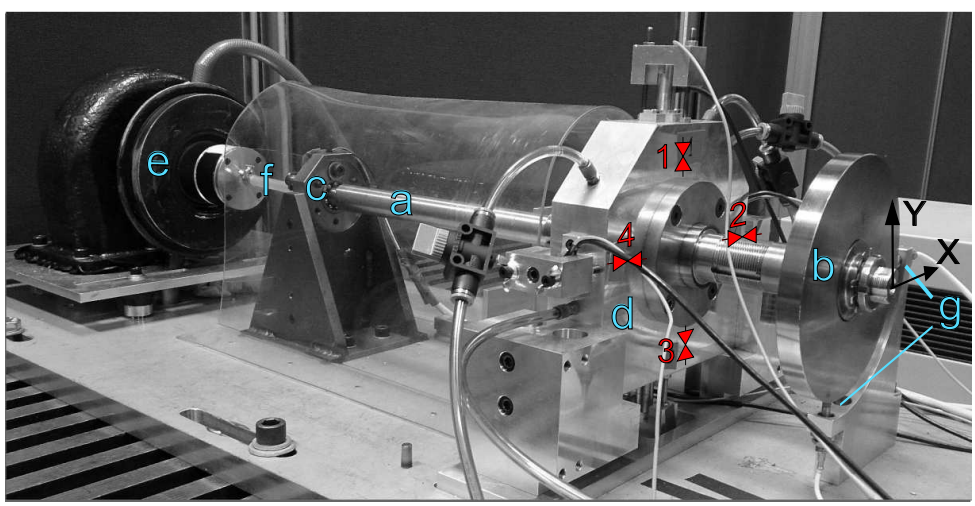

Figure H.1: The experimental controllable gas bearing setup.

Table H.1: Dimension of the controllable gas bearing test rig

Property	Value
Bearing diameter	40 mm
Bearing length	40 mm
Nominal clearance	25 μm
Injector orifice radius	1 mm
Shaft length	500 mm
Disc diameter	140 mm
Disc thickness	13 mm

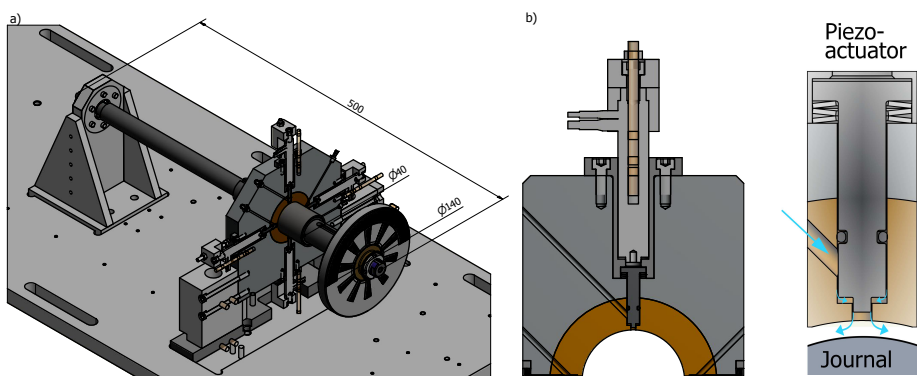

Figure H.2: CAD drawing of the test rig: a) the test rig with the controllable gas bearing cut in half. Major dimensions are included in millimetre $[mm]$. b) zoom of a piezoactuator. The piezo-electric stack pushes a pin, which controls the injector opening. c) zoom of the injector pin and journal. Pressurised air is supplied at the location of the upper left arrow. It then flows past the injector and into the journal to generate a force on the rotor. The air can flow out by the sides of the journal (in and out of the paper). An increase in supply voltage to the piezo-actuator expands it and reduces the flow.

Table H.2: Sensors and actuators

Eddy-current position sensors	TQ102 with a IQS603 signal conditioner
Piezo-actuators	Physik Instrumente P-841.3B.
Encoder	Agilen AEDB-9140
Data collection	dSPACE DS1104 R&D controller board with CP1104
Ball bearing	self aligning SKF 1200ETN9
Pressure transducer	Danfoss AKS 32

generates a *fluid film* that can levitate the rotor. When a voltage is applied to a piezo-actuator, it expands and pushes the plastic pin to reduce the flow and thereby the pushing force on the rotor. This actuation is opposite to active magnetic bearings (AMBs) where the electromagnets can only pull the rotor.

The sensor, actuator and mechanical component details are listed in Table H.2. The horizontal and vertical disc position is measured with eddy current sensors (g). The measurement noise when sampling at 5kHz is approximately $\pm 1\mu$m. A pressure transducer is mounted to measure the pressure of the air injected in the gas bearing. The pressure is measured before it is split to the four individual pipes that supply the air to the gas bearing. A three channel optical incremental encoder is mounted is mounted behind the ball bearing (c) and provides the angular position of the rotor with a precision of 2000 counts per revolution. The angular velocity is calculated as the time derivative of the angular position calculated using a backward finite difference approximation. The angular velocity estimate obtained with this procedure is noisy, and it can be low-pass filtered to reduce the noise.

Bibliography

[1] L. R. S. Theisen, F. G. Pierart Vásquez, H. H. Niemann, I. F. Santos, and M. Blanke. “Experimental Grey Box Model Identification of an Active Gas Bearing”. In: *Vibration Engineering and Technology of Machinery*. Ed. by J. Sinha. Springer, 2014, pp. 963–976.

[2] L. R. S. Theisen and H. H. Niemann. “Modelling of Rotor-gas bearings for Feedback Controller Design”. In: *Journal of Physics: Conference Series (Online)* 570 (2014).

[3] L. R. S. Theisen, H. H. Niemann, I. F. Santos, R. Galeazzi, and M. Blanke. “Modelling and identification for control of gas bearings”. In: *Mechanical Systems and Signal Processing* 70–71 (2016), pp. 1150–1170.

[4] L. R. S. Theisen, H. H. Niemann, I. F. Santos, and R. Galeazzi. “Experimental Investigations of Decentralised Control Design for The Stabilisation of Rotor-Gas Bearings”. In: *Proceedings of the XVII International Symposium on Dynamic Problems of Mechanics*. 2015.

[5] L. R. S. Theisen, H. H. Niemann, R. Galeazzi, and I. F. Santos. “Enhancing damping of gas bearings using linear parameter-varying control”. In: *Submitted to Journal of Sound and Vibration* (2016).

[6] L. R. S. Theisen, H. H. Niemann, R. Galeazzi, and I. F. Santos. “Gas Bearing Control for Safe Operation in Critical Speed Regions - Experimental Verification”. In: *Journal of Physics: Conference Series (Online)* 659.1 (2015).

[7] L. R. S. Theisen, H. H. Niemann, and J. F. Camino. “An Application of Gain-Scheduled Control Using State-Space Interpolation to Hydroactive Gas Bearings”. In: *Submitted for IEEE Multi-Conference on Systems and Control 2016* (2016).

[8] G. L. Agrawal. “Foil air bearings cleared to land”. In: *Mechanical Engineering* 120.7 (1998), pp. 78–80.

[9] I. F. Santos. *Vibrations in Rotating Machinery - Modelling, Analysis, Experimental Tests,Vibration Monitoring and Diagnosis*. lecture notes - Technical University of Denmark. 2014.

[10] R. Nicoletti and I. Santos. “Control System Design for Flexible Rotors Supported by Actively Lubricated Bearings”. In: *Journal of Vibration and Control* 14.3 (Mar. 2008), pp. 347–374.

[11] I. Santos. “Mechatronics Applied to Machine Elements with Focus on Active Control of Bearing, Shaft and Blade Dynamics”. Doctoral thesis - Technical University of Denmark - Mechanical Engineering. 2010.

[12] H. J. Ahn, E. H. Maslen, and T. Iwasaki. “Feasibility analysis for the rotordynamic performance of api617”. In: *American Society of Mechanical Engineers, International Gas Turbine Institute, Turbo Expo* 4 (2003), pp. 535–542.

[13] H. Heshmat. “Advancements in the performance of aerodynamic foil journal bearings: high speed and load capability”. In: *Journal of Tribology* (1994).

[14] C. Dellacorte, V. Lukaszewicz, M. Valco, K. Radil, and H. Heshmat. “Performance and durability of high temperature foil air bearings for oil-free turbomachinery”. In: *Tribology Transactions* 43.4 (2000), pp. 774–780.

[15] T. Kim and L. Andres. “Heavily loaded gas foil bearings: A model anchored to test data”. In: *Journal of Engineering for Gas Turbines and Power* 130 (2008).

[16] G. L. Agrawal. “Foil Air/Gas Bearing Technology—An Overview”. In: (). ASME Publication 97-GT-347 (fetched on 01-05-16).

[17] J. S. Larsen, A. C. Varela, and I. F. Santos. “Numerical and experimental investigation of bump foil mechanical behaviour”. In: *Tribology International* 74 (2014), pp. 46–56.

[18] A. B. Palazzolo. “Electromechanical Simulation and Testing of Actively Controlled Rotordynamic Systems With Piezoelectric Actuators”. In: *Journal of Engineering for Gas Turbines and Power* 115.April (1993).

[19] A. B. Palazzolo, R. R. Lin, R. M. Alexander, A. F. Kascak, and J. Montague. “Test and Theory for Piezoelectric Actuator-Active Vibration Control of Rotating Machinery”. In: *Journal of Vibration and Acoustics* 113.April (1991), pp. 167–175.

[20] O. Horikawa and A. Shimokohbe. “An Active Air Bearing - (Control of Radial Axis Motion and Stiffness)”. In: *Jsme International Journal Series Iii-vibration Control Engineering Engineering for Industry* 33.1 (1990), pp. 55–60.

[21] Y. Lihua, S. Yanhua, and Y. Lie. “Active control of unbalance response of rotor systems supported by tilting-pad gas bearings”. In: *Journal of Engineering Tribology Part J* 226.J2 (2012), pp. 87–98.

[22] C. Carmignani, P. Forte, and E. Rustighi. “Active control of rotor vibrations by means of piezoelectric actuators”. In: *Proceedings of the ASME Design Engineering Technical Conference* 6 (2001), pp. 757–764.

[23] J. Tuma, J. Simek, J. Skuta, and J. Los. “Active vibrations control of journal bearings with the use of piezoactuators”. In: *Mechanical Systems and Signal Processing* 36.2 (2013), pp. 618–629.

[24] H. Lau, K. Liu, P. Wong, and W. Wang. “A new design of smart journal bearing based on GMM actuators”. In: *Industrial Lubrication and Tribology* 64.3 (2012), pp. 147–151.

[25] H. Ulbrich. “Comparison of Different Actuator Concepts for Applications in Rotating Machinery”. In: *International Journal of Rotating Machinery* 1.1 (1994), pp. 61–71.

[26] S. Enemark and I. F. Santos. “Rotor-bearing system integrated with shape memory alloy springs for ensuring adaptable dynamics and damping enhancement-Theory and experiment”. In: *Journal of Sound and Vibration* 369 (2016), pp. 29–49.

[27] S. Enemark. “Integration of Shape Memory Alloys into Low-Damped Rotor-Bearing Systems: Modelling, Uncertainties and Experimental Validation”. DCAMM Special Report: S189. PhD thesis. 2015.

[28] H. Mizumoto, S. Arii, Y. Kami, K. Goto, T. Yamamoto, and M. Kawamoto. “Active inherent restrictor for air-bearing spindles”. In: *Precision Engineering* 19.2-3 (Oct. 1996), pp. 141–147.

[29] H. Mizumoto, S. Arii, Y. Yabuta, Y. Tazoe, and S. Yoshito. “Vibration control of a high-speed air-bearing spindle using an active aerodynamic bearing”. In: *International Conference on Control Automation and Systems* 2 (2010), pp. 2261–2264.

[30] J. Larsen. “Nonlinear Analysis of Rotors Supported by Air Foil Journal Bearings – Theory and Experiments”. Technical University of Denmark. PhD thesis. 2014.

[31] S. Morosi. “From Hybrid to Actively-Controlled Gas Lubricated Bearings – Theory and Experiment”. PhD thesis. Technical University of Denmark, 2011.

[32] G. Schweitzer and E. H. Maslen. *Magnetic bearings: theory, design, and application to rotating machinery*. Springer, 2009, 1 vol. (xv, 535 p.)

[33] C. Hoffmann and H. Werner. “A Survey of Linear Parameter-Varying Control Applications Validated by Experiments or High-Fidelity Simulations”. In: *IEEE Transactions on Control Systems Technology* 23.2 (2015), pp. 416–433.

[34] J. S. Larsen and I. F. Santos. “Compliant Foil Journal Bearings-Investigation of Dynamic Properties”. In: *Proceedings of the SIRM 2013, 10th International Conference on Vibrations in Rotating Machines*. 2013.

[35] J. W. Powell. “A review of progress in gas lubrication”. In: *Review of Physics in Technology* 1.2 (1970), p. 96.

[36] S. Morosi and I. F. Santos. “On The Modelling Of Hybrid Aerostatic - Gas Journal Bearings”. In: *Institution of Mechanical Engineers. Proceedings. Part J: Journal of Engineering Tribology* 225.7 (2011), pp. 641–653.

[37] O. Horikawa, H. Osada, and A. Shimokohbe. “An active Air Journal Bearing”. Jpn. In: *Journal of the Japan Society for Precision Engineering* 55.11 (1989), pp. 2063–2068.

[38] I. F. Santos. “Design and evaluation of two types of active tilting pad journal bearings”. In: *The Active Control of Vibration* (1994), pp. 79–87.

[39] I. F. Santos and F. H. Russo. “Tilting-Pad Journal Bearings With Electronic Radial Oil Injection”. eng. In: *Transactions of the ASME Journal of Tribology* 120.3 (1998), p. 583.

[40] I. F. Santos and A. Scalabrin. “Control System Design for Active Lubrication with Theoretical and Experimental Examples”. In: *Journal of Engineering for Gas Turbines and Power, ASME Trans* 125.1 (2003), pp. 75–80.

[41] S. Morosi and I. F. Santos. “Active lubrication applied to radial gas journal bearings. Part 1: Modeling”. In: *Tribology International* 44.12 (2011), pp. 1949–1958.

[42] F. Pierart and I. F. Santos. “Active lubrication applied to radial gas journal bearings. Part 2: Modelling improvement and experimental validation”. In: *Tribology International* 96 (2016), pp. 237–246.

[43] F. G. P. Vasquez. “Model-Based Control Design for Flexible Rotors Supported by Active Gas Bearings - Theory & Experiment”. PhD thesis. Technical University of Denmark, 2016.

[44] F. Pierart Vasquez and I. F. Santos. “Steady state characteristics of an adjustable hybrid gas bearing – Computational fluid dynamics, modified Reynolds equation and experimental validation”. In: *Institution of Mechanical Engineers. Proceedings. Part J: Journal of Engineering Tribology* 229.7 (2015), pp. 807–822.

[45] L. Ljung. *System identification - Theory for the User*. Prentice-Hall, 1999.

[46] G. Goodwin, S. Graebe, and M. Salgado. *Control System Design*. Prentice Hall, 2001.

[47] H. Ahn, S. Lee, S. Lee, and D. Han. "Frequency domain control-relevant identification of MIMO AMB rigid rotor". In: *Automatica* 39.2 (2003), pp. 299–307.

[48] H. M. N. K. Balini, I. Houtzager, J. Witte, and C. W. Scherer. "Subspace identification and robust control of an AMB system". In: *Proceedings of the 2010 American Control Conference* (2010), pp. 2200–2205.

[49] Z. Sun, Y. He, J. Zhao, Z. Shi, L. Zhao, and S. Yu. "Identification of active magnetic bearing system with a flexible rotor". In: *Mechanical Systems and Signal Processing* 49.1-2 (2014), pp. 302–316.

[50] R. Mohd-Mokhtar and L. Wang. "System identification of MIMO magnetic bearing via continuous time and frequency response data". In: *Mechatronics, 2005. ICM '05. IEEE International Conference on*. July 2005, pp. 191–196.

[51] H. Balini. "Advanced Systems Theory Applied to AMB Systems". PhD thesis. Delft University of Technology, 2011.

[52] H. M. N. K. Balini, J. Witte, and C. W. Scherer. "Synthesis and implementation of gain-scheduling and LPV controllers for an AMB system". In: *Automatica* 48.3 (2012), pp. 521–527.

[53] S. Mason, P. Tsiotras, and P. Allaire. "Linear Parameter Varying Controllers for Flexible Rotors Supported on Magnetic Bearings". In: *Proc. 6th Int. Symp. Magnetic Bearings* (1998), pp. 341–351.

[54] F. Loesch et al. "Identification and automated controller design for active magnetic bearing systems". PhD thesis. Diss., Technische Wissenschaften ETH Zurich, Nr. 14474, 2002, 2002.

[55] S. a. Howard. "Misalignment in Gas Foil Journal Bearings: An Experimental Study". In: *Journal of Engineering for Gas Turbines and Power* 131.2 (2009), p. 022501.

[56] a. Sekhar and B. Prabhu. "Effects of Coupling Misalignment on Vibrations of Rotating Machinery". In: *Journal of Sound and Vibration* 185.4 (1995), pp. 655–671.

[57] D. L. Dewell and L. D. Mitchell. “Detection of a Misaligned Disk Coupling Using Spectrum Analysis”. In: *Journal of Vibration Acoustics Stress and Reliability in Design* 106.1 (1984), p. 9.

[58] A. C. Varela and I. F. Santos. “Performance improvement of tilting-pad journal bearings by means of controllable lubrication”. In: *Mechanics & Industry* 13.1 (Apr. 2012), pp. 17–32.

[59] B. Aeschlimann. “Control aspects of high precision active magnetic bearings”. PhD thesis. Technical Ecole Polytechnique Federale de Lausanne, 2001.

[60] B. J. Hamrock, S. R. Schmid, and B. Jacobson. *Fundamentals of fluid film lubrication*. Marcel Dekker, 2004, 699 s.

[61] J. W. Lund. “The Hydrostatic Gas Journal Bearing With Journal Rotation and Vibration”. In: *Journal of Basic Engineering* 86.2 (1964), p. 328.

[62] D. C. Deckler, R. J. Veillette, F. K. Choy, and M. J. Braun. “Modeling of a Controllable Tilting Pad Bearing”. In: *Proceedings of the American Control Conference — 1997* June (1997), pp. 6–10.

[63] R. Herzog, M. Mohler, and C. Gähler. “Multivariable Identification of Active Magnetic Bearing Systems”. In: *JSME International Journal, Series C: Mechanical Systems, Machine Elements and Manufacturing* 40.4 (1997), pp. 584–592.

[64] S. Srinivasan and Y. M. Cho. “Modeling and system identification of active magnetic bearing systems”. In: *Control Applications, 1995., Proceedings of the 4th IEEE Conference on*. Sept. 1995, pp. 252–260.

[65] N.-C. Tsai, C.-H. Kuo, and R.-M. Lee. “Regulation on radial position deviation for vertical AMB systems”. In: *Mechanical Systems and Signal Processing* 21.7 (2007), pp. 2777–2793.

[66] N. Gibson and G. Buckner. “Real-time adaptive control of active magnetic bearings using linear parameter varying models”. In: *SoutheastCon, 2002. Proceedings IEEE*. 2002, pp. 268–272.

[67] H. Choi, G. Buckner, and N. Gibson. “Neural robust control of a high-speed flexible rotor supported on active magnetic bearings”. In: *Proceedings of the American Control Conference* 2006 (2006), pp. 3679–3684.

[68] J. Salazar and I. F. Santos. “Feedback-controlled lubrication for reducing the lateral vibration of flexible rotors supported by tilting-pad journal bearings”. In: *Institution of Mechanical Engineers. Proceedings. Part J: Journal of Engineering Tribology* 229.10 (2015), pp. 1264–1275.

[69] J. De Caigny, J. F. Camino, and J. Swevers. “Interpolation-Based Modeling of MIMO LPV Systems”. In: *IEEE Trans. Control Syst. Technol* 19.1 (2011), pp. 46–63.

[70] J. Shamma and M. Athans. “Gain scheduling: potential hazards and possible remedies”. In: *IEEE Control Systems* 12.3 (1992), pp. 101–107.

[71] J. De Caigny, J. F. Camino, and J. Swevers. “Interpolating model identification for SISO linear parameter-varying systems”. In: *Mechanical Systems and Signal Processing* 23.8 (2009), pp. 2395–2417.

[72] M. Lovera and G. Mercere. “Identification for gain-scheduling: A balanced subspace approach”. In: *Proceedings of the American Control Conference* (2007), pp. 4282899, 858–863.

[73] J. De Caigny, R. Pintelon, J. F. Camino, and J. Swevers. “Interpolated Modeling of LPV Systems”. In: *IEEE Transactions on Control Systems Technology* 22.6 (2014), pp. 2232–2246.

[74] M. Wassink, M. van de Wal, C. Scherer, and O. Bosgra. “LPV control for a wafer stage: beyond the theoretical solution”. In: *Control Engineering Practice* 13.2 (2005), pp. 231–245.

[75] P. Apkarian and R. Adams. “Advanced gain-scheduling techniques for uncertain systems”. und. In: *IEEE Transactions on Control Systems Technology* 6.1 (1998), pp. 21–32.

[76] F. Wu, X. H. Yang, a. Packard, and G. Becker. “Induced L_2-norm control for LPV systems with bounded parameter variation rates”. In: *International Journal of Robust and Nonlinear Control* 6 (1996), pp. 983–998.

[77] J. Qiu, J. Tani, and T. Kwon. “Control of self-excited vibration of a rotor system with active gas bearings”. In: *Journal of Vibration and Acoustics-transactions of the ASME* 125.3 (2003), pp. 328–334.

[78] I. F. Santos and S. Morosi. “Experimental investigations of active air bearings”. In: *Proceedings of ASME Turbo Expo 2012* 7.PARTS A AND B (2012), pp. 901–910.

[79] Z. Cai, M. S. D. Queirozt, and M. M. Khonsari. “Adaptive Control of Active Tilting-Pad Bearings”. In: *Proceedings of 2003 American Control Conference* (2003), pp. 2–7.

[80] D. C. Deckler, R. J. Veillette, M. J. Braun, and F. K. Choy. “Simulation and Control of an Active Tilting-Pad Journal Bearing”. In: *Tribology Transactions* 47.3 (July 2004), pp. 440–458.

[81] J. T. Sawicki and W. K. Gawronski. “Balanced Model Reduction and Control of Rotor-Bearing Systems”. In: *Journal of Engineering for Gas Turbines and Power-transactions of the ASME* 119.APRIL 1997 (2014).

[82] F. Matsumura, T. Namerikawa, K. Hagiwara, and M. Fujita. “Application of gain scheduled $\mathcal{H}_\infty$ robust controllers to a magnetic bearing”. In: *IEEE Transactions on Control Systems Technology* 4.5 (1996), pp. 484–493.

[83] H. Pizarro Viveros and R. Nicoletti. “Lateral Vibration Attenuation of Shafts Supported by Tilting-Pad Journal Bearing With Embedded Electromagnetic Actuators”. In: *Journal of Engineering for Gas Turbines and Power* 136.4 (Dec. 2013), p. 042503.

[84] I. S. Kuseyri. “Robust control and unbalance compensation of rotor/active magnetic bearing systems”. In: *Journal of Vibration and Control* 18.6 (Aug. 2011), pp. 817–832.

[85] J. Witte, H. Balini, and C. Scherer. “Robust and LPV control of an AMB system”. In: *American Control Conference (ACC)* (2010), pp. 2194–2199.

[86] M. Schlotter and P. S. Keogh. “The vibration control of speed-dependent flexible rotor/magnetic bearing systems using linear matrix inequality gain-scheduled H-infinity design”. In: *Proceedings of the Institution of Mechanical Engineers. Part I* 222.I2 (2008), pp. 97–107.

[87] A. A. G. Siqueira, R. Nicoletti, N. Norrick, K. L. Cavalca, H. Fiori De Castro, J. Bauer, and F. Dohnal. “Linear parameter varying control design for rotating systems supported by journal bearings”. In: *Journal of Sound and Vibration, J Sound Vib* 331.10 (2012), pp. 2220–2232.

[88] C. R. Burrows, P. S. Keogh, and M. N. Sahinkaya. “Proceedings of the Institution of Mechanical Engineers , Part C : Journal of Mechanical Engineering Science”. In: (2009).

[89] M. N. Sahinkaya, A.-H. G. Abulrub, C. R. Burrows, and P. S. Keogh. “A Multiobjective Adaptive Controller for Magnetic Bearing Systems”. In: *Journal of Engineering for Gas Turbines and Power* 132.12 (2010), p. 122503.

[90] W. S. Galinaitis and R. C. Rogers. “Compensation for hysteresis using bivariate Preisach models”. In: *Proceedings of the SPIE - the International Society for Optical Engineering* 3039 (June 1997). Ed. by V. V. Varadan and J. Chandra, pp. 538–547.

[91] K. Leang. “Iterative feedforward compensation of hysteresis in piezo positioners”. In: *42nd IEEE Conference on Decision and Control, Vols 1-6, Proceedings* (2003), pp. 2626–2631.

[92] N. Littrell. “Understanding and Mitigating Shaft Runout”. In: *http://rddynamics.com/foil-97-gt-347.pdf* (). Technical note by GE Energy.

[93] S. Skogestad and I. Postlethwaite. *Multivariable Feedback Control: Analysis and Design*. John Wiley & Sons, 2005.

[94] K. Glover and J. C. Doyle. “State-space formulae for all stabilizing controllers that satisfy an H_∞-norm bound and relations to risk sensitivity”. In: *Systems and Control Letters* 11.3 (1988), pp. 167–172.

[95] J. Doyle, K. Glover, P. Khargonekar, and B. Francis. “State-Space Solutions to Standard H-2 and H-Infinity Control-Problems”. In: *IEEE Transactions on Automatic Control* 34.8 (1989), pp. 831–847.

[96] P. Apkarian and H. D. Tuan. “Parameterized LMIs in Control Theory”. In: *SIAM Journal on Control and Optimization* 38.4 (2000), pp. 1241–1264.

[97] S. Boyd. *Linear Matrix Inequalities in Systems and Control Theory*. SIAM, 1994, 202 s.

[98] P. Apkarian and R. J. Adams. “Advanced gain-scheduling techniques for uncertain systems”. In: *Proceedings of the American Control Conference* 5 (1997), pp. 3331–3335.

[99] J. Lofberg. “YALMIP : a toolbox for modeling and optimization in MATLAB”. In: *Computer Aided Control Systems Design, 2004 IEEE International Symposium on* (2004), pp. 284–289.

[100] P. Apkarian. “On the discretization of LMI-synthesized linear parameter-varying controllers”. In: *Automatica* 33.4 (1997), pp. 655–661.

[101] N. Aouf, D. Bates, I. Postlethwaite, and B. Boulet. “Scheduling schemes for an integrated flight and propulsion control system”. In: *Control Engineering Practice* 10.7 (2002), pp. 685–696.

[102] R. A. Hyde and K. Glover. “The application of scheduled $\mathcal{H}_\infty$ controllers to a VSTOL aircraft”. In: *IEEE Transactions on Automatic Control* 38.7 (1993), pp. 1021–1039.

[103] W. J. Rugh and J. S. Shamma. “Research on gain scheduling”. In: *Automatica* 36.10 (2000), pp. 1401–1425.

[104] Freudenberg and Looze. “Right half plane poles and zeros and design tradeoffs in feedback systems”. In: *IEEE Transactions on Automatic Control* 30.6 (1985), pp. 555–565.

[105] H. M. N. K. Balini, C. W. Scherer, and J. Witte. “Performance Enhancement for AMB Systems Using Unstable H_∞ Controllers”. In: *IEEE Transactions on Control Systems Technology* 19.6 (2011), pp. 1479–1492.

[106] A. Cerda Varela. “Mechatronics Applied to Fluid Film Bearings: Towards More Efficient Machinery”. PhD thesis. Technical University of Denmark, 2013.

[107] H. Heshmat, J. A. Walowit, and O. Pinkus. “Analysis of Gas Lubricated Compliant Thrust Bearings”. In: *Journal of lubrication technology* (1983).

[108] H. Heshmat, J. A. Walowit, and O. Pinkus. “Analysis of Gas-Lubricated Foil Journal Bearings”. In: vol. 105. 4. 1982.

[109] L. San Andres and K. Ryu. “Hybrid Gas Bearings With Controlled Supply Pressure to Eliminate Rotor Vibrations While Crossing System Critical Speeds”. In: *Journal of Engineering for Gas Turbines and Power* 130.6 (2008), p. 062505.

[110] A. Dogan, K. Uchino, and R. E. Newnham. “Composite piezoelectric transducer with truncated conical endcaps cymbal”. In: *Ultrasonics, Ferroelectrics and Frequency Control, IEEE Transactions on* (1997).

[111] E. Hendricks, O. Jannerup, and P. H. Sørensen. *Linear Systems Control: Deterministic and Stochastic Methods*. Springer, 2008.

[112] H. Janocha and K. Kuhnen. “Real-time compensation of hysteresis and creep in piezoelectric actuators”. In: *Sensors and Actuators, A: Physical* 79.2 (2000). cited By 102, pp. 83–89.

[113] W. Cummins. *The impulse response function and ship motion,Technical Report 1661*. Tech. rep. David Taylor Model Basin - DTNSRDC, 1962.

[114] C. DellaCorte. “Oil-Free shaft support system rotordynamics: Past, present and future challenges and opportunities”. In: *Mechanical Systems and Signal Processing* 29 (2012), pp. 67–76.

[115] A. Z. Szeri. “Low friction composite-film bearings”. In: *2007 Proceedings of the ASME/STLE International Joint Tribology Conference, IJTC 2007* PART A (2008), pp. 215–217.

[116] S. Zheng, B. Han, Y. Wang, and J. Zhou. “Optimization of Damping Compensation for a Flexible Rotor System With Active Magnetic Bearing Considering Gyroscopic Effect”. In: *IEEE-ASME Transactions on Mechatronics* 19.4 (2014), pp. 1130–1137.

[117] F. G. Pierart and I. F. Santos. “Steady state characteristics of an adjustable hybrid gas bearing - Computational fluid dynamics, modified Reynolds equation and experimental validation”. In: *Proc. Inst. Mech. Eng. Part J.-j. Eng. Tribol* 229.7 (2015), pp. 807–822.

[118] H. H. Niemann, J. Stoustrup, and R. Abrahamsen. “Switching Between Multivariable Controllers”. In: *Optimal Control - Applications and Methods* 25.2 (2004), pp. 51–66.

[119] B. Paijmans, W. Symens, H. V. Brussel, and J. Swevers. “A gain-scheduling-control technique for mechatronic systems with position-dependent dynamics”. In: *American Control Conference, 2006* (June 2006), pp. 2933–2938.

[120] D. Leith and W. Leithead. “Survey of gain-scheduling analysis and design”. In: *International Journal of Control* 73.11 (2000), pp. 1001–1025.

[121] J. De Caigny, J. F. Camino, B. Paijmans, and J. Swevers. “An application of interpolating gain-scheduling control”. In: *Proceedings of IFAC Symposium on Power System, Structure and Control (2007)* 3.1 (2007), pp. 88–93.

[122] M. Kunze, A. Karimi, and R. Longchamp. “Gain-scheduled controller design by linear programming”. In: *2007 European Control Conference, Ecc 2007, Eur. Control Conf., Ecc* (2015), pp. 7068533, 5432–5438.

[123] B. P. Rasmussen and Y. J. Chang. “Stable controller interpolation and controller switching for LPV systems”. In: *Journal of Dynamic Systems, Measurement and Control, Transactions of the ASME* 132.1 (2010), pp. 1–12.

[124] J. D. Bendtsen, J. Stoustrup, and K. Trangbæk. “Multi-Dimensional Gain Scheduling with Application to Power Plant Control”. eng. In: *Proceedings of the IEEE Conference on Decision and Control* 6 (2003), pp. 6553–6558.

Technical University of Denmark
Department of Electrical Engineering
Automation and Control (AUT)
Elektrovej Building 326
DK-2800, Kgs. Lyngby
Denmark
Phone: (+45) 45 25 35 76
Email: info@elektro.dtu.dk
www.elektro.dtu.dk

ISBN: